

# **Diffeomorphic image registration with applications to deformation modelling between multiple data sets**

**Bartłomiej Władysław Papież**

A thesis submitted in partial fulfilment  
for the requirements of the degree  
of Doctor of Philosophy

The research presented in this thesis was carried out at the  
Applied Digital Signal and Image Processing Research Centre,  
School of Computing, Engineering and Physical Sciences,  
University of Central Lancashire,  
UK.

**October 2012**

# Declaration

I declare that, while registered as a candidate for the research degree, I have not been a registered candidate or enrolled student for another award of the University or other academic or professional institution.

I declare that no material contained in this thesis has been used in any other submission for an academic award and is solely my own work.

**Signature:**

**Type of award:** Doctor of Philosophy

**School:** Computing, Engineering and Physical Sciences

# Abstract

Over last years, the diffeomorphic image registration algorithms have been successfully introduced into the field of the medical image analysis. At the same time, the particular usability of these techniques, in majority derived from the solid mathematical background, has been only quantitatively explored for the limited applications such as longitudinal studies on treatment quality, or diseases progression. The thesis considers the deformable image registration algorithms, seeking out those that maintain the medical correctness of the estimated dense deformation fields in terms of the preservation of the object and its neighbourhood topology, offer the reasonable computational complexity to satisfy time restrictions coming from the potential applications, and are able to cope with low quality data typically encountered in Adaptive Radiotherapy (ART). The research has led to the main emphasis being laid on the diffeomorphic image registration to achieve one-to-one mapping between images. This involves introduction of the log-domain parameterisation of the deformation field by its approximation via a stationary velocity field.

A quantitative and qualitative examination of existing and newly proposed algorithms for pairwise deformable image registration presented in this thesis, shows that the log-Euclidean parameterisation can be successfully utilised in the biomedical applications. Although algorithms utilising the log-domain parameterisation have theoretical justification for maintaining diffeomorphism, in general, the deformation fields produced by them have similar properties as these estimated by classical methods. Having this in mind, the best compromise in terms of the quality of the deformation fields has been found for the consistent image registration framework. The experimental results suggest also that the image registration with the symmetrical warping of the input images outperforms the classical approaches, and simultaneously can be easily introduced to most known algorithms.

Furthermore, the log-domain implicit group-wise image registration is proposed. By linking the various sets of images related to the different subjects, the proposed image registration approach establishes a *common subject space* and between-subject correspondences therein. Although the correspondences between groups of images can be found by performing the classic image registration, the reference image se-

---

lection (not required in the proposed implementation), may lead to a biased *mean* image being estimated and the corresponding *common subject space* not adequate to represent the general properties of the data sets.

The approaches to diffeomorphic image registration have been also utilised as the principal elements for estimating the movements of the organs in the pelvic area based on the dense deformation field prediction system driven by the partial information coming from the specific type of the measurements parameterised using the implicit surface representation, and recognising facial expressions where the stationary velocity fields are used as the facial expression descriptors. Both applications have been extensively evaluated based on the real representative data sets of three-dimensional volumes and two-dimensional images, and the obtained results indicate the practical usability of the proposed techniques.

# Contents

<b>List of Figures</b>	<b>viii</b>
<b>List of Tables</b>	<b>x</b>
<b>List of Algorithms</b>	<b>xii</b>
<b>List of Symbols</b>	<b>xviii</b>
<b>List of Acronyms</b>	<b>xx</b>
<b>1 Introduction</b>	<b>1</b>
1.1 Image registration . . . . .	1
1.2 Motivation of work undertaken . . . . .	5
1.3 Organisation of thesis . . . . .	6
1.4 Contributions of the research . . . . .	8
<b>2 Principles of image registration</b>	<b>10</b>
2.1 Introduction . . . . .	10
2.2 Principles of image registration . . . . .	18
2.3 Similarity criteria . . . . .	20
2.4 Nature of transformation . . . . .	23
2.5 Additional image registration constraints . . . . .	29
2.6 Solving image registration problem . . . . .	35
2.7 Summary . . . . .	36
<b>3 Implementations of image registration</b>	<b>38</b>
3.1 Classical approaches to image registration . . . . .	38
3.1.1 Steepest descent approach . . . . .	39
3.1.2 Newton's iteration approach . . . . .	41
3.1.3 Demon approach . . . . .	44
3.2 Diffeomorphic image registration . . . . .	46
3.2.1 Small-step approaches . . . . .	47

3.2.2	Exponential updates . . . . .	49
3.2.3	Log-domain parameterisation . . . . .	50
3.3	Consistent image registration . . . . .	54
3.4	Image registration with symmetric warping . . . . .	61
3.4.1	Small-step multiple pass approach . . . . .	62
3.4.2	Direct inverse update estimation approach . . . . .	63
3.4.3	Log-domain parameterised approach with symmetric warping . . . . .	65
3.5	Summary . . . . .	67
<b>4</b>	<b>Comparison of image registration</b>	<b>70</b>
4.1	Introduction . . . . .	70
4.2	Environment for experiments . . . . .	75
4.2.1	Data set description . . . . .	75
4.2.2	Validation criteria . . . . .	78
4.2.3	Implementation remarks . . . . .	82
4.3	Qualitative and quantitative comparison . . . . .	83
4.3.1	Impact of the stationary velocity field parameterisation . . . . .	84
4.3.2	Impact of the inverse consistency criterion . . . . .	97
4.3.3	Impact of the symmetrisation of registration . . . . .	103
4.3.4	Comparison of different image registration methods . . . . .	107
4.3.5	Remarks on determining design parameters . . . . .	113
4.3.6	Validation of inverse deformation field estimation . . . . .	114
4.4	Summary . . . . .	115
<b>5</b>	<b>Group-wise image registration</b>	<b>118</b>
5.1	Introduction . . . . .	118
5.2	Log-domain group-wise registration . . . . .	120
5.3	Solution schemes . . . . .	123
5.4	Evaluation . . . . .	125
5.4.1	Evaluation criteria . . . . .	125
5.4.2	Evaluation examples . . . . .	126
5.5	Summary . . . . .	132
<b>6</b>	<b>Statistical modelling of deformations</b>	<b>133</b>
6.1	Introduction . . . . .	134
6.2	Inter-subject motion model . . . . .	136
6.3	Intra-subject motion model . . . . .	136
6.4	Surrogate representation . . . . .	137
6.5	Generation of 4D motion model . . . . .	137

---

6.6	Evaluation of proposed framework . . . . .	140
6.6.1	Synthetic example . . . . .	141
6.6.2	Real data evaluation . . . . .	142
6.7	Summary . . . . .	144
<b>7</b>	<b>Facial expression representation</b>	<b>145</b>
7.1	Introduction . . . . .	145
7.2	Common face space generation . . . . .	147
7.2.1	Diffeomorphic implicit group-wise image registration . . . . .	147
7.3	Facial expression modelling . . . . .	150
7.3.1	Velocity field based facial expression model . . . . .	150
7.3.2	Point Distribution Model . . . . .	150
7.4	Experimental results . . . . .	152
7.4.1	Separability analysis . . . . .	152
7.4.2	Facial expression recognition . . . . .	162
7.5	Summary . . . . .	168
<b>8</b>	<b>Contributions and future works</b>	<b>170</b>
8.1	Contributions . . . . .	170
8.2	Future works . . . . .	173
	<b>References</b>	<b>176</b>
<b>A</b>	<b>Results of registration using partially synthetic data</b>	<b>193</b>
<b>B</b>	<b>Results of facial expression recognition experiments</b>	<b>198</b>
<b>C</b>	<b>Publications</b>	<b>202</b>

# List of Figures

2.1	Classification of image registration methods. . . . .	12
2.2	Multimodal examples of the brain images taken from different scanners	23
2.3	Example of images of squares that shows the ambiguity arising from the non-regularised image registration. . . . .	26
2.4	Effects of different regularisation terms for registration of two images of square shapes . . . . .	27
2.5	Effects of different parameter values for the linear elastic regularisa- tion of deformation field of two images of square shapes . . . . .	28
3.1	Examples of the forward and backward integration of the velocity field for the sample images . . . . .	55
3.2	Examples of the inconsistency and consistency between forward and backward transformation . . . . .	56
3.3	Symmetric image registration scheme . . . . .	61
4.1	Example of the synthetically generated data . . . . .	76
4.2	Example of the partially synthetically generated data . . . . .	77
4.3	Example of MRI brain data used in the experimental validation. . . .	78
4.4	Example of CT lung data used in the experimental validation. . . . .	79
4.5	Example of MRI pelvic area data used in the experimental validation.	79
4.6	Results obtained for the simulated data set using different types of the steepest-like approach . . . . .	86
4.7	Results obtained for the simulated data set using different types of the Newton's iteration approach . . . . .	87
4.8	Results obtained for the simulated data set using different types of the Demon approach . . . . .	88
4.9	Results obtained for the MRI brain data set using different formula- tions of the steepest-like approach . . . . .	90
4.10	Results obtained for the MRI brain data set using different formula- tions of the Newton's iteration approach . . . . .	91

4.11	Results obtained for the MRI brain data set using different formulations of the Demon approach . . . . .	92
4.12	Results obtained for the MRI pelvic-area data set using different formulations of the steepest-like approach . . . . .	94
4.13	Results obtained for the MRI pelvic-area data set using different formulations of the Newton's iteration approach . . . . .	95
4.14	Results obtained for the MRI pelvic-area data set using different formulations of the Demon approach . . . . .	96
4.15	Results obtained for the CT lung data set using different formulations of the steepest-like approach . . . . .	98
4.16	Results obtained for the CT lung data set using different formulations of the Newton's iteration approach . . . . .	99
4.17	Results obtained for the CT lung data set using different formulations of the Demon approach . . . . .	100
4.18	Results obtained for the synthetic data set using different approaches	108
4.19	Results of evaluation the inverting methods for the synthetic data . .	116
5.1	Results of performing the log-domain implicit group-wise registration for the illustrative data set evaluation based on the Demon force . . .	128
5.2	Results of performing the log-domain implicit group-wise registration for the MRI pelvic-area data set evaluation based on the Demon force	129
5.3	Example of inconsistency in the MRI data acquisition . . . . .	130
5.4	Results of performing the log-domain implicit group-wise registration for the MRI brain data set evaluation based on the Demon force . . .	131
6.1	Bladder segmented from MRI and sequence of its implicit representation with highlighted surface position. . . . .	138
6.2	Training process and deformation field prediction using the implicit shape-based dense deformation field estimation model for prostate . .	140
6.3	Example of synthetic deformation field used in the experiments . . .	143
6.4	The variability of the major modes of the implicit shape representation of the prostate, bladder and rectum . . . . .	143
7.1	Scheme for establishing correspondences between faces using the log-domain implicit group-wise registration. . . . .	148
7.2	Grey-level average of mean face before registration, and after registration, obtained for different sets of images from training data set . .	149
7.3	Manually selected landmarks for neutral happiness and sadness expression . . . . .	151
7.4	Automatically selected landmarks for happiness and sadness expression	151

7.5	Variations of the major modes of the Point Distribution Model for automatically selected landmarks . . . . .	152
7.6	Variations of the major modes of the velocity fields representation . .	153
7.7	Sample subject showing seven basic expressions: neutral, angry, disgust, fear, happiness, sadness, and surprise. . . . .	154
7.8	Samples of happiness expression for of different expression intensity ranges from low, middle, high to highest. . . . .	154
7.9	Separability analysis for manually selected landmarks using first three principal components . . . . .	156
7.10	Separability analysis for automatically selected landmarks using first three principal components . . . . .	157
7.11	Separability analysis for deformation field representation using first three principal components . . . . .	158
7.12	Separability analysis for the velocity field representation using first three principal components . . . . .	159
7.13	Separability of expression for different features in terms of separability criterion . . . . .	160
7.14	Recognition rates of four classification methods for different intensity expression levels and for different facial expression representations . .	168
A.1	Results obtained for the partially simulated data set using different types of the steepest-like approach . . . . .	194
A.2	Results obtained for the partially simulated data set using different types of the Newton's iteration approach . . . . .	195
A.3	Results obtained for the partially simulated data set using different types of the Demon approach . . . . .	196
A.4	Results obtained for the synthetic data set using different approaches	197

# List of Tables

4.1	Average Region Overlapping values of the brain structures after 100 executed iterations for different image registration methods. . . . .	109
4.2	Average Region Overlapping values of the pelvic-area structures after 100 executed iterations for different image registration methods. . . . .	111
4.3	Experimental results of the computational effort for the presented method . . . . .	114
4.4	Comparison results for inverse deformation field estimation algorithms	115
5.1	Average Region Overlapping (ARO) values of the brain structures after log-domain implicit group-wise image registration. . . . .	130
6.1	Errors of estimation deformation fields obtained using different shape representations . . . . .	142
6.2	Errors of the prediction of the deformation fields with respect to the results of direct registration. . . . .	142
6.3	Minimum of the determinant of the Jacobian matrix for the variability of the trained motion model using the deformation fields and the stationary velocity fields. . . . .	144
7.1	Matrix of the expression separability criterion of for the manually selected landmarks . . . . .	161
7.2	Matrix of the expression separability criterion of for the automatically selected landmarks . . . . .	161
7.3	Matrix of the expression separability criterion of for the full deformation fields . . . . .	162
7.4	Matrix of the expression separability criterion of for the full velocity fields . . . . .	162
7.5	Confusion matrix of LDC for manually selected landmarks . . . . .	166
7.6	Confusion matrix of LDC for automatic selected landmarks . . . . .	166
7.7	Confusion matrix of LDC for full deformation fields . . . . .	166
7.8	Confusion matrix of LDC for full velocity fields . . . . .	166

---

7.9	Summary of the recognition rates from Tables 7.5 - 7.8. . . . .	167
7.10	Average recognition rates for different classifier methods . . . . .	167
B.1	Confusion matrix of QDC for the manually selected landmarks . . . .	198
B.2	Confusion matrix of QDC for the automatic selected landmarks . . .	199
B.3	Confusion matrix of QDC for the full deformation fields . . . . .	199
B.4	Confusion matrix of QDC for the full velocity fields . . . . .	199
B.5	Confusion matrix of NCC for the manually selected landmarks . . . .	199
B.6	Confusion matrix of NCC for the automatic selected landmarks . . .	200
B.7	Confusion matrix of NCC for the full deformation fields . . . . .	200
B.8	Confusion matrix of NCC for the full velocity fields . . . . .	200
B.9	Confusion matrix of NBC for the manually selected landmarks . . . .	200
B.10	Confusion matrix of NBC for the automatic selected landmarks . . .	201
B.11	Confusion matrix of NBC for the full deformation fields . . . . .	201
B.12	Confusion matrix of NBC for the full velocity fields . . . . .	201

# List of Algorithms

1	Steepest descent approach . . . . .	41
2	Newton's iteration approach . . . . .	43
3	Demon approach . . . . .	46
4	Fast exponential integration of velocity field . . . . .	50
5	Log-domain steepest descent approach . . . . .	53
6	Consistent log-domain steepest descent approach . . . . .	60
7	Direct inverse deformation field approach to image registration with symmetric warping . . . . .	64
8	Proposed method of inverting deformation field . . . . .	66
9	Log-domain image registration with symmetric warping . . . . .	68
10	Log-domain implicit reference group-wise image registration based on the symmetric Demon force . . . . .	125

# Acknowledgements

You see things; and you say "Why?" But I dream things that never were; and I say "Why not?"

George Bernard Shaw, "Back to Methuselah" (1921), part 1, act 1

During my doctoral studies and research conducted at the University of Central Lancashire (UCLan) in Preston, I met many wonderful people that I would like to thank; correspondingly I also would like to express my sincere gratitude to those who were far away from me.

First of all, I would like to thank Dr. Bogdan J. Matuszewski, the director of my PhD studies and the main advisor of my research project, for the more than two-year *lesson* on medical image processing and computer vision, for introducing me into the world of research, for countless scientific discussions, with great patience throughout the entire period of my work at the Applied Digital Signal and Image Processing Research Centre (ADSIP), for insightful guidance in editing research papers, and for the time spent in a very arduous task of preparing me for the presentation of our results.

I would also like to thank professor Lik-Kwan Shark, the second supervisor, for the valuable suggestions and comments during the writing up of this thesis as well as patient corrections of my language mistakes in the submitted scientific articles.

I am grateful to professor Tomasz P. Zieliński, the third supervisor, from the AGH University of Science and Technology (AGH UST) in Krakow, for influencing me to go ahead in the scientific work, and the kind comments and suggestions to my work and the published articles.

I would like to acknowledge professor Christopher Moore from the Christie Hospital NHS Foundation Trust in Manchester for providing helpful medical feedback on the undertaken research.

I would like to thank those whom I met every day at work: Dr. Wei Quan, and Lili Tao for a friendly atmosphere at our office and the help I received from you. I would like to give sincere thanks to Dr. Sarma Volety and his wife Anjani, for their

kindness, heartiness, warmth and long-evening enjoyable talks about everything and nothing. I also want to thank to Dr. Diana Yifan Xu and Marine Breuilly for their openness when I came first time to Preston and after. Thanks to the PhD students and post-doctoral assistants at the *second floor* of the School of Computing, Engineering and Physical Science (CEPS), who I met during my stay at UCLan, for making my stay in Preston not only working-time but also giving me the opportunity to explore the differences in our cultures and ways of thinking.

Thanks to all those who I have met through my crawl on the scientific paths, first during the studies on Electrical Engineering, and then Computer Science at the Faculty of Electrical Engineering, Automatics, Computer Science and Electronics at the AGH UST in Krakow, and those who motivated me, sometimes in very specific ways, to continue to deal with my weaknesses. I am especially grateful to Dr. Krystyna Wodnicka for her continuous interest on my academic work, and her advices at various points in my studies.

I would like to give my warmest thanks to my parents for their never-ending love and strong support that they bestow upon me from the beginning, and also for their effort and sacrifice to invest in my upbringing and education. Thanks to my sister and brothers: Malgosia, Marcin, Kuba, and Piotrek for consistent support and being interested in my research.

Last but not least, I owe my heartfelt thanks to the most important person in my life. I would have never pursued my passion on the science and technology to accomplish this work and following dissertation without your patience, your greatest sacrifice, and your constant encouragement every day. Just thank you, my fiancée Kingo.

Preston, March 2012

The presented work was partially supported by the Metrology Guided Radiation Therapy (MEGURATH) project.

# Podziękowania

Niektórzy ludzie postrzegają rzeczy w ich naturalnym stanie i zadają sobie pytanie: Dlaczego? Ja marzę o rzeczach, których nigdy nie było i mówię sobie: Dlaczego nie?

George Bernard Shaw, "Powrót do Matuzalema"(1921), część 1, akt 1

W czasie studiów doktoranckich i pracy naukowej w University of Central Lancashire w Preston spotkałem wielu wspaniałych ludzi, którym chciałbym w tym miejscu podziękować; tak samo zresztą tym, którzy byli daleko ode mnie a którym jestem winien jeszcze serdeczniejsze podziękowania.

Przede wszystkim chciałbym podziękować doktorowi Bogdanowi J. Matuszewskiemu, promotorowi i głównemu opiekunowi tej pracy doktorskiej, za ponad dwuletnią *lekcję* przetwarzania obrazów medycznych, wprowadzenie w świat badań naukowych, niezliczoną ilość dyskusji naukowych, olbrzymią cierpliwość w czasie całego okresu mojej pracy w Applied Digital Signal and Image Processing Research Centre (ADSIP), pomoc przy redagowaniu artykułów i referatów naukowych, mozolne przygotowywanie mnie do prezentacji naszych wyników badań.

Chciałbym również podziękować profesorowi Lik-Kwan Sharkowi, promotorowi, za czas poświęcony mi w czasie tych dwóch lat pracy w ADSIP Research Centre, cenne sugestie i uwagi w czasie pisania tej pracy doktorskiej jak również cierpliwe poprawianie moich błędów w zgłaszanych artykułach naukowych i tej pracy doktorskiej.

Profesorowi Tomaszowi P. Zielińskiemu z Akademii Górniczo-Hutniczej (AGH) w Krakowie, promotorowi, za namówienie mnie i motywowanie do pracy naukowej, życzliwe komentarze i uwagi do mojej pracy i publikowanych artykułów.

Dziękuję profesorowi Christopherowi Moore'owi z Christie Hospital NHS Foundation Trust w Manchesterze za uwagi dotyczące medycznych aspektów prowadzonych badań.

Chciałbym podziękować tym, których codziennie spotykałem w czasie pracy: doktorowi Weiowi Quanowi oraz Lili Tao za sympatyczną atmosferę w pracy i pomoc, którą od Was otrzymałem. Doktorowi Sarmie Volety i jego żonie Anjani, za

okazaną życzliwość, gościnność, serdeczność i przegadane wieczory *o wszystkim i o niczym*. Doktor Diana Yifan Xu i Marine Breuilly za otwartość, kiedy pierwszy raz pojawiłem się w Preston. Dziękuję doktorantom z *drugiego piętra* wydziału Computing, Engineering and Physical Science (CEPS), których spotykałem w czasie swojego pobytu w UCLan za to ten czas w Preston nie tylko był czasem pracy ale także czasem odkrywania różnic w naszych kulturach i sposobach myślenia.

Dziękuję tym wszystkim, których spotkałem stawiając pierwsze kroki na swojej naukowej drodze, podczas studiów na Elektrotechnice, a także Informatyce na Wydziale Elektrotechniki, Automatyki, Informatyki i Elektroniki w AGH, a którzy w różnoraki sposób motywowali mnie do ciągłej pracy nad sobą. Dziękuję szczególnie doktor Krystynie Wodnickiej za ciągle zainteresowanie moją pracą naukową, wsparcie w różnych momentach moich studiów i przypominanie, że *nie samą nauką żyje człowiek*.

Moje najserdeczniejsze podziękowania chce także skierować rodzicom, za ich bezgraniczną miłość, wsparcie którym mnie obdarzali i obdarzają od początku, za ich nieoceniony wysiłek i poświęcenie włożone w moje wychowanie i edukację. Dziękuję mojemu rodzeństwu: Małgosi, Marcinowi, Kubie i Piotrkowi za wspieranie dobrym słowem i zainteresowaniem moją pracą.

I Tej, która tutaj jest wymieniona na końcu a wszędzie indziej jest pierwszą; Tej, która obdarza mnie swoją miłością na każdym kroku mojego życia; bez Twojej *anielskiej* cierpliwości, Twojego największego poświęcenia, Twojej motywacji każdego dnia, nie mógłbym realizować swoich pasji naukowych i ukończyć tej pracy doktorskiej. Po prostu dziękuję Ci kochana Kingo.

Preston, Marzec 2012

Prezentowana praca była częściowo finansowana z projektu Metrology Guided Radiation Therapy (MEGURATH).

# List of Symbols

## Images

$I_f$	Fixed (reference) image
$I_m$	Moving image
$d$	Spatial dimension of image
$I(\vec{x})$	Intensity value of image $I$ at position $\vec{x}$
$I(\vec{\varphi})$	Image $I$ warped by the transformation $\vec{\varphi}$
$\nabla I$	Gradient of image $I$
$*$	Convolution operator
$G*$	Convolution by the Gaussian filter
$\mathbf{I}$	Set of images
$k$	Number of images in the set

## Transformation

$\vec{x}$	Spatial position on the regular grid
$x^l$	$l$ -th component of spatial position $\vec{x}$
$\vec{\varphi}$	Transformation
$\vec{u}$	Displacement field
$\circ$	Composition operator
$J(\cdot)$	Jacobian matrix
$\det(J)$	Determinant of Jacobian matrix
$\vec{d}u$	Update of the displacement field
$\vec{w}$	Time-dependent velocity field
$\vec{v}$	Stationary velocity field
$\vec{d}v$	Update of the velocity field
$\exp(\cdot)$	Exponential mapping
$\log(\cdot)$	Principal logarithm
$[\cdot, \cdot]$	Lie bracket operator
$BCH[\cdot, \cdot]$	Baker-Campbell-Hausdorff operator
$\mathbf{R}$	Rotation matrix

$\vec{T}$	Translation vector
$B$	B-spline polynomial
$\lambda_{diff}$	Diffusive parameter
$\mu_{elas}$	Elasticity parameter
$\lambda_{elas}$	Elasticity parameter
$\lambda_{curv}$	Curvature parameter

## Optimisation

$\varepsilon(\vec{u})$	Objective function with respect to displacement $\vec{u}$
$Sim(\cdot, \cdot)$	Similarity criterion
$\gamma$	Weighting similarity parameter
$\nu$	Edge parameter
$\eta$	Normalised gradient
$Reg(\cdot)$	Regularisation term
$\alpha$	Regularisation weight
$Pen(\cdot)$	Penalty term
$\beta$	Penalisation weight
$i$	Iteration index
$\nabla$	Gradient operator
$\Delta$	Laplace operator
$\nabla \cdot$	Divergence operator

## Other

$P(I_f, I_m)$	Joint probability density function of the intensity
$p(I_f)$	Marginal probability function of the intensity

# List of Acronyms

AAM	Active Appearance Model
ARO	Average Region Overlapping
ART	Adaptive Radiotherapy
BCH	Baker-Campbell-Hausdorff formula
CBCT	Cone-Beam Computed Tomography
CC	Correlation Coefficient
CR	Correlation Ratio
CT	Computed Tomography
ED	Euclidean Distance
FFD	Free Form Deformations
HCI	Human-Computer Interaction
HE	Harmonic Energy
ICA	Independent Component Analysis
ICC	Inverse Consistency Criterion
ICE	Inverse Consistency Error
IV	Intensity Variance
kPCA	kernel Principal Component Analysis
LDA	Linear Discriminant Analysis
LDC	Linear Discriminant Classifier
MI	Mutual Information

MRI	Magnetic Resonance Imaging
NBC	Naive Bayes Classifier
NGF	Normalised Gradient Field
NMI	Normalised Mutual Information
NNC	Nearest Neighbour Classifier
PCA	Principal Component Analysis
PDE	Partial Differential Equations
PDM	Point Distribution Model
PET	Positron Emission Tomography
RO	Region Overlapping
SSD	Sum of the Squared Differences
SSM	Statistical Shape Model
SSV	Shape Space Vector
QDA	Quadratic Discriminant Analysis
QDC	Quadratic Discriminant Classifier
TC	Topographic Context
TRE	Target Registration Error
US	Ultrasound Scanning

# Chapter 1

## Introduction

### 1.1 Image registration

Image registration is one of the fundamental tasks in medical image processing. It can be simply considered as a process of aligning/matching two or more images exhibiting some resemblance(s) in terms of their contents. For the most complicated cases, the images can be very hard to be compared directly and sometimes the correspondences between images can not be visually recognised even by the human observers. The images could have been captured at different times, from different viewpoints, using various types of scanners thereby representing different imaging modalities (e. g. Computed Tomography, Magnetic Resonance Imaging or Ultrasound Scanning, etc.). In addition, the complexity of image registration comes from the fact that images can represent either different instances of the same subjects (e. g. multiple scans of the same patient during the treatment/clinical trial) to enable intra-subject analysis, or different subjects having similar properties (e. g. the planning scans of the different patients) to model the inter-subject variability.

Over the last twenty years, a significant amount of work has been carried out on not only the theoretical and methodological aspects but also on application-driven developments of image registration. Thus, the most common approaches have been described in the standard textbooks [51, 90, 158, 134, 92] and surveys [81, 164]. The major research has been mainly focused on low-dimensional space parameterised registration (e. g. rigid and/or affine registration) or deformable registration when dense data sets (images) are available. Indeed, such kind of registration techniques can be stated as an optimisation problem of a predefined objective function with respect to the estimated transformation. The choice of the objective function (or to be more precise, the choice of the principal elements of the objective function such as similarity measure, regularisation term and penalty terms) is a matter of prior user knowledge of the characteristics of the input data that are to be registered,

and the desired properties of the estimated transformation. Thus, due to a wide range of data types, acquisition protocols, and different objects/organs represented in the data, etc., it is not surprising that there is an enormous number of image registration methods. Whereas most of these methods are strictly application-driven techniques developed to cope with the particular problem, some of them can be recognised as more general thereby they have been successfully applied to solve various issues. Examples of the commonly used methods may include original Demon approach [138] and its subsequent extensions [148, 143, 144, 145], methods based on the calculus of variations [56, 24, 57, 78], B-spline parameterisation of transformation [112, 118, 128, 115, 130, 43], or *optical flow* approaches [59, 154, 155, 60].

Recently, specific class of the image registration methods - the diffeomorphic image registration has been recognised as a very important technique to deal with a range of biomedical problems. *Diffeomorphism* can be simply considered as a smooth one-to-one transformation (mapping) that also has a smooth inverse transformation. Although at the first sight the strict mathematical formalism may give an impression of not adequate for real biomedical problems, the properties of the diffeomorphic transformation can provide very versatile solutions in many applications. As a matter of fact that in most real biomedical cases, the adapted transformation (deformation) model does not reflect the underlying mechanisms (true tissue properties) for the changes between images (or sets of images). The diffeomorphic formulation fulfils by definition the conditions such as continuity and preservation of the topology among organs to avoid cracks and folds in the estimated transformations. Maintaining of the objects' topologies is very important for applications such as automatic labelling and segmentation driven by the atlases, longitudinal studies on disease progression, or observations of the treatment outcomes due to therapy to name a few of them. There are various methodologies which have been considered to provide efficient diffeomorphic image registration formulation, the most know methods obey the *small step* constraint [56, 25, 115, 155], log-Euclidean framework that is expressed via stationary velocity field parameterisation [4, 5, 143, 144, 145, 53], or time dependent modelling of the displacement field flow [26, 15, 14].

On the other hand, in many practical situations the complete data sets are not available or the overall image quality is low, thereby the traditional registration methods, aiming at estimation of the dense deformation field, can not be directly applied to such data as the similarity measure for assessing the quality of the estimated deformation can not be reliably computed. Thus far, the corresponding dense displacement field has to be estimated based on incomplete data. However, in some cases it is possible to obtain high quality training data from which a deformation (motion) model can be built. Subsequently such model can be either

incorporated into the classical image registration process [3, 135] as an additional constraint (statistically-constrained image registration) or linked somehow to a partial information delivered by a measurement (sometimes also called surrogate) that is affected by the deforming tissue and therefore can be used to directly infer about the tissue deformation [159, 73, 75, 74, 36, 123, 124]. Although some efforts have been recently undertaken to improve the surrogate-based image registration and segmentation, it still remains a challenging problem particularly when it is to be applied as a part of a clinical procedures.

The aforementioned approaches require an appropriate measurement that suitably represents tissue deformations and in the same time it is easy to extract from often severely corrupted data. Currently, such surrogates are most often defined by a set of points. Some implementations of this methodology include online systems for simultaneous compensation of laparoscopic camera motion and respiration induced tissue deformations [93], 4D image-guided lung radiation therapy [159, 73, 75, 74], and pelvic area subject-specific [125] as well as population based [123, 124] organs modelling. For lung motion estimation the air content of a reference volume as a predictor was used [36]. Although the research in this area is ongoing, the results reported so far in literature are not satisfactory, mostly due to errors of establishing point correspondences between different representative phases of organs motion.

Equally important for prediction-based estimation of a dense deformation field is constructing the motion model that can capture a wide spectrum of possible variations of organs' motion. This task in itself is challenging as it requires an accurate calculation of the deformation field for the data present in the training data set, and subsequently multiple execution of the deformable image registration algorithms can be highly time consuming. Whereas the intra-patient motion model can be easily generated utilising multiple registrations between the acquired volumes representing different phases of organs' motion [125, 159], the inter-patient motion model that is built in a similar manner, is biased towards the chosen reference image. Therefore, a mean reference patient has to be estimated first and then the *common patient space* can be established [9, 28, 42, 153, 98]. Moreover, in many recent approaches [159, 73, 75, 74] due to a large dimensionality of data (three-dimensional deformation fields for each image), the statistical models of the deformation fields were obtained by directly applying the re-parameterisation and dimension reduction algorithms such as the Principal Component Analysis [16] to the deformation fields (or its B-spline parameterisation [113, 114, 22]). Although these approaches were to some extent successful in particular applications, this motion model has some disadvantages. The most important is that the eigenvectors do not form a vector space of valid deformation fields (e.g. diffeomorphism is not guaranteed to be preserved) [4].

Thus, the recently proposed log-domain parameterisation of the deformation field via stationary velocity fields [4, 17] theoretically gives a versatile tool to cope with the problem of an empirically learnt deformation model. Some results of calculating the *mean* motion model based on the velocity fields of the patient-independent respiratory cycle for the purpose of predicting the deformation field in the four-dimensional radiotherapy of lungs, were reported in [36]. Other works that aimed at calculating *vectorial* statistics on the diffeomorphic displacement fields, look into the white matter changes in the brains of the HIV/AIDS patients [135].

Another research question that has been considered in the computer vision thus far, is utilising the estimated deformation fields as the feature vectors in the facial expression modelling and recognition systems. The displacement fields can be calculated for two-dimensional static images or dynamic sequences to represent different subjects under a specific facial expression for the purpose of the subject recognition [60] or various subject's expressions for expression recognition [154, 126, 99, 98]. In all cases, the motion fields have been successfully considered as the automatically generated facial expression descriptors.

All in all, the first part of this thesis deals with the quantitative and qualitative assessment of the non-rigid image registration techniques mostly focusing on the diffeomorphic approaches such as the *small-step* approaches and the different methods utilising the stationary velocity fields parameterisation. An extensive comparison is included to show the adequacy of the log-domain parameterisation in several possible biomedical applications including brain labelling, and motion estimation of organs in the pelvic area and respiratory cycle. In addition, a novel image registration algorithm (that has been applied to the pelvic-area MRI data) is proposed, subsequently with a more robust method of direct inverting deformation field than the previously reported methods. Concerning the applications, the second part of this thesis presents the dense deformation field prediction framework that is built using in the principles of the previously investigated image registration methods and the implicit surfaces as a measurement parameterisation of the organs' of interest i. e. bladder and rectum. Similarly, when the facial expression recognition system based on the stationary velocity field parameterisation is introduced, the subject-independent facial expression descriptors are established utilising the log-domain implicit group-wise registration method and the consistent pair-wise face registration. Thus, this thesis is devoted to the methodological aspects and the direct applicability of image registration to the biomedical data.

## 1.2 Motivation of work undertaken

The primary motivation of the project was to develop a robust method for movement estimation of the prostate and adjacent organs for the possible radiotherapy applications. The motion estimation technique has to provide the necessary accuracy in terms of the prostate position in a suitable time scale, dealing additionally with the problem of the partially missing data, often severely corrupted by different types of noise. In the presented research an attempt to solve such registration problem is made with the help of an empirically learn deformation (motion) model. For this purpose, the training data has to be first pre-processed to extract information about possible dependencies between observed deformation fields and measurement domain (e. g. surfaces of the rectum or/and the bladder). This task itself is challenging as it requires an accurate calculation of the deformation field for the three-dimensional volumes included in the representative training data set by utilising the deformable image registration algorithm. Although, the data represent the same area of different subjects, each set used for training stage has to be first mapped to the so-called *common subject space* to make the calculated deformations subject-independent. Thus, an investigation of the method for finding an appropriate *common subject space* has to be additionally undertaken. The aforementioned deformation model has been constructed from training three-dimensional data, mainly MRI, taken from different but representative *phases* of organ's deformation. To keep overall consistency with respect to the diffeomorphic properties of the deformation fields, the log-domain framework is established. Moreover, the proposed method extends the current approaches by attempting first time to use the implicit shape representation of the selected measurements for regression model estimation.

The research also includes the systematic and quantitative evaluation of the previously proposed methods for pair-wise image registration and their comparison with the methods developed during the project with a major focus on the different formulations of the diffeomorphic image registration. The comparisons are performed both on the simulated data to show accuracy with respect to the ground truth parameters and on real data to show suitability of these methods for medical applications.

The main application outcomes of the proposed research are believed to have a potential for improving the accuracy of radiotherapy, but other medical applications could also benefit from the developed techniques.

## 1.3 Organisation of thesis

The thesis can be divided into two separate parts: methodologies and applications. The first part consists of a general overview of image registration, a detailed description of the methods investigated as well as qualitative and quantitative assessments of those methods. Additionally, a novel method for directly inverting deformation fields and the image registration that utilised this method are also introduced. The second part of the thesis is focused on the research of possible usage of the presented and proposed image registration algorithms for the image-guided adaptive radiotherapy of prostate cancer and for facial expressions recognition systems.

Chapter 1 puts the research described in the following chapters in the context of the current state-of-the-art of image registration. Secondly, the motivations of the research project are explained and the research questions are stated. This chapter also enumerates the author's contributions.

Chapter 2 gives an overview of the image registration problem that is studied in this thesis. First, the generic classification types are introduced to show the basic components of image registration such as similarity measures, models of transformation (deformation), incorporated constraints, and a wide range of medical applications. Also the importance of further investigation in this area is outlined, with a particular emphasis in the context of the biomedical applications. The following sections of this chapter look at the commonly known techniques and briefly describe their properties. Additionally, the notation used in this thesis is introduced.

Chapter 3 provides detailed analysis of the commonly used optimisation methods applied to the image registration algorithms such as the steepest descent-like method, the Newton's iteration method and the Demon method. Then, different formulations of the diffeomorphic image registration algorithms are introduced and discussed based on the results given in the literature. Furthermore, the inverse consistency criterion is considered as a biomedically important concept for improving the quality of the deformation fields. Image registration with symmetric warping of input images is also examined in details specifically in terms of the possible speeding up of the deformation field estimation process. Finally, Chapter 3 presents the author's contribution to the symmetric image registration as a novel algorithm for inverting the deformation field established in the optimisation framework, and the idea of the new symmetric image registration based on it.

Chapter 4 explains the need for the assessment of the image registration algorithms presented and briefly reviews the most known comparison works. Then, several criteria that can measure quality and quantify the obtained results are presented and their properties are discussed. Finally, a critical analysis is carried out based on the numerous experiments conducted on different data, including public

available data sets, with respect to the different criteria.

Chapter 5 extends the pairwise image registration techniques to group-wise image registration that is able to estimate the correspondences between multiple images in different set(s) including inter- and intra- subject data sets. Chapter 5 focuses on the implicit group-wise registration that is shown as not biased by the reference image selection. To maintain diffeomorphic consistency across this work, the previously proposed algorithm of implicit group-wise image registration is reformulated to the log-Euclidean framework. The experimental results are shown on both simulated and biomedical data including MRIs of prostate, MRIs of head, and facial expression images.

Chapter 6 presents possible application of the studied image registration algorithms to the pelvic-area medical data. The presented method used sets of the MRI images of different subjects to generate an inter-subject (subject independent) motion model of the prostate and adjacent tissues which is then utilised to build a novel system for prediction of the dense deformation field based on the partial information delivered by rectum and bladder segmentation. The evaluation of the proposed method is presented first using the data with synthetic deformation fields to give a systematic evidence for the correctness of the prediction generated. Furthermore, the examples including real MRI data are presented thereby demonstrating the potential usefulness of the proposed system for the Adaptive Radiotherapy.

Chapter 7 introduces the log-Euclidean parameterisation of the diffeomorphic deformation fields to the facial expressions representation. The implicit group-wise diffeomorphic image registration algorithm generates the *common face space* to normalise the neutral facial expressions across different subjects thereby making them subject-independent. Subsequently, sets of the images of different basic facial expressions are represented by the velocity fields, obtained through diffeomorphic registration. This chapter ends with an extensive experimental analysis of the proposed facial expression representation and comparison of robustness based on the separability analysis criterion and recognition rates.

Chapter 8 concludes the overall work undertaken in this thesis. Following the summaries of the contributions presented, the suggestions of the further possible extensions to this work are briefly outlined.

## 1.4 Contributions of the research

The work undertaken considers utilising the diffeomorphic image registration in areas of biomedical applications. Thus, the main contributions of this work can be found in two areas.

First, this work emphasises the increased robustness of the image registration algorithms with symmetric warping in comparison to the classical formulation. A new method for inverting dense deformation fields, that is crucial for some class of the symmetric image registration was proposed and based on it, a new method for symmetric image registration with directly inverted deformation fields has been introduced (Chapter 3). These findings and the results of performing different symmetric image registration methods were first presented at the Conference on Medical Image Understanding and Analysis (MIUA) 2011 and published in the conference proceedings with the title: **Direct inverse deformation field approach to pelvic-area symmetric image registration** [96]. Furthermore, due to the high-ranked reviews of this paper, the extended version entitled **Symmetric image registration with directly calculated inverse deformation field**, has been accepted to special issue of *The Annals of the British Machine Vision Association* and it is in press. The extensive comparison of the different formulations of diffeomorphic image registration algorithms for a wide range of medical data with qualitative and quantitative analysis of obtained results (presented in Chapter 4) is in preparation for submission.

From the application-driven point of view, the dense deformation field prediction system built via the log-Euclidean parameterised implicit group-wise registration establishes the *common subject space* (Chapter 6) can be seen as a novel methodology for deformation field estimation. Furthermore, utilising the implicit shape representation of the bladder and rectum instead of the commonly used Point Distribution Model was shown as an effective way to predict prostate position with a possible application in the Adaptive Radiotherapy. The concept of this prediction system and the preliminary results obtained from the real MRI data sets have been accepted to the 4th MICCAI Workshop on Computational and Clinical Applications of Abdominal Imaging and the paper is in press. The title of the publication is: **An implicit inter-subject shape driven image deformation model for prostate motion estimation**.

Another contribution presented in Chapter 7, is using the stationary velocity field parameterisation of the deformation field obtained for multiple diffeomorphic registration of face images as a robust feature vector for automatic facial expression recognition. The results from this application were presented at the International Conference on Pattern Recognition Applications and Methods (ICPRAM) and published at the conference proceedings with the title: **Facial expression recognition**

using log-Euclidean statistical shape models [98], Furthermore, this paper was invited in an extended format to be included in the *Springer Proceedings in Mathematics & Statistics (PROMS) - Mathematical Methodologies in Pattern Recognition and Machine Learning* with the title **Facial expression recognition using diffeomorphic image registration framework**.

The author's contributions to the methodology and applications of image registration can be summaries as follows:

- Various novel combinations of the optimisation methods and deformation field parameterisations have been considered and investigated in depth.
- A robust method has been proposed for inversion of a deformation field, alongside a new method for symmetric image registration.
- A comprehensive quantitative and qualitative assessments have been carried out of commonly known algorithms for the pairwise deformable image registration.
- A novel technique has been proposed for subject independent estimation of model-based image dense deformation fields based on the implicit shape representation of the organs surface and the velocity field parameterisation applied to the MRI pelvic data.
- A subject independent facial expression recognition methodology has been proposed and validated using the diffeomorphic image registration framework.

# Chapter 2

## Principles of image registration

This chapter gives a general overview of the image registration algorithms with detailed descriptions of the basic components of the deformable image registration. First, the similarity criteria for the intensity-based image registration are introduced, and their quantitative properties for measuring distance between different types of the images are described. Then, the essential role of the regularisation terms enabling solution of the image registration problem that in most interesting cases is ill-posed what means that, without regularisation, solution may not exist, may not be unique or may not be continuously dependent on the input data are described. In addition, numerous additional approaches of preserving the properties of the desired solution for some specific applications are presented and their reliability and robustness are discussed. Finally, some strategies for estimating an optimal transformation are briefly outlined. This chapter ends with the concluding remarks on the presented classifications and addresses several interesting challenges in the field of the biomedical image registration.

### 2.1 Introduction

Image registration establishes a meaningful correspondence between object(s) in the images or in multiple sets of images, by evaluating a deterministic process of finding a spatial transformation between the images. During the last decades, the number of applications using various image acquisition scanners has grown rapidly, thereby resulting in intensive research on image registration. The research efforts have led to notable scientific achievements in applications such as astrophysics, remote sensing, cartography, biological, medical (clinical) analysis, engineering (bioengineering), and computer vision to name a few [164].

From the biological and medical perspective, the estimation of a plausible transformation between images is a fundamental task, with an enormous number of the

practical applications. Medical image registration enables a great variety of image analysis by allowing not only multiple sets of images to be compared but also the information from them to be combined. For example, a comparison of images taken before, during, and after therapy (intervention) can provide a comprehensive knowledge about a treatment and increase the rate of recovery, or reduce the side effects of undertaken therapy. The state-of-the-art example of therapy taking the advantage of the image registration is the adaptive radiotherapy of lungs [116, 159, 74, 36], prostate [78, 148, 40, 53, 61, 123, 124], head and neck [148, 21, 94]. As pointed above, the equally important is combing information from different sources of images using image registration. In so-called multi-modal image registration, images coming from different scanners have to be first spatially registered to provide complementary knowledge about organ(s) of interest. The multi-modal image registration can be seen as a fusion of information in two ways, by either combing the structural (anatomical) knowledge about organs between images such as Computed Tomography (CT), Magnetic Resonance Imaging (MRI), Ultrasound Scanning (US) [61, 71, 29, 70], and Diffusion Tensor Image (DTI) [135], or finding the correspondence between structural and functional information from images such as Positron Emission Tomography (PET) [34] and functional MRI (fMRI) [42].

Additionally, image registration methods have been investigated for the longitudinal studies and clinical diagnosis of neurological disease progression, where the inter- and intra- subject normalisation is a crucial step. The results from those evaluations indicate that some patterns are to be detected by machine learning methods for the common neurodegeneration such as Alzheimer’s disease or dementia [5, 10]. In the same fashion based on performing multiple image registrations, the initial results of statistical analysis for the Diffusion Tensor Images were reported for the significant changes of white matter in HIV/AIDS patients [135]. In the field of computational anatomy, image registration presents a powerful tool to perform the population-based quantification of the anatomical variability of biological shapes [64, 132, 42, 146, 153]. Motion models, where image registration is a key step for the deformation field estimation, are promising solutions to the problems such as the image artifacts in the image acquisition stage [83], or the image-guided interventions in a non-static environment. Examples of utilisation motion models computed by image registration cover the studies on the respiratory motion [159, 73, 75, 74, 36, 88], the cardiac motion [22], the brain deformation [114, 17], prostate and the adjacent organs motion [125], and the liver motion induced by the respiratory cycle [93]. An important image registration task in computer-guided surgery is to provide effective and efficient (real-time or nearly real-time) motion compensation and registration of the pre-operative patient data (or patient model) to the intra-operative data coming

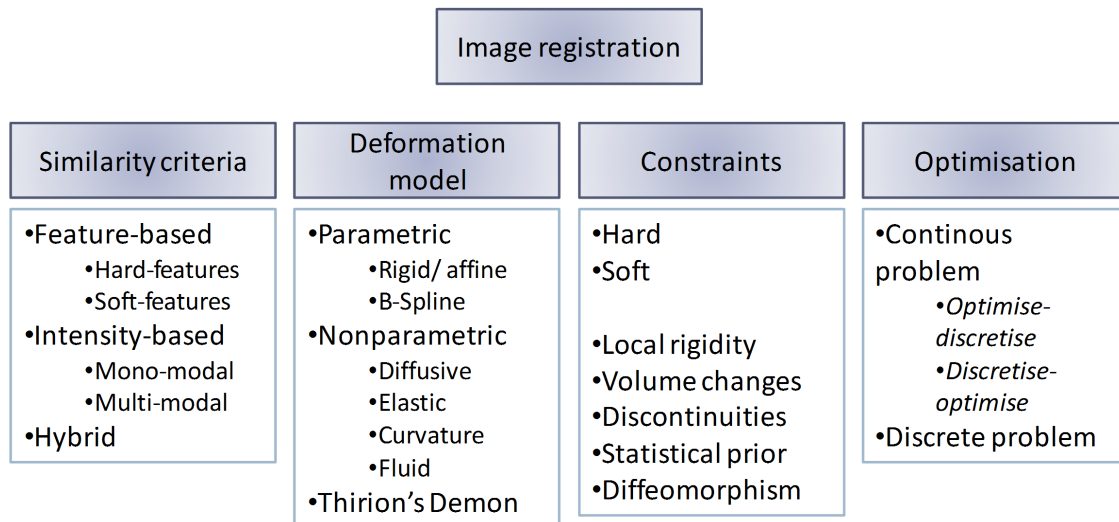


Figure 2.1: Classification of image registration methods.

from i.e. laparoscopy- [93] or endoscopy- [20, 23] based minimally invasive surgery (MIS) and needle aspiration biopsy (NAB).

Four principal aspects of image registration have to be considered before the most appropriate approach is to be chosen and evaluated in a particular application. These aspects are:

- objective function with the major focus on the similarity criterion driving alignment of the corresponding structures,
- image transformation model, that is a necessary condition to make image registration problem solvable,
- constraints, that tune the estimated solution to satisfy desired requirements,
- optimisation framework as a strategy of finding an optimal solution for a specific objective function.

The aspects enumerated above can be naturally coupled with the criteria to classify the image registration methods. A brief overview of the four principal aspects is presented in the following sections to describe the principles and primary important components of image registration. Additionally, Figure 2.1 summaries image registration classification.

The first aspect is linked to the main ingredient of image registration, similarity criterion (or discrepancy measure) is unavoidably incorporated into the definition of the image registration objective function. The impact of the selected similarity criterion in the image registration is so essential that naturally leads to the most common classification criterion of the registration methods: the feature-based image registration and the intensity-based image registration.

The feature-based image registration (also called landmark-based image registration [109, 164, 92], or geometric registration [43]) relies on establishing meaningful correspondences between some features, that firstly have to be extracted from the images either manually by expert(s) or via an automatic detection process. The features can be either extrinsic (*hard*) or intrinsic (*soft*). By the extrinsic features, it means the objects artificially introduced into the imaged space such as fiducial markers put directly into patient body in clinical case, while the intrinsic features can be some-how deduced from the obtained images based on the visible anatomical structures by automatic detection algorithms or expert's knowledge (i.e. points, contours, surfaces). The extraction process of any suitable features can be very challenging task because the obtained features have to represent relevant information from the analysed data, and the repeatability of the feature extraction process [134]. The objective of the feature-based image registration is to minimise the distance between those salient landmarks. The distance can be simply chosen as the Euclidean distance, or more sophisticated measures such as geodesic distance. Commonly the number of the selected landmarks is significantly lower than the overall image points thereby the computational cost of the registration is reduced, however, the interpolation strategies (e.g. Thin-Plate-Spline interpolation [90, 92]) are unavoidable to obtain a dense deformation field for all image points.

The intensity-based similarity criteria measure how similar are the input images with respect to their intensity patterns. The selection of a particular measure is strongly dependent on the source of input images. When the input images are acquired from the same device (with a repeatable acquisition protocol) or at least the similar intensity distribution can be assumed, the sum of the squared differences or the correlation coefficient [32, 57, 10] can be considered as the simplest to evaluate and an accurate measurement. When the problem of registering images from different scanners is tackled, more complex similarity measures have to be taken into account. In this case, the state-of-the-art example is the mutual information criterion [147, 31, 57, 136], derived from information theory. Other examples of possible measures include correlation ratio [108, 57], normalised mutual information [133, 112, 156], and entropy correlation coefficient [80]. These similarity criteria search for underlying statistical dependencies and intensity relations between images. A detailed overview of the mutual information-based metrics is given in [100]. From the assumption that the image intensity changes appear in the corresponding position, the normalised gradient fields distance [48] was derived. The normalised gradient fields have been investigated as a sufficient measure to determine the optimal transformation between some classes of the multi-modal images. In some applications, an intensity correction of the image content is introduced [45] rather

than exploiting the aforementioned general discrepancy measures.

In addition, considerable effort has been undertaken to combine the feature-based and intensity-based approaches to form the hybrid registration framework, incorporating the advantages of each approaches [63, 79, 43, 29].

Due to the inherent image registration problem of being ill-posed, an additional assumptions about an optimal solution have to be included. The common approach to encourage a desired solution, thereby making it (possibly) unique, is adapting a representative transformation model. Through the transformation model image registration can be broadly put in two main categories namely, parametric and non-parametric image registration.

The transformations that are restricted to any parametric space, can be subdivided into the groups either describing the global alignment or the local deformations. The most common global transformations are the rigid and affine models offering the low computational complexity due to reducing the number of variables to a few transformation parameters. Besides the high robustness of the low-dimensional parameterisation, the ability of modelling the local deformation is limited, since the local deformations can not be sufficiently explained by translation, rotation or scaling [112]. Thus their area of medical applications is very narrow i.e. the global position of the patient body (for rigid structures such as bones or skull) or the pre-processing step for higher order parameterisation or non-parametric schemes. More precise, but still a parametric model of describing the human anatomy variability is based on the B-spline transformation space parameterisation originally proposed in [112] and extended in [118]. The transformation is represented using B-spline parameterised control points on the regular grid [112] or non-uniformly distributed [118] that are not linked to any specific image features. Further extension was proposed in [84, 121] by describing interaction between the control points using physical analogies derived from the input images. It has to be mentioned that the low-dimensional parameterisation may restrict solution to be unique, however in general an additional regularisation is inevitable [92].

The opposite of the parametric-based image registration is non-parametric image registration. Instead of a set of parameters describing the transformation, a regularisation term (also called smoother) is added into similarity criterion to design a well-posed framework. An appropriate regularisation term should have properties to distinguish the plausible transformation (more often described with respect to the deformation field or displacement field in non-parametric registration) for a particular application. As in many cases, there is no ground truth available of the desired deformation field, so many regularisation techniques have been developed. The state-of-the-art regularisation terms are often derived from the physical

motivations related to the underlying properties of the objects included in the registration. Continuum mechanical models such as the linear elasticity model described by the Navier-Lame equations [11], or the diffusion model [59] (the membrane energy model) given by the Laplace equations have been particularly investigated as a general and practical form of regularisation. Other smoothers such as the curvature model (the bending energy model) have been designed for specific applications [38]. These models can be used for the regularisation of the deformation field and/or for regularisation of the update of the deformation field (fluid continuum model) [19]. Indeed both of them lead to a solution. While regularisation of the deformation field restricts the transformation to small deformations, regularisation on the update of the deformation field is extremely flexible. Besides, an interesting technique of deformation field smoothing was proposed in [138] (so-called Demon), where the deformations are regularised by the low-pass Gaussian convolution filter. Recently this approach was put into the optimisation framework and the fluid-like version (smoothing the update of the deformation field) was also proposed [143, 145]. Further investigations showed that Demon smoothing is related to the diffusive model of transformation [90, 82]. The detailed overview of the most common regularisers can be found in [151, 90, 92].

In most biomedical applications, the results of implementing a general image registration algorithm is not always suitable. Although the estimated transformation warps image/volume to be similar to the reference image/volume, this transformation may not be representative of the deformation expected in the biomedical cases e.g. due to folding. As a most compelling example, the human body deformations can occur in places where some tissues are highly elastic, some are deformable but do not change the volume, and other can be also totally rigid. For this reason, an additional knowledge have to be introduced to the registration process, to make the estimated results medically plausible. The important thing to realise is that this introduced user knowledge is not done to replace the regularisation term [39]. Having in mind a wide range of the common medical applications, a number of the proposed additional constrains is equally significant even without including the some-how redundant solutions of the same problem via different ways of defining problem. The way of the separating these constraints is by some means of the proposed *ad hoc* to be based either on the manner of introducing the additional information or on the desired properties.

The first way of dividing the additional knowledge into image registration is related to the soft-constrains approach, hard-constraints approach or even developing a full new registration problem formulation. The soft constraints are constraints that do not necessarily have to be fulfilled during image registration and some deviation

from the expected properties can happen [91]. In contrast, the hard constraints totally rule out the unwanted solutions [50]. In last case, the reformulation can be seen as transferring a problem from one domain into the other, that has the particular properties i. e. a diffeomorphic formulation of the image registration via flow in suitable infinite-dimensional group of smooth, invertible transformations [25], or via an approximation of a Lie group by a time-independent flow (stationery velocity field) [4, 5, 143, 144, 145, 82].

Taking into account the desired properties of the estimated transformation, the most common restrictions can be straightaway enumerated. The tissue deformation modelling requires the possession of the local rigidity characteristics implemented in many different manners [72, 84, 77, 65, 110, 128, 129, 49, 130, 91]; ensuring the considerable volume changes [47, 50, 82]; the discontinuities in motion for slipping objects i.e. lungs [111, 117, 107]. Motion estimation can be also restricted via pre-learnt statistical models [150, 3, 119, 34, 135].

During the past years many medical image algorithms have been restricted to the diffeomorphic framework. A diffeomorphic transformation is defined as a continuous differentiable mapping preserving the neighbourhood topology. As in general there is no unique solution, this approach offer a very consistent and biologically meaningful results that is valid for a large number of the problems where images represent the same objects but different in shapes. The earliest work are related to preserving the one-to-one mapping and consistency criterion directly [27, 63] and extended to different modalities [162, 136]. Other approaches ensuring the diffeomorphism are based on a flow under the specific group of the transformations [25]; the time-dependent flow [26, 15], the small step multi-pass technique [155], the B-spline parameterisation with additional constraints [115] or the geodesic shooting method [89, 6]. Recently, a new parameterisation has been adapted into the diffeomorphic registration derived from the Lie algebra [4, 5, 143, 144, 145, 82, 53].

The last criterion mentioned above for classifying the image registration techniques is the procedure of finding the optimal solution. In general, in the case of the deformable image registration, a high-dimension, non-linear, non-convex image registration problem has to be solved in a reasonable time. Various optimisation algorithms have been utilised to cope with this problem. One of the possible classes of solution strategy is related to the so-called *optimise-discretise* approach that aims at finding the analytical Euler-Lagrange equations, which are then discretised and solved with some sort of the selected solution schemes. Variational techniques of solving the image registration problem are discussed in [30]. The overall description of the *optimise-discretise* strategy is presented in [90]. The other strategy is known as the *discretise-optimise* technique [92], where an appropriate discretise scheme is

applied first to get a finite-dimensional optimisation problem that can be solved with an associated optimisation method. Besides the strategy used, there is always a chance to get trapped in a local minimum. The common technique to at least partially reduce this problem is adopting the multi-scale or the multi-resolution scheme.

Recently discrete optimisation techniques have been introduced in order to solve image registration problem [43, 54]. Contrary to the previously mentioned approaches, in this case domains and codomains of images and deformation field are approximated by a set of predefined labels rather than real numbers. Subsequently using different models such as Random Markov Field or graphs a solution of the desired energy function can be found using one of combinatorial optimisation methods (e.g. graph-cut algorithm).

As shown above, a significant number of approaches has been proposed to cope with estimation of the plausible transformations. Although many practical problems have been addressed, there are issues that have not been solved yet. Moreover, development of new scanners and acquisition protocols opens new areas of possible research to satisfy medical requirements. Recently, one of the most active research areas has been found in the diffeomorphic formulation of the image registration. The interesting thing to be investigated in future, seems to define the framework that can integrate a general diffeomorphic formulation with some real-life problems of a partial information, low-quality images, occlusions etc. Another issue that has to be listed as problematic in image registration is the validation criteria, to give an objective and quantitative result of performing a particular registration algorithm, and to compare different approaches. Currently the most common way of the validation is using the synthetic ground truth data (often not necessarily describing the real clinical conditions), phantom simulations, the numerical criteria describing some (usually limited) properties of the estimated transformations, or the biased visual inspections by the experts. All of these approaches towards validation have some drawbacks and limitations. Furthermore, although the new trends in computing have speeded up significantly the processing time during past years, in the same time the acquisition systems have been also improved resulting in larger data sets. In some applications demanding nearly real-time processing, the limitations on the computational time are very restrictive. Finally, probably all of the existing methods have some design parameters that have to be set before, or during the registration process. Having this in mind, the automatic or at least systems with limited human operator interactions are preferable in many cases.

To sum up, a brief overview and the common classifications of the image registration techniques were introduced. The basic principles of the different approaches to image registration from the mathematical point of view can be found in the

textbooks [90, 158, 92]. A general overview of image registration techniques for specific application areas are covered in [51, 164] and in [81, 134] where the discussed examples are focused in majority on the biomedical field.

## 2.2 Principles of image registration

Deformable image registration is a process of determining a spatial transformation that establishes plausible (i.e. the correctness in terms of e.g. biological tissue properties) correspondences between the object(s) in two (pair-wise image registration), or more images (group-wise image registration).

In this section, the pair-wise image registration will be considered for two given input images: image  $I_f$  that is termed fixed image (also called as reference image or target image), and image  $I_m$  that is termed moving image (named also as template image or source image):

$$I_f, I_m : \Omega \rightarrow \mathbb{R}, \Omega \subset \mathbb{R}^d \quad (2.1)$$

where  $d$  denotes the spatial dimension of image (the data dimensionality). Having two input images, the aim for the deformable image registration is to estimate an optimal, in some sense, transformation  $\vec{\varphi}_{opt}$ :

$$\vec{\varphi}_{opt} : \Omega \rightarrow \mathbb{R}^d, \Omega \subset \mathbb{R}^d \quad (2.2)$$

warping moving image  $I_m$  to be similar (in sense of the assumed criterion of similarity) to fixed image  $I_f$ :

$$I_f \approx I_m \circ \vec{\varphi} = I_m(\vec{\varphi}) \quad (2.3)$$

where  $\circ$  is a composition operator. The transformation (deformation field)  $\vec{\varphi}(\vec{x})$  can be also stated in term of a displacement field  $\vec{u}(\vec{x}) = [u^1(\vec{x}), \dots, u^d(\vec{x})]$  from a spatial position  $\vec{x} = [x^1, \dots, x^d] \in \Omega$ :

$$\varphi(\vec{x}) = \vec{x} + \vec{u}(\vec{x}) \quad (2.4)$$

The problem of finding an optimal displacement field  $\vec{u}_{opt}$  can be phrased as an optimisation problem:

$$\vec{u}_{opt} = \arg \min_{\vec{u}} \varepsilon(\vec{u}; I_f, I_m(\vec{u})) \quad (2.5)$$

The objective function  $\varepsilon(\vec{u})$  (often called an energy function) consists of a similarity criterion (also called as discrepancy or volumetric distance measure) *Sim* measuring how similar images are, and a regularisation term (smoother) *Reg* measuring the

reasonability (plausibility [92]) of the estimated displacement field:

$$\varepsilon(\vec{u}) = Sim(I_f(\vec{x}), I_m(\vec{x} + \vec{u}(\vec{x})))dx + \alpha Reg(\vec{u}(\vec{x}))dx \quad (2.6)$$

where:  $\alpha$  is a weighting factor to control the respective influence of *Sim* and *Reg* and  $\alpha > 0$ .

In some formulations of the image registration problem, an additional component, the penalty term *Pen*, is added to the energy function given by Equation 2.6, that discourages undesirable transformations [39]. Therefore, the energy function  $\varepsilon(\vec{u})$  can be phrased as follows:

$$\varepsilon(\vec{u}) = Sim(I_f(\vec{x}), I_m(\vec{x} + \vec{u}(\vec{x})))dx + \alpha Reg(\vec{u}(\vec{x}))dx + \beta Pen(\vec{u}(\vec{x}))dx \quad (2.7)$$

where  $\beta > 0$  denotes a penalty parameter to control the impact of the penalty term *Pen*. Contrary to the regularisation term *Reg*, that is necessary to guarantee the deformable image registration problem to be solvable, the penalty term *Pen* can only provide an improvement to the properties of the estimated transformation or a feasible way of including *a priori* knowledge into the registration process.

Although, the most intuitive approach for image registration seems to be direct minimisation of the similarity measure *Sim* without introducing any regularisation term, this expectation has some fundamental drawbacks. Firstly, the minimisation of the similarity measure is an ill-posed problem since many solutions can exist (many local and/or even global minima), and secondly, small changes of the input data can lead to significant changes of the estimated results. These basic requirements such as an existence and uniqueness of a solution and a continuous dependence of the result on the input data are so-called Hadamard terms of a well-posed problem [90, 30]. The reason for the inherent ill-possess of the image registration can be intuitively seen from the observation, that providing a scalar information of the image intensity, the vector valued transformation has to be estimated [39]. Moreover, in most situations when image registration is used, the additional assumptions have to be implicitly made to estimate a desirable deformation field. Thus, these considerations lead to conclusion that the explicit adding of the additional regularisation term *Reg* into the optimisation framework is unavoidable. Additionally, selection of an appropriate regularisation term is strictly dependent on a particular application and the desirable properties of the estimated transformation.

## 2.3 Similarity criteria

The similarity criterion can measure distance between features (landmarks) taken from images (feature-based image registration) or volumetric distance between image intensities (intensity-based image registration). In this work, the intensity-based image registration approaches are to be investigated, therefore the intensity-based criteria are described in this section.

The simplest choice of volumetric distance and for this reason very effective in the case of the mono-modal data, is the sum of the squared difference (SSD) defined as:

$$SSD(I_f, I_m(\vec{\varphi})) = \int_{\Omega} (I_f(\vec{x}) - I_m(\vec{\varphi}(\vec{x})))^2 dx \quad (2.8)$$

The SSD criterion is quite restrictive because it assumes that corresponding objects have the same intensities in both input images ( $I_f(\vec{x}) \approx I_m(\vec{\varphi}(\vec{x}))$ ). When the dependence between image intensity levels in images is linear ( $I_f(\vec{x}) \approx \kappa I_m(\vec{\varphi}(\vec{x}))$  where  $\kappa \in \mathbb{R}$  is a scalar value), cross correlation (CC) [32, 57] can be utilised. For images of the same modality, the SSD yields similar results as the CC and also the images with linear dependence of the intensity can be easily adjusted to be mono-modal images. One way of utilising SSD for the multi-modal images is to introduce an intensity correction of the image content [45]. The practical applications of the CC in computer vision can be utilised in term of robustness for the unpredictable illuminations or inhomogeneity in medical data (e.g. MRI) [10].

For any functional dependency of the image intensity (it may not be known *a priori*), a correlation ratio (CR) was proposed as a measure expressing a level of the functional dependence between two images. The CR is defined as follows:

$$CR(I_f, I_m(\vec{\varphi})) = \frac{\text{var}[E(I_f|I_m(\vec{\varphi}))]}{\text{var}(I_f)} \quad (2.9)$$

where  $\text{var}[E(I_f|I_m(\vec{\varphi}))]$  measures the part of  $I_f$  which is predicted by  $I_m(\vec{\varphi})$  and  $\text{var}(I_f)$  is a variance of  $I_f$ . The CR was successfully applied for the rigidly parameterised transformations estimation [108]. Furthermore, a general variational framework with analytically derived gradient of CR for the non-parametric image registration was proposed in [56, 24]. A wide range of medical data sets were evaluated for both approaches yielding the results that indicate visually correct alignment of anatomical structures. While the aforementioned similarity criteria such as the SSD, CC and Mutual Information (to be outlined in the next paragraph) are not dependent on the order of input images, particular care has to taken during evaluation of the CR due to asymmetric properties of this measure (in general  $CR(I_f, I_m) \neq CR(I_m, I_f)$ ) [108]. In addition, the CR-driven image registration can

fail when an underlying intensity dependence is not a monotonic function [57].

In general case, the statistical entropy-based (information theory-derived) measures such as Mutual Information (MI) [31, 147], have to be considered to find an intensity relation between images. The MI is commonly defined using the joint probability density function of the intensity distribution  $P(I_f(\vec{x}), I_m(\vec{\varphi}(\vec{x})))$  and the marginal probability density functions of the intensity distributions  $p(I_f(\vec{x}))$  and  $p(I_m(\vec{\varphi}(\vec{x})))$  for images  $I_f$  and  $I_m(\vec{\varphi})$  respectively. The MI between images  $I_f$  and  $I_m(\vec{\varphi})$  is given by:

$$MI(I_f, I_m(\vec{\varphi})) = - \int_{\Omega} \log \frac{P(I_f(\vec{x}), I_m(\vec{\varphi}(\vec{x})))}{p(I_f(\vec{x}))p(I_m(\vec{\varphi}(\vec{x})))} dx \quad (2.10)$$

The MI indicates how the intensity of the pair of images fail to be independent (or how much global information is shared by the pair of images). The analytical expression of the derivative of the MI was derived in [57] for the non-parametric case. Although the MI has been intensively investigated in many image registration algorithms for the images originating from a wide range of the applications (see [100] for detailed overview of MI-based registration methods), it suffers from some limitations due to the process of the joint intensity distribution estimation and it is extremely sensitive to the region of overlapping between images [80, 133, 156]. The first issue is due to the fact that in general the joint intensity distribution  $P(I_f(\vec{x}), I_m(\vec{\varphi}(\vec{x})))$  is unknown, and has to be estimated either using the histogram-based estimator or Parzen-window-based estimator. The second problem related to the negative effect of the varying image overlapping region was minimised by introducing the normalised mutual information (NMI) (proposed and evaluated in [133]). In the same way as for the MI, the analytical derivative of the NMI was derived in [156].

While the SSD seems to be too restrictive in many applications, the MI can be actually too general to use as well, and a normalised gradient field distance can be seen as a compromise between these similarity measures. The normalised gradient field distance measure (NGF) [48, 92] is based on the assumption that intensity changes of images with different modalities appear at corresponding positions. The NGF is defined by:

$$NGF(I_f, I_m(\vec{\varphi})) = \int_{\Omega} 1 - (\eta(I_f(\vec{x}))\eta(I_m(\vec{\varphi}(\vec{x}))))^2 dx \quad (2.11)$$

where  $\eta(I_f)$  and  $\eta(I_m(\vec{\varphi}))$  are normalised gradients of images  $I_f$  and  $I_m(\vec{\varphi})$  respec-

tively. The normalised gradient  $\eta(I_f(\vec{x}))$  is defined as:

$$\eta(I_f(\vec{x})) = \begin{cases} \frac{\nabla I_f(\vec{x})}{\sqrt{\|\nabla I_f(\vec{x})\| + \nu}} & \text{if } \nabla I_f(\vec{x}) \neq 0 \\ 0 & \text{otherwise} \end{cases} \quad (2.12)$$

where  $\nu$  is a parameter (so-called edge parameter) that determines whether gradient is to be considered as an edge or the noise in image [48].

The outlined similarity measures are calculated as a global criterion on the image domain where both reference and warped moving image are overlapping. In some applications, this can be seen as a shortcoming because the spatial dependencies are not incorporated into the registration process. Recently, a non-rigid image registration framework combining both global and local similarity criteria has been proposed [156]. The integration of the global similarity measure  $Sim_g$  and the local discrepancy  $Sim_l$  is done via a simple weighting scheme defined as:

$$Sim(I_f, I_m(\vec{\varphi})) = \gamma Sim_g(I_f, I_m(\vec{\varphi})) + (1 - \gamma) Sim_l(I_f, I_m(\vec{\varphi})) \quad (2.13)$$

where  $\gamma \in [0, 1]$  is a parameter that trades off between global and local statistics. The weighting scheme given by Equation 2.13 was applied to NMI with an adaptive procedure of  $\gamma$  adjustment in [156]. Another approach incorporating the spatial information into image registration was proposed in [55, 25]. However, an exploiting of the local similarity criterion only as such is not effective and likely to result in registration to be trapped in local minima [156].

From the theoretical point of view, evaluating more general similarity measures can lead to estimation of larger variety of possible transformations, with some hidden by more restrictive similarity measures. In the meantime, the similarity criterion should also indicate the most plausible transformation [92]. As a result of these concerns about the most appropriate similarity criterion, the choice of the similarity measure has to be relevant to intensity dependencies (or relations) between input images, as it can significantly influence the process of estimating the optimal transformation. Thus far, defining (or even in a simple case of selecting for some sort of images) a suitable criterion is a challenging task, and on its own, it is a subject of research for specific applications and data. From examples of the different modality images obtained for brain [1, 2] shown in Figure 2.2, it is noticeable that finding visual correspondences between relevant objects (structures) in different modalities images can be difficult even for a human observer.

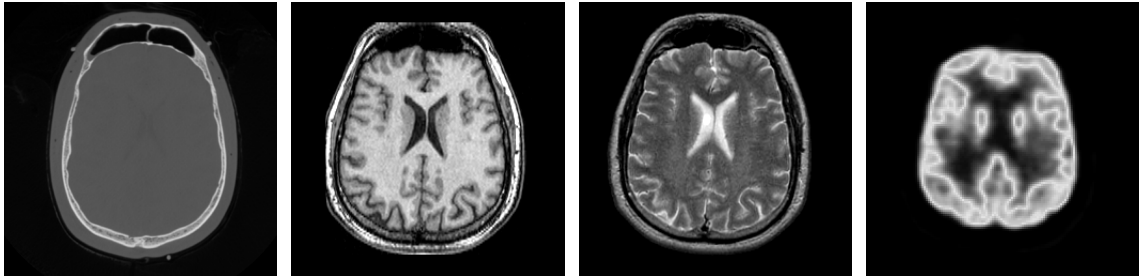


Figure 2.2: Multimodal examples of the brain images taken from different scanners: (from left to right) Computed Tomography [1], Magnetic Resonance Imaging T1 [2], Magnetic Resonance Imaging T2 [2], and Positron Emission Tomography [2].

## 2.4 Nature of transformation

Historically, the earliest works in the area of image registration restricted the estimated transformation to the low-dimensional space of transformation. A parameterised transformation  $\vec{\varphi}_q$  is typically defined as linear combinations of the basic functions and the parameters. The simple case of the two dimensional ( $d = 2$ ) rigid transformation  $\vec{\varphi}_{rigid}$  (which allows for translations and rotations) is defined in following way:

$$\vec{\varphi}_{rigid}(\vec{x}) = \mathbf{R} \cdot \vec{x} + \vec{T} \quad (2.14)$$

where  $\mathbf{R}$  is the rotation matrix with parameter  $\theta$

$$\mathbf{R} = \begin{bmatrix} \cos(\theta) & -\sin(\theta) \\ \sin(\theta) & \cos(\theta) \end{bmatrix} \quad (2.15)$$

and  $\vec{T} = [t^1, t^2]$  is the translation vector with parameters  $t^i$ ,  $i = 1, 2$  where  $t^i$  denotes translation in the  $i$ th direction of image domain. Another commonly used parameterised transformation is affine transformation that extends the rigid transformation to shearing and scaling. A detailed description of possible parametric transformations can be found in [158]. There was also another reason for the low-dimensional space restriction behind the ill-posed properties of the image registration problem related to the limited computational resources (computing speed). Although the simplicity of the parameterisation is noticeable, where only a few parameters have to be estimated to describe the transformation, the drawback is in very low accuracy of registering the local deformations. The intuitive approach is to extend the number of parameters to the desired level to alleviate the limitation of the small set of possible transformations associated with the affine or rigid transformations. In practice, to capture the local anatomical variability, the B-spline based parameterisation of the transformation was proposed [112]. The parameterisation of the

transformation  $\vec{\varphi}_{Bsl}$  can be done in terms of the deformation field  $\vec{u}_{Bsl}$ :

$$\vec{u}_{Bsl}(\vec{x}) = \sum_{l=0} \sum_{m=0} \sum_{n=0} B_l(x_b^1) B_m(x_b^2) B_n(x_b^3) \vec{c}_{i+l, j+m, k+n} \quad (2.16)$$

where  $B_l$  stands for the B-spline polynomial (usually of order 3 - the cubic B-Spline polynomial),  $\vec{c}$  denotes the control points which parameterise the deformation field and  $i, j$  and  $k$  denote the indices of the control point cells containing  $\vec{x}$ , and  $x_b^1, x_b^2$  and  $x_b^3$  are the relative positions of  $x^1, x^2$  and  $x^3$  [112, 65, 115]. The B-spline parameterised control points representing transformation can be either put on the regular grid [112] or non-uniformly distributed [118] that they may not be linked to any specific image features. In addition, the derivative of the transformation  $\vec{\varphi}_{Bsl}$  can be also expressed in terms of the B-spline coefficients, that offer an easy and efficient way of providing the gradients with respect to the deformation for optimisation strategy [112, 129]. The B-spline parameterisation of the transformation has been used in many different applications, showing in most cases good performance in terms of objects deformations modelling. The applications include not only the original applications to the MRI of the breast [112], but also the cardiac motion modelling [22], full body PET scans [77], and brain variability modelling [114, 115].

The parameterisation can limit the set of the transformation that can be estimated for one element set, but in general the additional regularisation has to be introduced [92]. This can be intuitively explained by considering the example images of squares shown in Figure 2.3. Despite of using the low-dimensional transformation space i.e. rigid transformation with only 3 parameters, the solution is not unique and can be obtained by translation or via rotations. However, adding the desired regularisation on the space of transformation parameters alleviate this problem and can lead to the unique set of the optimal parameters (regularised parametric image registration [112, 92]).

On the other hand, the non-parametric approaches restrict the estimated deformation field  $\vec{u}$  by the regularisation term  $Reg(\vec{u})$ . An appropriate regularisation term should have the properties of distinguishing the plausible transformations and sometimes it is designed for a particular application, especially is the variability of desired displacement is known *a priori* or can be determined empirically. Unfortunately, in most medical applications, the variability of the optimal transformation is not known. In those cases, the regularisation models are derived from the physical motivations linked in some unspecified ways to the underlying properties of the registered objects. Four commonly used types of the regularisation terms are described below including a diffusive regularisation, a linear elastic model, a curvature regularisation and the fluid model. In general, the selection of the one that can be

seen as the best one is not possible because each of them has some advantages and disadvantages.

The diffusive regularisation (a membrane energy model or Laplacian model) measures variations of the deformation field  $\vec{u}$ , and is defined as a sum of the partial derivatives [59, 90, 5, 92]:

$$Reg_{diff}(\vec{u}) = \frac{1}{2} \int_{\Omega} \sum_{j=1}^d \sum_{k=1}^d \lambda_{diff} \left( \frac{\partial u^j(\vec{x})}{\partial x^k} \right)^2 dx \quad (2.17)$$

where  $\lambda_{diff}$  is a diffusion parameter. A higher value of  $\lambda_{diff}$  encodes a lower amount of the deformation field variability, enforcing a smoother deformation field and minimising the oscillations of the deformation field [90]. The diffusive regularisation term was used in some applications such as adaptive radiotherapy [78, 159, 97]

It was shown that the diffusive regularisation is connected to the so-called Demon algorithm [138, 143, 144, 145], where the regularisation is performed by a low-pass Gaussian filtering procedure [90, 82]. The straightforward implementation of the Demon algorithm makes this regularisation type very common in many applications.

Another common choice of the possible regularisation is related to the physical properties of an elastic isotropic and homogeneous body. The linear elasticity regularisation [11] measures the energy (so called strain) introduced by deforming an elastic material, and is approximated for the small deformation by:

$$Reg_{elas}(\vec{u}) = \frac{1}{2} \int_{\Omega} \sum_{j=1}^d \sum_{k=1}^d \left( \lambda_{elas} \left( \frac{\partial u^j(\vec{x})}{\partial x^j} \right) \left( \frac{\partial u^k(\vec{x})}{\partial x^k} \right) + \frac{\mu_{elas}}{2} \left( \frac{\partial u^j(\vec{x})}{\partial x^k} + \frac{\partial u_k(\vec{x})}{\partial x^j} \right)^2 \right) dx \quad (2.18)$$

where  $\lambda_{elas}$  and  $\mu_{elas}$  are so-called Lamé parameters. A higher value of the parameter  $\lambda_{elas}$  encodes a less variation of  $\left( \frac{\partial u^j(\vec{x})}{\partial x^j} \right) \left( \frac{\partial u^k(\vec{x})}{\partial x^k} \right)$  leading to volume-preserving properties. In opposite, a smaller value of parameter  $\lambda_{elas}$  tends to maximise the expansion of the elastic body.  $\left( \frac{\partial u^j(\vec{x})}{\partial x^j} \right) \left( \frac{\partial u^k(\vec{x})}{\partial x^k} \right)$  is the divergence operator and indicates a change of volume. A higher value of the parameter  $\mu_{elas}$  leads to penalising scaling and shearing and allows for rotations [5]. The other interpretation of the parameters  $\mu_{elas}$  and  $\lambda_{elas}$  is often referred to the Young's modulus of the elasticity and the Poisson's contraction ratio [90] The linear elastic regularisation term has been used widely in many applications [56, 24, 27, 57].

The curvature regularisation is defined based on the second order derivatives of

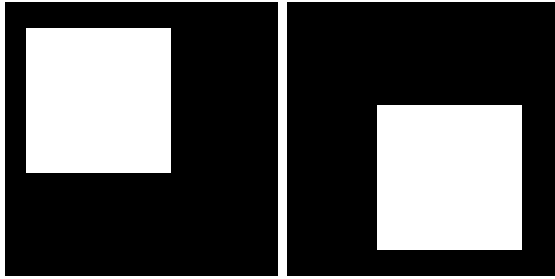


Figure 2.3: Example of images of squares that shows the ambiguity arising from the non-regularised image registration.

the deformation field  $\vec{u}$  to minimise the curvature of the deformation field [38, 90]:

$$Reg_{curv}(\vec{u}) = \frac{1}{2} \int_{\Omega} \sum_{j=1}^d \sum_{k=1}^d \sum_{l=1}^d \lambda_{curv} \left( \frac{\partial^2 u^j(\vec{x})}{\partial x^k \partial x^l} \right)^2 dx \quad (2.19)$$

where  $\lambda_{curv}$  is a curvature parameter. The motivation for deriving this regularisation model was found in the penalisation of the affine transformation properties of the diffusive and linear elastic smoothers. For this reason, the additional pre-registration (rigid or affine) has to be carried out to minimise the distances between the rigid structures.

The matrix stencils for a convolution operation of the described regularisation terms are presented in [90, 5].

The mentioned regularisation terms take as an input the deformation field  $\vec{u}$ , and the regularisation can be performed with respect to the update of the deformation field  $\vec{d}u$ . Performing regularisation (smoothing) on the deformation field restricts also the estimated transformations to small and local deformations. In some applications this restriction is too strong to recover the particular motions. The proposed solution to this issues is related to use the fluid continuum model of the body deformations [19, 90]. When the update of the deformation field is regularised, the image registration can be referred as a fluid image registration [19]. The fluid image registration is very powerful as in principle, it can deform any moving image to the reference image as long as they have the same range of the intensity level [90]. However, this is also a limitation for some sort of medical applications, because in general the organs do not deform in a fluid-like manner.

Although, the image registration with the regularisation terms is called non-parametric image registration, parameters  $\lambda_{diff}$ ,  $\lambda_{elas}$  and  $\mu_{elas}$ ,  $\lambda_{curv}$  are present in these models. In contrast to the parametric approach, where the set of the parameters describes the estimated transformation, the parameters from the regularisation terms are only influencing the deformation field during registration.

The illustrative example of performing image registration with different types of

## 2.4. NATURE OF TRANSFORMATION

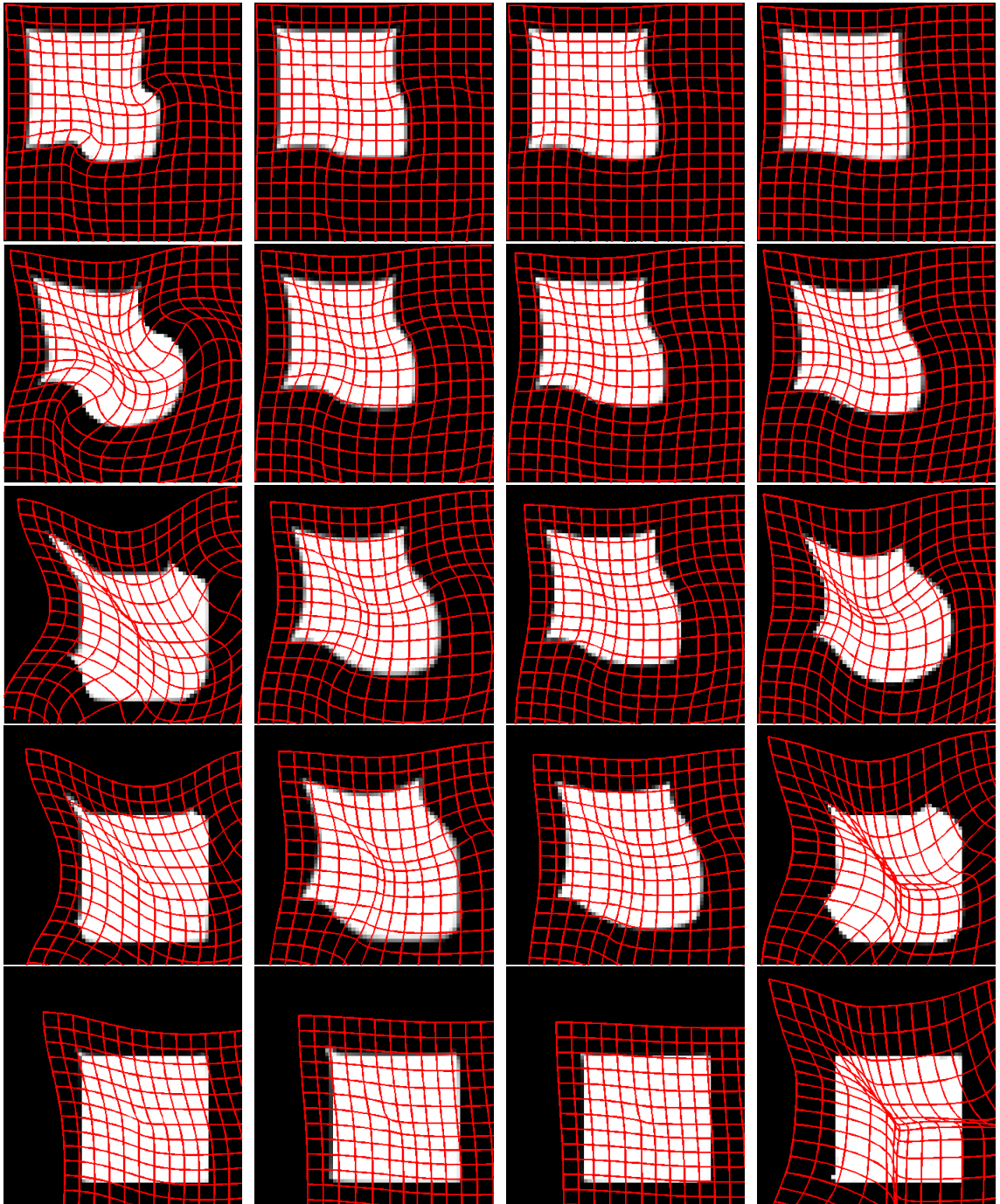


Figure 2.4: Effects of different regularisation terms for registration of two images of square shapes (shown in Figure 2.3). (From top to bottom) The intermediate warped image and the regular grid warped by the estimated transformation with increasing number of iterations using: (from left to right) a linear elastic regularisation, a diffusive regularisation, a Gaussian filtering on the deformation field, a Gaussian filtering on the update of the deformation field.

## 2.4. NATURE OF TRANSFORMATION

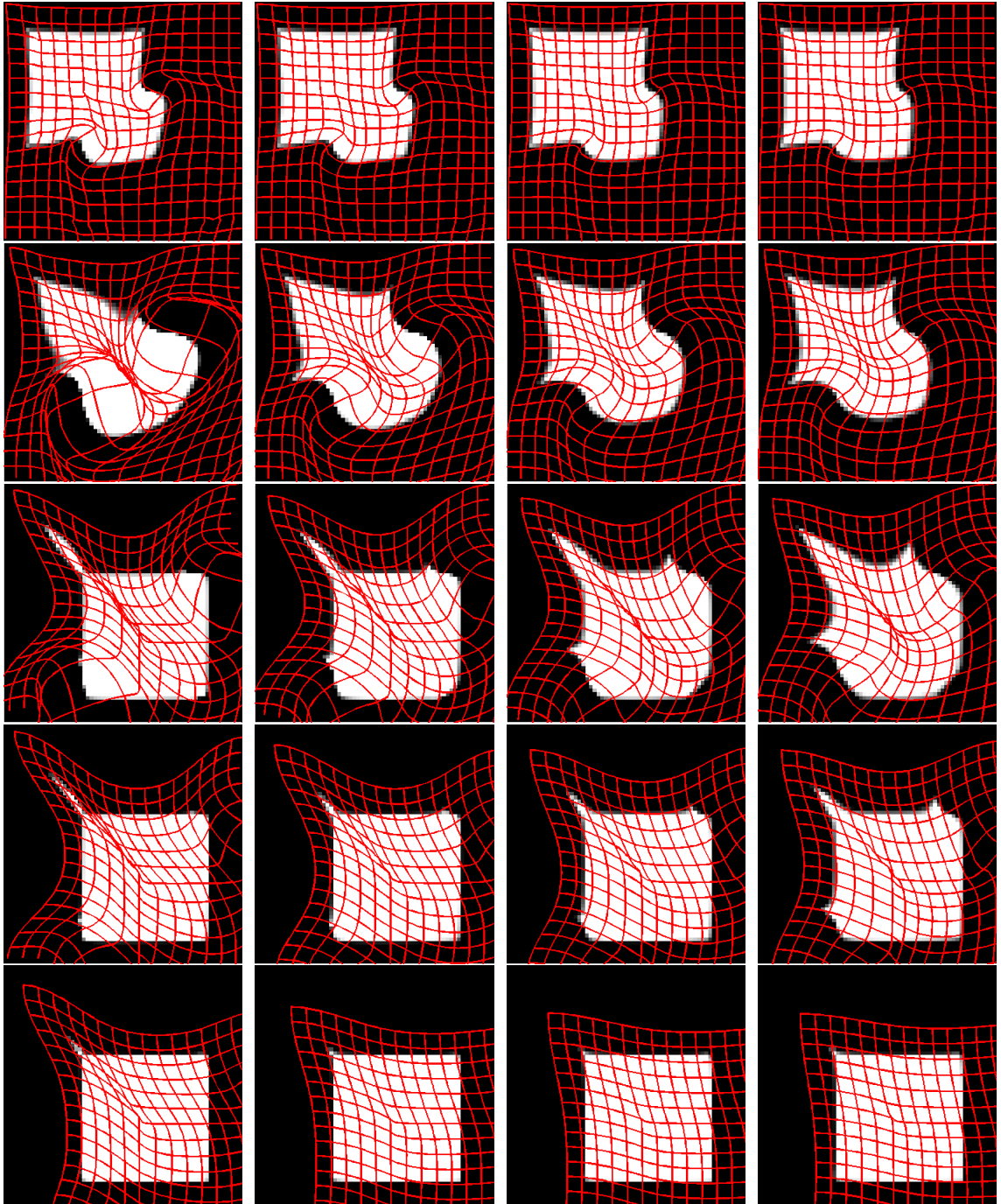


Figure 2.5: Effects of different parameter values for the linear elastic regularisation of deformation field of two images of square shapes (shown in Figure 2.3). (From top to bottom) The intermediate warped image and the regular grid warped by the estimated transformation with increasing number of iterations using: (from left to right) a linear elastic regularisation with values of the parameter set to 0.1, 0.3, 0.5 and 0.7 respectively.

the regularisation terms is shown in Figure 2.4. It can be seen that all regularisation terms allow to estimate a meaningful transformation that warps the moving image to be similar to the reference image (though small artifacts can occur due to image interpolation). As it is expected utilisation the various models for the regularisation term in registration produces a different transformation field. Coupled with the problem of selecting the appropriate regularisation is the problem of tuning the optimal parameters for the chosen regulariser. Having this in mind, the next example shown in Figure 2.5 presents the impact of the parameter value of the linear elastic regularisation for the deformation field. Even for the same type of the regularisation, it does not result in the same estimated deformation field while the warped images are seen to be visually correctly registered. All in all, the selection of the most plausible transformation has to be driven by the particular application.

## 2.5 Additional image registration constraints

The components of image registration that have been discussed previously are the inevitable parts of the objective function given by Equation 2.6. Solving the energy function that consists of the similarity measure  $Sim$  and regularisation term, ends with estimating a transformation relevant to the chosen components and their parameters. Although the estimated transformation warps the moving image to be similar to the reference image, the obtained transformation may not fulfil the particular application restrictions, even for the choice of the most appropriate regularisation. For example, as it can be seen in Figure 2.4, the estimated transformation for the fluid regularisation has some noticeable foldings. Another interesting conclusion can be drawn, when the square is assumed to be a rigid object and the surrounding background to be deformable. In this case, none of the solution shown is correct, because the elastic deformations occur inside the square. Indeed another more suitable regularisation can be found out, but it may not reflect all the desired properties for the objects in image. The above example corresponds to the common problem of medical image registration, where the transformation estimated by the general registration technique is not valid in terms of the biological correctness. For this reason, additional constraints have to be introduced to registration process, to make the estimated transformation usable in clinical applications.

### User-defined constraints

The common properties that model the specific deformation field can be either known *a priori* such as rigidity of bones, volume preservation, discontinuities of the slipping structures, preservation of the neighbourhood topology reflecting the

biological structure of organs, or learnt from the statistically constructed model(s) of the organs/tissue motion based on the representative set of data. In addition, the penalisation terms can be also included in image registration to make possible the visualisation of the structure variations between the timestamps of image acquisitions e.g. pre- and post- contrast injection images.

The local rigidity of the objects like bones was introduced into the non-rigid formulation of the image registration in several ways. One of the possibilities is to introduce the penalty term  $Pen$  (given in Equation 2.7), that must satisfy the rigidity conditions. The rigidity conditions derived from the rigid transformation properties (Equation 2.15) are as follows: the linearity (affinity), the orthogonality (orthonormality) and the orientation preservation (properness) [91] (the terminology in the brackets comes from [130]). The linearity condition is fulfilled when the second order derivatives are zero, while the orthogonality and the orientation preservation can be expressed in terms of the Jacobian matrix of the deformation. The Jacobian matrix of the deformation field  $\varphi$  is defined as follows:

$$J(\vec{u}(\vec{x})) = \begin{bmatrix} \frac{\partial u^1(\vec{x})}{\partial x^1} & \cdots & \frac{\partial u^1(\vec{x})}{\partial x^d} \\ \vdots & \ddots & \vdots \\ \frac{\partial u^d(\vec{x})}{\partial x^1} & \cdots & \frac{\partial u^d(\vec{x})}{\partial x^d} \end{bmatrix} \quad (2.20)$$

The orthogonality is defined as  $J(\vec{u}(\vec{x}))^T J(\vec{u}(\vec{x})) = Id$  and the orientation preservation as keeping the determinant of the Jacobian matrix  $det(J(\vec{u}(\vec{x})))$  equal one for all  $\vec{x}$  where  $Id$  denotes an identity matrix. Utilising the above conditions, numerous image registration algorithms were proposed to a wide range of the applications. Loeckx et al. [77] proposed the B-spline parameterised image registration method to punish the transformations that are not locally rigid, by imposing the above conditions with spatially varying weighting factor  $\beta$  (given in Equation 2.7). In [130] a similar approach was applied to the clinical data of the thorax containing the lung tumors, and to the 2-dimensional digital subtraction angiography. The parameter  $\beta$  in both approaches was selected manually, while in [110] the relation with the Computed Tomography intensity values was shown and applied to the image registration algorithm. Non-parametric image registration with the local rigidity was proposed in [91]. While the mentioned approaches defined the local rigidity as a so-called soft-penalty, where some perturbations with the estimated solution can occur and the local rigidity may not be fulfilled, a constrained registration was proposed [49]. By incorporating hard constraints, the results yielded by this framework are guaranteed to be rigid. Other techniques that preserve the local rigidity, are based on the adaptive context-based filtering of the deformation field [128], or modelling the interaction between control points using physical analogies derived from the in-

put images, and are capable to treat some preselected parts of the image as the rigid objects [84].

An important property from the medical point of view is tracking the structures that are incompressible e.g. tissue of the heart. Several approaches to cope with the volume-preserving image registration have been proposed. Similarly as in case of the local rigidity, the techniques based on penalising either the soft or hard constraints were proposed [47, 50]. The condition that transformation is a volume-preserving transformation is derived from the fact that the determinant of the incompressible transformation is equal one:  $\det(J(\vec{u}(\vec{x}))) = 1$ . Recently, it was shown that integrating divergence-free velocity fields produces the incompressible deformation field [82]. The proposed approach is more computationally efficient due to fast Demon-like implementation.

The aforementioned methods use regularisation terms to ensure smoothness of the deformation field and the additional constraint to make this deformation field realistic. In some applications such as estimation of the lung motion, the smoothness properties contradict motion physiology at the object boundaries. In this case, the lungs and chest slip each other during the respiratory cycle, and create discontinuities in real motion. The modelling of the sliding effect on the organs and tissues boundaries was proposed in [111] where a decomposition of the deformation field was performed to penalise an unwanted solution. Another approach based on the non-linear diffusive registration with the directional dependent regularisation that is applied to the lungs motion was presented in [117].

### Statistically-derived constraints

Until now, the additional constraints were some-how user defined, where a particular combination of the regularisation term and the soft- or hard- constraints was added to enforce a specific kind of the motion. The user knowledge was incorporated first by defining appropriate penalty term  $Pen(\vec{u})$  by either using the properties of the Jacobian matrix  $J_u$ , by decoupling the regularisation term, or by additional filtering operations. However, describing the anatomical deformation of the organs and/or tissues is possible only in relatively simple cases. To provide a reliable additional knowledge that can be first learnt from the representative data sets, statistically-derived constraints have been widely proposed. The statistical models can be built based either on the shapes or on the motion. Incorporating the statistical shape information was presented in [150] where the shapes boundaries were described by a set of the points. The mean and the major modes of the variations of the set of the aligned shapes were found out by applying the Principal Component Analysis (PCA) to them. Then the statistical shape information is incorporated into non-

rigid image registration by the additional criterion that tries to fit the registered shape(s) into the statistical model.

The second approach of incorporating the statistical knowledge into registration utilises the deformations models. In contrast to the previous approach, the representative images have to be first registered and then the PCA is applied to the obtained deformation fields (or parameters describing the deformation field in the case of the parametric approaches). The principal modes of the deformation are then incorporated into the registration framework and restrict the estimated transformation to be statistically related to the pre-learned model. The approaches, that rely on the statistical motion models, have been introduced to the lung motion estimation [76], to the partially missing and noisy data [3], to constrain image registration between structural CT and functional (PET) images and recently to construct the statistical regularisation for DTI of the brain [135]. In all cases, the obtained results suggest that the transformation additionally constrained by the statistical models has been improved to achieve the desired solution.

### **Diffeomorphism**

One of the main limitations of both the user-defined and the statistically created constraints is that they require either the explicit knowledge about the underlying organs/tissue properties or the representative data set(s) to be learnt from. However, this condition may not be fulfilled in many situations due to the lack of the reasonable models to describe the tissue deformation class, or the limitations of providing a sufficiently large data set. To provide the medical or biological correctness of the estimated transformations, the diffeomorphic image registration formulation has been considered as a powerful framework. The diffeomorphic image registration produces a smooth (differentiable), one-to-one transformation that additionally have smooth inverse transformations (by this it means that the inverse transformation may not be calculated explicitly during the registration, but can be calculated using some other methods [7, 27, 96] taking the advantage of being one-to-one transformation). In other words, the diffeomorphic transformation preserves the neighbourhood topologies of the objects in images. For those reasons, the diffeomorphic image registration frameworks are recognised as a worthy of being chosen to medical applications, especially when no additional knowledge about the desired solution can be assumed [5, 145]. Preventing from foldings (the examples of the foldings are visible in Figure 2.4 in the third and fourth column), that in most medical cases are not justified, opens a wide range of the possible applications where invertible transformations are plausible. Maintaining topologies and guaranteeing the connected objects in images remains connected after warping can also be utilised

for automatic segmentation and labelling the structures from electronic atlases [27].

The earliest research on the diffeomorphic image registration relies on the fluid registration with the time-dependent transformation  $\varphi(\vec{x}, t)$  [26]:

$$\varphi(\vec{x}, t) = \vec{x} + \vec{u}(\vec{x}, t) \quad (2.21)$$

Estimation of the diffeomorphic transformation  $\vec{\varphi}$  is linked to a time-dependent velocity field  $\vec{w}$  by evolving:

$$\frac{\partial \vec{u}(\vec{x}, t)}{\partial t} = \vec{w}(\vec{u}(\vec{x}, t), t) \quad (2.22)$$

An optimal solution  $\vec{\varphi}(\vec{x}, t = 1)$  is arising as a result of the integration of the flow given in Equation 2.22 in the following way:

$$\varphi_{opt}(\vec{x}, t = 1) = \vec{u}(\vec{x}, t = 0) + \int_{t=0}^{t=1} \vec{w}(\vec{u}(\vec{x}, t), t) dt \quad (2.23)$$

where  $\vec{u}(\vec{x}, t = 0)$  is an identity transformation. Therefore, the optimisation problem can be stated with respect to the velocity field  $\vec{w}$ :

$$\arg \min_{\vec{w}} \varepsilon(\vec{w}(\vec{x}, t)) = Sim(I_f, I_m(\vec{\varphi}(\vec{w}(\vec{x}, t)))) + \int_{t=0}^{t=1} \alpha Reg(\vec{w}(\vec{x}, t)) dt \quad (2.24)$$

The solution of Equation 2.24 was proposed by Christensen et al. [26] and is associated with first computing the force:  $\nabla Sim(I_f, I_m(\vec{\varphi}(\vec{w}(\vec{x}, t))))$  for the current transformation  $\vec{\varphi}(t)$ , then solving a linear partial differential equation (PDE) for the new velocity field  $\vec{w}(t)$  and finally performing the explicit Euler integration of the flow  $\vec{u}(t)$ . This problem was also studied in [15], where the Large Deformation Diffeomorphic Metric Mapping (LDDMM) algorithm generates a shortest geodesic distance (path) of the flow  $\vec{u}$ . In both cases, it requires an additional integration of the time-varying velocity field  $\vec{w}$ .

Recently, a stationary velocity field  $\vec{v}$  parameterisation of the diffeomorphic transformation was proposed [4], where the velocity field is constant over the integration time:

$$\frac{\partial \vec{u}(\vec{x}, t)}{\partial t} = \vec{v}(\vec{u}(\vec{x}, t)) \quad (2.25)$$

This approach has the advantage of being computationally effective due to a fast algorithm for the deformation field calculation (originally proposed in [4]). Further, this parameterisation of the diffeomorphic transformation was adapted to non-rigid image registration [5, 143, 144, 145, 53], and the obtained results suggest that stationary velocity fields are feasible way of describing the motion variability in medical

applications.

Diffeomorphic image registration can also be described in terms of the algebraic structure called a group. The group is defined as a algebraic structure consisting of a set of some elements and an operation on them. The operation takes two of the set elements and generates another element that still has the property of the set elements. To be quantified as a group, the set of elements and operation on them must hold four basic requirements defined as the group axioms. These requirements are as follows: closure, associativity, the neutral element existence, and inverse element existence. To put the diffeomorphic transformation estimation in another way, the set of the diffeomorphic transformations  $Diff$  and the composition operator  $\circ$  can be stated as (in the perfect case) a Lie group  $(Diff, \circ)$ . Any Lie group can be associated with another algebraic structure called a Lie algebra. The Lie algebra is a vector space (vector space of the velocity fields) with the associated operation called the Lie brackets and the Lie algebra captures the structure of the Lie group  $(Diff, \circ)$ . The Lie group and the Lie algebra are related through the exponential mapping  $\exp$  that is a smooth mapping from the neighbourhood elements of the Lie algebra to the elements of the Lie group that are *infinitesimally close* to the neutral element of this Lie group. The exponential mapping recaptures the structure of the Lie group from the Lie algebra. Thus, the estimation of the diffeomorphic transformation can be obtained as finding an update in the Lie algebra space and through the exponential mapping it is composed with the element from the Lie group [4, 145]. In addition, Arsigny et al. [4] showed that the principal logarithm (that is the inverse of the exponential mapping) corresponds to the stationary velocity field parameterisation of the diffeomorphic transformation. The efficient algorithms to compute the principal logarithm were proposed in [4, 17], while the fast algorithm for calculating exponential mapping of the vector field was proposed in [4]. The accuracy and the performance of the different variants of those algorithms were shown in [18].

The diffeomorphic framework was also applied to the non-rigid B-spline based image registration [115]. To preserve the properties of the diffeomorphic transformation for the estimated transformation, the multiple composition of B-spline transformations that are primary ensured to be one-to-one mapping, is repeated. As it was pointed in the previous section, the composition of the diffeomorphic transformations becomes also a diffeomorphic transformation. In the same manner, some of the non-parametric approaches were established to be diffeomorphic by the composition of the diffeomorphic update of the deformation fields. To prevent the update of the deformation from folding, the penalisation of the determinant below zero [27, 63] and the explicit limiting magnitude procedure were proposed [155].

## 2.6 Solving image registration problem

In general, in the case of the deformable image registration, a high-dimensional, non-linear, non-convex image registration problem has to be solved in a reasonable time. Various optimisation strategies have been utilised to cope with this problem.

As it was shown, the image registration problem can be stated as an optimisation problem (Equation 2.5) for the particular components of image registration. The most common strategy of finding the optimal transformation is using the iterative algorithms. The iterative algorithm starts with the initial guess about the solution and then by generating multiple steps converging to the solution. For non-rigid image registration the initial guess  $\vec{u}_0$  of the displacement is usually given as an identity transform or the solution of the parametric pre-registration:

$$\vec{u} = \vec{u}_0 + \vec{d}u_1 + \dots + \vec{d}u_i \quad (2.26)$$

where  $\vec{d}u_i$  is an update of the deformation field calculated by the iterative method and  $i$  is an iteration index.

The easiest way to consider estimation of the transformation (minimising the non-linear functional) is to calculate the gradient of the image registration function (given in Equation 2.6) and use the gradient-based steepest descent method. The updates of the displacement field are equivalent to finding the derivative  $\nabla\varepsilon(\vec{u})$  of the functional  $\varepsilon(\vec{u})$  (so-called the Gateaux derivative):

$$\nabla\varepsilon(\vec{u}) = \frac{\partial\varepsilon(\vec{u})}{\partial\vec{u}} \quad (2.27)$$

The update of the deformation field for the steepest descent strategy is summarised below:

$$\vec{d}u_{i+1} = -\tau_i \nabla\varepsilon(\vec{u}_i) \quad (2.28)$$

where  $\tau_i$  is a length step parameter. The strategies relying on the higher order schemes e.g. Newton method are not used commonly for non-parametric image registration due to required calculation of the high order derivatives of the images and similarity measures [90, 30].

Another possible strategy requires first to find the analytical Euler-Lagrange equations corresponding to the objective function, and then to discretise and solve them with the selected numerical solution schemes. The Euler-Lagrange equation is defined as follows:

$$A(\vec{u})(\vec{x}) - f(\vec{x}, \vec{u}(\vec{x})) = 0 \quad (2.29)$$

where  $A$  is a partial differential operator related the regularisation term, and  $f$  is

called a force linked to the similarity measure [90]. The partial differential equation (PDE) given by Equation 2.29 can be solved for example by the fixed-point iteration scheme [90]. The optimisation problem given by Equation 2.5 or the Euler-Lagrange equation 2.29 can be reformulated into a time-dependent process and finding the steady solution with change of the deformation field:

$$-\frac{\partial \vec{u}}{\partial t} = \frac{\partial \varepsilon(\vec{u})}{\partial \vec{u}} \quad (2.30)$$

Thus, a non-linear optimisation problem is rewritten to be solved as a linear problem. In practice, two schemes of the time discretisation are commonly used, explicit time discretisation and semi-implicit time discretisation [30]. The general overview of the computational techniques for solving an image registration problem is presented in [90, 30].

The aforementioned strategies are so-called *optimise-discretise* strategies [90] because first the analytical solution had to be found, then the numerical schemes are applied. The opposite class of the solution strategy that has to be mentioned, is known as a *discretise-optimise* technique [92]. The *discretise-optimise* technique relies on an appropriate discretising scheme that is applied first to get a finite-dimensional optimisation problem. Then the finite-dimensional problem can be solved with an associated optimisation method. This strategy is shown as computationally robust because the high order method can be used for estimation of the transformation.

Besides the strategy that is evaluated, there always is a chance to get trapped into the local minimum. The common technique to avoid this problem is adopting the multi-scale or the multi-resolution scheme.

## 2.7 Summary

The main purpose of this chapter was to introduce briefly the image registration problem, and the principle components involved in the estimation of the optimal, in some sense, transformation. The approaches described in this chapter are the most common techniques, that have been investigated in the past years. The major focus was on presenting the deformable image registration with the particular property such as diffeomorphism, that has been shown to be valuable formulation of the image registration applied to medical data. The mentioned formulation that allow a generic diffeomorphic framework to be defined, the log-Euclidean framework, is outlined as it is going to be critically assessed in the following chapters.

The four aspects of image registration were discussed and based on them the

classifications of the image registration algorithms were presented. As the first set of separation, the similarity criteria were chosen. A wide range of the volumetric distances between images was presented and the advantages in parallel with the main limitations were pointed out. Another classification was designed in terms of the transformation properties. The image registration was broadly divided into two categories namely, parametric- and non-parametric image registration. As it was shown, in majority of medical applications, some additional requirements for the transformation are necessary, and based on them, image registration was classified. The comparative section ends with a description of the optimisation strategies, that are commonly used to solve image registration problems.

The aim of these comparisons is not only to introduce the problem of image registration, but also to be used in the consecutive chapters as the theoretical background for the discussion on the obtained results for assessed image registration algorithms.

# Chapter 3

## Implementations of image registration

This chapter first considers the three commonly used image registration algorithms: the steepest descent approach (so-called *variational Optical Flow*), the Newton's iteration-based approach (originally named as *fast Free Form Deformation*), and the Demon approach. Then, the different formulations of diffeomorphic image registration are presented: the small-step approach, the exponential updates scheme, the log-Euclidean parametrisation of the deformation field, and image registration constrained by the inverse consistency criterion. Together with the detailed description of these formulations, the previously introduced algorithms are reformulated to establish them in the diffeomorphic manner. Equally important in this chapter is to present the details of the image registration algorithms that are based on the log-Euclidean parameterisation of the deformation fields via the stationary vector fields. The next step is to give a more in depth analysis of all those algorithms and their formulations. The aim of this analysis is to re-examine those approaches to determine their usefulness and robustness in possible medical-driven applications. This chapter ends by introducing the idea of the symmetrisation of the registration process by simultaneously warping input images into another one. A novel algorithm for the deformation field inversion is presented and based on it a new method of image registration with symmetric warping is also suggested.

### 3.1 Classical approaches to image registration

The previous chapter introduced numerous image registration approaches and gave a brief description of them. This chapter presents the details for a few of them, namely: the steepest descent approach (so-called *variational Optical Flow*), the Newton's iteration approach (originally named as *fast Free Form Deformation*), and

the Demon approach. The selection of this particular set of algorithms is driven by several objectives. Firstly, all of these methods are intensity-driven and can therefore be considered to be fully automatic approaches (up to the successful selection of the so-called design parameters embedded in these schemes). Secondly, most of the aforementioned algorithms are utilised in the biomedical applications, therefore, they can be seen as the most suitable for the further applications of the undertaken project. Furthermore, the investigation is going to be pursued on a specific class of the image registration algorithms - diffeomorphic image registration, leading to the practically useful outcomes covered in the application-driven part of this thesis. To sum up, some examples of the potentially biomedically favourable, automatic, intensity-based, diffeomorphic image registration methods are described in details in the following sections.

#### 3.1.1 Steepest descent approach

The variational techniques are often a common *first* choice method for finding an appropriate solution in many areas of computer vision, owing to both the excellent results that can be obtained through this approach and the strict mathematical formulation. The image registration based on the variational approach is phrased using the backgrounds of the calculus of variations. The general variational framework for image registration was presented in [56, 24, 57, 90], and it provides a simple method to integrate different similarity criteria and a suitable regularisation terms in one common energy functional that has to be either maximised or minimised.

As in the previous chapter, the problem of image registration is stated as a minimisation of the objective function:

$$\varepsilon(\vec{u}) = \int_{\Omega} Sim(I_f(\vec{x}), I_m(\vec{x} + \vec{u}(\vec{x})))dx + \alpha \int_{\Omega} Reg(\vec{u}(\vec{x}))dx \quad (3.1)$$

Assuming the existence of a local minimum  $\vec{u}_{opt}$  for the energy function (given by Equation 3.1), the functional derivative (or formally first Gateaux derivative [57])  $\nabla\varepsilon(\vec{u})$  of the energy function  $\varepsilon(\vec{u})$  at  $\vec{u}_{opt}$  must hold as follows:

$$\nabla\varepsilon(\vec{u}) = \vec{0} \quad (3.2)$$

Following reasoning from [56, 24, 57], it can be shown that the condition of the optimality given by Equation 3.2 is equivalent to gradient of the energy function  $\varepsilon(\vec{u})$ . As it was presented in the previous chapter, the optimisation for image registration is a non-linear problem due to non-linearity introduced by the dependence between the input images and displacement field. In the general framework given in [56, 24, 57],

### 3.1. CLASSICAL APPROACHES TO IMAGE REGISTRATION

---

a solution  $\vec{u}_{opt}$  is estimated by solving Equation 3.2 based on the steepest descent strategy with artificially introduced variable  $t$ :

$$\frac{\partial \vec{u}}{\partial t} = -\nabla \varepsilon(\vec{u}) \quad (3.3)$$

starting from a suitable initial guess  $\vec{u}_0$ . The direction of the steepest descent is dependent on the choice of the similarity criterion and the regularisation term:

$$\nabla \varepsilon(\vec{u}) = \nabla Sim(I_f, I_m(\vec{u})) + \alpha \nabla Reg(\vec{u}) \quad (3.4)$$

In the simple case when the sum of the squared differences is selected (Equation 2.8) as a similarity criterion, the force  $\nabla Sim(I_f, I_m(\vec{\varphi}(\vec{x})))$  is defined by:

$$\nabla Sim(I_f(\vec{x}), I_m(\vec{\varphi}(\vec{x}))) = (I_f(\vec{x}) - I_m(\vec{\varphi}(\vec{x}))) \nabla I_m(\vec{\varphi}(\vec{x})) \quad (3.5)$$

where  $I_m(\vec{\varphi}(\vec{x}))$  is moving image  $I_m$  warped via transformation  $\vec{\varphi}$ , and  $\nabla I_m(\vec{\varphi}(\vec{x}))$  is gradient of the warped moving image  $I_m(\vec{\varphi}(\vec{x}))$ . Furthermore, when the linear elastic model is assumed (2.18), the partial differential operator  $\nabla Reg(\vec{u})$  is defined as follows:

$$\nabla Reg(\vec{u}(\vec{x})) = (\mu \Delta \vec{u}(\vec{x}) + (\lambda + \mu) \nabla(\nabla \cdot \vec{u}(\vec{x}))) \quad (3.6)$$

where  $\Delta \vec{u}(\vec{x})$  is a Laplace operator, and  $\nabla \cdot \vec{u}(\vec{x})$  is divergence operator. Finally,  $\vec{u}_{opt}$  is estimated according Equation 2.26 by calculating the direction of update  $\vec{d}u_i$  for the deformation field at  $i$ th iteration in the following way:

$$\begin{aligned} \vec{d}u_i(\vec{x}) &= (I_f(\vec{x}) - I_m(\vec{\varphi}_{i-1}(\vec{x}))) \nabla I_m(\vec{\varphi}_{i-1}(\vec{x})) \\ &+ \alpha (\mu_{elas} \Delta \vec{u}_{i-1}(\vec{x}) + (\lambda_{elas} + \mu_{elas}) \nabla(\nabla \cdot \vec{u}_{i-1}(\vec{x}))) \end{aligned} \quad (3.7)$$

Equation 3.7 is finally discretised. The algorithm with the SSD and the linear elastic model is summarised in Algorithm 1. The matrix stencils for fast convolution of the deformation field (Algorithm 1 Line 5) can be found in [57, 90, 5].

Although in the original work the framework was called *variational Optical Flow* (or *variational approach*), here the method is referred as the steepest descent approach because the other methods that will be described also depend on variational principles.

The presented framework is very generic and a wide class of known similarity measures and regularisation terms can be chosen instead of the SSD and a linear elastic model. In [56, 24] the derivatives of Mutual Information, Correlation Coefficient and Correlation Ratio were introduced, to characterise the relation between images. That work was then extended by providing the local similarity criteria

---

**Algorithm 1** Steepest descent approach
 

---

**Input:** Images:  $I_f$  and  $I_m$

Weight of regularisation  $\alpha$

Design parameters (for linear elastic model:  $\lambda_{elas}, \mu_{elas}$ )

**Output:** Transformation  $\vec{\varphi}$

```

1:  $\vec{u}_0 = \vec{0}, i = 1$ 
2: repeat
3:   for all  $\vec{x} \in \Omega$  do
4:     calculate force  $\nabla Sim(I_f(\vec{x}), I_m(\vec{\varphi}_{i-1}(\vec{x})))$  (Equation 3.5)
5:     calculate  $\nabla Reg(\vec{u}_{i-1}(\vec{x}))$  (Equation 3.6)
6:     calculate update  $\vec{d}u_i(\vec{x})$  (Equation 3.7)
7:     update deformation field  $\vec{u}_i(\vec{x}) = \vec{u}_{i-1}(\vec{x}) + \vec{d}u_i(\vec{x})$ 
8:   end for
9:    $i = i + 1$ 
10: until (deformation field does not change) or ( $i \geq IterMax$ )
11: return  $\vec{u}$ 
  
```

---

[57, 25], to alleviate the assumption about the stationary distribution of the image intensities across spatial positions. Recently, Yi and Soatto [156] derived the Gateaux derivative for the Normalised Mutual Information. In place of the local similarity criterion, the weighted similarity criterion was introduced, to take advantages of the both global and local properties of images. The weighted similarity criterion is shown in Equation 2.13. All of the mentioned statistical measures enable finding the correspondences between images with different modalities. The main limitation of the explicit derivative calculation both the similarity criterion and the regularisation term (except the linear operators such as linear elasticity, diffusion, or curvature model) is usually the complex form of those derivatives. As a result, computing the analytical gradient of more sophisticated image registration components with respect to the non-parameterised deformation fields is a non-trivial task.

#### 3.1.2 Newton's iteration approach

While the steepest descent approach offers not only a general but also very flexible framework for image registration with a wide variety of possible similarity criteria and regularisation terms, the approach suffers from some limitations including slow convergence, typical for the steepest descent strategy, and the difficulties linked to

### 3.1. CLASSICAL APPROACHES TO IMAGE REGISTRATION

---

explicit calculation of the analytical gradients of first order in the case of complex form of similarity measures. The next method that is to be discussed here uses the Newton's iteration strategy to estimate the transformation.

In [78], the objective function (given by Equation 2.6):

$$\varepsilon(\vec{u}) = Sim(I_f(\vec{x}), I_m(\vec{x} + \vec{u}(\vec{x}))) + \alpha Reg(\vec{u}(\vec{x})) \quad (3.8)$$

consists of minimisation the sum of the squared differences (Equation 2.8) and the diffusive deformation model (Equation 2.17) for regularisation thereby the objective function is defined in the following way:

$$\varepsilon(\vec{u}) = \int_{\Omega} (I_f(\vec{x}) - I_m(\vec{x} + \vec{u}(\vec{x})))^2 dx + \lambda_{diff} \int_{\Omega} \sum_{j=1}^d \sum_{k=1}^d \left( \frac{\partial u^j(\vec{x})}{\partial x^k} \right)^2 dx \quad (3.9)$$

Similarly, as in the case of the steepest descent approach introduced in the previous section, using the calculus of variations, Equation 3.9 becomes a problem of solving a system of nonlinear elliptic partial differential equations (PDE):

$$(I_f - I_m(\vec{\varphi})) \nabla I_m(\vec{\varphi}) + \lambda_{diff} \Delta \vec{u} = \vec{0} \quad (3.10)$$

The Newton's iteration method estimates the solution in an iterative manner by evaluating:

$$u_i^l(\vec{x}) = u_{i-1}^l(\vec{x}) - \frac{L_i^l(\vec{x})}{\frac{\partial L_i^l(\vec{x})}{\partial u_{i-1}^l(\vec{x})}} \quad (3.11)$$

where  $\vec{L}_i(\vec{x}) = [L_i^1(\vec{x}), \dots, L_i^l(\vec{x}), \dots, L_i^d(\vec{x})]$  denotes the left side of Equation 3.10 and  $l$  is an index of image dimension. As a result of utilising the diffusive model of regularisation, each dimension  $d$  of the displacement  $\vec{u}_i$  (transformation) can be solved separately. To apply the Newton's iteration strategy for solving Equation 3.10, the equation is discretised by setting the finite difference method. The finite difference method approximates Equation 3.10 in the following way:

$$L_i^l(\vec{x}) = (I_f(\vec{x}) - I_m(\vec{\varphi}_{i-1}(\vec{x}))) \nabla^l I_m(\vec{\varphi}_{i-1}(\vec{x})) + \lambda_{diff} \Delta u_{i-1}^l(\vec{x}) \quad (3.12)$$

where  $L_i^l(\vec{x})$  corresponds to the specific dimension image/volume  $l$  at  $i$ th iteration. The derivative of  $L_i^l$ ,  $\frac{\partial L_i^l(\vec{x})}{\partial u_{i-1}^l}$  is derived from an approximated version of Equation 3.10 (details in [78]):

$$\frac{\partial L_i^l(\vec{x})}{\partial u_{i-1}^l} = -\lambda_{diff} - (\nabla^l I_m(\vec{\varphi}_{i-1}(\vec{x})))^2 \quad (3.13)$$

### 3.1. CLASSICAL APPROACHES TO IMAGE REGISTRATION

---

**Algorithm 2** Newton's iteration approach

---

**Input:** Images  $I_f$  and  $I_m$

Parameter:  $\lambda_{diff}$

**Output:** Transformation  $\vec{\varphi}$

```

1:  $\vec{u}_0 = \vec{0}, i = 1$ 
2: repeat
3:   for all  $\vec{x} \in \Omega$  do
4:     for all  $l$  do
5:       calculate  $L_i^l(\vec{x})$  (Equation 3.12)
6:       calculate  $\nabla^l L_i^l(\vec{x})$  (Equation 3.13)
7:       calculate update  $du_i^l(\vec{x})$  (Equation 3.14)
8:     end for
9:     update deformation field (Equation 3.11)
        $\vec{u}_i(\vec{x}) = \vec{u}_{i-1}(\vec{x}) + \vec{d}u_i(\vec{x})$ 
10:   end for
11:    $i = i + 1$ 
12: until (deformation field does not change) or ( $i \geq IterMax$ )
13: return  $\vec{u}$ 

```

---

The update of the deformation field for the Newton's iteration method is finally given in following way:

$$du_i^l(\vec{x}) = \frac{L_i^l(\vec{x})}{\frac{\partial L_i^l(\vec{x})}{\partial u_{i-1}^l(\vec{x})}} = - \frac{(I_f(\vec{x}) - I_m(\vec{\varphi}_{i-1}(\vec{x}))) \nabla^l I_m(\vec{\varphi}_{i-1}(\vec{x})) + \lambda_{diff} \Delta u_{i-1}^l(\vec{x})}{\lambda_{diff} + (\nabla^l I_m(\vec{\varphi}_{i-1}(\vec{x})))^2} \quad (3.14)$$

The Newton's iteration approach is summarised in Algorithm 2. Lu et al. [78] proposed to use the Gauss-Seidel method for calculating  $L_i^l$ , that uses the latest estimated value of the displacement field  $u_i^l(\vec{x})$  and warped moving image  $I_m(\vec{\varphi}_i(\vec{x}))$ . In [97] the other possible methods for calculating  $L_i^l$  were evaluated and compared, showing that the choice of the Gauss-Seidel method is a good trade off between simplicity and computational cost. Although the Successive Over-Relaxation (SOR) method achieved a slightly better convergence rate, it was necessary to find the embedded relaxation parameter that is data-dependent.

This algorithm was originally evaluated for radiotherapy-based applications [78], and also assessed in works done by Zhang et al. [159] and Papiez et al. [97] for the same purposes.

### 3.1.3 Demon approach

The large number of the applications where it was used makes the Demon algorithm [138] probably one of the best known image registration algorithm in computer vision. In contrast to the other approaches that have been discussed previously, originally the concept of the Demon method was neither established in any optimisation framework nor linked into any deformation model. The method was derived from the physics analogy with the Maxwell's demon in thermodynamics (detailed discussion in the seminal paper by Thirion [138]). The lack of the underlying mathematical proof of the possibility of estimating the optimal transformation have led to many variants of this methods, dependent on the experimental results. Besides the intuitive way of presenting this algorithm, some possible frameworks have been developed to put the Demon algorithm as an optimisation problem [90, 145, 163].

The Demon algorithm is derived from the basic assumption of the *optical flow* equation [59], where it is assumed that the intensity (brightness) of the moving image is constant over time (so-called brightness consistency criterion):

$$I_f \approx I_m(\vec{\varphi}) \quad (3.15)$$

For small changes of the displacement field  $\vec{d}u$ , the Taylor expansion of the images' intensity difference ( $I_f(\vec{x}) - I_m(\vec{x} + \vec{d}u(\vec{x}))$ ) holds:

$$(I_f(\vec{x}) - I_m(\vec{x} + \vec{d}u(\vec{x}))) = (I_f(\vec{x}) - I_m(\vec{\varphi}(\vec{x}))) + \nabla I_m(\vec{\varphi}(\vec{x}))\vec{d}u(\vec{x}) \quad (3.16)$$

providing the mentioned *optical flow* equation [59]. The unique solution of the Equation 3.16 can not be determined directly, thus Thirion [138] proposed to select the direction of the minimum length vector  $\vec{d}u$  towards the fixed image  $I_f$ :

$$\vec{d}u(\vec{x}) = \frac{I_f(\vec{x}) - I_m(\vec{\varphi}(\vec{x}))}{\|\nabla I_f(\vec{x})\|^2} \nabla I_f(\vec{x}) \quad (3.17)$$

The value of the above equation tends to infinity when the gradient of the fixed image  $\|\nabla I_f(\vec{x})\|^2$  is close to zero. For the purpose of stabilising it, an additional component  $\kappa$  has to be considered:

$$\vec{d}u(\vec{x}) = \frac{I_f(\vec{x}) - I_m(\vec{\varphi}(\vec{x}))}{\|\nabla I_f(\vec{x})\|^2 + \kappa} \nabla I_f(\vec{x}) \quad (3.18)$$

In the seminal paper of the Demon approach [138] the additional component was chosen to be  $\kappa = (I_f(\vec{x}) - I_m(\vec{\varphi}_i(\vec{x})))^2$ . Due to the fact that calculation of the update  $\vec{d}u$  once is not sufficient to estimate the transformation, the updates of

the displacement field can be computed in an iterative manner from the following formula:

$$\vec{d}u_i(\vec{x}) = \begin{cases} \frac{(I_f(\vec{x}) - I_m^{\vec{\varphi}_{i-1}}(\vec{x}))}{\|\nabla I_i(\vec{x})\|^2 + (I_f(\vec{x}) - I_m^{\vec{\varphi}_{i-1}}(\vec{x}))^2} \nabla I_i(\vec{x}) & \text{if } \|\nabla I_i(\vec{x})\|^2 + (I_f(\vec{x}) - I_m^{\vec{\varphi}_{i-1}}(\vec{x}))^2 > 0 \\ 0 & \text{otherwise} \end{cases} \quad (3.19)$$

where  $\nabla I_i(\vec{x})$  is chosen to be  $\nabla I_f(\vec{x})$  for the originally proposed method, and  $I_m^{\vec{\varphi}_{i-1}}(\vec{x}) = I_m(\vec{x} + \vec{u}_{i-1}(\vec{x}))$ . Using general notation of gradient  $\nabla I_i(\vec{x})$  in Equation 3.19 was motivated to emphasise that in principle other regularisation techniques of Equation 3.16 can be considered. It is mainly due to the shortcomings from the lack of any underlying optimisation framework in the original work. For this reason  $\nabla I_i$  can be calculated in many ways: the so-called fixed Thirion's gradient (a static gradient) that was originally proposed in [138]:

$$\nabla I_i(\vec{x}) = \nabla I_f(\vec{x}) \quad (3.20)$$

a moving Thirion's gradient (or an active gradient) taken from the assumption that at the end of the registration  $I_f(\vec{x}) \approx I_m(\vec{\varphi}(\vec{x}))$  and similarly the gradient of images  $\nabla I_f(\vec{x}) \approx \nabla I_m(\vec{\varphi}(\vec{x}))$ :

$$\nabla I_i(\vec{x}) = \nabla I_m(\vec{x} + \vec{u}_{i-1}(\vec{x})) \quad (3.21)$$

or the combination of both of them - the symmetric gradient [145]:

$$\nabla I_i(\vec{x}) = \frac{1}{2}(\nabla I_f(\vec{x}) + \nabla I_m(\vec{x} + \vec{u}_{i-1}(\vec{x}))) \quad (3.22)$$

The update of the displacement field (Equation 3.19) can be calculated for each image point, the contours, or the labels of the segmented objects [138]. The regularisation of Demon is done by smoothing via Gaussian filtering either for the update of displacement (denoted by  $G_{fluid}$ ) or directly displacement (denoted by  $G_{diff}$ ) [145].

Due to very high efficiency and widespread use in the multiple applications [138, 148, 21], several attempts to interpret and theoretically justify the Demon have been made. Modersitzki [90] showed the Demon as a variational problem of solving the SSD and the diffusive model as similarity criterion and regularisation term respectively. Another approach was given by Vercauteren et al. [145], where the Demon was presented as minimisation of a global energy function including the sum of the squared difference with additional hidden variable so-called correspondence, optimised using the Newton-like strategy. Recently, Zikic et al. [163] presented the general preconditioning system based on the steepest descent strategy to exploit dif-

---

**Algorithm 3** Demon approach
 

---

**Input:** Images:  $I_f$  and  $I_m$

Parameters:  $G_{fluid}$ ,  $G_{diff}$

**Output:** Transformation  $\vec{\varphi}$

```

1:  $\vec{u}_0 = \vec{0}$ ,  $i = 1$ 
2: repeat
3:   for all  $\vec{x} \in \Omega$  do
4:     calculate update  $\vec{d}u(\vec{x})$  (Equation 3.19)
5:     smooth update of the deformation field using Gaussian filter  $G_{fluid}$ :
        $\vec{d}u_i(\vec{x}) = G_{fluid} * (\vec{d}u(\vec{x}))$ 
6:     update deformation field  $\vec{u}_i(\vec{x}) = \vec{u}_{i-1}(\vec{x}) + \vec{d}u_i(\vec{x})$ 
7:     smooth deformation field  $\vec{u}_i(\vec{x})$  using Gaussian filter  $G_{diff}$ :
        $\vec{u}_i(\vec{x}) = G_{diff} * (\vec{u}_i(\vec{x}))$ 
8:   end for
9:    $i = i + 1$ 
10: until (deformation field does not change) or ( $i \geq IterMax$ )
11: return  $\vec{u}$ 

```

---

ferent similarity criteria using the Demon approach. The proposed preconditioning system modifies the magnitude of  $\nabla I(\vec{x})$ .

## 3.2 Diffeomorphic image registration

Until this section, image registration has been considered in the simplest formulation that involves estimating a smooth mapping establishing correspondences between the objects in the images. Section 2.5 introduced the theoretical concept of diffeomorphism as a common requirement for the estimated displacement field that is assumed to be a smooth, one-to-one differentiable mapping having a smooth and differentiable inverse. The importance of preserving the neighbourhood topology of the objects (that is given implicitly by the definition of diffeomorphism) has been shown in many medically driven applications. Because of these numerous applications, several different frameworks have been proposed to establish the diffeomorphic formulation of the image registration problem. The approaches investigated and analysed here, can be broadly divided into two groups. The first type of the diffeomorphic image registration is based on the assumption of the closure (consistency) under composition of two diffeomorphic transformations. In other words, if two transformations are diffeomorphic, the result of their composition will be also

diffeomorphic (up to certain numerical errors due to dealing with the discrete cases). The methods utilising the composition techniques are often called as a small-step approach. The second approach is formulated using the log-domain parameterisation of the displacement field by the stationary velocity field. Based on the group theory interpretation given in Section 2.5, these two approaches can be linked by the concatenation of the transformation operation done either for the diffeomorphic transformations or for the vector fields in the Lie algebra space.

As it was pointed out in the previous chapter, there are the other approaches that aim to formulate the diffeomorphic image registration e.g. time-dependent fluid image registration [26], time-dependent registration via estimating the geodesic path [15, 14], and the parametric image registration with constrained B-spline [115]. The choice of the *small-step* or the log-Domain frameworks to be investigated in this work, is particularly motivated by several reasons. First of all, the mentioned approaches are subjected to some conditions that are embedded into the underlying mathematical formulation e.g. the mathematical statement of the *small enough* steps of updating deformation fields in the case of the *small-step* approach. This work aims at providing the experimental evidences of the value of that quantity e. g. the length of the *small-step*. Another reason lies in an attempt to apply these image registration algorithms to a new application, to the pelvic area of body. It is done because the major works have been done in the field of the brain data analysis. Applications of these methods to analysis of the pelvic area data bring new challenges. Although in general, the pelvic organs can be described as keeping diffeomorphic properties, from time to time, some exceptions such as gas bowels, and/or changes of the rectum contents can occur. Additionally, the changes of the pelvic-area organ shapes can be also relatively significant in comparison to the variability of the brain shapes. Finally, the computational effort of the methods that are chosen to be investigated, is reported to be significantly reduced compared to the time-dependent diffeomorphic algorithms [26, 15, 14].

### 3.2.1 Small-step approaches

The *small-step* approach utilises the closure of the diffeomorphic transformations under composition operator  $\circ$ . The displacement estimated based on the *small-step* technique can be seen as multiple compositions of the updates of deformation field  $\vec{d}u_i$  calculated in each iteration  $i$  of the image registration:

$$\vec{u} = \vec{u}_0 \circ \vec{d}u_1 \circ \dots \circ \vec{d}u_i \tag{3.23}$$

where  $\vec{u}_0$  is an initial guess of the displacement (usually  $\vec{u}_0 = \vec{0}$  or the result of the pre-registration). Due to memory restrictions and in order to simplify the aspects of the implementation, the above formula can be rewritten as a composition of the already known displacement field (estimated in the previous iteration)  $\vec{u}_{i-1}$  and the currently calculated update of the deformation field  $\vec{d}u_i$ :

$$\vec{u}_i = \vec{u}_{i-1} \circ \vec{d}u_i \tag{3.24}$$

Various approaches have been proposed to restrict the magnitude of update of the deformation field to be diffeomorphic transformation. Chafd’hotel et al. [25] presented the theoretical framework of the diffeomorphic flow of the multi-modal similarity criterion based force with regularisation applied to the update of the deformation field. Thereby, it can be seen as fluid-like time-dependent flow in a suitable infinite-dimensional space of the invertible transformation [26]. In order to obtain the *sufficiently smooth* update of the deformation field, the Gaussian filtering procedure was applied when practical implementations of this framework were carried out.

The common way of checking whether the calculated update of the deformation field preserves one-to-one mapping, is computing the determinant of the Jacobian matrix  $\det(J(\vec{u}))$  of that update [26, 27]. The positive value of  $\det(J(\vec{u}))$  indicates that the one-to-one mapping property is not broken. In [131], the idea of the magnitude limiting procedure was derived to guarantee the invertibility of the updated deformation field. The concept of the magnitude limiting procedure can be explained in the following way. When the vectors representing the update of the deformation field associated with two neighbourhood intensity points have a norm (length) larger than some threshold, they can cross each other and folding can occur. If these vectors are small enough (their norm is below the threshold), they represent an invertible transformation. It was shown intuitively that the maximum magnitude (norm) of the update of the deformation field that preserves one-to-one mapping, has to be below half of the voxel/pixel size (image spacing). In the same manner, the diffeomorphic formulation of the B-spline parameterised image registration via multiple compositions was proposed in [115]. In contrast to the previous, intuitive explanation of the threshold value for the invertible transformation, the local injectivity theorem of the cubic B-spline was introduced. From that theorem, the maximum displacement of the control points was deduced to be 0.4 of the spacing of the control points grid. In the registration algorithm proposed by Yang et al. [155], the indirect adaptation of the conclusion given in [115] was done to the Demon-like update of the deformation field. The procedure of the limiting magnitude proposed

in [155] that is defined as follows:

$$\vec{d}u_i(\vec{x}) = \begin{cases} \vec{d}u_i(\vec{x}) & \text{if } \|\vec{d}u_i(\vec{x})\| \leq 0.4 \\ 0.4 \frac{\vec{d}u_i(\vec{x})}{\|\vec{d}u_i(\vec{x})\|} & \text{otherwise} \end{cases} \quad (3.25)$$

is evaluated at every iteration  $i$  and simultaneously the update of deformation field  $\vec{d}u_i$  is additionally smoothed using Gaussian filtering. Although, this explicit procedure ensures the update of the displacement field to be a diffeomorphic transformation, it seems to be too restrictive in comparison to the statement from the previous approaches, especially when compared to the threshold value given in [131].

The advantages of using the compositive way of updating the deformation field (Equation 3.23) in place of the additive scheme (given by the Equation 2.26) were discussed in [145], where the compositive version of the Demon algorithm was also proposed, evaluated and compared against the original additive formulation. The Demon algorithm with composition of the update deformation field was shown experimentally to preserve local one-to-one mapping for small updates.

#### 3.2.2 Exponential updates

In Section 2.5, the Lie group interpretation of the diffeomorphic transformation was introduced based on the work done by Arsigny et al. [4]. As it was pointed out, the Lie group is associated with the Lie algebra via exponential mapping  $\exp(\cdot)$ . Considering that the smooth vector field can be mapped to diffeomorphic transformation using this exponential mapping, the image registration algorithm searching for the update of the deformation field on the Lie algebra was proposed by Vercauteren et al. [145]. Rather than calculating the update of deformation field  $\vec{d}u$ , the update on the Lie algebra  $\vec{d}v$  is computed and then projected onto the Lie group and composed with previous estimated updates in the following way:

$$\vec{u} = \vec{u}_0 \circ \exp(\vec{d}v_1) \circ \dots \circ \exp(\vec{d}v_i) \quad (3.26)$$

The fast algorithm of calculating the exponential mapping  $\exp(\cdot)$  implemented in the recursive manner based on the Scaling and Squaring (SS) technique was originally proposed in [4] (and it is also summarised in Algorithm 4). As in the case of the *small-step* approach, Equation 3.26 can be rewritten for the memory efficient implementation:

$$\vec{u}_i = \vec{u}_{i-1} \circ \exp(\vec{d}v_i) \quad (3.27)$$

The update  $\vec{d}v_i$  on the Lie algebra is calculated in a similar fashion to the update of the deformation field  $\vec{d}u$ . In the case of the Demon algorithm, the update  $\vec{d}v$  is

---

**Algorithm 4** Fast exponential integration of velocity field

---

**Input:** Velocity field:  $\vec{v}$

Parameters:  $N_{\text{exp}}$

**Output:** displacement field  $\vec{u}$

- 1:  $\vec{u}_0 \leftarrow \frac{1}{2^{N_{\text{exp}}}} \cdot \vec{v}$
  - 2: **for**  $i = 1$  **to**  $N_{\text{exp}}$  **do**
  - 3:      $\vec{u}_i = \vec{u}_{i-1} \circ \vec{u}_{i-1}$
  - 4: **end for**
  - 5: **return**  $\vec{u}$
- 

given by Equation 3.28 where  $\vec{\varphi}_i(\vec{x}) = \vec{x} + \vec{u}_i(\vec{x})$  and  $\nabla I_i(\vec{x})$  can be chosen in the similar fashion as for the Demon approach (Section 3.1.3).

$$\vec{d}v_i(\vec{x}) = \frac{(I_f(\vec{x}) - I_m(\vec{\varphi}_{i-1}(\vec{x})))}{\|\nabla I_i(\vec{x})\|^2 + (I_f(\vec{x}) - I_m(\vec{\varphi}_{i-1}(\vec{x})))^2} \nabla I_i(\vec{x}) \quad (3.28)$$

In [155] it was argued that exponential mapping  $\exp(\vec{d}v)$  is only a rough approximation of the diffeomorphic transformation and the explicit limiting procedure (given by Equation 3.25) is more efficient but neither theoretical nor experimental proof was given. Contrary to that statement, it was shown in [145] that for small updates of the deformation field the composition of the updates of the deformation field  $\vec{d}u$  produces similar results to those obtained with the exponential update on the Lie algebra  $\exp(\vec{d}v)$ . A detailed discussion of the exponential mapping based image registration and related theoretical inaccuracies is presented in [145].

The performance of the scaling and squaring technique that is an essential step for calculating the exponential mapping was assessed in [18]. The experimental results suggest that the SS-based technique offers the best trade-off between accuracy and computational time. In [5] it was found out that the optimal number of the recursion levels  $N_{\text{exp}}$  is between eight and ten. The larger number of recursion levels is prone to numerical errors due to dealing close to computational precision. Other techniques to estimate the exponential mapping were also compared [18].

### 3.2.3 Log-domain parameterisation

The updates on the Lie algebra mapped through the exponential mapping can be seen as one of the possible adaptations of the outcomes of the work done on the stationary velocity field parameterisation of the diffeomorphism by Arsigny et al. [4]. Other approaches taking advantages of the log-domain parameterisation of the diffeomorphic transformation are the Diffeomorphic Anatomical Registration

using Exponentiated Lie Algebra (DARTEL) algorithm proposed in [5], and the log-domain Demon approach proposed in [144]. In contrast to the exponentiation of the updates on the Lie algebra  $\exp(\vec{d}v)$ , the mentioned log-domain image registration algorithms parameterise the displacement field  $\vec{u}$  as a stationary velocity field  $\vec{v}$ . Then, the diffeomorphic transformation  $\vec{\varphi}(\vec{x})$  can be defined in following way:

$$\vec{\varphi}(\vec{x}) = \vec{x} + \vec{u}(\vec{x}) = \vec{x} + \exp(\vec{v}(\vec{x})) \quad (3.29)$$

The diffeomorphic update and the displacement field are calculated through the exponential mapping and can be concatenated using the composition operator  $\circ$  (the composition operation on the Lie group). This composition is given by:

$$\exp(\vec{v}_i) = \exp(\vec{v}_{i-1}) \circ \exp(\vec{d}v_i) \quad (3.30)$$

while the current velocity field  $\vec{v}_i$  can be expressed as follows:

$$\vec{v}_i = \log \left( \exp(\vec{v}_{i-1}) \circ \exp(\vec{d}v_i) \right) \quad (3.31)$$

The drawback of Equation 3.31 is that estimation of the velocity field  $\vec{v}_i$  is linked with computing the principal logarithm  $\log(\cdot)$  which is reported to have high computational burden (e.g. volume of size 256x256x60 in 60 minutes using a standard computer [4]). In order to represent the velocity field  $\vec{v}_i$  in the log-domain through an efficient way in a reasonable time, the Baker-Campbell-Hausdorff (BCH) formula [17, 144] has to be applied to approximate the current velocity field  $\vec{v}_i$ :

$$\vec{v}_i = BCH \left[ \vec{v}_{i-1}, \vec{d}v_i \right] \quad (3.32)$$

where the BCH formula for any two velocity fields  $\vec{v}_{i-1}$  and  $\vec{d}v_i$  is given by:

$$BCH \left[ \vec{v}_{i-1}, \vec{d}v_i \right] = \vec{v}_{i-1} + \vec{d}v_i + \frac{1}{2} \left[ \vec{v}_{i-1}, \vec{d}v_i \right] + \frac{1}{12} \left[ \vec{v}_{i-1}, \left[ \vec{v}_{i-1}, \vec{d}v_i \right] \right] + \dots \quad (3.33)$$

The Lie bracket  $\left[ \vec{v}_{i-1}, \vec{d}v_i \right]$  is the operation on the Lie algebra vector space defined in the following way [17, 144];

$$\left[ \vec{v}_{i-1}(\vec{x}), \vec{d}v_i(\vec{x}) \right] = \sum_{j=1}^d \left( v_{i-1}^j(\vec{x}) \frac{\partial \vec{d}v_i(\vec{x})}{\partial x^j} - dv_i^j(\vec{x}) \frac{\partial \vec{v}_{i-1}(\vec{x})}{\partial x^j} \right) \quad (3.34)$$

where  $\vec{v}_{i-1}(\vec{x}) = [v_{i-1}^1(\vec{x}), \dots, v_{i-1}^d(\vec{x})]$  and  $\vec{d}v_i(\vec{x}) = [dv_i^1(\vec{x}), \dots, dv_i^d(\vec{x})]$ . Utilisation of the BCH formula approximates the current velocity field  $\vec{v}_i$ , thereby allows one to establish the image registration algorithm in the log-domain space in a very efficient

way. As an illustration of this reformulation of the image registration objective, the energy function is presented by Equation 3.35.

$$\varepsilon(\vec{v}) = \int_{\Omega} Sim(I_f(\vec{x}), I_m(\vec{x} + \exp(\vec{v}(\vec{x}))))dx + \alpha \int_{\Omega} Reg(\vec{v}(\vec{x}))dx \quad (3.35)$$

In contrast to the general image registration problem given by Equation 2.6, the log-domain formulation estimates the velocity field, and the final transformation is returned by the exponential mapping. The additional outcome of the parameterisation via the stationary velocity field is that the inverse of the transformation  $\vec{\varphi}^{-1}$  can be quickly estimated through the backward integration of the velocity field [5, 144]:

$$\vec{\varphi}^{-1}(\vec{x}) = \vec{x} + \exp(-\vec{v}(\vec{x})) \quad (3.36)$$

The example presenting the forward and backward exponentiation (integration) of the velocity field  $\vec{v}$  is shown in Figure 3.1.

It is interesting that the algorithm proposed by Ashburner [5] treats the updates of the velocity field  $\vec{d}v_i$  in the additive optimisation framework (given by the Equation 3.37) without considering whether such velocity field  $\vec{v}$  theoretically exists.

$$\vec{v} = \vec{v}_0 + \vec{d}v_1 + \dots + \vec{d}v_i \quad (3.37)$$

Considering the BCH formula, the additive way of concatenation of the updates of the velocity fields can be seen as the approximation of the velocity field using just first two elements of the BCH formula (Equation 3.33). It was shown experimentally in [17, 144], that using more than three first elements of BCH formula does not lead to a significant increase in accuracy. In addition, Bossa et al. [17] showed that the approximation using the BCH formula produces errors on the similar level to those in the case of the direct calculation of the principal logarithm.

In order to take advantage of the parameterisation of the displacement field via the stationary velocity field, the algorithms presented in the first section of this chapter (Section 3.1), are reformulated here to their log-domain versions. Instead of calculating the update of the displacement field  $\vec{d}u_i$ , the update of the velocity field  $\vec{d}v_i$  on the Lie algebra space is computed and then concatenated with the current velocity field based on the BCH formula (Equation 3.33). The regularisation is performed on the velocity field (and/or update of the velocity field) rather than on the displacement field (and/or update of the displacement field). The update of the velocity field for the steepest descent approach is given by Equation 3.38, and Equation 3.39 provides the update for the Newton's iteration approach. The Demon method's update of the velocity field was presented in the previous section

---

**Algorithm 5** Log-domain steepest descent approach

---

**Input:** Images:  $I_f$  and  $I_m$

Weight of regularisation  $\alpha$

Design parameters (for linear elastic model:  $\lambda_{elas}, \mu_{elas}$ )

**Output:** Velocity field  $\vec{v}$ , transformation  $\vec{\varphi}$

- 1:  $\vec{v}_0 = 0, i = 1$
  - 2: **repeat**
  - 3: exponentiation of velocity field:  $\vec{u}_i = \exp(\vec{v}_i)$
  - 4: **for all**  $\vec{x} \in \Omega$  **do**
  - 5: calculate update of velocity field:  $\vec{d}v_i(\vec{x})$  (Equation 3.38)
  - 6: update velocity field  $\vec{v}_i(\vec{x}) = BCH \left[ \vec{v}_{i-1}(\vec{x}), \vec{d}v_i(\vec{x}) \right]$
  - 7: **end for**
  - 8:  $i = i + 1$
  - 9: **until** (velocity field does not change) **or** ( $i \geq IterMax$ )
  - 10: calculate transformation  $\vec{\varphi}$  (Equation 3.29)
  - 11: **return**  $\vec{v}$  and  $\vec{\varphi}$
- 

(given by Equation 3.28) and the regularisation of output is performed via Gaussian filtering of the velocity field/update of the velocity field rather than the displacement field/update of the displacement.

$$\vec{d}v_i(\vec{x}) = (I_f(\vec{x}) - I_m(\vec{\varphi}_{i-1}(\vec{x}))) \nabla I_m(\vec{\varphi}_{i-1}(\vec{x})) + \alpha(\mu \Delta \vec{v}_{i-1}(\vec{x}) + (\lambda + \mu) \nabla(\nabla \cdot \vec{v}_{i-1}(\vec{x}))) \quad (3.38)$$

$$\vec{d}v_i^l(\vec{x}) = -\frac{(I_f(\vec{x}) - I_m(\vec{\varphi}_{i-1}(\vec{x}))) \nabla^l I_m(\vec{\varphi}_{i-1}(\vec{x})) + \lambda_{diff} \Delta v_{i-1}^l(\vec{x})}{\lambda_{diff} + (\nabla^l I_m(\vec{\varphi}_{i-1}(\vec{x})))^2} \quad (3.39)$$

The overall log-domain image registration algorithm based on the steepest descent approach is summarised in Algorithm 5. The log-domain Newton's iteration approach can be deduced in the similar manner, when the update of the velocity field calculated using Equation 3.38 (Line 5 of Algorithm 5) has to be replaced by the update calculated using Equation 3.39. The presented log-domain algorithms extend the original works (the Newton's iteration method [78, 97], and the steepest descent approach [56, 24]), and enable to take advantages of the diffeomorphic framework.

The log-domain parameterisation of the diffeomorphic transformation has interesting properties when utilised for calculating the statistics on the displacement fields [4, 144]. It is important to realise that performing the Euclidean statistics on

the diffeomorphic displacement fields does not preserve the diffeomorphic properties of the results of those statistics. The most compelling example can be shown easily by taking the average of the diffeomorphic transformations:

$$\vec{u}_{ave} = \frac{1}{N} \sum_{j=1}^N \vec{u}_j \quad (3.40)$$

where  $N$  is the number of the displacement fields used for the calculation of the average. While the input displacement fields  $\vec{u}_i$  can be enforced to be diffeomorphic (e. g. as a result of performing a diffeomorphic algorithm), the output displacement  $\vec{u}_{ave}$  may no longer be diffeomorphic. This occurs due to the fact that the displacement fields are not vector fields. The framework proposed by Arsigny et al. [4] showed that calculating the principal logarithm of the diffeomorphic transformations, results in well-defined vector fields. As a consequence, the Euclidean statistics on those vector fields can be obtained. For example, when the average of the velocity fields is considered, the output is also a velocity field and the diffeomorphic displacement field associated with this velocity field can be obtained through the exponential mapping:

$$\vec{u}_{ave} = \exp \left( \frac{1}{N} \sum_{j=1}^N \log(\vec{u}_j) \right) \quad (3.41)$$

As it was outlined, calculating the principal logarithm is a time-consuming procedure [4, 17] but, when the parameterisation of the displacement field is enforced explicitly in the image registration, the output of this registration is already the velocity field. Indeed, the calculation of the principal logarithm can be avoided using the log-domain image registration approaches.

### 3.3 Consistent image registration

The diffeomorphic transformation  $\vec{\varphi}$  estimated during the evaluation of the procedures described above is a smooth displacement field, preserving one-to-one mapping properties. Although, the smooth inverse transformation  $\vec{\varphi}^{-1}$  also exists (due to the determinant of the Jacobian matrix for the transformation  $\vec{\varphi}$  being locally positive), it is usually not calculated explicitly during the registration process (except in the log-domain approaches). Intuitively, it should be easily to estimate the inverse transformation  $\vec{\varphi}^{-1}$  by changing the order of the input images i.e. a reference image becomes a moving image and a moving image becomes a reference image. Whereas the diffeomorphic formulation preserves that every image point in the moving image  $I_m$  is mapped onto the image point in the reference image  $I_f$ , there is no reason why the transformation estimated for the swapped input images will map the im-

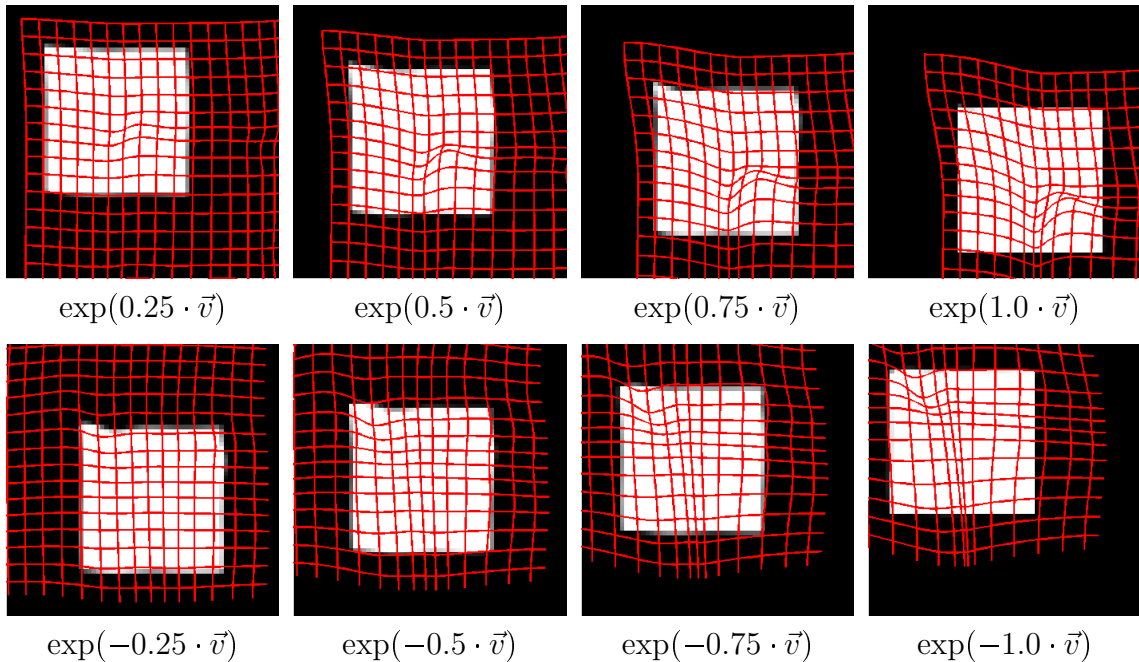


Figure 3.1: Examples of the forward and backward integration of the velocity field for the sample images. (Top row) The forward integration of the velocity field  $\vec{v}$  at different times provides the deformation field for warping the moving image, while (Bottom row) the backward integration of the velocity field  $\vec{v}$  at different times provides the deformation field for warping the fixed image

age points from the moving image to the corresponding image points in the fixed image. In other words, the transformation estimated between the fixed and moving image (named the forward transformation)  $\vec{\varphi}_{forw}$  is not the same as the inverse of the transformation calculated for the moving and fixed image  $\vec{\varphi}_{back}$  (named the backward transformation or reverse transformation [27, 63]). This inconsistency

$$\vec{\varphi}_{forw} \neq \vec{\varphi}_{back}^{-1} \quad (3.42)$$

comes partially from the fact of the ill-posed of the image registration and in some cases can also be a result of choosing a similarity criterion with asymmetric properties such as the Correlation Ratio [108]. The Inverse Consistency Error (*ICE*) that describes the inconsistency between the forward transformation  $\vec{\varphi}_{forw}(\vec{x}) = \vec{x} + \vec{u}_{forw}(\vec{x})$  and backward transformation  $\vec{\varphi}_{back}(\vec{x}) = \vec{x} + \vec{u}_{back}(\vec{x})$  can be defined at every spatial position  $\vec{x}$  as follows:

$$ICE(\vec{\varphi}_{forw}(\vec{x}), \vec{\varphi}_{back}(\vec{x})) = \|\vec{x} - (\vec{\varphi}_{forw} \circ \vec{\varphi}_{back})(\vec{x})\| \quad (3.43)$$

where  $\|\cdot\|$  is a Euclidean distance [27, 127]. An example presenting the inconsistency between the forward and backward transformation estimated using the classical

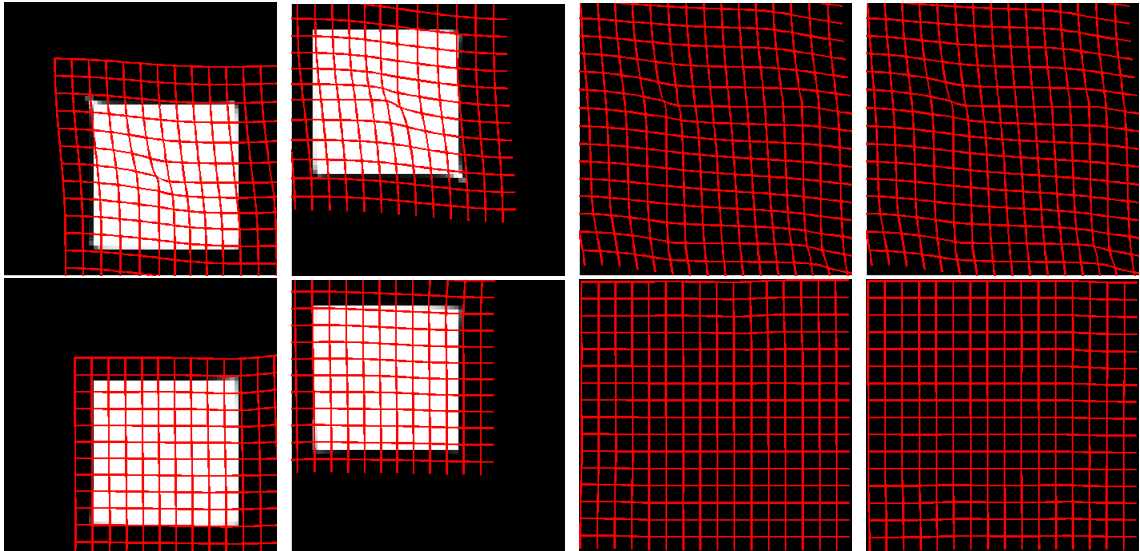


Figure 3.2: Examples of the inconsistency between forward and backward transformation estimated using classical Demon algorithm (top row) and results of ensuring the inverse consistency criterion during the consistent Demon registration (bottom row). (From left to right) forward transformation, backward transformation,  $(\vec{x} - (\vec{\varphi}_{forw} \circ \vec{\varphi}_{back}))(\vec{x})$ , and  $(\vec{x} - (\vec{\varphi}_{back} \circ \vec{\varphi}_{forw}))(\vec{x})$ . In perfect case of fulfilling the inverse consistency criterion,  $(\vec{x} - (\vec{\varphi}_{forw} \circ \vec{\varphi}_{back}))(\vec{x})$  and  $(\vec{x} - (\vec{\varphi}_{back} \circ \vec{\varphi}_{forw}))(\vec{x})$  should be represented by the regular grid.

Demon algorithm is shown in Figure 3.2. In the perfect case of preserving the inverse consistency criterion,  $(\vec{x} - (\vec{\varphi}_{forw} \circ \vec{\varphi}_{back}))(\vec{x})$  should be represented by the regular grid. However, the transformations that were first estimated for the fixed and moving image and then with the swapped input images are not consistent thereby the grid is significantly distorted (top row of Figure 3.2). On the other hand, when using the consistent log-domain Demon algorithm, the obtained forward and backward transformations are close to the ideal case of the consistency. Indeed, the grid showing  $(\vec{x} - (\vec{\varphi}_{forw} \circ \vec{\varphi}_{back}))(\vec{x})$  is almost regular (see bottom row of Figure 3.2). In addition, the transformations estimated via consistent algorithms look smoother (for the same set of the design parameters).

The earliest work on overcoming the aforementioned inconsistency was done by the symmetrisation of the similarity measure  $Sim$  and explicit minimisation of the inverse consistency error via joint estimation of the forward and backward transformations [27]. The symmetrisation of the similarity criterion is defined in following manner:

$$Sim_{sym}(I_f, I_m, \vec{\varphi}_{forw}, \vec{\varphi}_{back}) = Sim(I_f, I_m \circ \vec{\varphi}_{forw}) + Sim(I_f \circ \vec{\varphi}_{back}, I_m) \quad (3.44)$$

while the minimising of the  $ICE$  can be seen as an additional penalty term given

by:

$$Pen_{ICE}(\vec{u}_{forw}, \vec{u}_{back}) = \int_{\Omega} \|\vec{u}_{forw}(\vec{x}) - \vec{u}_{back}^{-1}(\vec{x})\|^2 dx + \int_{\Omega} \|\vec{u}_{back}(\vec{x}) - \vec{u}_{forw}^{-1}(\vec{x})\|^2 dx \quad (3.45)$$

In addition, the general energy function of this image registration is coupled with the regularisation terms for each displacement field  $Reg(\vec{u}_{forw})$  and  $Reg(\vec{u}_{back})$  to preserve their smoothness and the constraints ( $Pen_{Jac}(\vec{u}_{forw})$  and  $Pen_{Jac}(\vec{u}_{back})$ ) that prevent determinant of the Jacobian matrix for both transformations from going below zero. The overall cost function for the consistent image registration proposed in [27] can be summarised by:

$$\begin{aligned} \varepsilon(\vec{u}_{forw}, \vec{u}_{back}) = & Sim_{sym}(I_f, I_m, \vec{u}_{forw}, \vec{u}_{back}) + Reg(\vec{u}_{forw}) + Reg(\vec{u}_{back}) + \\ & Pen_{Jac}(\vec{u}_{forw}) + Pen_{Jac}(\vec{u}_{back}) + Pen_{ICE}(\vec{u}_{forw}, \vec{u}_{back}) \end{aligned} \quad (3.46)$$

The inverse displacement fields involved in the penalty term  $Pen_{ICE}$ , are calculated directly by the algorithm presented in the mentioned work (it is also summarised in the Section 3.4.2). Although the input images here are still differentiated by the subscripts  $f$  and  $m$  to name the fixed and moving image, this has only been done in order to keep notation consistent throughout the thesis. The order of the input images in the consistent image registration is not important due to symmetric properties and joint estimation of both forward and backward transformations. The detailed description of the framework for consistent image registration proposed by Christensen and Johnson [27] is motivated by two principal reasons. In the first place, this framework can be considered as the state-of-art method for consistent image registration. Furthermore, each condition that must be fulfilled to keep the image registration algorithm consistent is demonstrated explicitly in the energy function  $\varepsilon$  (Equation 3.46). This means it can be used as a reference to assess whether the other methods are preserving all the consistency criteria.

A variational multi-modal framework of the consistent image registration was proposed in [162]. Besides the use of the different similarity criterion to enable multi-modal registration, the direct inversion of the deformation fields that is a crucial step in [27] was avoided by a different formulation of the problem. The energy function is defined there by:

$$\begin{aligned} \varepsilon(\vec{u}_{forw}, \vec{u}_{back}) = & Sim_{sym}(I_f, I_m, \vec{u}_{forw}, \vec{u}_{back}) + Reg(\vec{u}_{forw}) + Reg(\vec{u}_{back}) \\ & + Pen_{ICE}(\vec{u}_{forw}, \vec{u}_{back}) \end{aligned} \quad (3.47)$$

and then the Gateaux derivatives are calculated with respect to both the forward

and backward transformations. As a result of the two Euler-Lagrange equations, the PDE for both the forward and the backward transformations has to be solved. Multi-modal consistent image registration was also investigated in [136], where the Demon-like flows of the Mutual Information were calculated. In contrast to aforementioned techniques, the *ICE* is not included directly in the objective function but it is minimised by the additional iterative procedure inserted into the image registration framework. Although both approaches minimise the *ICE* in every iteration, the ensurance of the one-to-one mapping is questionable, because no restrictions on the determinant of the Jacobian matrix are introduced.

The consistent landmark-based image registration algorithms were proposed in [63]. Although the registration of the landmarks is usually consistent due to finding the forward and backward transformations (correspondences) for the same set of the features, the forward and backward dense deformation fields interpolated for the regions away from the features are not consistent. One of the proposed algorithms first registers the landmarks and then minimises the *ICE* between estimated forward and backward transformations by a repeatable procedure as long as the distance between landmarks and the *ICE* is reduced below the desired levels. The second method combines the above landmark-matching procedure with the intensity-based registration proposed in [27].

#### **Log-domain consistent image registration**

The log-domain parameterisation of the displacement field provides some interesting outcomes that can be incorporated straightaway into the formulation of the consistent image registration. The major advantage that is offered by the stationary velocity field parameterisation is the fact that the estimated transformation is diffeomorphic (this provides a smooth transformation with a locally positive determinant of the Jacobian matrix for this transformation). The second advantage of the log-domain image registration is derived from the fact that the backward (inverse) transformation can be quickly calculated from the velocity field obtained for the forward transformation based on the backward integration. When compared to the state-of-the-art consistent image registration [27], the missing component of the registration to be consistent is reducing the *ICE* between the forward and backward transformations. For this purpose, Vercauteren et al. [144] proposed the averaging procedure for the forward and backward velocity fields that guarantees the symmetry of the results and make registration consistent. The origin of the averaging procedure applied in [144] to the velocity fields can be derived from the seminal paper for the Demon algorithm. Thirion [138] proposed procedure to compose the forward and the backward transformation and then take the half of the composition

result to add to the forward transformation and subtract from the backward transformation. This procedure there was performed to enforce that the transformation would be a one-to-one mapping.

Formally, the consistent log-domain image registration can be stated as optimisation of the single velocity field  $\vec{v}$  defined by the following energy term:

$$\varepsilon(\vec{v}) = Sim_{sym}(I_f, I_m, \exp(\vec{v}), \exp(-\vec{v})) + Reg(\vec{v}) \quad (3.48)$$

During the optimisation of the above energy function, the log-domain consistent image registration requires calculation of the forward and the backward update of the velocity field. The forward  $\vec{d}v_{i,forw}(\vec{x})$  and backward  $\vec{d}v_{i,back}(\vec{x})$  updates of the velocity field for the steepest descent approach are given by:

$$\begin{aligned} \vec{d}v_{i,forw}(\vec{x}) &= (I_f(\vec{x}) - I_m(\vec{\varphi}_{i-1}(\vec{x})))\nabla I_m(\vec{\varphi}_{i-1}(\vec{x})) \\ &\quad + \alpha(\mu\Delta\vec{v}_{i-1}(\vec{x}) + (\lambda + \mu)\nabla(\nabla \cdot \vec{v}_{i-1}(\vec{x}))) \end{aligned} \quad (3.49)$$

$$\begin{aligned} \vec{d}v_{i,back}(\vec{x}) &= (I_m(\vec{x}) - I_f(\vec{\varphi}_{i-1}^{-1}(\vec{x})))\nabla I_f(\vec{\varphi}_{i-1}^{-1}(\vec{x})) \\ &\quad + \alpha(\mu\Delta(-\vec{v}_{i-1}(\vec{x})) + (\lambda + \mu)\nabla(\nabla \cdot (-\vec{v}_{i-1}(\vec{x})))) \end{aligned}$$

The forward  $\vec{d}v_{i,forw}(\vec{x})$  and backward  $\vec{d}v_{i,back}(\vec{x})$  updates of the velocity field for Newton's iteration approach are given by:

$$\begin{aligned} \vec{d}v_{i,forw}^l(\vec{x}) &= -\frac{(I_f(\vec{x}) - I_m(\vec{\varphi}_{i-1}(\vec{x})))\nabla^l I_m(\vec{\varphi}_{i-1}(\vec{x})) + \lambda_{diff}\Delta v_{i-1}^l(\vec{x})}{\lambda_{diff} + \nabla^l I_m(\vec{\varphi}_{i-1}(\vec{x})) \cdot \nabla^l I_m(\vec{\varphi}_{i-1}(\vec{x}))} \\ \vec{d}v_{i,forw}^l(\vec{x}) &= -\frac{(I_m(\vec{x}) - I_f(\vec{\varphi}_{i-1}^{-1}(\vec{x})))\nabla^l I_f(\vec{\varphi}_{i-1}^{-1}(\vec{x})) + \lambda_{diff}\Delta(-v_{i-1}^l(\vec{x}))}{\lambda_{diff} + \nabla^l I_f(\vec{\varphi}_{i-1}^{-1}(\vec{x})) \cdot \nabla^l I_f(\vec{\varphi}_{i-1}^{-1}(\vec{x}))} \end{aligned} \quad (3.50)$$

The forward  $\vec{d}v_{i,forw}(\vec{x})$  and backward  $\vec{d}v_{i,back}(\vec{x})$  updates of the velocity field for the Demon approach are given by:

$$\begin{aligned} \vec{d}v_{i,forw}(\vec{x}) &= \frac{(I_f(\vec{x}) - I_m(\vec{\varphi}_{i-1}(\vec{x})))}{\|\nabla I_i(\vec{x})\|^2 + (I_f(\vec{x}) - I_m(\vec{\varphi}_{i-1}(\vec{x})))^2} \nabla I_i(\vec{x}) \\ \vec{d}v_{i,back}(\vec{x}) &= \frac{(I_m(\vec{x}) - I_f(\vec{\varphi}_{i-1}^{-1}(\vec{x})))}{\|\nabla I_i(\vec{x})\|^2 + (I_m(\vec{x}) - I_f(\vec{\varphi}_{i-1}^{-1}(\vec{x})))^2} \nabla I(\vec{x}) \end{aligned} \quad (3.51)$$

The log-domain consistent image registration algorithm based on the steepest descent approach is summarised in Algorithm 6. The Newton's iteration algorithm and the Demon approach can be deduced in the same straightforward manner. Ori-

nally the consistent symmetric Demon approach was proposed in [144], where it was called the *symmetric log-domain Demon approach* to emphasise the symmetrisation of the similarity criterion in the objective function. The consistent log-domain methods based on the steepest descent approach and Newton's iteration approach presented in this section benefit from the log-domain parameterisation and enforce the inverse consistency criterion, thereby opening the already known algorithms to new applications.

---

**Algorithm 6** Consistent log-domain steepest descent approach

---

**Input:** Images:  $I_f$  and  $I_m$ ,  $\alpha$

Parameters:  $\alpha$ ,  $\lambda_{elas}$ ,  $\mu_{elas}$

**Output:** Velocity field  $\vec{v}$ , Transformations  $\vec{\varphi}_{forw}$  and  $\vec{\varphi}_{back}$

- 1:  $\vec{v} = 0$ ,  $i = 1$
  - 2: **repeat**
  - 3:     forward integration of velocity field:  $\vec{u}_{i,forw} = \exp(\vec{v}_{i-1})$
  - 4:     backward integration of velocity field:  $\vec{u}_{i,back} = \exp(-\vec{v}_{i-1})$
  - 5:     **for all**  $\vec{x} \in \Omega$  **do**
  - 6:         calculate forward update of the velocity field:  
 $\vec{d}v_{i,forw}(\vec{x})$  (Equation 3.50)
  - 7:         calculate backward update of the velocity field:  
 $\vec{d}v_{i,back}(\vec{x})$  (Equation 3.50)
  - 8:         calculate forward velocity field  $\vec{v}_{forw}$ :  
 $\vec{v}_{forw}(\vec{x}) = BCH \left[ \vec{v}_{i-1}(\vec{x}), \vec{d}v_{i,forw}(\vec{x}) \right]$
  - 9:         calculate backward velocity field  $\vec{v}_{back}$ :  
 $\vec{v}_{back}(\vec{x}) = BCH \left[ -\vec{v}_{i-1}(\vec{x}), -\vec{d}v_{i,back}(\vec{x}) \right]$
  - 10:         average forward and backward velocity field:  
 $\vec{d}v_i(\vec{x}) = \frac{1}{2}(\vec{v}_{forw}(\vec{x}) + \vec{v}_{back}(\vec{x}))$  (Equation 3.41)
  - 11:         update velocity field  $\vec{v}_i(\vec{x})$ :  
 $\vec{v}_i(\vec{x}) = \vec{d}v_i(\vec{x})$
  - 12:     **end for**
  - 13:      $i = i + 1$
  - 14: **until** (velocity field does not change) **or** ( $i \geq IterMax$ )
  - 15: calculate forward transformation  $\vec{\varphi}_{forw}$  (Equation 3.29)
  - 16: calculate backward transformation  $\vec{\varphi}_{back}$  (Equation 3.36)
  - 17: **return**  $\vec{v}$ ,  $\vec{\varphi}_{forw}$ ,  $\vec{\varphi}_{back}$
-

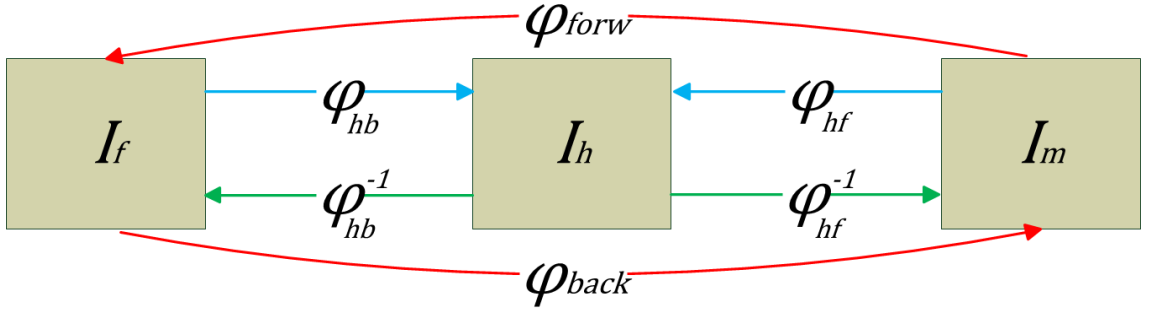


Figure 3.3: Symmetric image registration scheme

### 3.4 Image registration with symmetric warping

The consistent diffeomorphic image registration has been reported as almost ideally suited for image registration for the major biomedical applications. However, in some cases the relatively large deformation has to be estimated and the desired level of accuracy in terms of the similarity measure or the *ICE* may not be achieved. In order to improve the overall robustness of the consistent image registration algorithm, the symmetric warping of the input images toward the intermediate, hidden *mean*, was presented in [14, 10, 155, 53, 96]. The image registration with symmetric warping of the images can be stated as an optimisation problem:

$$\varepsilon(\vec{u}_{hf}, \vec{u}_{hb}) = Sim(I_f(\vec{\varphi}_{hf}), I_m(\vec{\varphi}_{hb})) + Reg(\vec{u}_{hf}) + Reg(\vec{u}_{hb}) \quad (3.52)$$

where  $\vec{\varphi}_{hf}(\vec{x}) = \vec{x} + \vec{u}_{hf}(\vec{x})$  and  $\vec{\varphi}_{hb} = \vec{x} + \vec{u}_{hb}(\vec{x})$  are the corresponding transformations warping, respectively, image  $I_f$  and image  $I_m$  to an intermediate image  $I_h$ . The subscripts *hf* and *hb* stand for the *half-way* forward and backward transformations respectively [53]. The results of the symmetric registration towards the intermediate image  $I_h$ :  $\vec{\varphi}_{hf}$  and  $\vec{\varphi}_{hb}$  have to be inverted and the final transformations  $\vec{\varphi}_{forw}$  and  $\vec{\varphi}_{back}$  are the compositions of  $\vec{\varphi}_{hf}$  and  $\vec{\varphi}_{hb}$  and their inverses  $\vec{\varphi}_{hf}^{-1}$  and  $\vec{\varphi}_{hb}^{-1}$ :

$$\vec{\varphi}_{forw} = \vec{\varphi}_{hf} \circ \vec{\varphi}_{hb}^{-1} \quad (3.53)$$

and

$$\vec{\varphi}_{back} = \vec{\varphi}_{hb} \circ \vec{\varphi}_{hf}^{-1} \quad (3.54)$$

The overall scheme of the symmetric image registration process is illustrated in Figure 3.3.

The best known image registration algorithms proposed with the symmetric warping of the input images are as follows. Beg and Khan [14] extended the LD-DMM image registration algorithm [15] and experimentally showed an improvement

in the accuracy of the *ICE* and the Region Overlapping (*RO*) of the investigated organs. Similar conclusions can be drawn from the work presented in [10], where symmetric warping improves the cross-correlation-driven diffeomorphic image registration adapted to the normalisation of the brain degenerations. Other possible schemes for image registration with symmetric warping are described in detail in the following sections.

#### 3.4.1 Small-step multiple pass approach

The *small-step multiple pass approach* originally proposed in [155] is derived from the computational simplification of the approaches proposed in [14, 10] using the Demon-like update of the displacement field for estimation the transformations:

$$\vec{d}u_i(\vec{x}) = \frac{I_f(\vec{\varphi}_{i-1,hf}(\vec{x})) - I_m(\vec{\varphi}_{i-1,hb}(\vec{x}))}{\|\nabla I_{i,sym}(\vec{x})\|^2 + (I_f(\vec{\varphi}_{i-1,hf}(\vec{x})) - I_m(\vec{\varphi}_{i-1,hb}(\vec{x})))^2} \nabla I_{i,sym}(\vec{x}) \quad (3.55)$$

where gradient  $\nabla I_{i,sym}(\vec{x})$  is defined in the following way:

$$\nabla I_{i,sym}(\vec{x}) = \frac{1}{2} (\nabla I_f(\vec{\varphi}_{i-1,hf}(\vec{x})) + \nabla I_m(\vec{\varphi}_{i-1,hb}(\vec{x}))) \quad (3.56)$$

The symmetric warping gradient (Equation 3.56) is similar to the symmetric gradient proposed in [145] (compare to Equation 3.22).

In general in the *small-step multiple pass approach*, it is assumed that the half-way forward displacement field  $\vec{u}_{i,h-f}(\vec{x})$ :

$$\vec{u}_{i,hf}(\vec{x}) = G_{diff} * \left( \vec{u}_{i-1,hf}(\vec{x}) \circ \left( G_{fluid} * \left( \vec{d}u_{i,hf}(\vec{x}) \right) \right) \right) \quad (3.57)$$

and the backward displacement field  $\vec{u}_{i,hb}(\vec{x})$ :

$$\vec{u}_{i,hb}(\vec{x}) = G_{diff} * \left( \vec{u}_{i-1,hb}(\vec{x}) \circ \left( G_{fluid} * \left( \vec{d}u_{i,hb}(\vec{x}) \right) \right) \right) \quad (3.58)$$

are linked by the assumption that the forward and the backward updates of the deformation field can be approximated by:

$$\vec{d}u_i(\vec{x}) = \vec{d}u_{i,hf}(\vec{x}) = -\vec{d}u_{i,hb}(\vec{x}) \quad (3.59)$$

where  $G_{diff}*$  and  $G_{fluid}*$  represent Gaussian kernel convolutions which operate on updated displacement fields  $\vec{u}_{i,hf}$  and  $\vec{u}_{i,hb}$ , and the update of the displacement field  $\vec{d}u_i$  respectively. This assumption simplifies significantly the estimation of the deformation fields but it holds only for small updates [5]. Due to the fact that the diffeomorphism adapted for this approach relies on the small-step technique

and the Demon-like force does not guarantee, the explicit procedure of the limiting the deformation magnitude (given by Equation 3.25) is applied when the estimated update is greater than 0.4 voxel spacing size (this limit was chosen *ad hoc* by [155] following the limits that were determined for B-Spline deformable image registration [115]). Therefore, the small-step update manner (see Section 3.2.1) is kept.

#### 3.4.2 Direct inverse update estimation approach

The direct inverse deformation field approach proposed by Papiez and Matuszewski [96] is inspired by the need to check how good the approximation of the inverse update given by the Equation 3.59 is in practice. To assess this, the direct inverse approach is built on the previous approach by directly inverting the update of the deformation field in each iteration. The proposed update scheme is defined for the half-way forward displacement field as follows:

$$\vec{u}_{i,hf}(\vec{x}) = G_{diff} * \left( \vec{u}_{i-1,hf}(\vec{x}) \circ \left( G_{fluid} * \left( \vec{d}u_{i,hf}(\vec{x}) \right) \right) \right) \quad (3.60)$$

and for the half-way backward displacement field by;

$$\vec{u}_{i,hb}(\vec{x}) = G_{diff} * \left( \vec{u}_{i-1,hb}(\vec{x}) \circ \left( G_{fluid} * \left( \vec{d}u_{i,hb}(\vec{x}) \right) \right) \right) \quad (3.61)$$

where the update of the half-way backward transformation  $\vec{d}u_{i,hb}(\vec{x})$  is calculated as the inverse of the update of the half-way forward transformation  $\vec{d}u_{i,hf}(\vec{x})$ :

$$\vec{d}u_{i,hb}(\vec{x}) = \vec{d}u_{i,hf}^{-1}(\vec{x}) \quad (3.62)$$

The technique applied to the update scheme in Equation 3.61 and in Equation 3.62 are in contrast with the approximation given by Equation 3.59 (compare formula for updating  $\vec{u}_{i,hb}$  given in Equation 3.58) as it uses the direct inverse update of the deformation which does not suffer from the limitations of the *small-step multiple pass approach* (because  $\vec{d}u_i \circ (\vec{d}u_i)^{-1}(\vec{x}) = \vec{x}$ ). The direct inverse deformation based algorithm is summarised in Algorithm 7.

For the *small-step multiple pass approach* and the direct inverse approach, there is a need to estimate the inverse deformation fields  $\vec{\varphi}_{hf}$  and  $\vec{\varphi}_{hb}$ . This has to be done accurately and fast, especially for the direct inverse approach, where the inverse is also calculated in each iteration. In the *small-step multiple pass approach*, the inverse transformations of  $\vec{\varphi}_{hf}$  and  $\vec{\varphi}_{hb}$  are calculated using the method proposed by [7]. Here, a novel method is presented (based on the method proposed by [27]) that is more accurate than the previously reported methods.

### 3.4. IMAGE REGISTRATION WITH SYMMETRIC WARPING

---

**Algorithm 7** Direct inverse deformation field approach to image registration with symmetric warping

---

**Input:** Images:  $I_f$  and  $I_m$

Parameters:  $G_{fluid}$ ,  $G_{diff}$

**Output:** Forward transformation  $\vec{\varphi}_{forw}$ , backward transformation  $\vec{\varphi}_{back}$

- 1:  $\vec{u}_{forw} = \vec{0}$ ,  $\vec{u}_{back} = \vec{0}$ ,  $i = 1$
  - 2: **repeat**
  - 3:     **for all**  $\vec{x} \in \Omega$  **do**
  - 4:         calculate forward update  $\vec{d}u_{i,hf}(\vec{x})$  (Equation 3.55 )
  - 5:         smooth update of the deformation field using Gaussian filter  $G_{fluid}$ :  
 $\vec{d}u_{i,hf}(\vec{x}) = G_{fluid} * (\vec{d}u_{i,hf}(\vec{x}))$
  - 6:         calculate backward update  $\vec{d}u_{i,hb}^{-1}(\vec{x})$  using the Algorithm 8
  - 7:         update forward displacement field  $\vec{u}_{i,hf}(\vec{x}) = \vec{u}_{i-1,hf}(\vec{x}) \circ \vec{d}u_{i,hf}(\vec{x})$
  - 8:         smooth forward displacement field  $\vec{u}_{i,hf}(\vec{x})$  using Gaussian filter  $G_{diff}$ :  
 $\vec{u}_{i,hf}(\vec{x}) = G_{diff} * (\vec{u}_{i,hf}(\vec{x}))$
  - 9:         update backward deformation field  $\vec{u}_{i,hb}(\vec{x}) = \vec{u}_{i-1,hb}(\vec{x}) \circ \vec{d}u_{i,hb}(\vec{x})$
  - 10:         smooth backward deformation field  $\vec{u}_{i,hb}(\vec{x})$  using Gaussian filter  $G_{diff}$ :  
 $\vec{u}_{i,hb}(\vec{x}) = G_{diff} * (\vec{u}_{i,hb}(\vec{x}))$
  - 11:     **end for**
  - 12:      $i = i + 1$
  - 13: **until** (deformation fields do not change) **or** ( $i \geq IterMax$ )
  - 14: calculate the inverse of the  $\vec{\varphi}_{hf}$  and the inverse of the  $\vec{\varphi}_{hb}$   
using the Algorithm 8
  - 15: calculate forward transformation (Equation 3.53) and backward transformation  
(Equation 3.54) by composition of the half-way transformations
  - 16: **return**  $\vec{\varphi}_{forw}$  and  $\vec{\varphi}_{back}$
- 

#### Christensen's method

The procedure used to compute the inverse transformation proposed in [27] assumes that an input transformation  $\vec{\varphi}$  is a continuously differentiable mapping from  $\Omega \rightarrow \Omega$  with a positive determinant of the Jacobian  $\det(J(\vec{\varphi}(\vec{x})))$  for all spatial position  $\vec{x} \in \Omega$ . An inverse deformation field can be found by selecting a point at a spatial position  $\vec{y} = [y^1, \dots, y^d] \in \Omega$  and carrying out an iterative process to search for a point  $\vec{x}$  which makes distance  $\|\vec{y} - \vec{\varphi}(\vec{x})\|$  smaller than a desired threshold  $\xi$ . The

iterations defining the inverse transformation are given by:

$$\vec{x}_{i+1} = \vec{x}_i + \frac{\vec{y} - \vec{\varphi}(\vec{x}_i)}{2} \quad (3.63)$$

The initially selected point  $\vec{x}_0$  should not be far from the final estimate  $\vec{x}$ . The drawback of this method is that it is not established via a formal mathematical scheme. Although the method has been shown to converge to good results when the minimum value of the determinant of Jacobian is greater than zero, the method has been validated for relatively small deformations fields (i.e. the CT and MRI brain scans [27], [63]).

#### Proposed deformation field inversion model

In the proposed method the inversion of the deformation field is achieved by using a Newton-Raphson like method. Let a point misalignment function  $\vec{f}(\vec{x})$  be defined as:

$$\vec{f}(\vec{x}) = \vec{y} - \vec{\varphi}(\vec{x}) \quad (3.64)$$

For each  $\vec{y} \in \Omega$ , the aim is to find a corresponding  $\vec{x}$  which will make  $\vec{f}(\vec{x})$  as close to zero as possible. This is achieved in an iterative fashion:

$$\vec{x}_{i+1} = \vec{x}_i + \vec{d}x_i \quad (3.65)$$

Approximating the misalignment function using a first order Taylor series expansion gives:

$$\vec{f}(\vec{x} + \vec{d}x) \approx \vec{f}(\vec{x}) + J(\vec{f}(\vec{x}))\vec{d}x \quad (3.66)$$

where  $J(\vec{f}(\vec{x}))$  denotes the Jacobian matrix. Assuming  $\vec{f}(\vec{x} + \vec{d}x) = 0$  and introducing regularisation, the updates  $\vec{d}x_i$  can be calculated from a set of linear equations:

$$J(\vec{f}(\vec{x})) + \rho D \vec{d}x = -\vec{f}(\vec{x}) \quad (3.67)$$

where  $D$  is an  $d$ -dimensional diagonal matrix, and  $\rho$  is a position dependent regularisation parameter. The regularisation is introduced only for the areas where the determinant of  $J(\vec{f}(\vec{x}))$  is close to zero.

#### 3.4.3 Log-domain parameterised approach with symmetric warping

As other registration formulations, the log-domain-based framework with symmetric warping can be introduced to represent diffeomorphic forward  $\vec{\varphi}_{forw}$  and backward

---

**Algorithm 8** Proposed method of inverting deformation field

---

**Input:** Transformation  $\vec{\varphi}$  Parameter:  $\xi$

**Output:** Inverse of transformation  $\vec{\varphi}^{-1}$

```

1: for all  $\vec{y} \in \Omega$  do
2:      $i = 0$ 
3:      $\vec{x} = \vec{0}$ 
4:     repeat
5:         calculate determinant of the Jacobian matrix  $det(J(\vec{f}(\vec{x})))$ 
6:         if  $det(J(\vec{f}(\vec{x}))) \leq 0$  then
7:             add regularisation  $\rho D$ 
8:         end if
9:         solve a set of linear equations given by Equation 3.67
10:        update the current estimation of  $\vec{x}_i$ :
11:            $\vec{x}_{i+1} = \vec{x}_i + \vec{dx}_i$ 
12:            $i = i + 1$ 
13:        until ( $\|\vec{f}(\vec{x})\| \geq \xi$ ) or ( $i \geq IterMax$ )
14:        $\vec{\varphi}^{-1}(\vec{y}) = \vec{x}$ 
15: end for
16: return  $\vec{\varphi}^{-1}$ 

```

---

transformations  $\vec{\varphi}_{back}$  via a stationary velocity field  $\vec{v}$ . Based on this framework an inverse consistent symmetric image registration has been proposed by Han et al. [53], where the displacement fields  $\vec{u}_{hf}$  and  $\vec{u}_b$  are calculated from corresponding velocity fields  $\vec{v}_f$  and  $\vec{v}_b$ , that are parameterised using a single stationary velocity field  $\vec{v}$  expressed in the following way:

$$\vec{v}_{i,hf} = \log(\exp(\vec{v}_{i-1}) \circ \exp(\vec{dv}_i)) \quad (3.68)$$

$$\vec{v}_{i,hb} = \log(\exp(-\vec{v}_{i-1}) \circ \exp(-\vec{dv}_i)) \quad (3.69)$$

where  $\vec{dv}_i$  is defined in the following way:

$$\vec{dv}_i(\vec{x}) = \frac{I_f(\vec{\varphi}_{i-1,hf}(\vec{x})) - I_m(\vec{\varphi}_{i-1,hb}(\vec{x}))}{\|\nabla I_{i,sym}(\vec{x})\|^2 + (I_f(\vec{\varphi}_{i-1,hf}(\vec{x})) - I_m(\vec{\varphi}_{i-1,hb}(\vec{x})))^2} \nabla I_{i,sym}(\vec{x}) \quad (3.70)$$

where gradient  $\nabla I_{i,sym}(\vec{x})$  is defined by Equation 3.56 and the half-way forward transformation is defined as  $\vec{\varphi}_{i,hf}(\vec{x}) = \vec{x} + \exp(\vec{v}_i(\vec{x}))$  and the half-way backward transformation by  $\vec{\varphi}_{i,hb}(\vec{x}) = \vec{x} + \exp(-\vec{v}_i(\vec{x}))$ .

To maintain the inverse consistency criterion the velocity field  $\vec{v}_i$  is calculated based on the average of the forward and backward velocity fields in log-domain space as follows:

$$\vec{v}_i = \frac{1}{2} \log(\exp(\vec{v}_{i,hf}) \circ \exp(\vec{v}_{i,hb})) \quad (3.71)$$

The principal logarithm of exponential mappings for Equation 3.68, Equation 3.69 and Equation 3.71 is approximated using the Baker-Campbell-Hausdorff formula given by Equation 3.33. The advantage of this approach is that the final transformations  $\vec{\varphi}_{forw}$  and  $\vec{\varphi}_{back}$  can be obtained by the composition of exponentiation of the velocity field  $\vec{v}$ :

$$\begin{aligned} \vec{\varphi}_{forw} &= \vec{x} + \exp(\vec{v}) \circ (\exp(-\vec{v}))^{-1} = \vec{x} + \exp(2\vec{v}) \\ \vec{\varphi}_{back} &= \vec{x} + \exp(-\vec{v}) \circ (\exp(\vec{v}))^{-1} = \vec{x} + \exp(-2\vec{v}) \end{aligned} \quad (3.72)$$

Although the results presented in [53] show good performance, it was also shown that computing the exponential mapping has some limitations for large deformations [18] and the quality of the BCH formula approximation for concatenating the half-way velocity field was not assessed.

## 3.5 Summary

This chapter gives the details of the most common image registration algorithms with respect to the optimisation schemes adapted to solve image registration problems. The described methods cover the steepest descent-like approach and Newton's iteration approach obtained using the calculus of the variations. The Demon approach was also presented.

Moreover, this chapter also describes the various formulations of the image registration frameworks. The formulations presented here maintain diffeomorphic properties by taking the advantage of small-step restrictions or via log-Euclidean parameterisation related to the stationary velocity fields approximation. The stationary velocity fields are exploited in two ways either applied to the updates of the deformation field, or directly to the deformation field. Furthermore, the inverse consistency criterion is incorporated to the mentioned algorithms thereby the consistent forward and backward transformations are simultaneously estimated. Finally, image registration with symmetric warping of input images is presented and its theoretical advantages are outlined.

This chapter presented a novel method for inverting the deformation field which can be seen as an extension to the previously reported method [27]. Unlike the existing method described in [27], the proposed method for inverting the transfor-

---

**Algorithm 9** Log-domain image registration with symmetric warping

---

**Input:** Images:  $I_f$  and  $I_m$

Parameters:  $G_{fluid}$ ,  $G_{diff}$

**Output:** Forward transformation  $\vec{\varphi}_{forw}$ , backward transformation  $\vec{\varphi}_{back}$ , velocity field  $\vec{v}$

- 1:  $\vec{v} = \vec{0}$ ,  $i = 1$
  - 2: **repeat**
  - 3:     forward integration of velocity field:  $\vec{u}_{i,forw} = \exp(\vec{v}_{i-1})$
  - 4:     backward integration of velocity field:  $\vec{u}_{i,back} = \exp(-\vec{v}_{i-1})$
  - 5:     **for all**  $\vec{x} \in \Omega$  **do**
  - 6:         calculate update of velocity field  $\vec{d}v_i(\vec{x})$  (Equation 3.70 )
  - 7:         smooth update of the velocity field using Gaussian filter  $G_{fluid}$ :  
 $\vec{d}v_i(\vec{x}) = G_{fluid} * (\vec{d}v_i(\vec{x}))$
  - 8:         calculate forward velocity field  
 $\vec{v}_{i,hf}(\vec{x}) = BCH \left[ \vec{v}_{i-1}(\vec{x}), \vec{d}v_{i,hf}(\vec{x}) \right]$
  - 9:         calculate backward velocity field  
 $\vec{v}_{i,hb}(\vec{x}) = BCH \left[ -\vec{v}_{i-1}(\vec{x}), -\vec{d}v_{i,hb}(\vec{x}) \right]$
  - 10:        average forward and backward velocity field:  
 $\vec{d}v_i(\vec{x}) = \frac{1}{2}(\vec{v}_{forw}(\vec{x}) + \vec{v}_{back}(\vec{x}))$  (Equation 3.71)
  - 11:        update velocity field  $\vec{v}_i(\vec{x})$ :  
 $\vec{v}_i(\vec{x}) = \vec{d}v_i(\vec{x})$
  - 12:        smooth velocity field  $\vec{v}_i(\vec{x})$  using Gaussian filter  $G_{diff}$ :  
 $\vec{v}_i(\vec{x}) = G_{diff} * (\vec{v}_i(\vec{x}))$
  - 13:     **end for**
  - 14:      $i = i + 1$
  - 15: **until** (velocity field does not change) **or** ( $i \geq IterMax$ )
  - 16: concatenate half-way velocity field  $\vec{v}$  (Equation 3.72)
  - 17: **return**  $\vec{\varphi}_{forw}$ ,  $\vec{\varphi}_{back}$ ,  $\vec{v}$
- 

mation is established in the optimisation framework using the Newton's method. Furthermore, a new image registration algorithm with symmetric warping is presented which makes use of the newly proposed method of the inverting deformation field.

Finally, this chapter gives systematic overviews on image registration methodologies presented from different points of view. These different views include methods used for optimisation an objective function, various approaches to establish the diffeomorphic image registration, and additional constraints that can either improve

the quality of the estimated transformation (enforcing the inverse consistency criterion using consistent image registration), or speed up the registration process (image registration with symmetric warping). Although the steepest descent method, Newton's iteration method, are already known image registration approaches, their different versions discussed in this chapter can be also seen as new image registration methods.

# Chapter 4

## Comparison of image registration

This chapter presents the experimental results of the assessment of the algorithms presented and proposed in Chapter 3 and the different formulations of the image registration problem. First, the impact of the parameterisation of the deformation field using the stationary velocity field is shown. Then, the importance of the inverse consistency criterion for several applications is assessed based on the experiments, that are carried out for the consistent image registrations. As the next step of the evaluation, improved robustness of the image registration algorithms with symmetric image warping is presented. Finally, the described methods are compared against each another to find out the most appropriate for the specific medical applications. All of the performed tests, that produced the following results, were done both on the simulated data to show the accuracy with respect to the known parameters of the ground truth data, and on the data coming from the real applications. A wide range of the executed experiments and types of the data involved in these experiments, make this comparison a comprehensive and critical analysis of the presented algorithms. Following evaluations can be potentially useful as a kind of the *look-up* tables of the expected behaviour of the presented algorithms in the particular applications.

### 4.1 Introduction

Qualitative and quantitative comparison of the image registration algorithms is an important part of utilising these algorithms in practical applications. The reason for the critical assessment of the image registration algorithms is unquestionably linked to the ill-posed properties of the image registration, where small changes of the input data can lead into significant changes in the estimated transformations [90, 92]. As it was pointed out in the previous chapters, introducing the regularisation term and the additional penalisation is inevitable, but this still may not entirely support the

stability of the solution. Moreover, a number of parameters inherently involved in the chosen deformation models (so-called the design parameters), can significantly lengthen in time the estimation process of the most desired solution, specifically when these parameters are tuned by a trial-and-error procedure. It may commonly happen that the set of the optimal parameters for the specific set of images does not work properly with another set of images, that are visually similar. The mentioned issues lead to the necessity of the critical analysis of the known image registration algorithms using different setups for both data and parameters. Before the experimental results are given and furthermore discussed, a brief overview of the known comparison works is provided here, firstly to show the lack of the general assessment of the image registration comparison, secondly to present common frameworks to benchmark algorithms and finally to point out some of the interesting conclusions from these works.

The most commonly referred algorithm in the biomedically-driven image registration applications seems to be the Demon approach. It is customary referred to be a state-of-the-art method to be compared against a proposed method. The Thirion's Demon [138] and its *active* gradient-based modification [148] were implemented and assessed against each other for the image-guided radiation therapy procedures in [148]. The wide variety of the conducted experiments, and various data sets used in those experiments indicate better robustness of the *active* gradient-based approach (given in Equation 3.21). The results from the verification using deformable pelvis phantom confirm the clinical reasonability/correctness of using the Demon-based approaches in the radiotherapy procedures.

Different variants of the image intensity gradients thereby the various Demon algorithms were implemented for the graphic processing units (GPU) using the compute unified device architecture (CUDA) and compared against each other in [44]. The major focus of that investigation was to find out the trade off between the computational cost and the accuracy (assessed both based on the manually selected landmarks and for the intensities of images involved in the registration using correlation coefficient) for the thoracic CT data. As it may be expected, the fastest method is based on the fixed Thirion's gradient (Equation 3.20 and [138]) due to only one gradient calculation operation during all image registration procedures. On the opposite side, due an additional computational cost of gradient of moving image calculation at each iteration, the symmetric gradient (Equation 3.56) used in the consistent image registration based on the Demon approach with symmetric warping was the slowest one. The overall accuracy of all Demon methods was similar. The weak point of this comparison is that it was evaluated using only one data set consisting of five three-dimensional CT volumes. In order to get some general

conclusions, the comparison should be performed also on data from other common radiotherapy applications.

The comparison of the Newton's iteration approach with the Demon is given in [78]. The experiments were carried out on the synthetic and medical data, and also phantom studies were presented. The main limitations of this comparison are as follows. Firstly, the simulated data consist of the data set of the deformation fields that are restricted to the harmonic deformations, and moreover, no evidences either theoretical or experimental are given to prove the relevance of this type of the deformations linked to the real-life deformations. Secondly, the properties of the estimated deformation fields such as smoothness or preservation of the one-to-one mapping that are essential in the treatment applications, are not assessed.

To the best knowledge of the author, the extensive comparison involving the variational approach proposed by Chéfd'hotel et al. [24], Hermosillo et al. [56, 57] have not been done. The only experimental results that have been found to be evaluated, are those, described in [24, 56, 57] where limited examples of the medical applications are presented with the main emphasis on the presented technique rather than the medical outcomes.

In general, the impact of the stationary velocity field parameterisation was not critically assessed. The seminal papers where either the displacement fields [5, 144] or the updates of the deformation field [143, 145] were parameterised via the stationary velocity field, give some fundamental comparisons of the new concept but they are limited to the Demon approach. The mentioned evaluations are more oriented to explain the idea of the log-domain registration whereas the provided experimental results do not cover any particular area of applications. In addition, Han et al. [53] gives only the statement that the log-domain image registration with symmetric warping performs better than the original log-domain algorithm. No additional quantitative measures are evaluated.

The comparison of the Large Deformation Diffeomorphic Metric Mapping (LDDMM) algorithm reformulated so the stationary velocity field is used instead of the originally time-dependent version and the diffeomorphic Demon approach is presented in [58]. The most important conclusions given there are the following. Both algorithms produce similar results in terms of the accuracy assessed by the image intensities comparison. Although, the Demon algorithm is shown as slightly faster, the overall convergence rate is slower than in the case of stationary LDDMM. The stationary LDDMM has advantages when the characteristics of the estimated deformation fields such as the smoothness or the inverse consistency criterion are crucial. Finally, it is worth to emphasise that the results shown in that work indicate the existence of sets of the design parameters that produce non-diffeomorphic transfor-

mations. It also indicates that the theoretical (mathematical) justification on the diffeomorphism embedded in the proposed frameworks does not prevent from failing to fulfil one-to-one mapping properties.

The quantitative evaluation of the consistent log-domain Demon algorithm was performed in [94] for the cone-beam CT guided radiotherapy procedures of the neck and head. The obtained results indicate that the Demon based approach can be successfully utilised for the images obtained from the same type of the scanners and offers acceptable trade-off between accuracy and the computational cost. The validation was performed using several criteria to assess the image quality after registration such as correlation coefficient, the quality of the estimated transformation via harmonic energy, and the accuracy in terms of the distances between the manually selected landmarks.

The general comparison of common non-rigid methodologies with a particular focus on the radiotherapy applications is presented in [21]. The three algorithms, used there for the evaluation, are: original Thirion's Demon algorithm [138], *fastFFD* (here called as a the Newton's iteration approach) [78] and the level-set inspired approach proposed by Vemuri et al. [142]. All of these methods are implemented in four different manners including the originally proposed implementation, additional Gaussian smoothing procedure of the input images, and with and without the embedded rigid preregistration. These different strategies were compared against each other and with the results were obtained by the parameteric registration using the rigid transformation model driven by the Mutual Information. The presented results in terms of the volumetric criterion (correlation coefficient) and the region overlapping of segmented organs (Equation 4.10) suggest that the Demon-based approaches yield the best robustness for the head and neck data sets. Comparison between the Newton's iteration algorithm and the Demon approach gives the opposite conclusions that these were summarised in [78]. The reason for this inconsistency can be partially explained by the different types of the data used in the performed evaluations. In that comparison work, the quality of the estimated deformation fields in terms of the medical correctness (one-to-one mapping, inverse consistency criterion) was not assessed.

The comparison of the three common image registration algorithms such as Demon [138], B-spline approach [112] and the spring mass system [84, 121] was presented in [122]. The evaluation was done in two trials: firstly using the set of simulated images either with different types of the noise included in the images or without any noise, secondly using the real clinical CBCT and CT data from the radiotherapy of the neck and the pelvis area. The Demon algorithm was shown as having the best robustness when no noise is present in the input data. In terms

of the sensitivity to noise, the Demon algorithm fails to estimate the ground truth deformation field when the images are affected by the Gaussian noise or the structured noise. In this particular evaluation driven by the radiotherapy applications, the spring mass system [84, 121] achieved the best performance.

The largest evaluation done for the 14 non-linear and one linear image registration algorithms was conducted by Klein et al. [68]. The aim of this evaluation was to assess the quality of the automatic brain images labelling process using the image registration techniques. The data set used as the test data set was restricted to 80 MRI brain volumes obtained from four different sources. From the perspective of the other work, the most interesting finding outlined in this work is the statement that *the relative performance of the registration methods under comparison appear to be little affected by the choice of the subject population, labelling protocol, and type of overlap measure*. Thus, it suggests that at least for the brain analysis, the new images taken either from new subjects or using the new protocols can be successfully registered with the desired level of accuracy by the mentioned methods.

Due to the lack of the ground truth data available to validate and compare the image registration algorithms, the interesting functionality is going to be offered by the Non-rigid Image Registration Evaluation Program (NIREP) [127]. The NIREP aims to developing the tools, the relevant metrics and the data sets to provide a rigorous and consistent testing procedure for any image registration algorithm. The NIREP will enable comparison of the performance of the algorithms under specific conditions and for the particular applications in the controlled setup. At the time of evaluating the algorithms described in this work, the NIREP was in the prototype stage and was not available to produce any kind of the assessments. At this work, some metrics that are used in the NIREP are evaluated.

Recently, a general evaluation methodology for computer vision applications and a collection of the databases of the ground truth flows for the optical flow based registration methods were presented by Baker et al. [12]. Interestingly, one of the conclusions emphasises that *no single method is yet able to achieve strong performance across a wide variety of data types*. Although this statement is made for the general and real-world applications in computer vision, it can be easily applied to the medical image registration due to the same nature of problems inseparably linked with any type of the motion estimation.

To sum up, the assessment of different image registration algorithms and different formulations of the diffeomorphic approaches such as registration with the exponential update, the log-domain parameterisation for the deformation field, and the small step multi-pass approach can be potentially useful in many areas e.g. to build more sophisticated systems where image registration acts as a tool for further

data processing. Similarly, it seems to be interesting enough to assess the outcomes given by ensuring the inverse consistency criterion for the consistent image registration. Finally, the questionable benefits coming from the symmetrisation of the registration process can be checked.

## 4.2 Environment for experiments

The image algorithms have been extensively assessed with different types of experiments, thereby enabling calculating a great variety of evaluation statistics.

Firstly, the impact of the parameterisation of the deformation field using the stationary velocity fields is investigated. The original version of the algorithm, and the two possible implementations (the exponential update, and the log-domain approach) are included during this stage of investigation. Although, the similar experiments were conducted in the original work introducing the log-Euclidean parameterisation into image registration [143, 144, 145], this work extends them by evaluating different image registration methods (the steepest descent method, the Newton's iteration method, and the Demon method). This is done to assess whether the log-Euclidean parameterisation gives the similar effects on the estimated deformation fields as it was shown for the well-known Demon algorithm.

The second set of the experiments was carried out with respect to the three solution schemes: estimation of the transformation from the moving image to the reference image, the consistent framework (joint estimation of the forward and backward transformation), and the image registration framework with symmetric warping.

Finally, between-method analysis was conducted to show robustness of the described methods with respect to possible applications in computer vision, medical image analysis and biomedical motion modelling. Three described methods: the steepest descent method, the Newton's iteration method, and the Demon method are validated with wide spectrum of the design parameters, and compared against each other using different data sets.

### 4.2.1 Data set description

This section describes both the synthetically generated data and the clinical data used for the image registration assessment.

#### Random synthetic data generation

The synthetic data set consists of the synthetically generated reference images, and the ground truth deformation fields (velocity fields) warping the reference images to

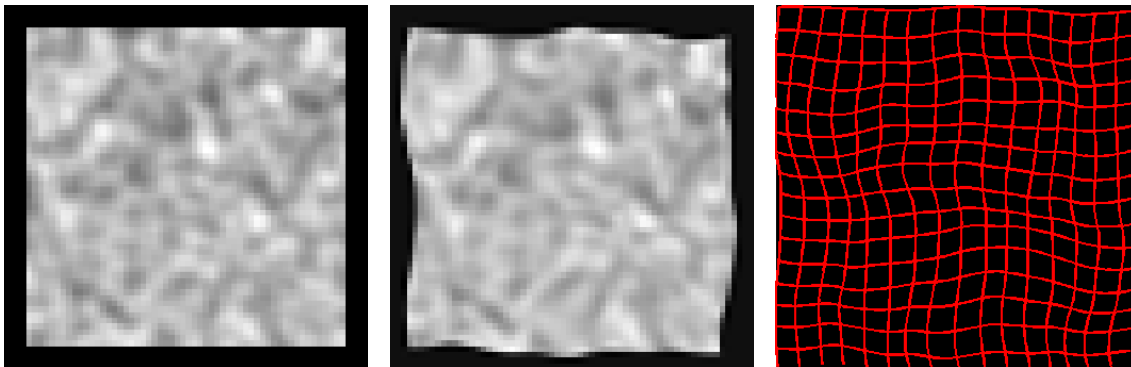


Figure 4.1: Example of the synthetically generated data: (from left to right) - fixed image, fixed image warped by the deformation field, and the grid warped by synthetically generated deformation field.

obtain the moving image.

The reference images were generated from a random zero-mean and unit variance Gaussian *image process* defined for all points of a two-dimensional regular grid of size  $64 \times 64$ . Then, the generated image is smoothed by a low-pass filter, scaled into the range  $[0.0, 1.0]$ , and padded with a black border to avoid the edge artifacts during image registration. The sample of the synthetically generated image is shown in Figure 4.1.

The known velocity fields were generated from two independent random zero-mean and a three pixel standard deviation Gaussian *velocity process* defined on the selected knots of the sparse two-dimensional regular grid of size  $12 \times 12$ . Then, for both components of the velocity field the repeatable low-pass filtering procedure was applied to obtain a desirable smoothness (the determinant of the Jacobian matrix has to be positive). Finally, velocity fields were interpolated to the finer grid resolution ( $64 \times 64$ ) with cubic spline interpolation and then scaled and exponentiated to get a wide range magnitudes of diffeomorphic deformation fields. This procedure of generating deformation field is similar to the state-of-the-art method described in [17] that was used to validate the Baker-Campbell-Hausdorff formula for calculation of the velocity fields. The sample of the synthetically generated deformation field is shown in Figure 4.1 and in Figure 4.2.

### Real data

The real data used for the validation consist of two public available data sets and one available at the University of Central Lancashire.

The data sets include:

- POPI (POPI stands for the Point-validated Pixel-based Breathing Thorax Model) computed tomography of lungs with the landmarks manually selected

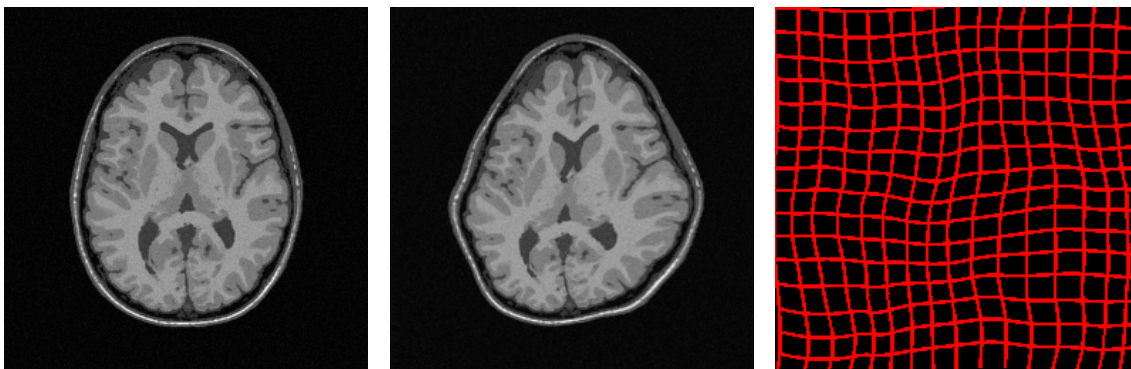


Figure 4.2: Example of the partially synthetically generated data: (from left to right) fixed image - the axial slice from MRI brain volume, fixed image warped by the deformation field, and the grid warped by synthetically generated deformation field.

by the medical experts for assessment of the image registration quality. The data were obtained by the Léon Bérard Cancer Center & CREATIS Laboratory in Lyon, France and are freely available to download from the Internet. For the data, the set of the landmarks is attached thereby the target registration error ( $TRE$ ) can be calculated as a quantitative measure and compared to other method published on the aforementioned web page. Further details of the data sets can be found in [141]. The data set consists of ten volumes with the size of  $482 \times 360 \times 141$  and the resolution is  $0.976562mm \times 0.976562mm$  with a slice thickness of  $2.0mm$ . This particular set was used for validation of the registration method by [43]. Thus far, various in-house data sets of the lungs were usually used for the validation [159, 73, 75, 74, 36]. The example of CT lung data are shown in Figure 4.4.

- *BrainWeb* data set consists of 20 anatomical models of 20 normal brains [8]. Each anatomical model is labelled thus each tissue class (each brain structure) can be found in the volume. The structure of brains is divided into 12 classes: Background, CSF, Gray Matter, White Matter, Fat, Muscle, Muscle/Skin, Skull, Blood vessels, Connective (region around fat), dura mater and bone marrow. Therefore, the registration quality can be assessed by the segmentation accuracy. With one of the models used as a reference and the remaining models registered to it, the ground truth labelling of the reference image is compared with the labelling achieved by the warping labels of the registered images. The segmentation accuracy is calculated based on the region overlapping ( $RO$ ) of the different structures. The data set consists of 20 volumes of size  $256 \times 256 \times 181$  with the spatial resolution of  $1.0mm \times 1.0mm \times 1.0mm$ . In this comparison work, the first ten volumes was used only. The reason

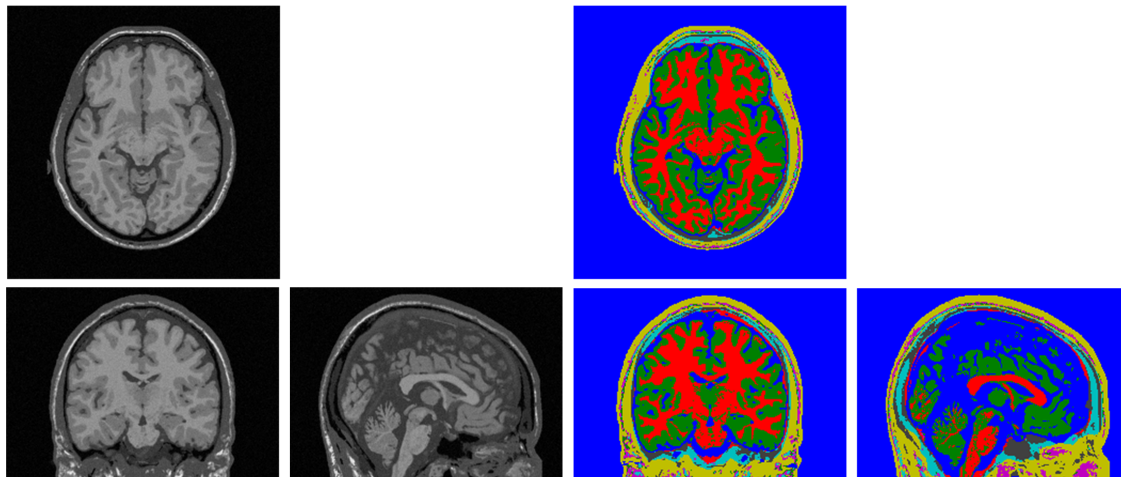


Figure 4.3: Example of MRI brain data (left) and their ground truth (manual) labelling (right) used in the experimental validation.

for selecting the brain image data set is motivated by the literature findings, where the brain annotation is most often used as a quantitative measure of the image registration algorithms [27, 162, 4, 143, 144, 145, 136, 68]. The example of MRI brain data are shown in Figure 4.3.

- Data set of the MRI images of the pelvic-area organs. The data exhibit significant changes of the bladder size and shape. The quality of the registration can be assessed in a similar manner as in the case of the brain data due to the labelling provided for the anatomical structures such as the prostate and the bladder. The data set consists of five volumes of size  $240 \times 320 \times 30$  with the spatial resolution of  $1.0\text{mm} \times 1.0\text{mm} \times 3.0\text{mm}$  representing one subject with shape changes of bladder, rectum, and prostate. The pelvic-area image registration is also very common issue as the potential benefits of the accurate registration can be entirely applied to the radiotherapy of the prostate cancer. The example of MRI brain data are shown in Figure 4.5.

### 4.2.2 Validation criteria

Validating the performance of the image registration methods was accomplished through several evaluation statistics quantifying the obtained results. The quantification was done in several ways, either for the warped images, or with respect to the estimated transformations, or in terms of the biomedical quantities.

Due to the mono-modal data set, the sum of the squared differences ( $SSD_I$ ) is chosen as the measure of the similarity between two images. The  $SSD_I$  matching

## 4.2. ENVIRONMENT FOR EXPERIMENTS

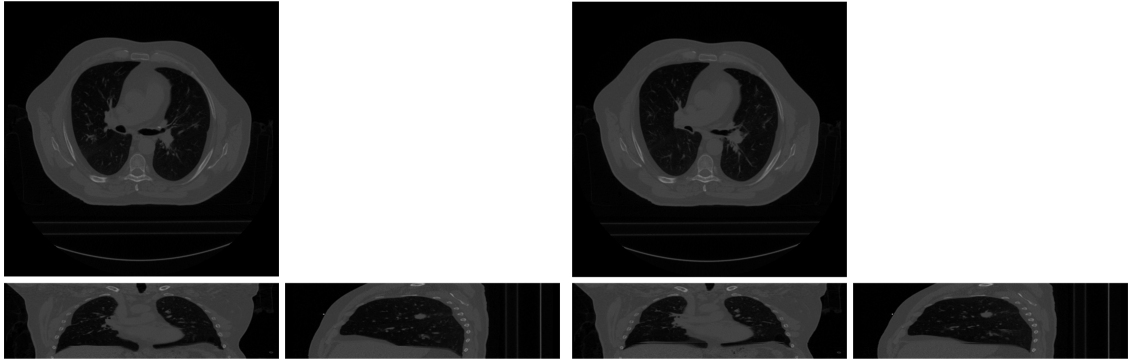


Figure 4.4: Example of CT lung data used in the experimental validation: (left) the end-inhalation (right) exhalation phase are shown.

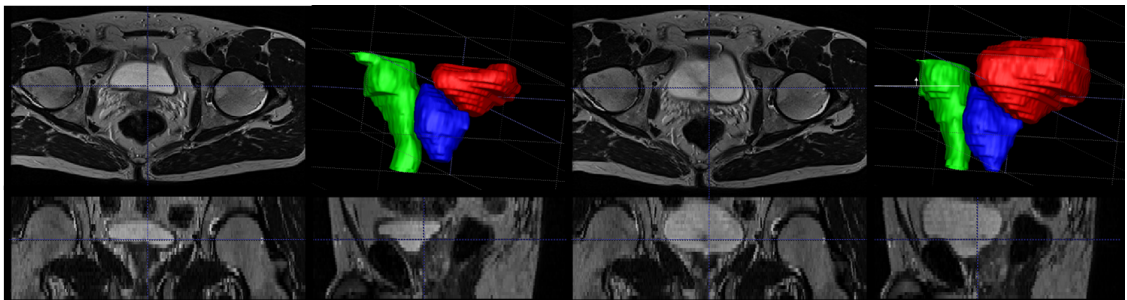


Figure 4.5: Example of MRI pelvic area data used in the experimental validation with a ground truth annotation of the organs of interest: bladder (red), rectum (green), and prostate with seminal vesicles (blue).

criterion is defined by:

$$SSD_I(I_j, I_k) = \frac{1}{N} \sum_{\vec{x}} (I_j(\vec{x}) - I_k(\vec{x}))^2 \quad (4.1)$$

where  $I_j$  and  $I_k$  are the assessed images and  $N$  is the number of image points (pixels/voxels). During the evaluation of the synthetic data with the ground truth deformation field, the sum of the squared differences  $SSD_{\vec{\varphi}}$  for the estimated transformation  $\vec{\varphi}_{est}$  and the known transformation  $\vec{\varphi}_{org}$  can be calculated. The  $SSD_{\vec{\varphi}}$  is defined as follows:

$$SSD_{\vec{\varphi}}(\vec{\varphi}_{org}, \vec{\varphi}_{est}) = \frac{1}{N} \sum_{\vec{x}} \|\vec{\varphi}_{org}(\vec{x}) - \vec{\varphi}_{est}(\vec{x})\|^2 \quad (4.2)$$

The distance to the known Jacobian of transformation ( $distJac$ ) is computed in the following way:

$$distJac(\vec{\varphi}_{org}, \vec{\varphi}_{est}) = \frac{1}{N} \sum_{\vec{x}} (\det(J(\vec{\varphi}_{org}(\vec{x}))) - \det(J(\vec{\varphi}_{est}(\vec{x}))))^2 \quad (4.3)$$

This criterion is often used to track the deformation field estimation when the ground truth data are available [144, 145]. To enable further comparison of the estimated deformation fields, the determinant of the Jacobian matrix of the transformations is also calculated to track the minimum of the Jacobian matrix determinant ( $minJac$ ). The minimum of the determinant of the Jacobian matrix is defined as follows:

$$minJac(\vec{\varphi}) = \min_{\vec{x}} (\det(J(\vec{\varphi}(\vec{x})))) \quad (4.4)$$

Tracking of  $minJac$  is important because it reflects the volume changes of a point mapped through the estimated transformation [27]. A positive value of  $minJac$  indicates that the estimated transformation is one-to-one mapping between image points, while a negative value suggests that the transformation locally folds the domain inside out. The smoothness of the estimated deformation field was measured by evaluating the harmonic energy (HE) criterion [144, 145, 94]. The harmonic energy is defined as:

$$HE(\vec{\varphi}(\vec{x})) = \frac{1}{N} \sum_{\vec{x}} \sum_{j=1}^d \sum_{k=1}^d \left( \frac{\partial \varphi_k(\vec{x})}{\partial x_j} \right)^2 \quad (4.5)$$

In many applications (especially in medical and biological image analysis), it is commonly assumed that each spatial point in moving image  $I_m$  is mapped to the corresponding point in fixed image  $I_f$ . This also applies for the backward transfor-

mation i.e. the point from fixed image  $I_f$  has a corresponding point in moving image  $I_m$ . Nevertheless, most of the image registration algorithms estimate the forward transformation that does not invert the backward transformation and *vice versa*. This inconsistency (described in details in Chapter 3.3) for the estimated transformations can be assessed with respect to the inverse consistency criterion (*ICC*). A computable criterion reflecting the inability to provide unique description of the correspondence between two images is the inverse consistency error (*ICE*). The *ICE* is defined here as an average distance between the original points in one image and their positions in this image after mapping to another image and subsequent mapping back to the original image as follows:

$$ICE(\vec{\varphi}_{forw}(\vec{x}), \vec{\varphi}_{back}(\vec{x})) = \|\vec{x} - (\vec{\varphi}_{forw} \circ \vec{\varphi}_{back})(\vec{x})\|^2 \quad (4.6)$$

The inverse consistency error measures only the consistency between the forward and backward transformation, while the accuracy of transformation is not assessed (a detailed discussion is presented in [27, 127]). In the case of the perfectly consistent transformations, the *ICE* is equal to zero. During the validation the average of the *ICE* (*aveICE*) is also calculated as follows:

$$aveICE(\vec{\varphi}_{forw}, \vec{\varphi}_{back}) = \frac{1}{2} \left( \frac{1}{N} \sum_{\vec{x}} \|\vec{x} - (\vec{\varphi}_{forw} \circ \vec{\varphi}_{back})(\vec{x})\| + \frac{1}{N} \sum_{\vec{x}} \|\vec{x} - (\vec{\varphi}_{back} \circ \vec{\varphi}_{forw})(\vec{x})\| \right) \quad (4.7)$$

and maximum *ICE* (*maxICE*) as follows:

$$maxICE(\vec{\varphi}_{forw}, \vec{\varphi}_{back}) = \max(\max_{\vec{x}} \|\vec{x} - (\vec{\varphi}_{forw} \circ \vec{\varphi}_{back})(\vec{x})\|, \max_{\vec{x}} \|\vec{x} - (\vec{\varphi}_{back} \circ \vec{\varphi}_{forw})(\vec{x})\|) \quad (4.8)$$

All aforementioned criteria indicate the quantity with respect to either the image similarity measures or the deformation field statistics, while they somehow do not reflect the anatomical correctness of the results. Thus far, there is a lack of the ground truth data in the clinical applications and alternative criteria for the physical measures of accuracy have to be used. From the medical point of view, the algorithms were validated with respect to the Region Overlapping (RO) (or sometimes called Dice Similarity Index (DSI)). The Region Overlapping for organ of interest  $P$  is defined as:

$$RO_P(P_{ref}, P_{warp}) = \frac{numberOfVoxels(P_{ref} \cap P_{warp})}{numberOfVoxels(P_{ref} \cup P_{warp})} \quad (4.9)$$

where  $P_{ref}$  is an organ segmented in the reference image, and  $P_{warp}$  is the same

organ segmented in the warped image.  $RO_P$  assesses how well two segmentations of the organ of interest agree or disagree with each other [127]. It can be also defined as follows:

$$RO_{P\%}(P_{ref}, P_{warp}) = RO_P(P_{ref}, P_{warp}) * 100 \quad (4.10)$$

Another, common choice of the description for the anatomical registration accuracy is based on the salient, corresponding points between images identified by the medical experts. This enable the target registration error ( $TRE$ ) to be used by measuring the distance between those selected landmarks before and after registration. The  $TRE$  is defined as follows:

$$TRE(H_{fix}, H_{mov}) = \frac{1}{N_L} \sum_{\vec{x}} \|\vec{h}_{fix} - \vec{h}_{mov}\|^2 \quad (4.11)$$

where  $H_{fix}$  and  $H_{mov}$  are sets of manually selected landmarks in the fixed (reference) image  $\vec{h}_{fix}$  and in the moving image  $\vec{h}_{mov}$ , and  $N_L$  is the number of selected landmarks. After image registration, the selected landmarks in the moving image  $H_{mov}$  are warped using the resulting deformation field and the target registration error is calculated between the points in the reference image and points mapped by the estimated transformation. In the case of perfect matching, the distance should be zero.

### 4.2.3 Implementation remarks

Whereas the pseudo-code formulations of all the described algorithms were given in the previous chapter, numerical schemes that are crucial to the related approaches, are detailed in this section.

Discrete matrix stencils for the regularisation terms used in the described approaches are presented in the textbooks [90, 92] and papers [24, 57, 5].

The convolution by a Gaussian kernel is approximated by the fast recursive filter implemented by the smoothing operator, originally proposed in [35]. This specific type of Gaussian filtering is already included in *CImg Library*, and also was used in the originally presented image registration algorithm [56, 57, 24].

The  $d$ -linear interpolation method is used to calculate the intensity value of an arbitrary spatial position. The gradients of images are calculated using the central difference forms. Furthermore, the gradients during the registration process are calculated for the input images that are warped by the currently known estimation of the deformation field instead of performing the interpolation of input image gradients. Calculating gradients directly on the newly warped images has similar computational cost, while it was shown to improve robustness in terms of

the registration force quality in [131]. A detailed discussion on different interpolation methods, their computational cost, quality of interpolation and quantitative comparison in the context of the medical applications can be found in [137].

The described algorithms benefit significantly in terms of the execution time by the C++ implementation as a MATLAB mex file in the majority utilising the open-source, C++, image processing toolkit *CImg Library*. Although the included methods and classes of this toolkit offer high portability for different operating systems, the algorithms were evaluated under Windows 7 system.

## 4.3 Qualitative and quantitative comparison

This section presents experimental results of validation for all the algorithms that were described in the previous sections using both synthetic and real clinical data sets.

The synthetic part of the validation consists of the experiments conducted on the data generated by the procedure described in Section 4.2.1. Experiments were carried out with a completely controlled setup. The procedure of generating the deformation fields via their velocity fields produces 100 random deformation fields that were used to warp the synthetic images (example is shown in Figure 4.1) and then each version of the presented algorithms was run to estimate the already known deformation field. Subsequently, the random transformations were also applied to two-dimensional real images coming from three-dimensional MRI brain volumes (example of axial slice used in validation is shown in Figure 4.2). The algorithms were always initiated with an identity transformation and the same default set of design parameters. The design parameters for the Demons approaches are set as  $G_{diff} = 1.0$  and  $G_{fluid} = 1.0$ , following most of the cited papers; for the Newton's iteration approach  $\lambda_{diff} = 0.1$  as the default value in [78, 159, 21]; for the steepest-like method one of the set of the parameters from [56, 57, 24] was chosen with  $\alpha = 0.1$  for the weight of parameterisation and  $\mu_{elas} = 1.0$  as the simplified elasticity parameter [56]. Since the main emphasis was put on the comparison of the different algorithms and their various formulations, the multi-resolution manner was not used at this stage of experiments. To enable observations of the convergence rate of the specific criterion and their further analysis, each algorithm was evaluated multiple times with a fixed number of iterations starting from 1 and ending with 50.

The second part of the validation was carried out on the real clinical data where the ground truth deformation fields were not known. The aim of the comparisons is to show advantages and weak points of the particular algorithms and their different versions in the typical cases of the medical applications. Examples include 3D

volumes concerning different applications in medical image analysis and medical motion analysis (presented in Chapter 6) using data such as MRI brain images (Figure 4.3), MRI pelvic-area (Figure 4.5), and CT of lungs (Figure 4.4). Although the ground truth data are not available, the numerical assessment can be still done in somehow quantitative manner using the criteria described in the previous section. All methods were evaluated in the multi-resolution manner with the number of levels depending on the volumetric size of the particular data set: four levels for brain data sets and for pelvic-area data, and three levels for the lung data set. Finally, the number of iterations and the various combinations of the design parameters were checked during these comparisons to find out their impact on the final results.

#### 4.3.1 Impact of the stationary velocity field parameterisation

This section summarises the experiments that were carried out to examine the parameterisation of the deformation field by the stationary velocity fields. The parameterisation was introduced to all the investigated algorithms in two possible manners: parameterisation of the update deformation field (exponential update of the deformation field introduced in Section 3.2.2), and a parameterisation of the full deformation field as the stationary velocity field that is then exponentiated to get the displacement field (described in Section 3.2.3).

##### Synthetic data

The results for the assessment done for the synthetic data are presented in Figure 4.8 for the Demon approaches, in Figure 4.7 for the Newton's iteration approaches, and in Figure 4.6 for the steepest-like approaches. These figures show the evolutions of the several criteria that are chosen to describe the important properties of the deformation fields over the executed iterations. In addition, the evaluated algorithms utilise two types of gradients, gradient calculated using the original version of the algorithm that is denoted in figures as *org gr* and the symmetric gradient that uses the intensity information from the fixed and moving image at the same time is denoted in figures by *sym gr* (Equation 3.22). In the case of image registration with symmetric warping, only symmetric gradient is calculated (Equation 3.56).

In general, the parameterisation via the stationary velocity field introduced to either the update of the deformation field or displacement field, produces slightly smoother transformations in terms of the harmonic energy (HE) for all evaluated algorithms. The most noticeable results are achieved for the steepest-like method (Figure 4.6c) where the *HE* of the deformation field estimated using the exponen-

tial update technique is about 10% better than that for the original method. For the Newton’s iteration method, the  $HE$  decreases for the log-domain formulation, while for the exponential update version it stays at the same level of the originally proposed method. Both the exponential update version and the log-domain version of the Demon approaches produce slightly smoother transformation than its original Thirion’s version.

In all cases, the original methods show better convergence in terms of minimising the  $SSD_I$  between registered images.

#### Brain MRI data

The results obtained for the MRI brain data set are presented in Figure 4.11 for the Demon approaches, in Figure 4.10 for the Newton iteration approaches, and in Figure 4.9 for the steepest-like approaches

All algorithms with the incorporated exponential update scheme and the log-domain parameterised version of them perform worse in terms of the  $SSD_I$  between images than their original formulations. This difference is more notably seen for the log-domain formulation (especially for the Newton’s method in Figure 4.10g). After executing 100 iterations, the log-domain Demon, the log-domain Newton’s iteration and, the log-domain steepest-like method produce the  $SSD_I$  that is 7.0%, 9.0% and 9.0% worse than those  $SSD_I$  produced by their original versions. Correspondingly after the same number of performed iterations, the  $SSD_I$  for the algorithms with the exponential update scheme are only about 3.0% worse than that by the original methods.

In the same time, the harmonic energy is reduced for both types of the approaches: with exponential update and log-domain parameterisation. The deformation fields estimated after 100 iterations by the Demon with exponential update and the log-domain Demon are about 5.0% and 1.5% smoother respectively in terms of the  $HE$  than the deformation field estimated using the original Demon version. For the Newton’s method, the smoothness is significantly reduced in both types of the parameterisation by a level of 15.0% when compared to the original Newton’s iteration method. Similarly, the steepest-like method with exponential update ensures the smoothness of the deformation fields to be about 12.0% more than the original steepest-like method, while the log-domain version is about 13.0%.

Finally, the results of assessment of the segmentation accuracy obtained for all methods indicate that the parameterisation of the deformation field either via exponential update or introducing the full log-domain framework slightly decreases the values of the  $ROs$  for all measured structures. The average  $RO$  is about 0.5 worse for the approach with exponential update and 1.0 worst for the log-domain

### 4.3. QUALITATIVE AND QUANTITATIVE COMPARISON

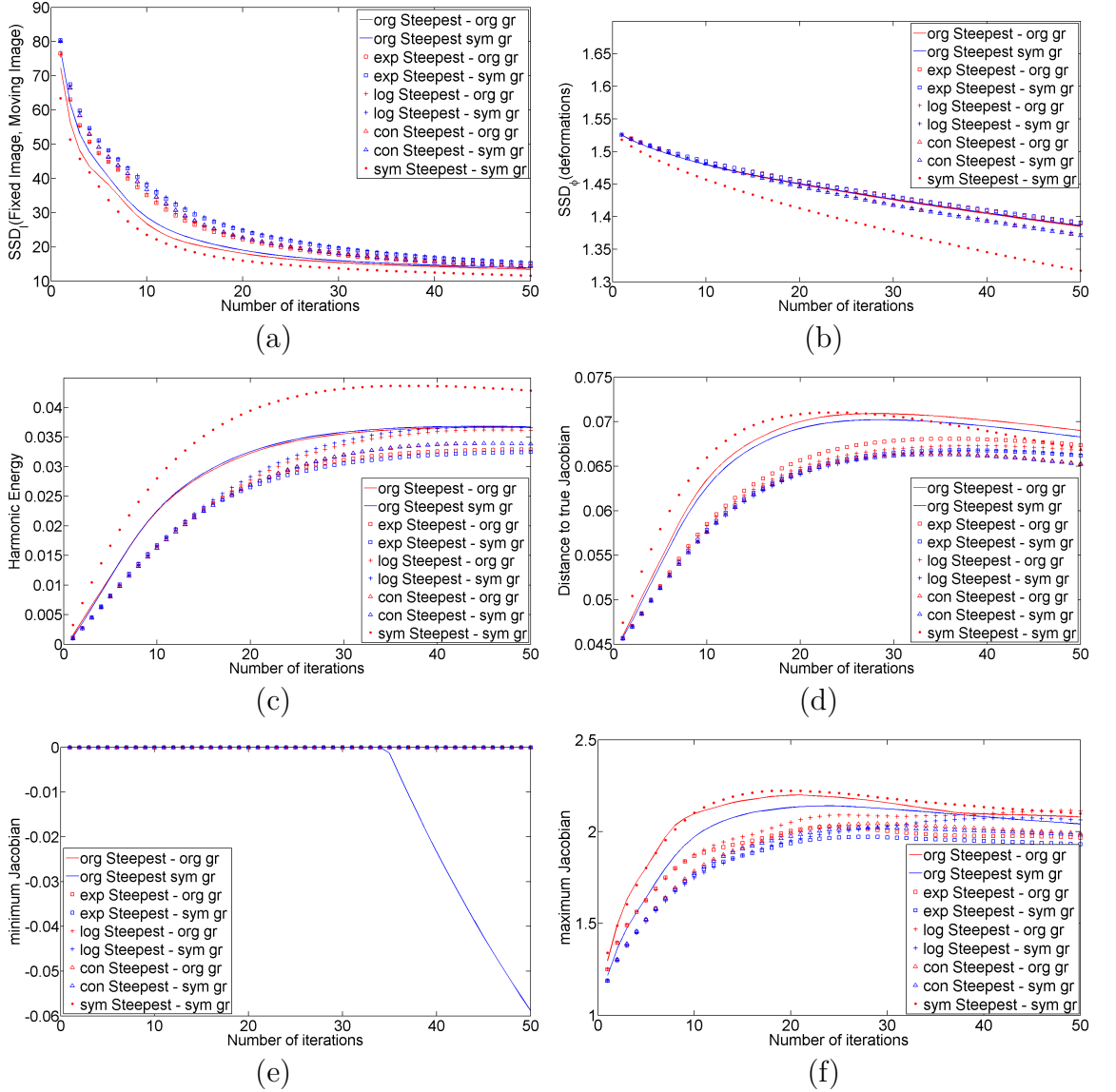


Figure 4.6: Results obtained for the simulated data set using different types of the steepest-like approach (Algorithm 1). The convergence studies are shown for: (a) the average of the  $SSD_I$  between images, (b) the average of the  $SSD_\phi$  between estimated deformation field and ground truth deformation field, (c) the average  $HE$ , (d) the average distance to the real Jacobian, (e) the minimum and (f) the maximum determinant of the Jacobian matrix of the estimated transformation.

### 4.3. QUALITATIVE AND QUANTITATIVE COMPARISON

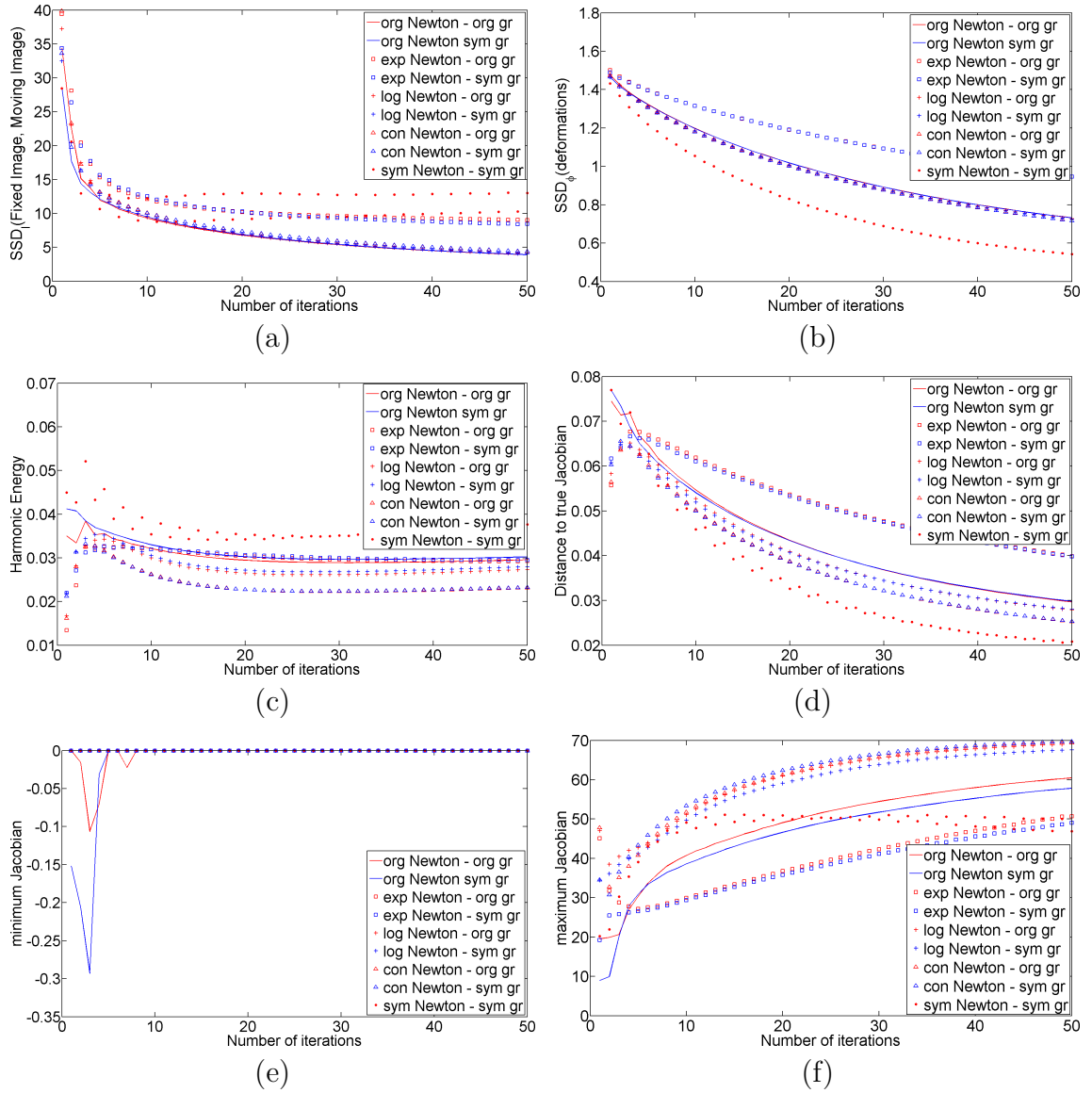


Figure 4.7: Results obtained for the simulated data set using different types of the Newton's iteration approach (Algorithm 2). The convergence studies are shown for: (a) the average of the  $SSD_I$  between images, (b) the average of the  $SSD_{\bar{\varphi}}$  between estimated deformation field and ground truth deformation field, (c) the average  $HE$ , (d) the average distance to the real Jacobian, (e) the minimum and (f) the maximum determinant of the Jacobian matrix of the estimated transformation.

### 4.3. QUALITATIVE AND QUANTITATIVE COMPARISON

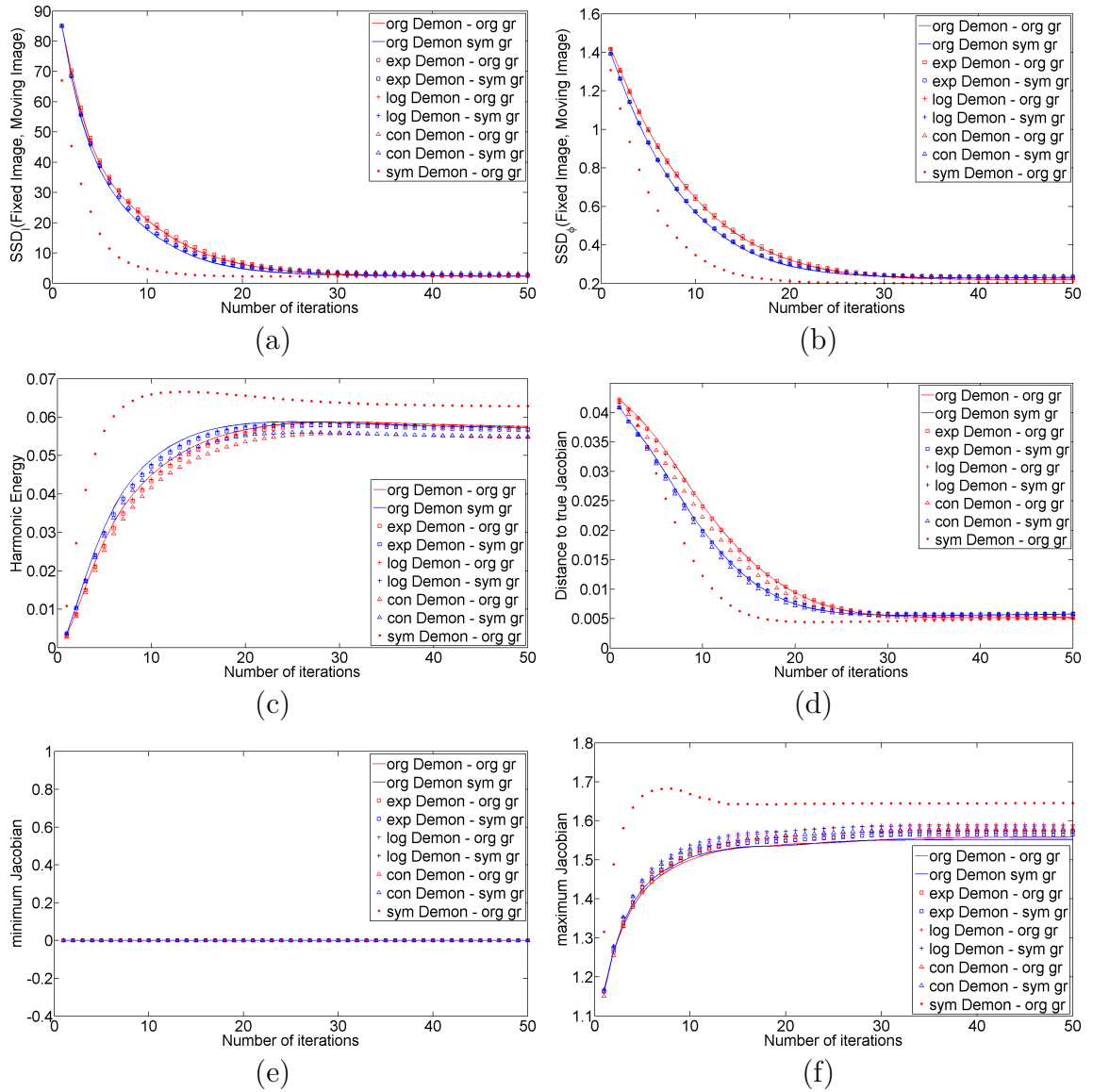


Figure 4.8: Results obtained for the simulated data set using different types of the Demon approach (Algorithm 3). The convergence studies are shown for: (a) the average of the  $SSD_I$  between images, (b) the average of the  $SSD_{\bar{\varphi}}$  between estimated deformation field and ground truth deformation field, (c) the average  $HE$ , (d) the average distance to the real Jacobian, (e) the minimum and (f) the maximum determinant of the Jacobian matrix of the estimated transformation.

parameterisation than in the case of the original versions.

To sum up, the outlined results suggest that the parameterisation of the displacement field via the stationary velocity field introduced either for the update of the deformation field or for the deformation field has minor impact on the overall performance of the presented image registration algorithms. The accomplished experiments show a slightly decreased accuracy for the segmentation using the estimated deformation fields, whereas the smoothness properties of these transformations that are desirable in the brain images analysis are remarkably improved.

#### **Pelvic-area MRI data**

The results obtained for the different formulations of the presented image registration methods using the MRI pelvic-area data set are shown in Figure 4.14 for the Demon approaches, in Figure 4.13 for the Newton's iteration methods and in Figure 4.12 for the steepest-like approaches.

From the perspective of the  $SSD_I$  between the registered images and the harmonic energy, the general behaviour the parameterised algorithms is similar as that from the evaluation performed on the MRI data of brain. The methods with the exponential update of the deformation field and the log-domain formulated methods produce slightly worse  $SSD_I$ . The most noticeable difference can be observed for the Newton's iteration method (Figure 4.13g) where the  $SSD_I$  calculated for the original formulation is about 8.0% better than in the case of the parameterised versions. Similarly, the harmonic energy decreases for all parameterised methods while this reduction for the Demon and the steepest-like approaches is negligible. However, the Newton's iteration method with the exponential update and its log-domain version can be characterised by the reduction of 15% when compared to the original method. In addition, the  $HE$  for the Newton's iteration method grows rapidly at the beginning of the registration process and then is minimised through execution of more iterations.

The values of the  $RO$  calculated for the prostate do not enlarge the impact of the parameterisation incorporated into the registration framework. The maximum difference between  $RO$  calculated for the prostate using the original method and the parameterised methods is notice for the Newton's iteration method and it is equal 0.75. Comparatively, the  $RO$  of bladder shows slightly more noticeable variability, but still the maximal difference between the original method and the parameterised method was found to be 1.8 in the case of the Demon approach, 3.0 for the Newton's iteration approach, and 1.4 for the steepest-like approach (all for the exponential update scheme).

Altogether, the conclusions that can be drawn for the MRI pelvic-area data are

### 4.3. QUALITATIVE AND QUANTITATIVE COMPARISON



Figure 4.9: Results obtained for the MRI brain data set using different types of the steepest-like approach (Algorithm 1). The average values of the  $RO$  for: (a) the original, (b) with exponential update, (c) the log-domain, (d) the inverse consistent, and for (e) the log-domain with symmetric warping. (f) The average  $RO$  for the different formulations after 100 iterations. The convergence of the average of: (g) the  $SSD_I$  between images, and (h) the  $HE$ .

### 4.3. QUALITATIVE AND QUANTITATIVE COMPARISON



Figure 4.10: Results obtained for the brain data set using different types of the Newton's iteration approach (Algorithm 2). The average values of the  $RO$  for: (a) the original (a), (b) with exponential update, (c) the log-domain, (d) the inverse consistent, and for (e) the log-domain with symmetric warping. (f) The average  $RO$  for the different formulations after 100 iterations. The convergence of the average of: (g) the  $SSD_I$  between images, and (h) the  $HE$ .

### 4.3. QUALITATIVE AND QUANTITATIVE COMPARISON



Figure 4.11: Results obtained for the brain data set using different types of the Demon approach (Algorithm 3). The average values of the  $RO$  for: (a) the original, (b) with exponential update, (c) the log-domain, (d) the inverse consistent, and for (e) the log-domain with symmetric warping. (f) The average  $RO$  for the different formulations after 100 iterations. The convergence of the average of: (g) the  $SSD_I$  between images, and (h) the  $HE$ .

similar to those for the MRI brain data. The stationary velocity field representation provides a versatile framework to estimate the transformations. Therefore, the accuracy in terms of the  $RO$  of the segmented structures is comparable to the original formulations optimising in the space of the displacement fields instead of the velocity fields, meanwhile the smoothness of the transformations indicated by the reduced  $HE$  is improved.

#### Lung CT data

The last set of experiments that were carried out to check the impact of the stationary velocity field representation, was using the CT lung data set. The obtained results are shown in Figure 4.17 for the Demon approaches, in Figure 4.16 for the Newton's iteration methods and in Figure 4.15 for the steepest-like approaches.

Similarly to all previous cases, the  $SSD_I$  between images and the harmonic energy shows corresponding patterns of the behaviour for the assessed parameterisation. After performing 100 iterations, the  $SSD_I$  stays at the similar level with the slightly worse results for the parameterised versions of the algorithms. The most noticeable difference is seen for the Newton's iteration approach, where the difference between  $SSD_I$  for the original version and the parametrised version is equal to 10.0% of the original  $SSD_I$ . In all other cases this difference is negligible.

The harmonic energy is reduced by 4.5% the Demon approach with the exponential update and by about 1.5% for the log-domain version. The reduction of the  $HE$  for the Newton's iteration approach is about 5.0% for the log-domain framework, while for the scheme with the update of the deformation field, the  $HE$  increased about 1.0%. The steepest-like approach implemented in the log-domain manner reduces the  $HE$  by 13.5% and with the exponential update by 12.5%.

The target registration error ( $TRE$ ) after 100 iterations for the Demon approaches with and without parameterisation is similar at  $1.87mm$ . The  $TRE$  for the original Newton's iteration approach and its log-domain version also stays at the same level of  $2.25mm$ , whereas the scheme with the exponential update produces significantly worse results of  $2.58mm$ . The  $TRE$  for the steepest-like approach differs between the original implementation and its parameterised versions but the difference is  $0.14mm$  for the log-domain framework, and  $0.07mm$  for the method with the exponential update scheme.

To sum up, the parameterisation of the deformation fields via stationary velocity fields is also robust for the estimation of the respiratory motion using the CT images. The only exception for this is the example of the Newton's iteration method with the exponential update that produces somehow unexpected result of the  $HE$  and the  $TRE$ . Although, it may indicate that this particular method is not suited well

### 4.3. QUALITATIVE AND QUANTITATIVE COMPARISON

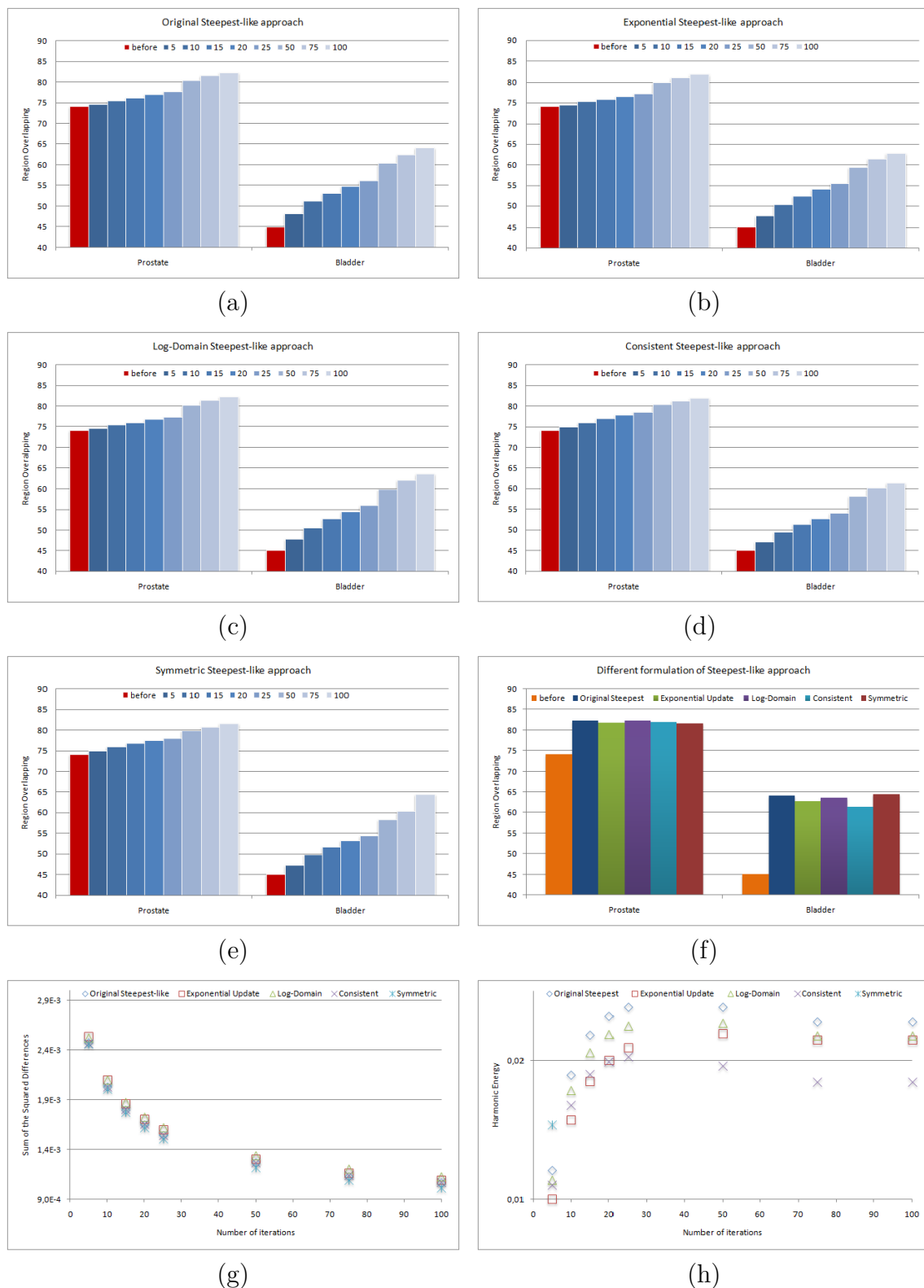


Figure 4.12: Results obtained for the MRI pelvic-area data set using different types of the steepest-like iteration approach (Algorithm 1). The average values of the  $RO$  for: (a) the original, (b) with exponential update, (c) the log-domain, (d) the inverse consistent, and for (e) the log-domain with symmetric warping. (f) The average  $RO$  for the different formulations after 100 iterations. The convergence of the average of: (g) the  $SSD_I$  between images, and (h) the  $HE$ .

### 4.3. QUALITATIVE AND QUANTITATIVE COMPARISON

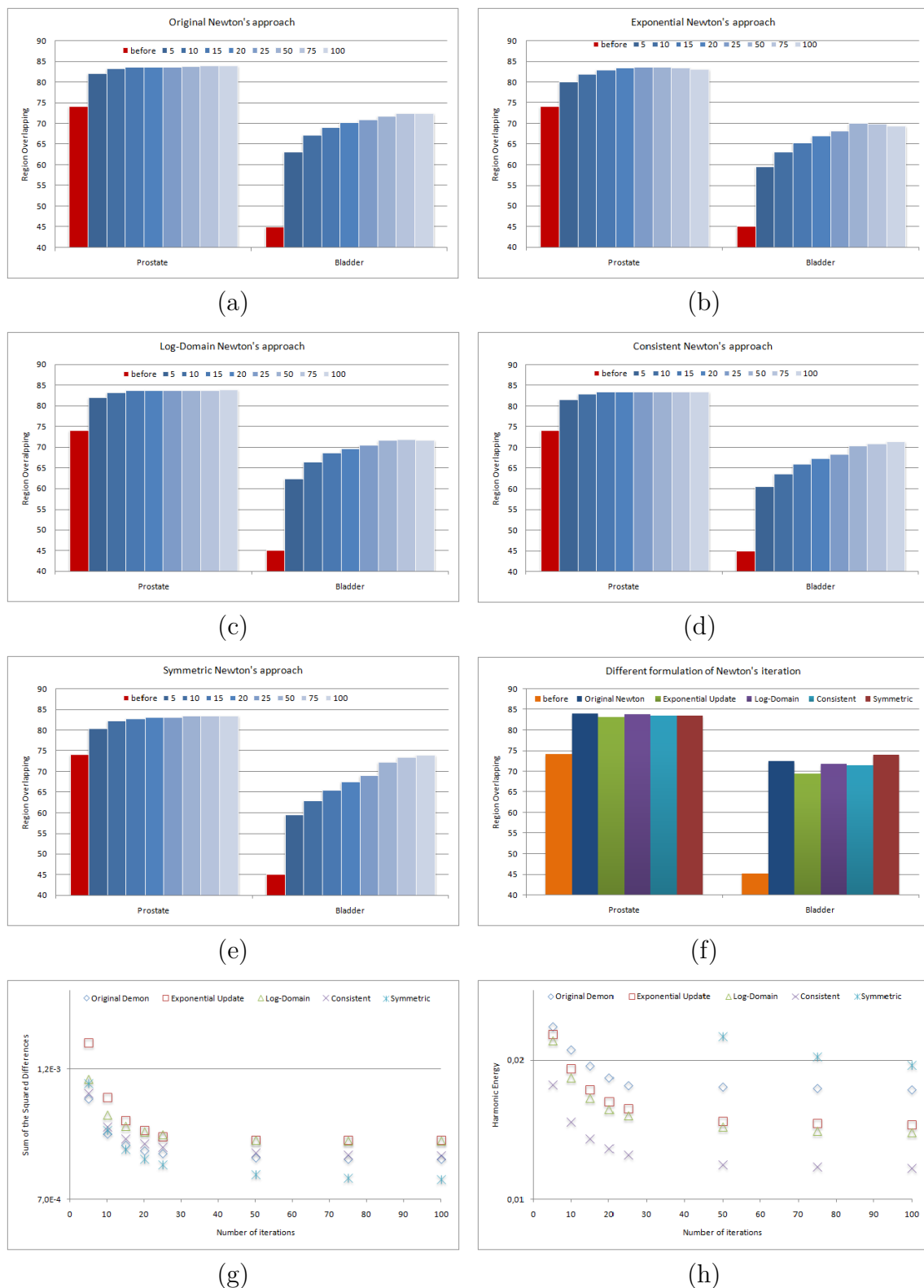


Figure 4.13: Results obtained for the MRI pelvic-area data set using different types of the Newton's iteration approach (Algorithm 2). The average values of the  $RO$  for: (a) the original, (b) with exponential update, (c) the log-domain, (d) the inverse consistent, and for (e) the log-domain with symmetric warping. (f) The average  $RO$  for the different formulations after 100 iterations. The convergence of the average of: (g) the  $SSD_I$  between images, and (h) the  $HE$ .

### 4.3. QUALITATIVE AND QUANTITATIVE COMPARISON

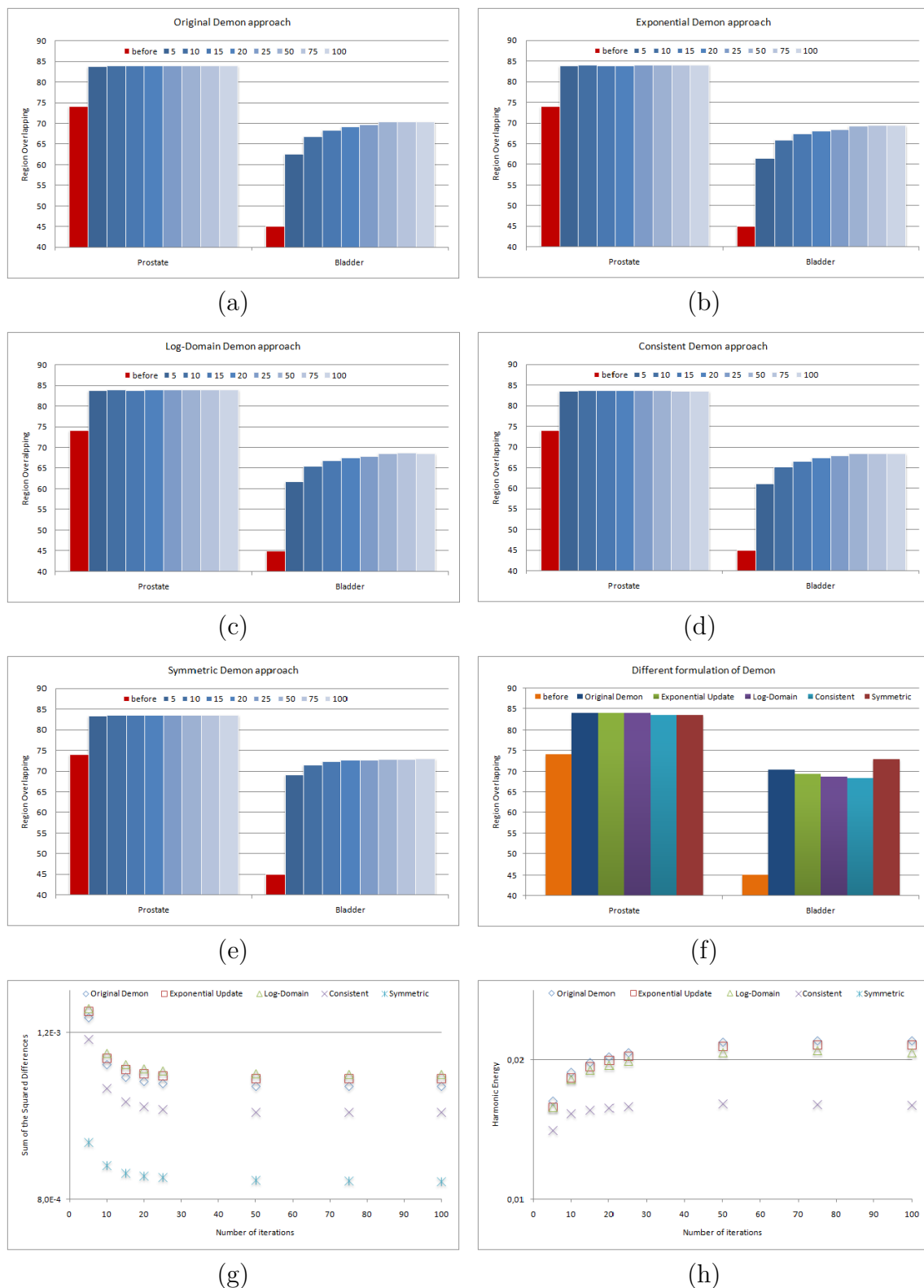


Figure 4.14: Results obtained for the MRI pelvic-area data set using different types of the Demon approach (Algorithm 3). The average values of the  $RO$  for: (a) the original, (b) with exponential update, (c) the log-domain, (d) the inverse consistent, and for (e) the log-domain with symmetric warping. (f) The average  $RO$  for the different formulations after 100 iterations. The convergence of the average of: (g) the  $SSD_I$  between images, and (h) the  $HE$ .

for this application, the  $TRE$  is consistent with the worst result of  $SSD_I$  calculated for the same method.

#### Observations on the stationary velocity field parameterisation

In general, the presented results suggest, that the parameterisation of the displacement field done either for the update of the deformation field or for the full deformation field as the log-domain framework, improve the estimated transformations in terms of the smoothness properties (here, quantified by the harmonic energy). In some cases the harmonic energy was reduced up to 15.0% (such examples include the Newton's iterations approach for the MRI of brain and pelvic-area). Although the values of the region overlapping for the segmented objects of interests are shown to be worse than those calculated utilising the original approaches, the differences are negligible in the majority cases due to the fact that the variance of the  $RO$ 's values can be introduced at the same level by the medical experts in data annotating process. Similarly, the target registration error between manually selected landmarks indicates good overall robustness of the parameterised algorithms.

#### 4.3.2 Impact of the inverse consistency criterion

This section presents the results of the experiments performed to check the impact on enforcing the inverse consistency criterion ( $ICC$ ) during the registration process. First, the results from the experiments evaluated in the controlled setup are shown. Then, the experimental results obtained for the different real data sets are presented and discussed.

##### Synthetic data

The most noticeable impact on enforcing the inverse consistency criterion is observed for the harmonic energy. The  $HE$  is reduced for all consistent methods when compared to other formulations.

Additionally, the consistent versions of the algorithms produce the deformation fields that have the determinant of the Jacobian similar to the true determinant of the Jacobian. In the same fashion, the consistent Newton's iteration and the consistent steepest-like method produce the deformation fields that are remarkable similar to the expected ground truth data (for the Demon approach this difference is negligible).

### 4.3. QUALITATIVE AND QUANTITATIVE COMPARISON

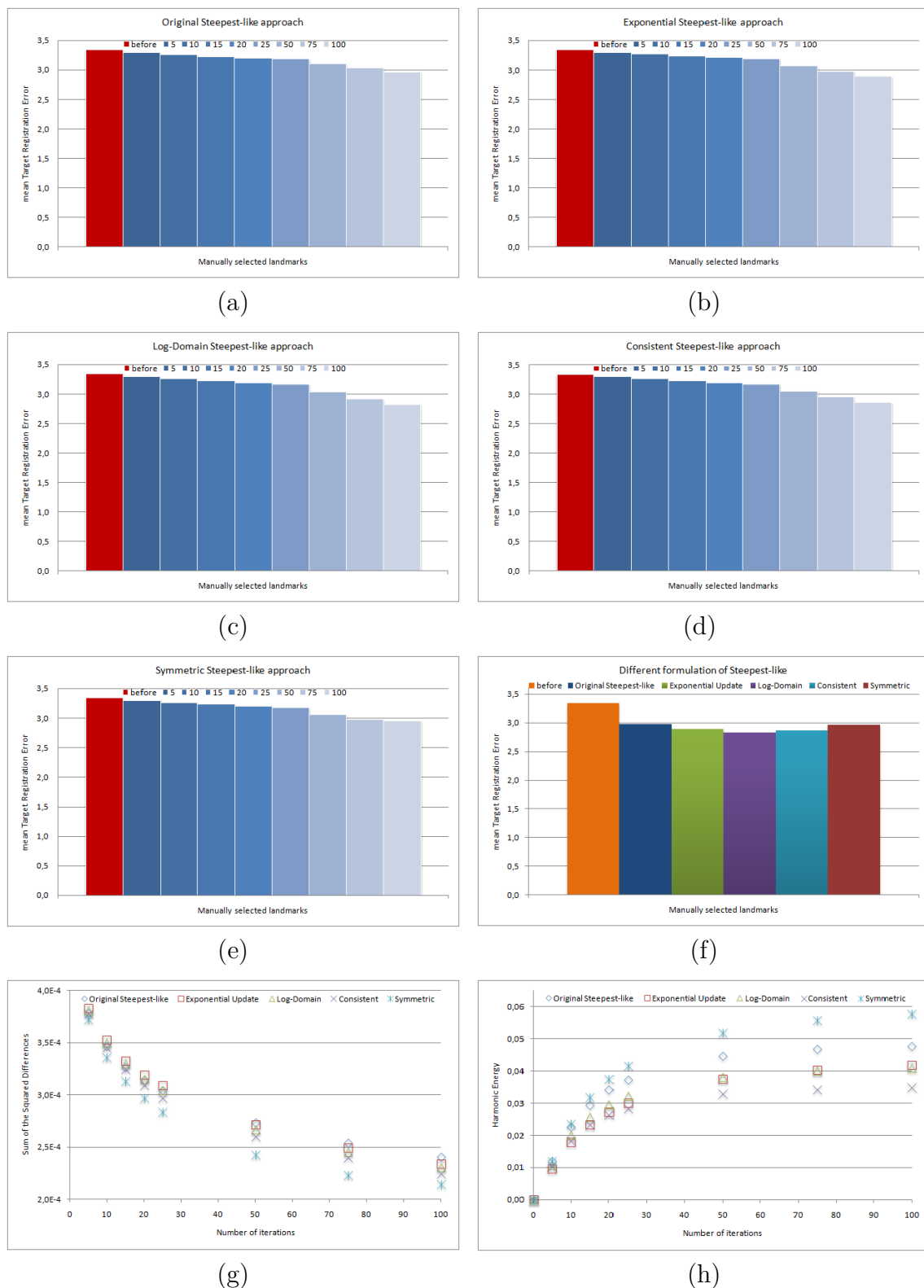


Figure 4.15: Results obtained for the CT lung data set using different types of the steepest-like approach (Algorithm 1). The average values of the  $TRE$  for: (a) the original, (b) with exponential update, (c) the log-domain, (d) the inverse consistent, and for (e) the log-domain with symmetric warping. (f) The average  $TRE$  for the different formulations after 100 iterations. The convergence of the average of: (g) the  $SSD_I$  between images, and (h) the  $HE$ .

### 4.3. QUALITATIVE AND QUANTITATIVE COMPARISON

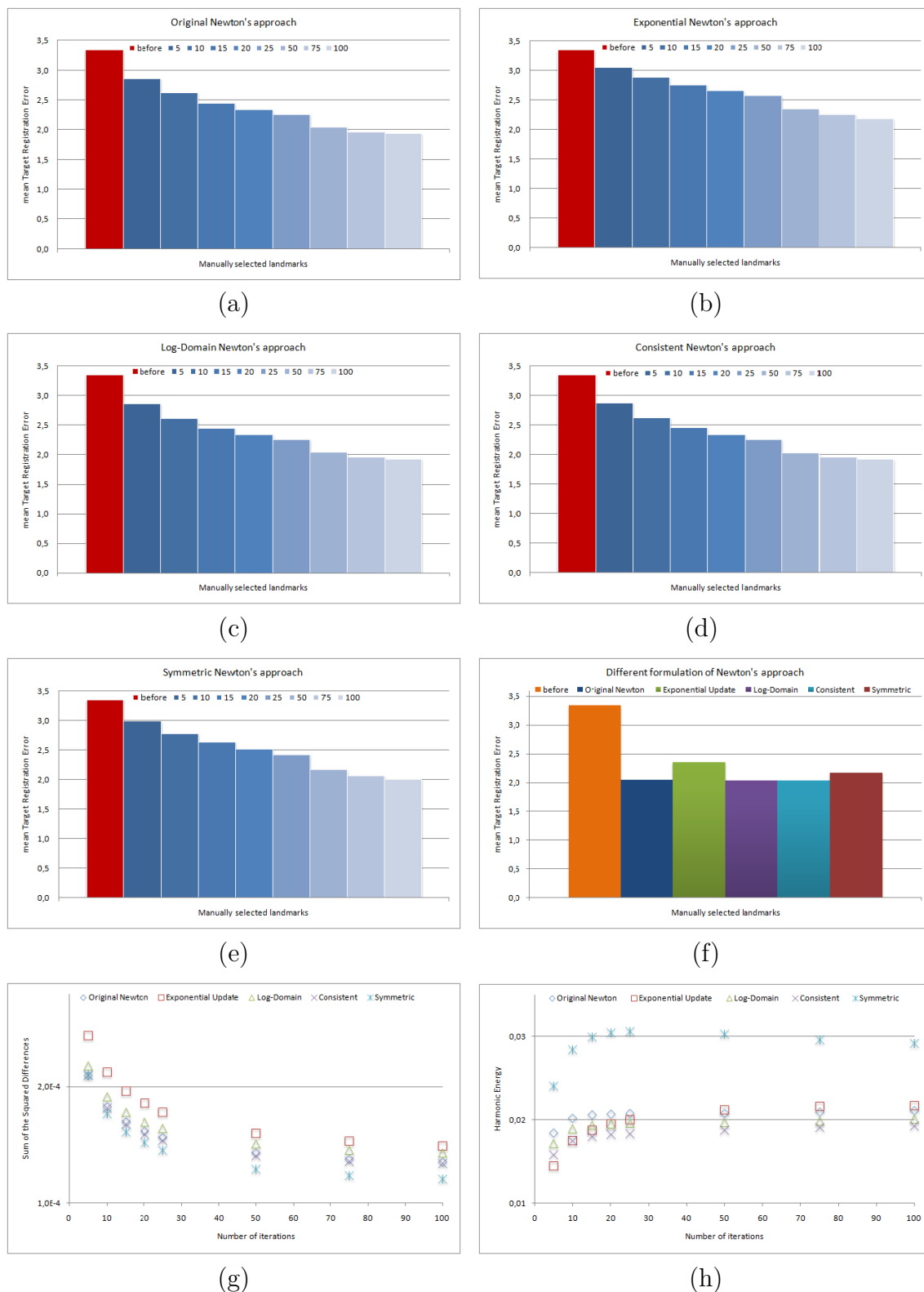


Figure 4.16: Results obtained for the CT lung data set using different types of the Newton's iteration approach (Algorithm 2). The average values of the  $TRE$  for: (a) the original, (b) with exponential update, (c) the log-domain, (d) the inverse consistent, and for (e) the log-domain with symmetric warping. (f) The average  $TRE$  for the different formulations after 100 iterations. The convergence of the average of: (g) the  $SSD_I$  between images, and (h) the  $HE$ .

### 4.3. QUALITATIVE AND QUANTITATIVE COMPARISON

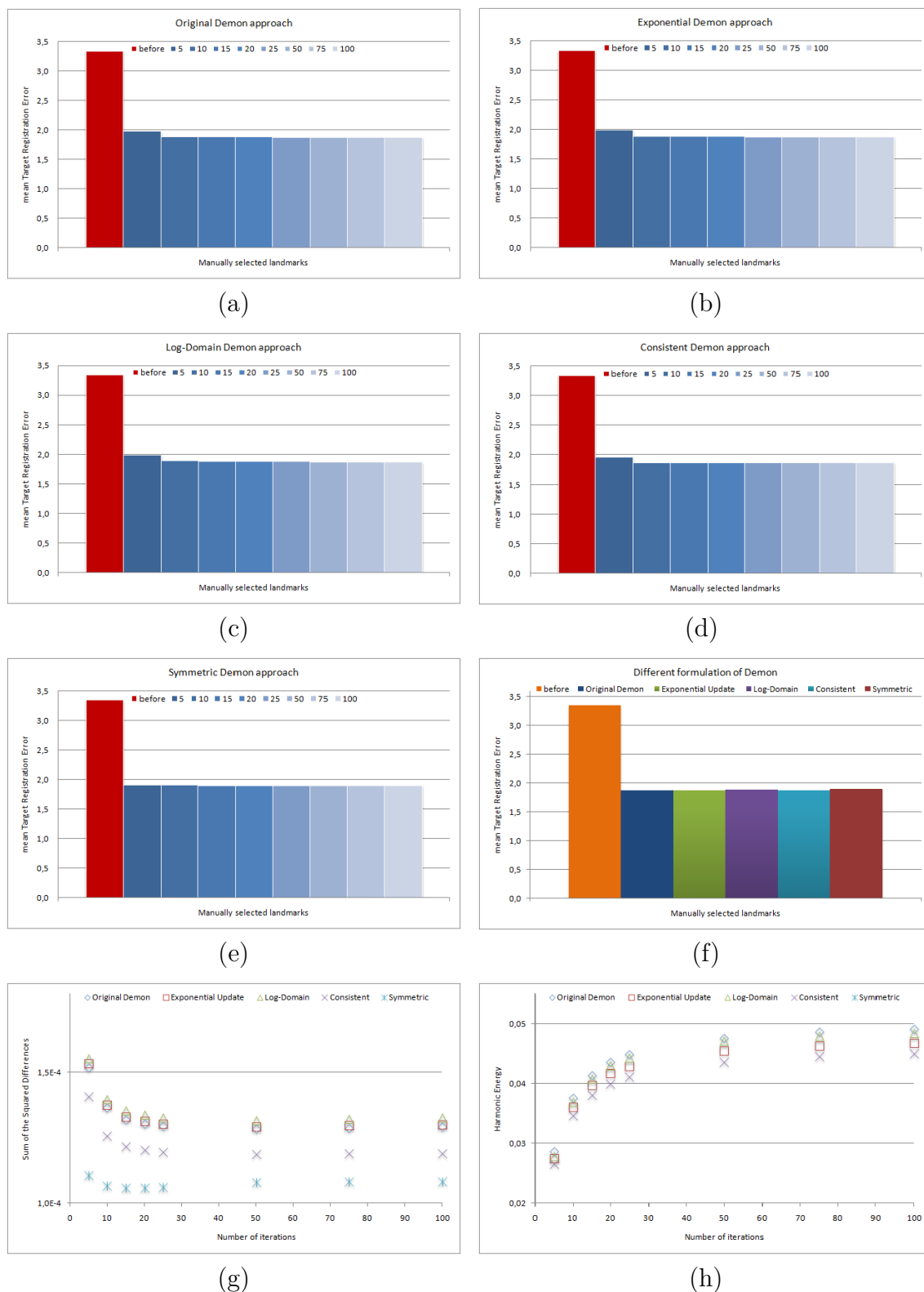


Figure 4.17: Results obtained for the CT lung data set using different types of the Demon approach (Algorithm 3). The average values of the  $TRE$  for: (a) the original, (b) with exponential update, (c) the log-domain, (d) the inverse consistent, and for (e) the log-domain with symmetric warping. (f) The average  $TRE$  for the different formulations after 100 iterations. The convergence of the average of: (g) the  $SSD_I$  between images, and (h) the  $HE$ .

#### Brain MRI data

The results of the carried out experiments are shown in Figure 4.11d for the consistent Demon approach, in Figure 4.10d for the consistent Newton’s iteration approach, and in Figure 4.9d for the consistent steepest-like approach.

The  $SSD_I$  between the registered images for all of the consistent image registration approaches is surprisingly small, about 1.0% worse than that for the original versions of the algorithms. This can be explained by looking deeply at the way of calculating the *forces* for the registration process. The gradient calculated for the consistent image registration is similar to the symmetric gradient that was previously reported as more efficient in the image registration [145].

The harmonic energy of the deformation fields estimated by the consistent image registration is always smaller than those produced by any other formulations of the image registration. For the Demon approach it is 8.5% better compared to the original Demon, 4.0% better compared to the Demon with exponential update, and 7.0% better compared to the log-domain Demon.

The  $HE$  of the consistent Newton’s iteration approach is characterised by about 30% reduction in comparison to the original approach. Furthermore, the  $HE$  is also better. Compared to the version with the exponential update and the log-domain, they are about 15.8% and 16.7% better. The consistent steepest-like method reduces the  $HE$  by 26.7% when compared to the original method, and 16.4% and 15.0% when compared to the approach with the exponential update and the log-domain version.

The segmentation accuracy assessed by calculating the  $RO$ s of the particular brain structure is on the average 0.4 worse than that for the original methods. For the structure of the skin and the dura mater, the values of the  $RO$  were slightly better for the consistent methods (except the consistent steepest-like method for the skin where the performance is similar). This may suggest, that the structure that are very thin and thereby very easy to be *lost* during the registration can potentially benefit from the consistent formulation of the image registration.

From the medically-driven application side, it can be concluded that the consistent image registration can provide very useful properties such as the significantly improved smoothness of the estimated deformation fields, at a very small cost of reduced  $SSD_I$  thereby increasing the accuracy of automatic labelling for some structures.

#### Pelvic-area data

The results of the experiments performed on the MRI pelvic-area data using the consistent image registration are shown in the following figures: Figure 4.14d shows

the results for the Demon approach, Figure 4.13d for the Newton’s iteration method, and Figure 4.12d for the steepest-like method.

The  $SSD_I$  achieved by the consistent Demon is about 5.7% better than the  $SSD_I$  achieved by the original Demon. For the Newton’s method and the steepest-like method the  $SSD_I$  achieved by the original versions is better than the  $SSD_I$  of the consistent approaches.

The harmonic energy is minimised significantly in all the approaches enforcing the consistency during the registration. The most noticeable reduction is observed for the consistent Newton’s iteration approach and it is 31.6% better compared to the original version. The consistent Demon and the consistent steepest-like approach reduce the  $HE$  21.5% and 19.0% with respect to their original versions. In addition, all of the presented consistent algorithms produce better  $HE$  than their diffeomorphic approaches using either the exponential update scheme or the log-domain formulation.

Finally, the results of the segmentation accuracy through the evaluating of the consistent image registration show the negligibly worst values of the  $RO$  for the prostate (worse less than 0.5). Similarly, the  $RO$  of bladder is also worse for the consistent approaches, but the maximum difference between the  $RO$  achieved using the original and the consistent version of the algorithm is equal to 4.2% for the steepest-like approach. For the Demon and the Newton’s iteration approach, the  $RO$  is worse about 2.7% and 1.6% respectively.

#### Lung CT data

The results of the assessment conducted on the CT of lung for the consistent image registration based on the Demon approach is shown in Figure 4.17d, on the Newton’s iteration approach in Figure 4.16d and on the steepest-like approach in Figure 4.15d.

The  $SSD_I$  achieved by the consistently formulated algorithms is better when compared to their original versions. For the consistent Demon and the steepest-like approach, the  $SSD_I$  is reduced by 7.8% and 6.8% respectively when compared to the original versions, whereas for the consistent Newton iteration method is almost similar to the original method.

The harmonic energy of the deformation fields produced the consistent Demon and Newton’s iteration approach is reduced by 8.5%, while for the steepest-like approach it is minimised more notably up to 26.8% when compared to the original versions.

The target registration error of the manually selected landmarks for the consistent Demon approach and the consistent Newton’s iteration approach stays at the same level of their original versions. For the consistent steepest-like method, the

$TRE$  is minimised to the level of  $2.87mm$  that is about 0.1 less than that of the original steepest-like method.

To sum up, the presented results strongly suggest, that the inverse consistency criterion has the minor impact on the respiratory motion estimation process using the CT volumes. Although, the  $SSD_I$  between registered images is minimised and the smoothness criterion is also reduced, the  $TRE$  does not change when compared to the other formulations.

#### Observations on the consistent image registration

Ensuring the inverse consistency criterion during the registration process has different impacts on the various data. In general, the consistent image registration framework produces better values of the  $SSD_I$  between registered images thereby it suggests better matching after registration. The improvement in terms of the  $SSD_I$  can be explained by comparing the gradients used for the image registration force calculation. The gradient for the consistent image registration is similar to the symmetric gradient that was reported in the literature as more efficient for the mono-modal registration [145]. Additionally, the registration with the inverse consistency criterion minimisation, estimates the deformation fields that are more smooth in terms of the  $HE$ . The reduction of the  $HE$  can be explained as a result of performing the embedded procedure of averaging the forward and the backward transformations to make them consistent. Both criteria the  $SSD_I$  and the  $HE$  are improved due to consistent registration, thus the results of either the segmentation accuracy or the target registration errors are expected to be improved as well. Thus far, the experimental evidence of this improved performance was found only in the case of some brain structures. These structures such as the skin or the dura mater, are very thin. The results achieved for the pelvic-area data or the lung data, may indicate that the motion to be estimated is somehow not consistent. The respiratory motion is not diffeomorphic in the principles due to the slipping effect on the lung boundaries [117]. On the other hand, the motion of the bladder is driven by the edges of this organ, while the motion of the bladder context is induced by the regularisation term, thus may not be adequate.

#### 4.3.3 Impact of the symmetrisation of registration

The third set of experiments consists of utilising the three methods implemented in the symmetric warping manner. Similar as the previous assessments, first the experiments were conducted with the synthetically generated data, then the different real data sets were used to quantify the performance of the aforementioned symmetric

algorithms in the particular biomedical applications. In general, the deformation fields estimated by utilising the image registration with the symmetric warping are more accurate in terms of the distance to the ground truth deformation fields. Also the distance to the true Jacobian is reduced (except the steepest-like method).

#### Synthetic data

The symmetrisation incorporated into the registration algorithms was found to provide many interesting observations when applied to the synthetic data.

Firstly, the image registration algorithms perform significantly better in terms of the  $SSD_I$  when compared to their original versions. The algorithms have also faster convergence for this criterion. The harmonic energy ( $HE$ ) of the image registration with the symmetric warping is always worse than in the case of the original registration techniques. It is mostly due to *double* forces that register images in two independent ways by providing more information into registration.

#### Brain MRI data

The results of the carried out experiments are shown in Figure 4.11e for the consistent Demon approach, in Figure 4.10e for the consistent Newton's iteration approach, and in Figure 4.9e for the consistent steepest-like approach.

The results obtained by the image registration with symmetric warping on the MRI brain images are characterised by the significant minimisation of the  $SSD_I$  between registered images. The  $SSD_I$  obtained by the symmetric Demon approach is 26.5% better than in that case of the original Demon, for the symmetric Newton's iteration and the symmetric steepest-like approach the  $SSD_I$  is reduced by 20.6% and 12.7% when compared to the original methods.

Contrary to the other assessed approaches, the image registration with symmetric warping increases the value of the harmonic energy. Thus, the  $HE$  for the symmetric Demon is twice worse than that of the original Demon approach. The  $HE$  for the symmetric version of the Newton's and the steepest-like method is increased by about 20% when compared to their original versions.

The image registration with symmetric warping increases on the average the values of the  $ROs$  for the brain structures up to 4.0 for the symmetric Demon, to 2.2 for the Newton's iteration method, and only about 1.1 for the symmetric steepest-like method when compared to their original versions. The best improvements are observed for the structure such as dura matter (17.2% for the Demon, 15.7% for the Newton's method, 11.3% for the steepest-like method), CSF (14.6% for the Demon, 8.8% for the Newton's method, 6.2% for the steepest-like method), white mater (12.8% for the Demon, 6.6% for the Newton's method, 3.1% for the steepest-like

method) and grey matter (10.7% for the Demon, 5.8% for the Newton's method, 3.6% for the steepest-like method). These structures (except dura mater) occupy the largest area of the brain.

The image registration with symmetric warping shows an improved performance in terms of automatic labelling of the brain structures, thereby it can be considered for the practical utilisation. Although the  $HE$  is significantly worse than that produced by any other approaches, the results suggest that it does not decrease overall robustness of the symmetric framework.

#### **Pelvic-area MRI data**

The results of the experiments performed on the MRI pelvic-area data using the image registration with symmetric warping are shown in the following figures: Figure 4.14e shows the results for the Demon approach, Figure 4.13e for the Newton's iteration method, and Figure 4.12e for the steepest-like method.

All the image registration algorithms with the symmetric warping reduce the  $SSD_I$ . The maximum reduction is gained by symmetric Demon approach and it is 21.3% better than that of the original version. For the symmetric Newton's iteration and the symmetric steepest-like method, the  $SSD_I$  is better by about 9.1% and 4.5%, respectively.

The harmonic energy is increased for all methods. For the symmetric Demon approach, the  $HE$  is twice worse than that of the original Demon. For the Newton's and the steepest-like method, the  $HE$  is worse only by 9.5% and 49.0%, respectively.

Although, there is a significant reduction of the  $SSD_I$  between registered images, the values of the  $RO$  for the prostate stays at the same level, while the  $RO$  for the bladder is better by only about 3.7%, 2.0% and 0.5% for the Demon, the Newton's iteration and the steepest-like method when compared to their original versions.

The presented results suggest that the benefits of using the symmetric warping approach for the MRI pelvic-area data is negligible.

#### **Lung CT data**

The results of the assessment conducted on the CT of lungs for the images registration with the warping based on the Demon approach is shown in Figure 4.17e, on the Newton's iteration approach in Figure 4.16e and on the steepest-like approach in Figure 4.15e.

Similar to the previous cases, the image registration algorithms with the symmetric warping, produces the significantly better  $SSD_I$  between registered images than that of the originally proposed methods. The  $SSD_I$  is better by about 16.3%,

10.7%, and 10.8% for the symmetric version of the Demon, the Newton's iteration and the steepest-like method.

Also the harmonic energy has similar patterns. The  $HE$  is twice worse for the symmetric Demon, whereas the symmetric Newton's iteration and the steepest-like method produce the deformation fields with the  $HE$  being 38.4% and 21.1% worse than that of the original methods.

The distances between the manually selected landmarks for the Demon method and the steepest-like method with symmetric warping stays at the same level as that of the original methods, while for the Newton's iteration method the  $TRE$  is slightly worse (the  $TRE$  is worse by about 0.1mm). The differences are not significant.

Altogether, the symmetrisation of the image registration does not have the practical advantages on the respiratory motion estimation. Although, the  $SSD_I$  between registered images is reduced, it does not lead to further improvement of the landmarks positions estimation.

#### Observations on the symmetrisation of the registration

The significant improvement of the image registration with symmetric warping in terms of the  $SSD_I$  is not surprising. Indeed, this registration takes the advantage of the *double* forces to warp the moving image to the *mean* image and simultaneously the reference image to the same *mean* image. In addition, the increased  $HE$  is somehow linked to this *double* forces by providing more deformation in every iteration. The final composition of two half-way velocity field (half-way deformation fields) has a minor impact on the final velocity field (deformation field) [17].

The presented results of the image registration with symmetric warping show symmetrisation improves the performance of the registration only in some cases. The experimental evidence was found for the MRI brain data set, where some structures were better labelled than those by utilising either the original or diffeomorphic algorithms. Further investigations on other data sets do not show similar improvement of the image registration in terms of the  $RO$  of prostate or the  $TRE$  between selected landmarks in the lungs. The results achieved for the pelvic-area do not confirm the statement from [53] where the symmetric image registration was claimed as having better performance than the log-domain registration. The presented results for the brain labelling are consistent with the results reported in [10], where registration with symmetric warping was shown as producing slightly better  $RO$ s of the different areas of brain.

#### 4.3.4 Comparison of different image registration methods

Last assessment was devoted to compare the presented algorithms in their original version. Thus, the conducted experiments show the positive and negative aspects of the aforementioned algorithms thereby enabling selection of the most appropriate in the particular applications.

##### Synthetic data

The results of the assessment of the algorithms evaluated on the synthetic data are shown in Figure 4.18.

The Newton's iteration approach offers the fastest convergence of the  $SSD_I$  between registered images. Only a few iterations are needed to be close to the final solution. Although the Demon approach is slightly slower in terms of minimising the  $SSD_I$ , it overtakes the Newton's iteration method after 18 iterations. The steepest-like approach is the worst of the assessed method with twice higher error in terms of the  $SSD_I$ .

On the other hand, when  $SSD_{\vec{\varphi}}$  between the estimated and the ground truth deformation fields are taken into account, the Demon performance is the best. The Demon algorithm estimates the most similar deformation field to the desired one. On the opposite, the deformation field estimated by the steepest-like method has an average error around 1.4 pixel size.

The harmonic energy ( $HE$ ) of the estimated deformation fields differs significantly between the presented methods. The smoothest transformations are estimated using the Newton's iteration approach. Due to quick convergence rate the Newton's iteration algorithm produces a worse value of the  $HE$  at the beginning and then through the registration process, the  $HE$  is reduced. The  $HE$  of the transformations estimated by the Demon approach is almost twice worse than that of the Newton's iteration approach. The reason of the significantly worse value of the  $HE$  for the Demon approach can be possibly explained by the manner of the regularisation incorporated into the method. The Gaussian filtering infers stronger the local deformation than the regularisation directly embedded in the registration process.

The fourth criterion of the assessment is the distance to the true Jacobian. The best performance was achieved by the Demon approach, whereas the steepest-like method performs the worst.

### 4.3. QUALITATIVE AND QUANTITATIVE COMPARISON

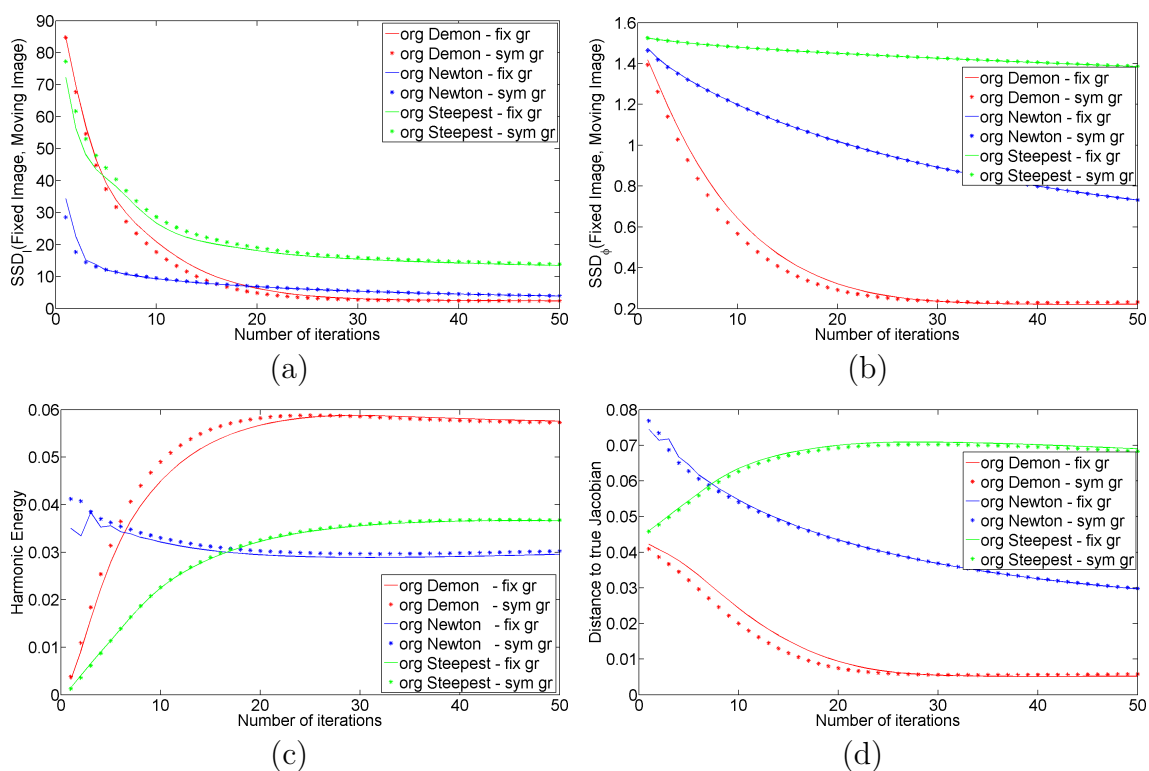


Figure 4.18: Results obtained for the synthetic data set using different approaches. The convergence of the average value of: (a) the  $SSD_I$  between images, (b) the  $SSD_{\hat{\varphi}}$  between the estimated transformation and the ground truth transformation, (c) the  $HE$ , and (d) the distance to the true Jacobian.

### 4.3. QUALITATIVE AND QUANTITATIVE COMPARISON

method	CSF	GM	WM	Fat	Muscle	Skin
Average Region Overlapping						
Demon	46.33	<b>61.79</b>	<b>61.20</b>	31.78	23.42	64.98
Newton	<b>46.51</b>	57.63	54.62	<b>41.37</b>	<b>24.32</b>	<b>66.83</b>
Steepest	42.55	54.36	51.37	37.81	22.82	65.49
Average Region Overlapping						
	Skull	Vessels	Around fat	Dura mater	Bone marrow	
Demon	49.03	<b>17.31</b>	7.28	<b>19.80</b>	<b>35.03</b>	
Newton	<b>49.69</b>	13.60	<b>8.96</b>	18.58	33.73	
Steepest	46.05	11.30	8.22	17.02	31.36	

Table 4.1: Average Region Overlapping values of the brain structures after 100 executed iterations for different image registration methods.

#### Brain MRI data

The results obtained for the brain images data set using different registration algorithms in their originally proposed version show in general, good overall robustness of the Demon and the Newton’s iteration approach. When  $SSD_I$  between registered images is considered as the criterion, the best alignment of images after 100 iterations is found by the Newton iteration method ( $SSD_I = 0.0024$ ), and it is followed by the Demon approach ( $SSD_I = 0.0027$ ). Although, the worse result is obtained for the steepest-like method ( $SSD_I = 0.0028$ ), Figure 4.9g shows a trend for this value to be minimised more iterations (reduction of  $SSD_I$  between 50 and 100 iterations is more than 12%). Contrary to this, the reduction of  $SSD_I$  between 50 and 100 iterations for the Demon and Newton’s iteration method (see in Figure 4.11g and Figure 4.10g) is negligible (less than 1%).

The smoother transformation in terms of the harmonic energy is estimated using the steepest-like method ( $HE=0.048$ ), while the worst value of  $HE$  is achieved by the Newton’s iteration method ( $HE=0.052$ ) and the Demon approach ( $HE=0.049$ ).

The methods in their original version were found to produce some transformations that do not preserve one-to-one correspondences. This was indicated by the negative determinant of the Jacobian of the estimated transformation. Correspondingly, the highest average values of the determinant of the Jacobian were obtained using the Newton’s iteration and steepest-like method (above 5.0). The highest average values of the determinant of the Jacobian calculated for transformations estimated by the Demon approach was 2.65.

Table 4.1 shows the best results of the region overlapping for the structures of brains for all evaluated methods. The results indicate that, there is no one best

method to achieve the best alignment of all brain structures.

The Newton's iteration method achieves better results in the *thin* areas with higher values of the images intensity gradients (can be considered as edges) such as skin, skull, fat (20% better than Demon) and areas around fat. The *RO* was better for the Demon approach for the larger structures such as grey matter (7% better than the Newton's iteration method) or white matter (about 10% better than the Newton's iteration method) and remaining structures: vessels (20% better than the Newton's iteration method), dura mater and bone marrow. The steepest-like method achieves the worst results in most cases. Although it is difficult to find any general conclusions, it is worth to mention, that the Newton's iteration method that achieves the lowest error in terms of the  $SSD_I$  between images, never provides the lowest region overlapping for any structure. Moreover, the high values of the maximum determinant of the Jacobian for the estimated transformations and the high value of the smoothness term may indicate good properties of local registration for small brain structures. On the other hand, the low values of the harmonic energy and the maximum determinant of the Jacobian for the estimated transformations may be well-suited for larger structures such grey matter (GM) or white matter (WM).

In terms of speed of calculations, it seems that increasing the number of executed iterations for the Demon and the Newton's iteration algorithms above 50 iterations, does not change significantly the results whereas the steepest-like method requires at least twice more iterations to achieve comparable values of the chosen criteria.

#### **Pelvic-area MRI data**

This section describes the results obtained for the assessment using the MRI pelvic-area data. Similar to the MRI data of brain, the best results in terms of the  $SSD_I$  between images used in registration was achieved by the Newton's iteration method ( $SSD_I=0.00085$ ). The  $SSD_I$  for the Demon and steepest-like method is on average about 0.00107 and 0.00106 respectively. When the convergence rate of reducing the  $SSD_I$  is taken into account, the Newton's iteration and the Demon method does not change it significantly after executing 50 iterations (the  $SSD_I$  is reduced by less than 1%), whereas the steepest-like method reduces the  $SSD_I$  about 22% from 0.00127 to 0.00106.

The harmonic energy is the worst for the steepest-like and the Demon method ( $HE=0.021$  for both method), while for the Newton's iteration approach it is 0.015. Furthermore, the notable difference is observed, that in the case of the Newton's iteration method, the  $HE$  grows rapidly during first few iteration (Figure 4.13f) and then is minimised gradually when more iterations of registration is performed.

method	Prostate	Bladder
	Average Region Overlapping	
Demon	<b>84.01</b>	70.37
Newton	83.95	<b>72.53</b>
Steepest	82.27	64.10

Table 4.2: Average Region Overlapping values of the pelvic-area structures after 100 executed iterations for different image registration methods.

Again, all methods produce transformations that have locally negative determinant of the Jacobian. The highest average value of the determinant of the Jacobian comes from the transformations estimated using the Newton’s iteration method (3.16), while for the Demon and the steepest-like method it is averaged at 2.18 and 3.0 respectively.

The average values of the region overlapping for the prostate and bladder are presented in Table 4.2. While, the differences between the results obtained for the prostate are negligible (the best for the Demon at 84.01, and the worst for the steepest-like method at 82.27), the  $RO$ s of the bladder are expressively different. The highest value was gained by the Newton’s iteration method ( $RO_{bl}=72.53$ ). The worst result was produced by the steepest-like method with  $RO_{bl}=64.1$  (it is about 11% less than that for the Newton’s iteration method, and about 9% less than that for the Demon method).

In terms of speed of calculations, it seems that increasing the number of executed iterations for the Demon and the Newton algorithms above 75 iterations, does not change significantly the results whereas the steepest-like method requires at least twice more iterations to achieve comparable values of the chosen criteria.

#### Lung CT data

The results of the CT lung comparison show that the Demon method achieves the best value of the  $SSD_I$  between registered images ( $SSD_I$  for the Demon approach is  $129.0 \cdot 10^{-3}$ ). For the Newton’s iteration method the  $SSD_I$  is slightly worse and it is  $135.0 \cdot 10^{-3}$ , whereas for the steepest-like method it is almost twice worse ( $SSD_I=241.0 \cdot 10^{-3}$ ).

The harmonic energy is similar for the Demon and the steepest-like approach (for the Demon it is 0.049, while for the steepest-like it is 0.048). The deformation fields estimated by the Newton’s iteration method have twice better value and it is 0.021.

The results in terms of the  $SSD_I$  somehow can be linked to the target registration

error, where the Demon algorithm achieves the best performance with the result equal to  $1.87mm$ . The second method is the Newton's iteration approach (also the second one in terms of the  $SSD_I$ ) that produces the  $TRE$  at the level of  $1.94mm$ . The worst performance is from the steepest-like method and the  $TRE$  is equal to  $2.97mm$ .

#### Observations

The presented results give a clear conclusion that the estimated transformations and their characteristics are strongly dependent on the input data.

The assessment using the simulated data with already known ground truth deformation fields, suggests that the Demon approach is the most robust method. The Demon approach achieves the best value of the  $SSD_I$  between registered images, the deformation fields estimated using this technique were the closest to the ground truth data, and has the shortest distance to the true Jacobian. The Newton's iteration approach was the quickest in convergence at the beginning in terms of the  $SSD_I$ . Other properties of the deformation fields estimated by the Newton's iteration method were worse when compared to the Demon method, but it has better performance than the steepest-like method.

The results achieved by the Newton's iteration method suggest that this method performs better when the higher contrast data are to be registered such as MRI of brains or MRI of pelvic-area organs utilised in this chapter. Whereas for the data of lower quality such as CT of lungs, the results were slightly worse than those produced by the Demon approach.

The results of the CT of lungs assessment are somehow consistent with the results presented in other papers in comparison of the Demon method with the Newton's iteration method [21]. On the other hand, the results are opposite to the results presented in [78], where the Newton's iteration method was originally introduced. The conclusion there suggested that the Newton's iteration method performs better in the radiotherapy applications when CT images are used.

The methods presented in [141, 43] produce the smaller  $TRE$  between manually selected landmarks when compared with the results presented in this chapter. This can be explained by looking deeper into the methods proposed in these papers. First, evaluation done by Vandemeulebroucke et al. [141] used the approach that is specifically designed to register images coming from the respiratory cycles [116] thereby the method is strictly application-oriented, thus performs better for this particular data set. The results presented in [116] shows that the proposed registration method reduces distances between manually selected landmarks twice better than that of the original Demon method. Secondly, the framework proposed in [43]

uses not only the intensity information (involved in the similarity measure  $Sim$ ) but additionally incorporates the knowledge from the provided landmarks into the registration process. Therefore, the registration described there, can benefit from support of the landmarks as from *a priori* knowledge to produce more accurate results.

#### 4.3.5 Remarks on determining design parameters

##### Computational cost of the iteration

The results presented in the previous sections indicate that all presented methods have different convergence rates thus the number of the iterations needed to estimate the final transformation varies between them. Additionally, the presented methods have also different computational effort related directly to the manner of calculating the registration *forces*. In order to get the measures showing the differences in time between these methods, the presented methods and their different formulations were assessed also with respect to their computational cost. Each algorithm was run with two-dimensional simulated data with fixed number of iteration without multi-resolution implementation. The number of iteration was chosen to be equal to 5000. The cost of one iteration of the original Demon was selected as the reference time unit, and all other times were normalised with respect to this unit. The results of this experiment is summarised in Table 4.3. The steepest-like approach is the fastest algorithm whereas the Demon algorithm is the slowest approach. The reason that the Demon algorithm is more than twice slower than the other two can be explained by the way of introduced regularisation. Although, all methods calculate the force that updates the deformation field, in the Demon algorithm, the additional procedure of the Gaussian smoothing has to applied either for the update of the deformation field, or to the deformation field, or to both of them.

The methods parameterised with the stationary velocity field either for the update of the deformation field or the deformation field require at least twice more time than the original methods. The increased time is due to calculating the exponential mapping using the scale and squaring algorithm. The approaches utilising the consistency criterion and the symmetrisation of the flow are the slowest due to calculations of two gradients: gradient of the reference image and the gradient of the warped moving image for the consistent image registration, or gradients of warped input images as in the case of the image registration with symmetric warping.

method	Demon	Newton	Steepest
original	1.00	0.46	0.44
exponential	2.42	1.92	1.91
log-domain	2.26	1.74	1.37
consistent	4.11	3.34	3.23
symmetric	4.22	3.50	3.38

Table 4.3: Experimental results of the computational effort for the presented method. The results are given with respect to computational cost of one Demon iteration.

### 4.3.6 Validation of inverse deformation field estimation

This section presents the comparison results of the inverse deformation field methods. The method for inverting the deformation field are essential for some classes of the consistent image registration [27, 63] and the image registration with symmetric warping [155, 96].

Validation of the inverse deformation field estimation methods is conducted using the spatial deformation field calculated during the symmetric image registration. The results of this registration towards the intermediate image  $I_h$ :  $\vec{\varphi}_{hb}$  and  $\vec{\varphi}_{hf}$  are used as an input data for the methods inverting the deformation field. In the experiments the Christensen’s (section 3.4.2, [27]), the proposed (section 3.4.2), and Ashburner’s [7] methods were tested. For the Christensen’s and the proposed methods the iterations are terminated when they reach either the maximum iterations number of 1000 or the desired distance threshold value of 0.001. For the proposed method, parameter  $\rho$  (in Equation 3.67) was chosen to make the minimum value of  $\det(J(\vec{f}(\vec{x})))$  greater than 0.1. For the Ashburner’s method [7], its implementation from the SPM library [41] was used in the experiments.

For the synthetic data, Figure 4.19 shows that the inverse deformation field produced by the proposed method (Figure 4.19f) is much smoother than that produced by the Christensen’s method (Figure 4.19b), especially in the area where the Jacobian determinant has large values (Figure 4.19e). In terms of the  $ICE$  values shown in Figure 4.19c-d,g-h, although both methods have the maximum  $ICE$  value around the middle of the image, the  $ICE$  maximum value produced by the Christensen’s method is significantly higher. Furthermore, the mean value of  $ICE$  and the maximum value of  $maxICE$ , both calculated from all the pixel locations, computed based on  $\vec{\varphi}_{hb}/\vec{\varphi}_{hb}^{-1}$ , and  $\vec{\varphi}_{hf}/\vec{\varphi}_{hf}^{-1}$  are also listed in the first rows of Table 4.4, where both the mean  $ICE$  and maximum  $maxICE$  values for the Christensen’s method are seen to be higher.

For the MRI volumetric images, the data set consist of five volumes, and image

Inverse consistency error				
		$\vec{\varphi}_{hb}$ and $\vec{\varphi}_{hb}^{-1}$		$max$
	Christensen	Ashburner	proposed method	$det(J)$
(2D) Fig.	0.210 (38.5)	-	0.158 (28.9)	2.1
(3D) Set 2	0.015 (0.65)	0.134 (4.67)	0.015 (0.65)	4.9
(3D) Set 3	0.016 (0.52)	0.150 (3.75)	0.015 (0.51)	5.9
(3D) Set 4	0.017 (2.56)	0.186 (5.45)	0.016 (0.76)	8.4
(3D) Set 5	0.021 (6.64)	0.261 (12.0)	0.020 (1.11)	12.0

		$\vec{\varphi}_{hf}$ and $\vec{\varphi}_{hf}^{-1}$		$max$
	Christensen	Ashburner	proposed method	$det(J)$
(2D) Fig.	0.736 (49.0)	-	0.004 (0.89)	14.9
(3D) Set 2	0.015 (0.49)	0.131 (4.76)	0.015 (0.49)	4.7
(3D) Set 3	0.016 (0.83)	0.147 (5.78)	0.016 (0.83)	4.3
(3D) Set 4	0.017 (1.10)	0.197 (10.3)	0.017 (1.09)	5.5
(3D) Set 5	0.021 (3.62)	0.296 (16.4)	0.021 (1.67)	8.0

Table 4.4: Comparison results for inverse deformation field estimation algorithms. The mean of  $ICE$ , maximum of  $maxICE$  (in brackets), and maximum of  $det(J)$  are shown for each algorithm and each test data. Both 2D synthetic data and real 3D MRI data, showing pelvic region, were used in the experiments.

registration was performed with respect to the first volume. The results of the  $ICE$  values produced by the two commonly used methods [27, 7] and the proposed method are tabulated in Table 4.4. From Table 4.4, it is seen that the maximum value in the Jacobian determinant is increasing from set 2 to set 5 which correspond to increasing organ shape changes between the images. In terms of performance, Ashburner’s method is seen to be the worst with highest average and maximum  $ICE$  values, the proposed method is seen to be the best with similar average and maximum  $ICE$  values as those from Christensen’s method for small organ shape deformation, and smallest average and maximum  $ICE$  values for the largest organ shape deformation.

## 4.4 Summary

This chapter focused on presentation and discussion of the assessments results of registration methods with the comprehensive list of utilised optimisation algorithms, deformation field parameterisations and image registration formulations, introduced and proposed in Chapter 3.

In term of the image registration optimisation, algorithms such as the Demon approach, the Newton’s iteration method, and the steepest-like method were evalu-

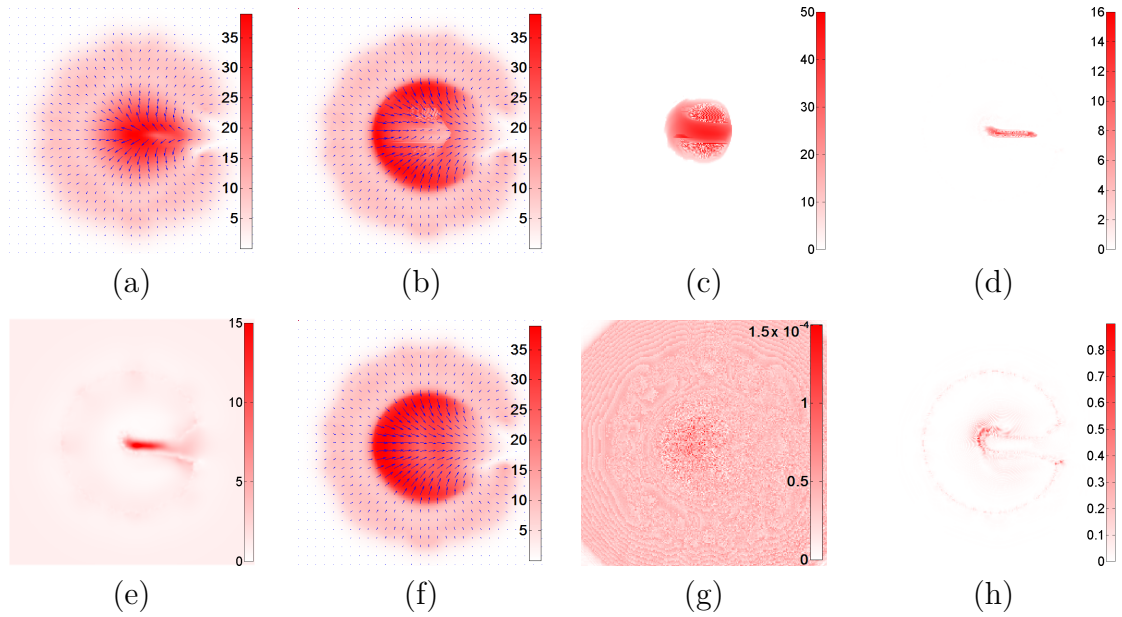


Figure 4.19: Results of evaluation the inverting methods for the synthetic data: (a) input deformation field, (b) inverse deformation field estimated using [27], (c)  $ICE$  for  $\vec{\varphi}_{hf} \circ \vec{\varphi}_{hf}^{-1}$  and (d)  $ICE$  for  $\vec{\varphi}_{hf}^{-1} \circ \vec{\varphi}_{hf}$  using [27], (e) Jacobian of the input transformation, (f) inverse deformation field estimated using the proposed method, (g)  $ICE$  for  $\vec{\varphi}_{hf} \circ \vec{\varphi}_{hf}^{-1}$  and (h)  $ICE$  for  $\vec{\varphi}_{hf}^{-1} \circ \vec{\varphi}_{hf}$  using the proposed method.

ated. The obtained results suggest that the best performance was achieved by the Demon and Newton’s iteration methods. In all cases, the steepest descent method was the worst.

Moreover, various formulations of the image registration were assessed in terms of the properties of estimated deformations fields and their usefulness in several practical applications such as brain structures labelling, pelvic-area organs and respiratory cycle motion estimation. These formulations include the original version of the image registration algorithms, and the formulations ensuring the diffeomorphism either by the exponential update or by the log-domain parameterisation. These different diffeomorphic formulations are shown to be versatile methods in the investigated applications. The different parameterisations of the displacement field have been found to have minor impact on the overall performance of the presented image registration algorithms. Although, the accomplished experiments show a slightly decreased accuracy for the segmentation using the estimated deformation fields, the smoothness properties of these transformations that are desirable in some applications (e.g. the brain images labelling) are remarkably improved.

The obtained results show also that the consistent image registration algorithms are somehow the best choice for the used data sets. They offer the good performance in terms of the  $RO$  for the segmented structures (or the  $TRE$  in the case of the

manually selected landmarks assessment) that is only slightly worse than in the case of the original versions and furthermore for some specific structures better than for the original versions e.g. skin and dura mater. Although, the smoothness properties of the estimated deformation fields are improved, these have been expected from the way how the consistent image registration is defined by introduction of the additional averaging procedure of the forward and the backward transformations.

Finally the image registration with symmetric warping of the input images was assessed. The results obtained for brain data set labelling indicate improved performance of terms of the *RO*. Other applications investigated in this chapter do not benefit significantly from the symmetrisation of image registration.

This chapter also presented results for the assessment of a new method for estimation of the inverse deformation field proposed in Chapter 3.4.2. Using the maximum value of the Jacobian determinant,  $\max(\det(J))$ , as an indicator of the level of deformation, the performance of the Christensen's method is seen to deteriorate strongly with  $\max(\det(J))$  exceeding 6, whereas the proposed method is able to handle large deformation with  $\max(\det(J))$  significantly greater than 6.

All in all, the presented results show advantage of using diffeomorphic approaches established in the consistent framework. In addition, a minor impact of the stationary velocity field parameterisation was found when the quantitative measures were evaluated.

# Chapter 5

## Group-wise image registration

This chapter describes an implicit reference group-wise image registration that jointly estimates the correspondences between a group (set) of images/volumes taken from different subjects. It can be seen as an extension to the pairwise image registration with symmetric warping described in Section 3.4. By simultaneous indirect estimation of transformations between images from a set to the *hidden* group average, firstly, the bias associated with the reference image chosen is alleviated, and secondly the *mean* intensity image is generated (an intensity atlas). Due to the adapted log-domain parameterisation of the deformation fields, the presented log-domain implicit reference group-wise image registration produces the set of the diffeomorphic transformations, that can be further used for vectorial statistical analysis of the between-subject variability.

In this chapter a brief overview of the inter-subject spatial normalisation is first presented to show the importance of the group-wise image registration techniques in the different areas of biomedical image analysis (Section 5.1). Then, the concept of the implicit reference group-wise image registration framework is introduced and its log-domain parameterised version is proposed (Section 5.2). Section 5.3 presents optimisation schemes to solve the mentioned group-wise registration problem. Finally, in Section 5.4 two annotated data sets (MRI images of pelvic area and brain) were used to evaluate the performance of the proposed framework.

### 5.1 Introduction

The pairwise image registration techniques were described as approaches that enable the establishment of the correspondences between the reference image and the moving image, while the group-wise image registration algorithms aim at spatial normalisation among groups (sets) of images (not necessarily belonging to the same subject). Thus, a wide variety of group-wise image registration approaches have been

studied in recent years that have been addressing the most important objectives of medical image analysis. From several of the recently investigated applications, the increasing number of works has been particularly undertaken in specific areas including brain analysis based on structural and functional images [42], brain atlas formation [46, 9, 132, 28, 153], building shape models of the brain [33, 113, 114], building motion models of the myocardium [22] and organs in the pelvic-area [125], and longitudinal tracking of disease progression [66, 67].

Historically, the first attempt of the spatial normalisation sets of images was done utilising the pairwise registration with the reference image selected entirely. In the simplest case, one image from this group can be chosen as a reference image and the remaining images are registered to it by multiple evaluation of the pairwise image registration. In [125], patient-specific inter-fractional abdomen organs and adjacent organs' deformations were modelled utilising results obtained from multiple registration of several CTs taken during the treatment to the CT used for planning. In a similar fashion, when a patient disease record is represented by a time series of images that was taken over his/her longitudinal progression of disease, the within-subject anatomical changes over this time can be straightway addressed [66, 67]. Although of the simplicity of these approaches, they were highly limited to between-subject registration due to the bias introduced by the selection of the reference image. In addition, choosing the outlying reference image can lead to generating the common image space (given by a selected image), that is not adequate to the group of images.

To overcome the aforementioned problems related to the group-wise registration with the selected reference image, methods with an iterative updating manner of the selected reference image were proposed [46, 64, 28]. The approach proposed by Guimond et al. [46] produces first the intensity average of images obtained from pairwise image registration to the chosen reference image, and afterwards warp this average by the average of the deformation fields in order to generate the *mean* image (and therefore, the common image space). Some kind of simplification of the method mentioned above has been proposed by Christensen et al. [28] where only the selected reference image is updated by the transformations average to synthesise the *mean* image. Regardless of the updating process, the selection of the reference image is still noticeable. In the method proposed by Joshi et al. [64], the reference image is constructed iteratively by averaging intensity of group of images, using the transformation estimated from registration of the images to the temporary available average. Although, the main issue with the reference image selection is solved in this approach, the method itself has some drawbacks. Its main limitation is the averaging procedure, which gives very fuzzy average image especially at the beginning of the

registration. This may lead to several difficulties such as slow convergence of the group-wise registration, degeneration of the anatomical details, and the problem with establishing reliable correspondences between sharp images and the blurred average image (detailed discussion is presented in [153]).

To state the group-wise image registration from another perspective, the definition of the group-wise image registration can be linked to the symmetric pairwise image registration, where a *mean* of two images is somehow generated as an additional result of the minimisation of the similarity criterion between the input images with an additional regularisation term (presented in Section 3.4). Indeed, this *mean* image can be then seen as a reference image for the *common image space* of two input images, due to finding the correspondences between the input images and this *mean*, and eliminating of the bias according to the reference image selection. In the similar manner, minimisation of the similarity measure between each pair of images in the given sets, leads to the simultaneous estimation of multiple transformations mapping each image to a hidden (implicit) common reference image. The methodology, in which selection of the reference image is entirely omitted, provides superior transformations in terms of the within-group variance after registration, and avoids the bias associated with the reference image chosen [42]. Methods that utilised the framework described above can assume either a large deformation model [64], or a small deformation linear elastic model [42]. Meanwhile, in most cases the linear average of deformations is calculated. However, it was shown in [9], that linear averaging of the deformation fields does not necessary preserve the large deformation model, and should be replaced by the geodesic averaging.

In this chapter, the log-domain parameterisation of the deformation fields will be considered using the optimisation frameworks discussed in Section 3.1. This parameterisation tackles the problem of the average calculation via the principal logarithm of the diffeomorphic deformation fields and allows the Euclidean operations to be performed on them. Furthermore, the log-domain parameterisation ensures that the estimated transformations maintain the one-to-one mappings properties.

## 5.2 Log-domain group-wise registration

During this chapter, the group-wise image registration will be considered for the given set (group) of the input images  $\mathbf{I}$  denoted by:

$$\mathbf{I} = \{I_k : \Omega \rightarrow \mathbb{R}, \Omega \subset \mathbb{R}^d, k = 1, \dots, K\} \quad (5.1)$$

where:  $d$  denotes a spatial dimension of image and  $K$  is the number of images in the group. Having the set of images  $\mathbf{I}$ , the main aim of the deformable group-wise image registration is to estimate the optimal, in some sense, set of transformations  $\tilde{\varphi}^{\text{opt}}$ :

$$\tilde{\varphi}^{\text{opt}} = \{\tilde{\varphi}_k^{\text{opt}} : \Omega \rightarrow \mathbb{R}^d, \Omega \subset \mathbb{R}^d, k = 1, \dots, K\} \quad (5.2)$$

warping the images taken from  $\mathbf{I}$  to a common space image  $I^{\text{com}}$ :

$$I^{\text{com}} \approx I_k \circ \tilde{\varphi}_k = I_k(\tilde{\varphi}_k) \quad (5.3)$$

In general, the problem of finding a set of the optimal displacement fields  $\tilde{\mathbf{u}}^{\text{opt}}$  can be formulated as an optimisation problem:

$$\tilde{\mathbf{u}}^{\text{opt}} = \arg \min_{\tilde{\mathbf{u}}} \varepsilon(\tilde{\mathbf{u}}; \mathbf{I}) \quad (5.4)$$

When  $I^{\text{com}}$  is entirely given either by the selection of one image from the given group [46, 28] or via the intensity average calculation of all images in the set [64], the process of estimating the set of transformations is called the reference-based group-wise registration and the objective function  $\varepsilon(\tilde{\mathbf{u}})$  can be defined as:

$$\varepsilon(\tilde{\mathbf{u}}) = \sum_{k=1} \int_{\Omega} \text{Sim}(I^{\text{com}}(\vec{x}), I_k(\vec{x} + \vec{u}_k(\vec{x}))) dx + \alpha \sum_{k=1} \int_{\Omega} \text{Reg}(\vec{u}_k(\vec{x})) dx \quad (5.5)$$

Similarly, the implicit reference group-wise image registration problem [42] can be stated as an estimation of the set of the transformations from each image  $I_k$  in the group  $\mathbf{I}$  to an unknown common space image  $I^{\text{com}}$ . Thereby the estimation is considered as minimising the sum of the similarity measures and the regularisation terms between each pair of deformed images as follows:

$$\begin{aligned} \varepsilon(\tilde{\mathbf{u}}) = \sum_{k=1} \sum_{\substack{l=1 \\ k \neq l}} \int_{\Omega} \text{Sim}(I_k(\vec{x} + \vec{u}_k(\vec{x})), I_l(\vec{x} + \vec{u}_l(\vec{x}))) dx \\ + \alpha \sum_{k=1} \int_{\Omega} \text{Reg}(\vec{u}_k(\vec{x})) dx \end{aligned} \quad (5.6)$$

In contrast to Equation 5.5 where  $I^{\text{com}}$  was directly involved in registration process and explicitly generated in each step of the registration, in the implicit reference group-wise registration given by Equation 5.6,  $I^{\text{com}}$  is generated as an additional result of establishing the unknown common space. In particular, when a similarity criterion  $\text{Sim}$  is the sum of the squared differences (defined by Equation 2.8), and the linear elastic regularisation term (Equation 2.18) is used, the objective function is similar as that proposed in [42].

Indeed, the objective function presented in Equation 5.6 provides a well-posed framework for the implicit reference group-wise image registration. Similarly as the case of the pair-wise image registration (presented in Chapter 2) the estimated displacement fields  $\tilde{\mathbf{u}}$  may not be diffeomorphic. Although, the diffeomorphic approaches can be somehow easily introduced by the above formulation, the averaging procedure of the deformation fields can lead to producing a non-diffeomorphic average deformation field [4]. Additionally, it was shown that for the large deformation motion model, the linear averaging of the deformation field is not valid [9].

For this purpose, it seems that the parameterisation using the log-Euclidean space [4] is the appropriate framework, addressing the aforementioned problems. This parameterisation enables the Euclidean operations to be performed on the principal logarithm of the deformation field.

Similarly as in the case of the log-domain pairwise image registration (chapter 3.2), the set of the displacement fields  $\tilde{\mathbf{u}}$  is parameterised by the set of the stationary velocity fields  $\tilde{\mathbf{v}}$  denoted by:

$$\tilde{\mathbf{u}} = \{\exp(\vec{v}_k), k = 1, \dots, K\} \quad (5.7)$$

and the log-domain implicit reference group-wise diffeomorphic image registration is now defined as:

$$\begin{aligned} \varepsilon(\tilde{\mathbf{v}}) = \sum_{k=1} \sum_{\substack{l=1 \\ k \neq l}} \int_{\Omega} Sim(I_k(\vec{x} + \exp(\vec{v}_k(\vec{x}))), I_l(\vec{x} + \exp(\vec{v}_l(\vec{x})))) dx \\ + \alpha \sum_{k=1} \int_{\Omega} Reg(\vec{v}_k(\vec{x})) dx \end{aligned} \quad (5.8)$$

The efficient algorithm of calculating exponential mapping  $\exp(\vec{v}_k(\vec{x}))$  was summarised in Algorithm 4 in Chapter 3 (originally proposed in [4]). In contrast to Equation 5.6 where optimisation is performed with respect to the set of the displacements  $\tilde{\mathbf{u}}$ , the optimisation described by Equation 5.8 is done for the set of the velocity fields  $\tilde{\mathbf{v}}$ . The optimisation of the objective function given by Equation 5.8 can be performed using different methods.

The set of transformations  $\tilde{\varphi}$  estimated during the implicit reference group-wise image registration links the images in the group  $\mathbf{I}$  to the common reference image  $I^{com}$ . Therefore, the transformation  $\tilde{\varphi}_{k,l}$  between images  $I_k$  and  $I_l$  ( $k \neq l$ ) can be estimated as a composition of the transformation  $\tilde{\varphi}_{k,com}$  and the inverse transformation of  $\tilde{\varphi}_{l,com}$ :

$$\tilde{\varphi}_{k,l} = \tilde{\varphi}_{k,com} \circ \tilde{\varphi}_{l,com}^{-1} \quad (5.9)$$

Due to the stationary velocity field parameterisation in the log-domain, the inverse

---

of the transformation  $\vec{\varphi}_{l,com}$  can be obtained at almost no computation cost by a backward integration of the velocity field  $\vec{v}_l$ .

$$\vec{\varphi}_{k,l} = \exp(\vec{v}_k) \circ \exp(-\vec{v}_l) \quad (5.10)$$

Another way of calculating the transformation  $\vec{\varphi}_{k,l}$  between images  $I_k$  and  $I_l$  ( $k \neq l$ ) is to take advantage of the Baker-Campbell-Hausdorff (BCH) formula for the velocity field concatenation (described in details in Section 3.2.3) [17]:

$$\vec{\varphi}_{k,l} = \exp(BCH[\vec{v}_k, -\vec{v}_l]) \quad (5.11)$$

### 5.3 Solution schemes

The objective function of the group-wise image registration defined by Equation 5.8 can be solved using different methods. Similarly, as it was done for the pairwise image registration, three image registration forces can be introduced.

From the fact that the symmetric image registration can be seen as an implicit reference image registration, with only two input images, the minimisation process of Equation 5.8 is similar to the methods presented in Section 3.4. In this case, three commonly used forces have been reformulated to enable them to be used in the implicit reference group-wise image registration: the steepest gradient approach [56, 57, 24] symmetric force defined as:

$$\vec{d}v_{kl}^i(\vec{x}) = (I_k^{\varphi_k^{i-1}}(\vec{x}) - I_l^{\varphi_l^{i-1}}(\vec{x}))(\nabla I_k^{\varphi_k^{i-1}}(\vec{x}) + \nabla I_l^{\varphi_l^{i-1}}(\vec{x})) \quad (5.12)$$

the Newton's iteration approach force [78, 97] defined in the symmetric way:

$$\vec{d}v_{kl}^i(\vec{x}) = \frac{(I_k^{\varphi_k^{i-1}}(\vec{x}) - I_l^{\varphi_l^{i-1}}(\vec{x}))(\nabla I_k^{\varphi_k^{i-1}}(\vec{x}) + \nabla I_l^{\varphi_l^{i-1}}(\vec{x}))}{\|\nabla I_k^{\varphi_k^{i-1}}(\vec{x}) + \nabla I_l^{\varphi_l^{i-1}}(\vec{x})\|^2 + \lambda} \quad (5.13)$$

and the Demon force [145] used in the symmetric manner [155, 96] in the following way:

$$\vec{d}v_{kl}^i(\vec{x}) = \frac{(I_k^{\varphi_k^{i-1}}(\vec{x}) - I_l^{\varphi_l^{i-1}}(\vec{x}))(\nabla I_k^{\varphi_k^{i-1}}(\vec{x}) + \nabla I_l^{\varphi_l^{i-1}}(\vec{x}))}{\|\nabla I_k^{\varphi_k^{i-1}}(\vec{x}) + \nabla I_l^{\varphi_l^{i-1}}(\vec{x})\|^2 + (I_k^{\varphi_k^{i-1}}(\vec{x}) - I_l^{\varphi_l^{i-1}}(\vec{x}))^2} \quad (5.14)$$

where  $I_k^{\varphi_k^{i-1}}(\vec{x}) = I_k^{ne}(\varphi_k^{i-1}(\vec{x}))$ ,  $I_l^{\varphi_l^{i-1}}(\vec{x}) = I_l^{ne}(\varphi_l^{i-1}(\vec{x}))$  are warped images and  $\nabla I_k^{\varphi_k^{i-1}}(\vec{x})$ ,  $\nabla I_l^{\varphi_l^{i-1}}(\vec{x})$  are gradients of those images, and  $i$  is an iteration index.

Although, according to Equation 3.41 the log-Euclidean mean requires calculat-

ing the logarithm, which is reported to be a time-consuming process [4, 17], the proposed symmetric forces are assumed to be represented in the log-domain space. In consequence, the principal logarithm of transformation is produced as an output of image registration and therefore the logarithm is not calculated directly. The average update of the velocity field is calculated using the log-Euclidean mean for vector fields  $\vec{d}v_{kl}^i$  given by (according to Equation 3.41):

$$\vec{d}v_k^i(\vec{x}) = \frac{1}{K} \sum_l (\vec{d}v_{kl}^i(\vec{x})) \quad (5.15)$$

Finally, the deformation field  $\vec{u}_k^{i+1}(\vec{x})$  for the steepest descent approach and the Newton's iteration approach is calculated via exponential mapping for the updated velocity field under the BCH formula [17, 144]:

$$\vec{v}_k^{i+1}(\vec{x}) = BCH \left[ \vec{v}_k^i(\vec{x}), \vec{d}v_k^i(\vec{x}) \right] \quad (5.16)$$

while for the Demon approach the additional smoothing by the low-pass Gaussian filter ( $G_{fluid}^*$ ) is applied to the  $\vec{d}v_k^i(\vec{x})$  resulting in:

$$\vec{v}_k^{i+1}(\vec{x}) = BCH \left[ \vec{v}_k^i(\vec{x}), G_{fluid}^* (\vec{d}v_k^i(\vec{x})) \right] \quad (5.17)$$

The resulting implicit reference group-wise image registration with the symmetric Demon force is summarised in Algorithm 10. The steepest descent symmetric force (Equation 5.12) and the Newton iteration approach force (Equation 5.13) can be put in place of line 5 and then the smoothing procedure can be omitted (lines 8 and 10).

As an additional result of performing the implicit reference group-wise image registration, the common space reference image can be generated by averaging the intensity of all images after registration:

$$I^{com}(\vec{x}) = \frac{1}{K} \sum_k I_k(\vec{\varphi}_k(\vec{x})) \quad (5.18)$$

The sample images of common space reference image  $I^{com}$  estimated using different data sets are presented in the following figures. Results are shown in Figure 5.1e-h for the illustrative example data set, in Figure 5.2 for the pelvic-area MRIs, in Figure 5.4 for the brain data set, and in Figure 7.2 (Chapter 7) for the 2D neutral face expression training set.

---

**Algorithm 10** Log-domain implicit reference group-wise image registration based on the symmetric Demon force

---

**Input:** Set of the images  $\mathbf{I}$

Parameters:  $G_{fluid}$ ,  $G_{diff}$

**Output:** Set of velocity fields  $\tilde{\mathbf{v}}$

```

1:  $\tilde{\mathbf{v}}^0 \leftarrow \mathbf{0}$ ,  $i=1$ 
2: repeat
3:   for  $k = 1$  to  $K$  do
4:     for  $l = 1$  to  $K$  and  $l \neq k$  do
5:       Calculate update velocity field  $\vec{d}v_{kl}^i$  according to
       Equation 5.17
6:     end for
7:     Calculate average of updates  $\vec{d}v_k^i$  according to
       Equation 5.15
8:     Smooth average velocity field update using Gaussian filter  $G_{fluid}$ :
        $\vec{d}v_k^i = G_{fluid} * (\vec{d}v_k^i)$ 
9:     Update velocity field  $\vec{v}_k^{i+1}$  according to
       Equation 5.17
10:    Smooth velocity field using Gaussian filter  $G_{diff}$ :
        $\vec{v}_k^{i+1} = G_{diff} * \vec{v}_k^{i+1}$ 
11:   end for
12:    $i = i+1$ ;
13: until (velocity fields  $\tilde{\mathbf{v}}$  do not change) or ( $i > maxIteration$ )
14: return  $\tilde{\mathbf{v}}$ 

```

---

## 5.4 Evaluation

The evaluation of the proposed parameterisation of the implicit reference group-wise image registration was done using four types of the data: the synthetic shapes [42], the MRI data of pelvic-area, the MRI data of the brain [8], and two-dimensional data set of static face images [157]. The quantitative assessment of the image registration performance was carried out by performing the several known validation criteria.

### 5.4.1 Evaluation criteria

The quantitative performance of group-wise registration includes the Intensity Variance ( $IV$ ) criterion [127]. The intensity variance measures the similarity of the group of images (population) based on the pixel intensity differences. The  $IV$  is

computed in the following way:

$$IV(\vec{x}) = \frac{1}{K-1} \sum_k^K (I_k(\varphi_k(\vec{x})) - I^{com}(\vec{x}))^2 \quad (5.19)$$

where  $I^{com}$  is given by Equation 5.18. The perfect group-wise registration results for images of the same modality should be characterised with minimum pixel intensity differences between registered images.

The Region Overlapping between two organs of interest (or structures from organs) from the group of images ( $RO_{kl}^p$ ) is calculated using the definition given by Equation 4.10 for pairwise registration. The  $RO_{kl}^p$  is stated as follows:

$$RO_{kl}^p = \frac{\text{numberOfVoxels}(P_k \cap P_l(\vec{\varphi}_{l,k}))}{\text{numberOfVoxels}(P_k \cup P_l(\vec{\varphi}_{l,k}))} \quad (5.20)$$

where  $P_k$  is an organ segmented in image  $I^k$ ,  $P_l(\vec{\varphi}_{l,k})$  is the same organ segmented in image  $I^l$  warped by transformation  $\vec{\varphi}_{l,k}$ , and  $p$  is a label index describing an evaluated organ  $P$ . Transformation  $\vec{\varphi}_{l,k}$  is obtained by the concatenation of the velocity fields (following Equation 5.11). For any group of images, the Average Region Overlapping ( $ARO$ ) with respect to the common reference image that can be calculated in the following way:

$$ARO_R^p = \frac{1}{K \cdot (K-1)} \sum_{\substack{l=1 \\ k \neq l}} \sum_k \frac{\text{numberOfVoxels}(P_k(\vec{\varphi}_k) \cap P_l(\vec{\varphi}_l))}{\text{numberOfVoxels}(P_k(\vec{\varphi}_k) \cup P_l(\vec{\varphi}_l))} \quad (5.21)$$

When the group-wise image registration with selected reference image  $I^k$  is evaluated, the  $ARO^p$  is simplified as follows:

$$ARO_k^p = \frac{1}{K-1} \sum_{\substack{l=1 \\ k \neq l}} RO_{kl}^p \quad (5.22)$$

where the transformation  $\varphi_{l,k}$  used in  $RO_{kl}^p$  is obtained by the direct estimation using the pairwise image registration.

## 5.4.2 Evaluation examples

### Illustrative example data set evaluation

A data set of four two-dimensional images of size of 256x256 that consists of a circle (Figure 5.1a), two ellipses (Figures 5.1b-c), and a square (Figure 5.1d) was used to show that the estimated transformations deform each shape present in the data set to common shape - *mean shape*. The input images are shown in Figure 5.1a-d, while

the input images mapped to the implicit common space are shown in Figure 5.1e-h. Figures 5.1i-l show the estimated deformation fields mapping the input images to the common shape space. The results show that the implicit reference group-wise image registration brings each of the input shapes to the common shape of all input shapes, and all warped shapes are similar to the average of them - *mean* shape. Visualisation of the *IV* before and after performing the registration (Figures 5.1o-m) also shows the significant reduction of the *IV* after registration.

### Inter-patient data examples evaluation

A data set of pelvic-area MRI data was used for evaluation of the log-domain implicit group-wise image registration. It consists of five volumes taken from different subjects. The average of these volumes before registration is shown in Figure 5.2a. The intensity variance of volumes before registration is shown in Figure 5.2b. After performing the registration, both the average of the volumes and the intensity variance are significantly improved. Figure 5.2c shows the *mean* intensity volume after registration and Figure 5.2d shows the intensity variance after registration. The *IV* after registration is noticeably lower than that before registration. The relatively high value of the *IV* on the body boundaries results from differences in the MRI data acquisition for different subjects (the example is shown in Figure 5.3).

The Average Region Overlapping (*ARO*) calculated between the segmented organs before registration and after registration indicate that organs registered using the log-domain implicit group-wise registration have good overlap in the common space. The *ARO* for prostate before registration is  $17.72 \pm 10.62$ , for rectum is  $25.28 \pm 15.08$ , whereas for bladder is  $34.64 \pm 5.91$ . The *ARO* for prostate after registration is  $55.79 \pm 7.69$ , for rectum is  $61.63 \pm 4.28$ , and for bladder is  $62.68 \pm 4.92$ . The aforementioned results are worse than the results shown in Table 4.2 (Chapter 4) for the pelvic-area organs. Reasons for that inconsistencies are the following. First of all, in the previous example the *ARO* was calculated for data acquired for the same patient, so the between-subjects anatomical differences are not present in the data set, and the registration has an *easier* problem to solve. Secondly, the *ARO* in Table 4.2 is expected to be higher since the *ARO* is calculated in the specific patient space for the data of this particular patient.

### Brain images labelling

A data set of MRI brain data was used for evaluation of the log-domain implicit group-wise image registration. It consists of ten volumes taken from different subjects [8]. The average of those volumes before registration is shown in Figure 5.4a. The intensity variance of volumes before registration is shown in Figure 5.4b. After

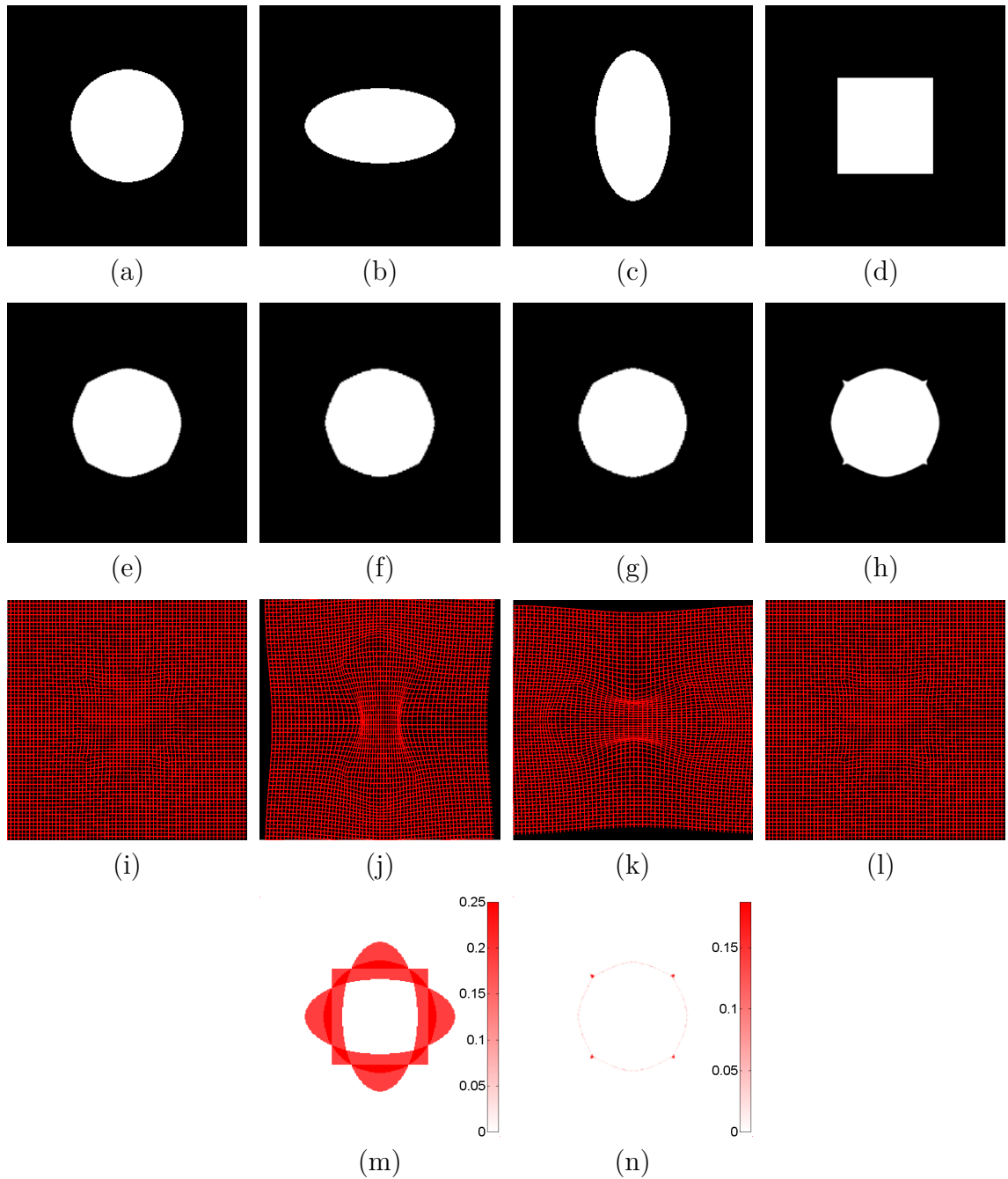


Figure 5.1: Results of performing the log-domain implicit group-wise registration for the illustrative data set evaluation based on the Demon force: (a)-(d) input images; (e)-(h) input images warped into common space; (i)-(l) estimated deformation fields warping the regular grid; (m)  $IV$  before registration, (n)  $IV$  after registration.

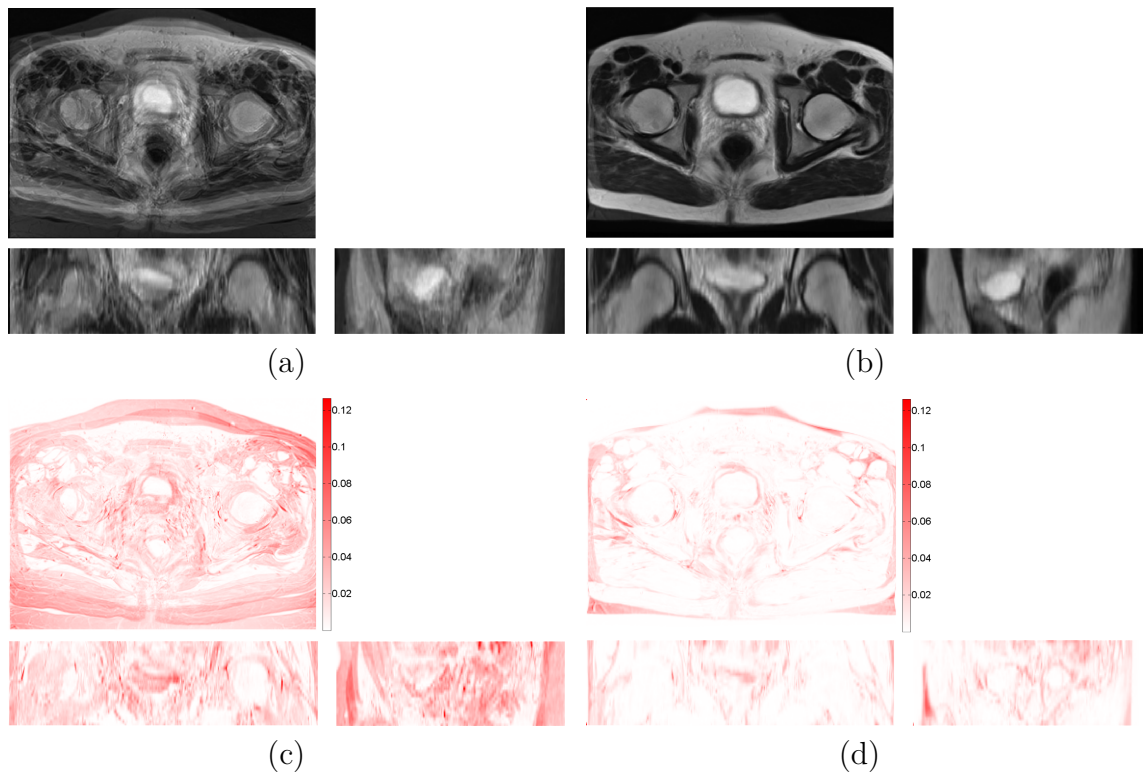


Figure 5.2: Results of performing the log-domain implicit group-wise registration for the MRI pelvic-area data set evaluation based on the Demon force: (a) average of the input volumes; (b)  $IV$  before registration; (c) average of the input volumes after performing registration; (d)  $IV$  after registration.

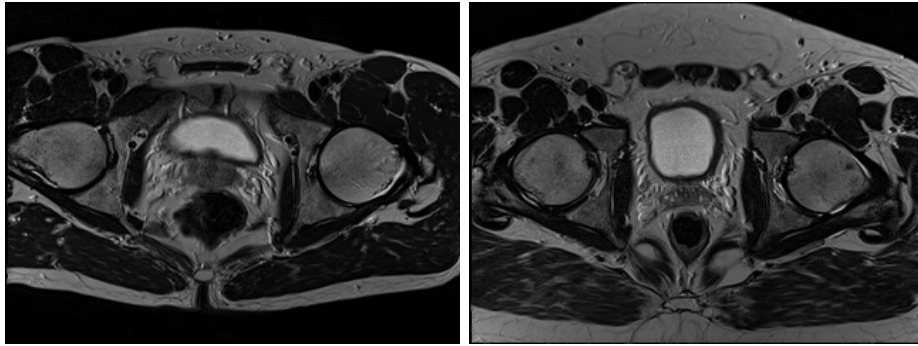


Figure 5.3: Example of inconsistency in the MRI data acquisition. Two axial slices of the MRI pelvic-area data coming from different subjects.

	CSF	GM	WM	Fat	Muscle	Skin
Average Relative Overlapping						
before	23.61	45.96	44.92	7.93	9.10	40.85
after	52.73	71.60	71.69	28.67	23.38	67.19

	Skull	Vessels	Around fat	Dura matter	Bone marrow
Average Relative Overlapping					
before	25.94	5.95	2.13	8.02	14.29
after	55.76	21.60	6.18	22.61	31.93

Table 5.1: Average Region Overlapping (ARO) values of the brain structures after log-domain implicit group-wise image registration.

performing the group-wise registration, both the average of the volumes and the intensity variance are visually improved. Figure 5.4c shows the *mean* intensity volume after registration and Figure 5.4d shows the intensity variance after registration.

The segmentation results through the warping labels are summarised in Table 5.1. The results suggest that the log-domain implicit group-wise registration estimates the transformations that map the input volumes into the common space. The values of the Average Region Overlapping for all segmented structures were improved. When these results are compared with the results obtained for the pairwise image registration assessment (Table 4.1) that can be considered as the group-wise image registration with directly selected reference image, the implicit group-wise registration produces slightly better results in most cases. The improved performance is noticeable for larger structures such as white matter and grey matter, and it is about 10%.

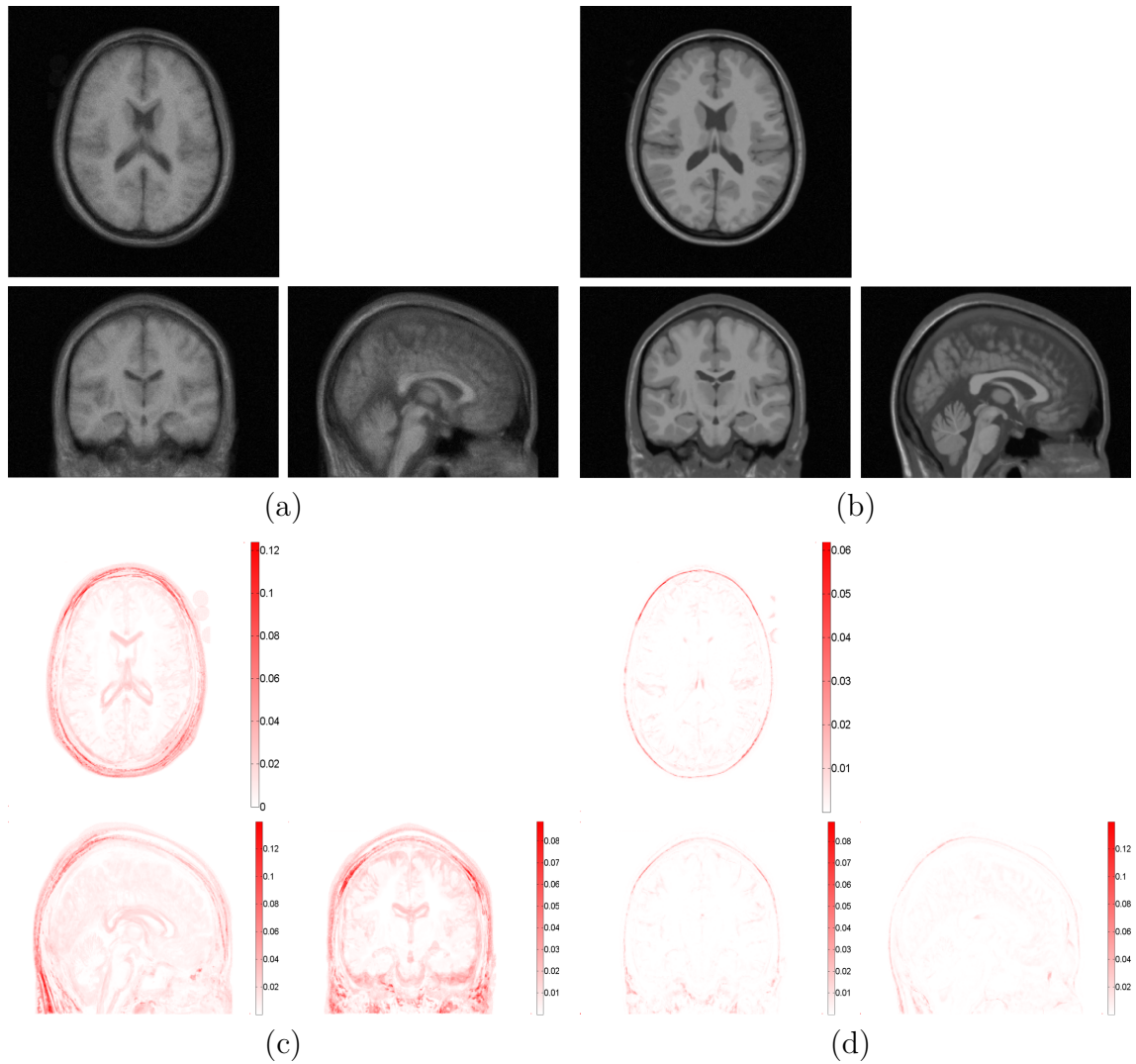


Figure 5.4: Results of performing the log-domain implicit group-wise registration for the MRI brain data set evaluation based on the Demon force: (a) average of the input volumes; (b)  $IV$  before registration; (c) average of the input volumes after performing registration; (d)  $IV$  after registration.

## 5.5 Summary

The concept and the implementation details of the diffeomorphic implicit group-wise image registration taking the advantage of the parameterisation of deformation fields via stationary velocity fields were presented in this chapter.

The proposed method of *mean image* estimation is motivated by the method proposed by Geng et al. [42] where Equation 5.6 is solved by the parameterisation of the displacement fields using the three-dimensional Fourier series and estimated by the gradient descent algorithm. The details of this representation and the solution scheme can be found in [27]. In contrast to this method, in the proposed method the transformations are parameterised by the stationary velocity fields and all operations on them are performed in the log-Euclidean domain to ensure diffeomorphism. Furthermore, the utilisation of the velocity fields provides a feasible way of computation of the inverse transformation  $\vec{\varphi}_i^{-1}$  while the method proposed in [42] requires an additional step of calculation of the inverse transformation (described in [27]). The results of performing the proposed group-wise registration method can be directly used for calculation of the vectorial statistics.

Finally, the computational complexity of the presented approach is approximately linear with respect to the number of input images, since the number of the transformations to be estimated equals exactly the number of input images.

## Chapter 6

# Statistical modelling of 4D deformations using diffeomorphic image registration

This chapter describes a new model based technique for estimation of a dense deformation field utilising an implicit representation of shape changes. Unlike existing methods based on the Point Distribution Model (PDM), the proposed method is not effected by an incorrect point correspondence which is a major limiting factor in practical applications of the PDM with clinical data. The proposed method uses regression between parametric representations of organ's shapes and corresponding dense displacement field parameterised by the stationary vector field. The regression function is estimated based on training data with an inverse-consistent estimation of the velocity field, established in the log-Euclidean diffeomorphic formulation. To enable calculation of the inter-subject statistics, the *mean* shape of the patients in the training data set is built, and the estimated intra-subject transformations are mapped into the *common patient space*. The evaluation of the proposed method is carried out on MRI prostate imaging examples with synthetic deformation fields to provide systematic experimental evidence of correctness of the implicit shape representation for shape-driven prediction of the deformation field. Additionally, real MRI data are used to show accuracy in terms of the deformation field prediction thereby the prostate position. The results show an increased robustness of the proposed framework in comparison to the PDM approaches and demonstrate the potential of its application to the Adaptive Radiotherapy (ART) of prostate.

## 6.1 Introduction

Deformation modelling is an essential tool for improving accuracy and robustness of image segmentation [160, 161] and registration [3] especially when data are of very poor quality; very noisy and/or partially missing. For example, with such data traditional registration methods, aiming at estimation of the dense deformation field, can not be directly applied as the similarity measure for assessing the quality of the estimated deformation can not be reliably computed. In such cases a partial information, delivered by a surrogate somehow linked to the tissue deformations, is often used instead. A surrogate is generally defined as a measurement which is affected by the deforming tissue and which can be used to indirectly infer the tissue deformation. Although some efforts have been recently undertaken to improve the surrogate-based image registration and segmentation, it still remains a challenging problem particularly when it is to be applied as a part of a clinical procedure. Such approach requires an appropriate surrogate which suitably represents tissue deformations and in the same time it is easy to extract from often severely corrupted data. Currently, such surrogates are most often defined by a set of points.

In [93] an online system is described for simultaneous compensation of laparoscopic camera motion and periodic, respiration induced, deformation of tissue in the abdominal region based on a measurement of liver surface represented by a small number of points. Some other implementations of this methodology used in a 4D image-guided radiation therapy of lungs, use the most superior point of diaphragm's position along the longitudinal axis [159], or a whole lung region segmented from CT [75, 73], cone-beam CT [74], which was represented using a standard PDM with a fixed number of points selected from segmented shape contour. Recently, the boundary correspondences established across the different prostate shapes using the deformable shape models were utilised in the fast method of the deformation field estimation for non-boundary regions of prostate [123, 124].

Similarly, the methods of modelling organ deformation and correlated motion of adjacent structures were applied to data sets of prostate, bladder and rectum in [125]. The contours of organs of interest were delineated by the same physician for each CT data. Then, the set of corresponding points forming the shape surface of each organ was generated based on a biomechanical model of tissue and represented using the major modes of the Principal Component Analysis. The evaluated experiments indicated that the individual variation of measured organs can be characterised by few dominant eigenvectors, thereby it can assist adaptive radiotherapy planning. The shape variability of rectum and bladder with applications to radiotherapy planning and delivery was also considered in [102], where the statistical deformation model was built on parameters of spherical harmonics used to

represent organs surface with surrogates defined by a very small number of points interactively selected by an operator. The population model of the prostate shape was generated by the method proposed in [123, 124] where the thin-plate model algorithm was used to register the patient CT images and deformable shape model to segment and establish the correspondences between boundary points among the training data set.

All the methods mentioned above require to estimate correspondence between points detected in images representing different deformation phases. Although this can be relatively reliably achieved during the model training phase by careful time consuming, often manual selection of corresponding points, such task is prone to occurrence of gross errors during the model evaluation where often near real time performance is required. It will be shown, later in this chapter, that such correspondence errors significantly affect the accuracy of the estimated deformation field. To avoid problems associated with the point correspondence it is proposed here to use an implicit shape representation for shape description. The implicit shape representation was considered and successfully utilised for segmentation of medical images containing known types of objects [140], and also in a global alignment and local registration of shapes [62]. In both cases, this representation solves difficulties by finding correspondences.

Whereas the intra-subject motion model can be easily generated utilising multiple registration between acquired volumes representing different phases of organs' motion [125, 159], the inter-subject motion model that is built in a similar manner, is biased towards the chosen reference image. Therefore, a *mean* reference subject has to be estimated first and then the *common subject space* can be established [42]. Moreover, in many recent approaches ([159, 73, 74, 123, 124]), the statistical models of the deformation fields were obtained by directly applying the PCA to the deformation fields (or B-spline parameterisation [114]). Although these approaches were to some extent successful in particular applications, this motion model has some disadvantages. The most important is that such eigenvectors do not form a vector space of valid deformation fields (e.g. diffeomorphism is not guaranteed to be preserved). Here, the log-Euclidean framework [4, 17, 144] is applied to parameterise non-linear diffeomorphic deformation fields.

The main contribution of this chapter is a novel approach to dense deformation field estimation. The proposed method uses the implicit surfaces to represent the shape of bladder and rectum. The presented results show the advantages of this shape descriptor in comparison to PDM. Moreover, the *common subject space* that is essential for the presented method, is established in the log-Euclidean framework by performing the implicit group-wise registration. The results obtained for the sim-

ulated and real MRI data are shown to demonstrate the plausibility of the described prediction system.

## 6.2 Inter-subject motion model

In the proposed approach, each subject  $k : k = 1, \dots, K$  is described by a set of  $n$ -dimensional images  $\mathbf{I}^k = \{I_l^k : \Omega \subset \mathbb{R}^n \rightarrow \mathbb{R}, l = 0, \dots, L^k\}$ . A transformation  $\vec{\varphi}_{0l} : \Omega \rightarrow \Omega$  that warps image  $I_l^k$  to image  $I_0^k$ , is represented by a stationary velocity field  $\vec{v}_{0l}^k$ , related to a diffeomorphic displacement field  $\vec{u}_{0l}^k$  through the exponential mapping  $\vec{\varphi}_{0l}^k(\vec{x}) = \vec{x} + \vec{u}_{0l}^k(\vec{x}) = \vec{x} + \exp(\vec{v}_{0l}^k(\vec{x}))$  [4, 144].

Calculating the velocity fields for each set of patient images can only provide a patient specific motion model. In order to obtain the general motion model, the *common subject space* have to be established. To avoid possible bias due to selecting a particular reference image, the implicit group-wise image registration was proposed in [42]. Contrary to the original method, to maintain diffeomorphic consistency in this work, the displacement fields are parametrised via stationary velocity fields. The energy function  $\varepsilon(\vec{\mathbf{v}})$  is given in Equation 6.1 where *Sim* is a similarity measure and *Reg* is a regularisation term [144], and the Demon-like approach is used to minimise it.

$$\varepsilon(\vec{\mathbf{v}}) = \sum_{k_1=1}^K \sum_{\substack{k_2=1 \\ k_1 \neq k_2}}^K \text{Sim}(I_0^{k_1}(\exp(\vec{v}_0^{k_1})), I_0^{k_2}(\exp(\vec{v}_0^{k_2}))) + \alpha \sum_{k_1=1}^K \text{Reg}(\vec{v}_0^{k_1}) \quad (6.1)$$

The implicit group-wise registration estimates the set of transformations  $\vec{\varphi}_{0m}^k$  that warps each planning image  $I_0^k$  to the *mean* intensity image  $I_m$ , that finally can be calculated as an average of all warped images  $\frac{1}{K} \sum I_0^k(\vec{\varphi}_{0m}^k)$ .

## 6.3 Intra-subject motion model

Generation of the deformation model requires estimation of numerous non-linear diffeomorphic transformations between different stages of organs' motion. Owing to already estimated transformations  $\varphi_{0m}^k$ , the intra-patient deformations are calculated for the images  $J_l^k = I_l^k(\vec{\varphi}_{0m}^k)$  in the *common subject space*. To assure a symmetry of the registration with respect to input images and impose the inverse consistency criterion, the consistent log-domain intensity-based algorithm is used. This approach implements a fast and efficient Demon method that minimises the

energy:

$$\varepsilon(\vec{v}_{0l}^k) = Sim(J_0^k, J_l^k(\exp(\vec{v}_{0l}))) + Sim(J_l^k, J_0^k(\exp(-\vec{v}_{0l}))) + \alpha Reg(\vec{v}_{0l}) \quad (6.2)$$

The main advantage of using this method of registration is that the output velocity field  $\vec{v}_{0l}$  minimising energy  $\varepsilon$  (Equation 6.2) can be directly used for the log-domain calculation of deformation statistics without explicit computing logarithm of the displacement field, that is time consuming [4, 17]. However, different methods of registration can be used instead as long as they allow to perform the *vectorial* statistics and preserve the invertibility constraint [4].

## 6.4 Surrogate representation

To evaluate the proposed surrogate-based image deformation estimation methodology the experiments were conducted with MRI volumetric data acquired for the pelvic region with the shape of bladder and rectum treated as a surrogate (measurement) for the dense displacement field estimation. Segmentation of these organs is a relatively simple task because of usually high intensity contrast between bladder/rectum and surrounding tissues and can be easily achieved using one of many proposed automatic or semi-automatic segmentation algorithms [160]. As a result of segmentation of an  $n$ -dimensional image  $J_l^k$  a binary image  $S_l^k : \Omega \subset \mathbb{R}^n \rightarrow \{0, 1\}$  representing the organ of interest is produced. The sign distance function  $\phi_l^k(\vec{x})$  is defined as the minimum Euclidean distance from a given voxel position  $\vec{x} = [x^1, \dots, x^n] \in \Omega$  to the shape's  $S_l^k$  boundary, multiplied by 1 or -1 depending on which side of boundary  $\vec{x}$  is located. The positive or negative distance is assigned to all voxels inside or outside  $S_l^k$  respectively, whereas for all voxels on the shape boundary the distance function has value zero. An efficient algorithm, with the linear computation time, for exact Euclidean Distance (ED) calculation for arbitrary dimensional binary images was proposed by Maurer et al. [87]. An example of such implicit shape representation of a bladder segmented from an MRI image is shown in Figure 6.1.

## 6.5 Generation of 4D motion model

During the training process the motion model, linking shape and corresponding deformation field, is estimated using a data set of implicit shapes and matched velocity fields. First, due to a high dimensionality of the velocity field and adopted shape representation, direct estimation of the motion model is computationally pro-

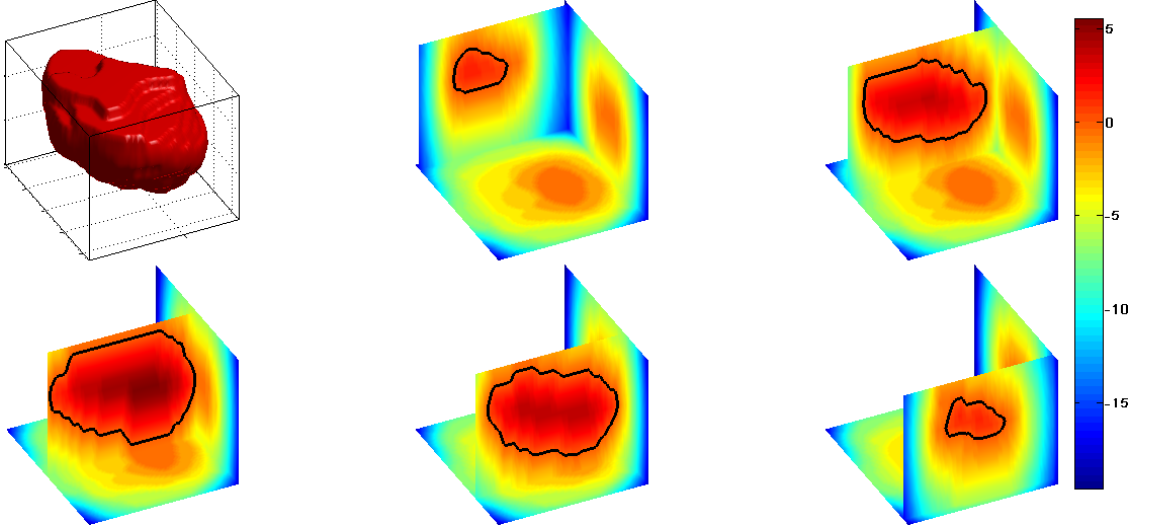


Figure 6.1: Bladder segmented from MRI (top left) and sequence of its implicit representation with highlighted surface position (black).

hibitive. A commonly used technique for reducing dimensionality of data is PCA [159, 73, 75, 74, 123, 124]. In this case, it allows extraction of the major modes of variation of shape and velocity field. For each registered image  $J_p$  ( $p = 1, \dots, P$ ; where  $P$  is the number of volumes in the database, different from the reference volume  $P = K \cdot (L - 1)$ ) the corresponding velocity field and implicit shapes are formed as a vector:

$$V_p = [\vec{v}_p(\vec{x}_0), \dots, \vec{v}_p(\vec{x}_d), \dots, \vec{v}_p(\vec{x}_D)] \quad (6.3)$$

where  $\vec{v}_p(\vec{x}_d) = [v_p^1(\vec{x}_d), \dots, v_p^n(\vec{x}_d)]$  is the velocity vector at  $\vec{x}_d$ , with  $d$  representing voxel index  $d = 1, \dots, D$ ; and  $D$  denoting the number of voxels in the volume. Similarly for the implicit shape(s):

$$\Phi_p = [\phi_p(\vec{x}_0), \dots, \phi_p(\vec{x}_d), \dots, \phi_p(\vec{x}_D)] \quad (6.4)$$

where  $\phi_p(\vec{x}_d)$  is a value of the signed distance function at  $\vec{x}_d$ . After carrying out PCA using all  $V_p$ , the velocity field can be approximated as:

$$V_p \simeq \mu_V + \sum_{i=1}^{E_V} \gamma_{pi} \vec{w}_i = \mu_V + \Gamma_p W_V \quad (6.5)$$

where  $\mu_V$  is the sample mean velocity field,  $\vec{w}_i$  is the  $i$ th eigenvector,  $\gamma_{pi}$  are coefficients,  $W_V$  is a matrix of eigenvectors and  $\Gamma_p$  is vector of coefficients with  $E_V$  representing the number of the major velocity field eigenmodes observed in the

training data set. Similarly, for the implicit shape representation:

$$\Phi_p \simeq \mu_\Phi + \sum_{i=1}^{E_\Phi} \theta_{pi} \vec{z}_i = \mu_\Phi + \Theta_p Z_\Phi \quad (6.6)$$

where  $\mu_\Phi$  is the sample mean implicit shape,  $\vec{z}_i$  is the  $i$ th eigenvector,  $\theta_{pi}$  are coefficients,  $Z_\Phi$  is a matrix of eigenvectors and  $\Theta_t$  is a vector of coefficients with  $E_\Phi$  representing the number of the major implicit shape eigenmodes present in the training data set. Although, the sign distance function is not closed under additive operation of shape eigenvectors, it was shown in [140] that this theoretical inconsistency does not affect the performance of this shape representation in practice. Moreover, the shape descriptors are not used directly to reconstruct the object shape but rather to provide features to estimate the parameters of the stationary velocity model (a vector space), therefore the reconstruction of a valid deformation is ensured. The motion model  $M$  linking observed organ deformations with the corresponding velocity field is built via the multivariate linear regression between coefficients matrices  $\Gamma = [\Gamma_0^T, \dots, \Gamma_p^T, \dots, \Gamma_P^T]^T$  and  $\Theta = [\Theta_0^T, \dots, \Theta_p^T, \dots, \Theta_P^T]^T$ :

$$M = (\Theta^T \Theta + \rho D)^{-1} \Theta^T \Gamma \quad (6.7)$$

where  $\rho$  denotes a regularisation parameter for the prediction model and  $D$  is an identity matrix [124].

Once the model  $M$  is learnt, it can be utilised in a practical way both on the new images for patient already included in the model and for images of the new patients. In both cases, the new image has to be first mapped to the *common patient space* and then segmented to obtain the shape descriptor. Then, the implicit representation of any new shape  $\Phi_{new}$  can be directly projected onto the shape eigenvector space  $Z_\Phi$  to get shape coefficients  $\Theta_{new}$ . Subsequently corresponding velocity coefficients  $\Gamma_{new}$  can be calculated using the estimated motion model:  $\Gamma_{new} = \Theta_{new} M$ . Then, under the Baker-Campbell-Hausdorff formula for the composition of the diffeomorphic deformations [17], the predicted diffeomorphic deformation field  $u_{new}$  can be approximated by exponentiation of the sum of the velocity fields eigenvectors:

$$u_{new} = \exp(\mu_V + \Gamma_{new} W_V) \quad (6.8)$$

The computational burden of the developed training scheme is highly time-consuming, mostly due to required multiple registration of volumes, but it is performed only once during the learning of the motion model  $M$ . However, the model evaluation is fast as it involves only calculation of the implicit shape descriptors, matrix multiplication and calculation of the exponential map. The scheme presenting the proposed

model training framework and the corresponding model evaluation process is shown in Figure 6.2.

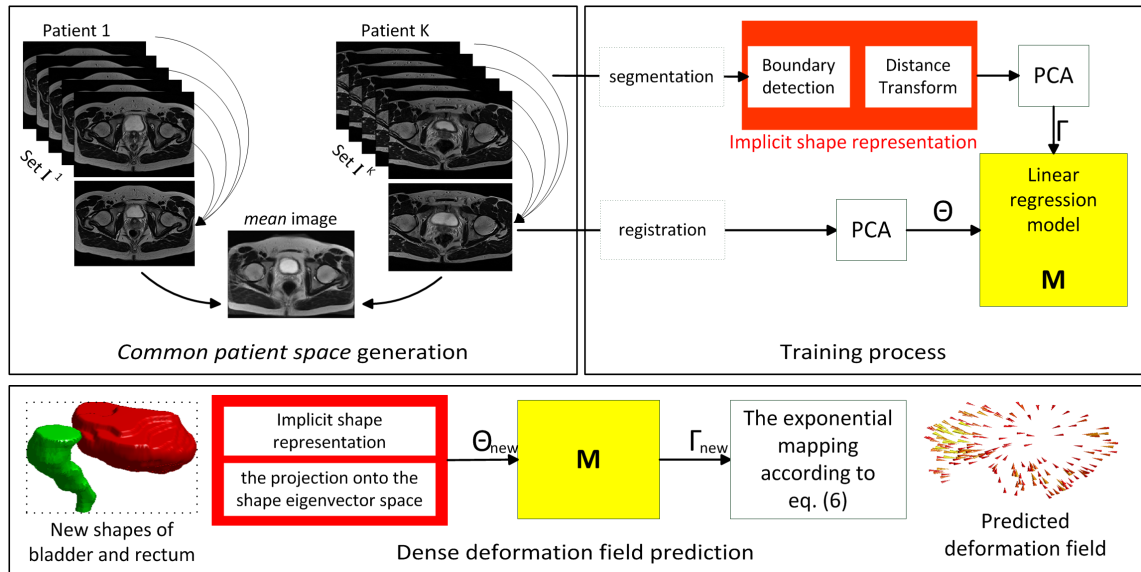


Figure 6.2: Training process and deformation field prediction using the implicit shape-based dense deformation field estimation model for prostate

## 6.6 Evaluation of proposed framework

The proposed use of the implicit shape representation as a surrogate for estimation of the dense displacement field has been validated using two sets of tests.

For the first set a number of different deformation fields were synthetically generated and applied to real MRI volumetric data acquired from a male pelvic area. Using such data, with the ground truth displacement field available, a number of trials were carried out to assess the method accuracy. These results were also compared against the results obtained using the previously proposed Point Distribution Model (PMD).

For the second part of the experiments, real MRI data were used. The data set consists of 25 scans obtained from 5 subjects. For each subject images were collected in equal intervals over 40 minutes showing significant shape changes of bladder/rectum. Then images were normalised to the spatial resolution of  $1.0 \times 1.0 \times 3.0 \text{ mm}$  and the anatomical structures used in the experiments were manually annotated. For each experiment, four sets were chosen as training data, the remaining one as test data. The experiments were repeated 5 times, every time with a different set selected as test data.

### 6.6.1 Synthetic example

The registration method used for training stage was implemented using the log-domain consistent Demon approach. The parameters of the image registration were chosen to be  $K_{fluid} = 1.0$  for fluid-like regularisation and  $K_{diff} = 1.0$  for diffusion-like regularisation.

The simulated data set consists of 50 volumes of size 320x240x30 which were warped by known (ground truth) deformation fields. The known velocity fields were generated from a random zero-mean Gaussian *velocity process* defined on selected knots of a sparse 3D regular grid of size 30x20x15, which were heavily smoothed by a low-pass filter. The selected knots were chosen in the area close to bladder. Finally, velocity fields were interpolated to the finer grid resolution with cubic splines and then scaled and exponentiated to get a wide range of diffeomorphic deformation fields. This procedure of generating deformation field is similar to the method described in [17] which was used to validate the Baker-Campbell-Hausdorff formula of calculation the velocity fields. An example of the generated synthetic deformation field is shown in Figure 6.3. Such generated data set was divided into two parts. The first part with 40 volumes was used for instantiation of the motion model, whereas the second part of 10 remaining volumes was used for model evaluation. The experiments were repeated 5 times, each time for a different and randomly selected training data set. For all the tests segmented bladder was used as a surrogate, represented either by the signed distance function or by 167 points uniformly distributed on the bladder surface for the PDM. The number of points for bladder description is smaller than that used in [125], but the probability of the occurrence of gross errors increases when more points are used. To model the occurrence of wrong point-to-point correspondences, the gross error was introduced to PDM representation during the method validation. The implemented gross error is characterised by:  $\varsigma$  -representing expected percentage of points affected by the gross error and,  $\tau_{min}^{max}$  - encoding the minimum (*min*) and maximum (*max*) magnitude of the gross error, with actual simulated error magnitude selected randomly from a uniform distribution. In all cases the points where selected on the bladder surface.

The results shown in Table 6.1 indicate that the implicit shape representation performs similarly as PDM without gross error. PDM accuracy deteriorates quite quickly with even a small level of the gross error (with only one or two points affected out of 167 used for shape representation) leading to the estimated deformation field not reliable any longer. The estimation error gets bigger with the increasing magnitude of gross error  $\tau$  or when more points are affected by it (for larger  $\varsigma$ ).

## 6.6. EVALUATION OF PROPOSED FRAMEWORK

Table 6.1: Errors of estimation deformation fields obtained using different shape representations: (PDM perf.) - PDM with ground truth correspondence; (PDM norm.) - PDM with Gaussian noise  $\mu = 0.0$ ,  $\sigma = 1.0$  representing typical measurement error; (PDM gros1.) - PDM norm. with gross error  $\varsigma = 5\%$ ,  $\tau_{10}^{20}$ ; (PDM gros2.) - PDM norm. with gross error  $\varsigma = 5\%$ ,  $\tau_{20}^{40}$ ; (PDM gros3.) - PDM norm. with gross error  $\varsigma = 1\%$ ,  $\tau_{20}^{40}$ . All results are given in *mm*.

	Trial 1		Trial 2		Trial 3		Trial 4		Trial 5		avg $\pm$ std
	avg	max									
PDM perf.	0.23	3.61	0.25	3.90	0.21	3.36	0.18	2.75	0.18	2.7	0.21 $\pm$ 0.12
PDM norm.	0.47	4.94	0.52	6.63	0.49	4.82	0.44	4.46	0.44	3.83	0.47 $\pm$ 0.11
PDM gros1.	0.79	8.77	0.72	7.26	0.76	12.04	0.60	6.52	0.65	6.26	0.70 $\pm$ 0.22
PDM gros2.	1.19	17.59	1.24	13.11	1.14	12.18	1.07	16.45	1.06	10.16	1.14 $\pm$ 0.34
PDM gros3.	0.63	6.08	0.59	7.22	0.64	10.17	0.54	5.81	0.67	7.71	0.61 $\pm$ 0.22
implicit	0.31	5.36	0.36	4.14	0.30	5.34	0.25	3.42	0.28	4.13	0.30 $\pm$ 0.14

Table 6.2: Errors of the prediction of the deformation fields with respect to the results of direct registration.

	Trial 1	Trial 2	Trial 3	Trial 4	Trial 5	Trial 1-5
	avg $\pm$ std ( <i>mm</i> )					
Deformation characteristics	7.40 $\pm$ 3.39	4.07 $\pm$ 0.84	8.61 $\pm$ 3.03	5.94 $\pm$ 2.42	3.57 $\pm$ 1.39	5.92 $\pm$ 2.14
Error of prediction	2.45 $\pm$ 1.16	1.45 $\pm$ 0.15	2.71 $\pm$ 0.98	2.05 $\pm$ 0.78	1.25 $\pm$ 0.41	1.98 $\pm$ 0.62

### 6.6.2 Real data evaluation

For the second part of the experiments, real MRI data were used. In order to get quantitative results and to estimate ground truth deformation fields, the registration was independently performed between corresponding pairs of images that were used to compare with those estimated using the prediction system. The overall robustness in terms of the accuracy with respect to the ground truth deformation fields is summarised in the 2<sup>nd</sup> row of Table 6.2 whereas the 1<sup>st</sup> row characterises the ground truth data. Based on these results, it can be concluded that the proposed method is able to estimate the dense deformation field with error less than  $2.0 \pm 0.62$  mm. Additionally, the computation speed is significantly reduced when compared with the classical registration. The average time of prediction when the motion model is already trained is about 1s while the registration process takes about 180s.

Figure 6.4 presents the variation of the first three modes of the implicit shape representation. The first mode can be seen as the mode linked to the changes of the bladder size. Also some changes of the rectum shape are noticeable. The second mode seems to be related mostly to the rectum and the bladder shape changes

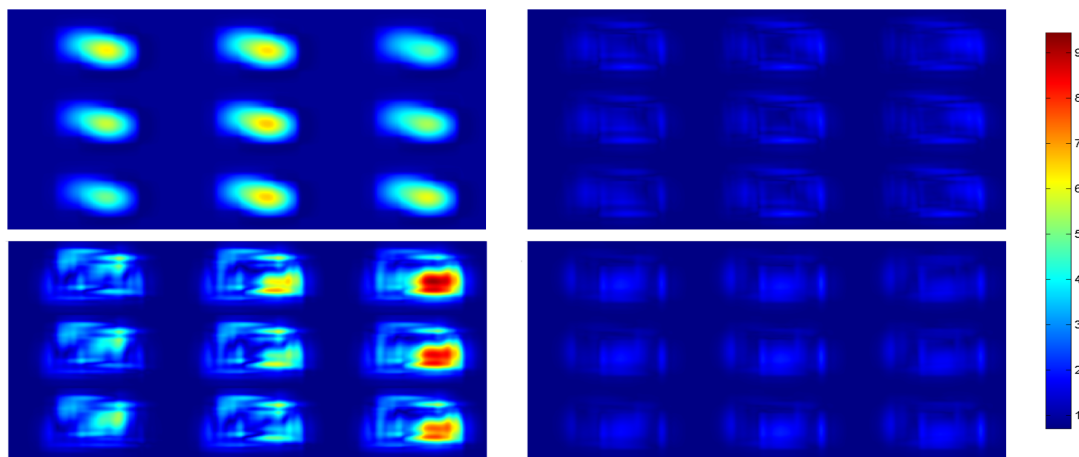


Figure 6.3: Example of synthetic deformation field used in the experiments (top left), Estimation error examples: using PDM with Gaussian noise  $\mu = 0.0$ ,  $\sigma = 1.0$  (top right), PDM with gross error  $\varsigma = 5\%$ ,  $\tau_{20}^{40}$  (bottom left) and using the implicit representation (bottom right)

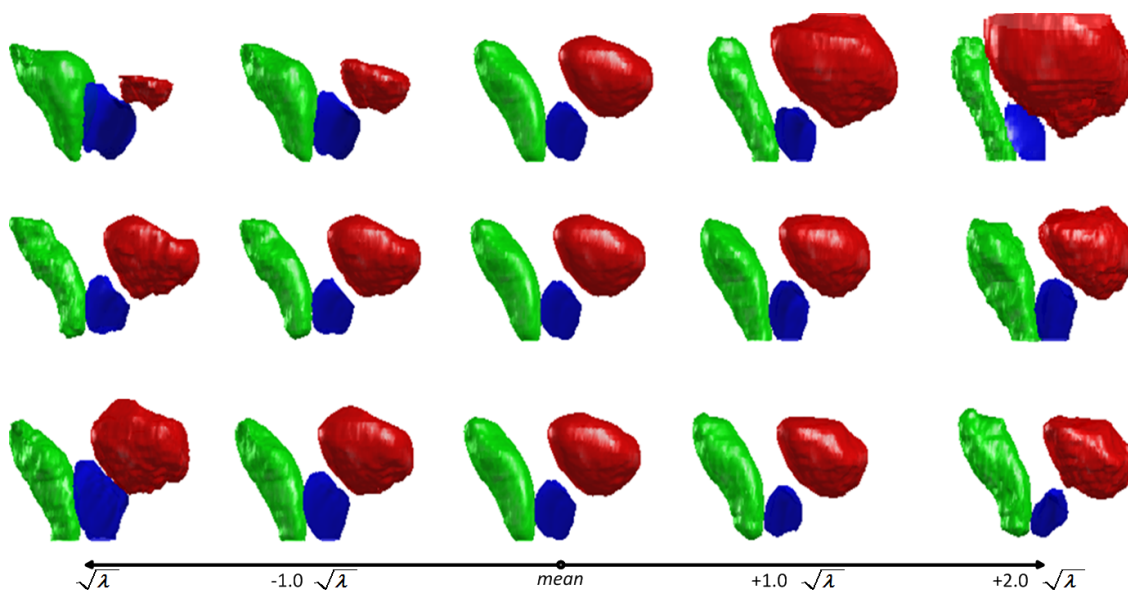


Figure 6.4: The variability of the major modes of the implicit shape representation of the prostate (blue), bladder (red) and rectum (green).

that are likely to model the patient variability. The most remarkable impact of the third mode is linked to changes of the prostate size. Although the implicit shape representation does not preserve entirely the neighbourhood topologies, the shapes in the presented visualisation do not overlap between each other.

The practical advantage of the deformation fields parameterisation using the stationary velocity fields is shown in Table 6.3. The deformation fields estimated using the major modes of the motion model that is built using the diffeomorphic deformation fields can be non-diffeomorphic, whereas the deformation fields estimated

Deformation field representation					
	$-3.0 \cdot \lambda_r$	$-1.5 \cdot \lambda_r$	$0.0 \cdot \lambda_r$	$1.5 \cdot \lambda_r$	$3.0 \cdot \lambda_r$
Minimum determinant of Jacobian					
$r = 1$	<b>-0.306</b>	0.080	0.109	0.113	0.017
$r = 2$	<b>-0.062</b>	0.094	0.109	0.125	0.136
$r = 3$	0.086	0.104	0.109	0.114	<b>-0.213</b>

Velocity field representation					
	$-3.0 \cdot \lambda_r$	$-1.5 \cdot \lambda_r$	$0.0 \cdot \lambda_r$	$1.5 \cdot \lambda_r$	$3.0 \cdot \lambda_r$
Minimum determinant of Jacobian					
$r = 1$	0.048	0.097	0.113	0.119	0.123
$r = 2$	0.064	0.096	0.113	0.118	0.121
$r = 3$	0.100	0.106	0.113	0.115	0.109

Table 6.3: Minimum of the determinant of the Jacobian matrix for the variability of the trained motion model using the deformation fields and the stationary velocity fields.

utilising the log-domain parameterised deformation fields to build the motion model are always diffeomorphic. Thus, the parameterisation of the transformations via stationary velocity fields is indicated as the robust methodology due to preserving the one-to-one properties of the estimated deformation fields.

## 6.7 Summary

The chapter describes a novel technique for model-based dense deformation field estimation with an implicit surface representation used as an effective and robust deformation descriptor. The proposed framework uses motion model estimated from a training data set of shapes and corresponding displacement fields parameterised via stationary velocity fields estimated using a fast and efficient diffeomorphic registration scheme, formulated in the log-Euclidean framework. It has been also demonstrated that with the help of the proposed method, it is possible to predict dense displacement fields solely from the measured deformations of the implicit surface. The experiments conducted with the real data show that it is possible to predict deformation field thereby position of the prostate from shape deformations of the bladder/rectum. As it is relatively easier to segment bladder (rectum) in the CBCT data when compared to prostate segmentation, it can be concluded that the proposed methodology can be potentially useful for adaptive radiation therapy of prostate. Thus, further investigation is suggested to combine the motion model built from MRI data with shape descriptors extracted from radiotherapy imaging.

# Chapter 7

## Facial expression recognition using log-Euclidean statistical shape models

This chapter presents a new method for facial expression modelling and recognition based on the diffeomorphic image registration parameterised via stationary velocity fields in the log-Euclidean framework, that was described in the previous chapters. First, Section 7.1 briefly presents an overview of the current facial expression representations and introduces the concept of using the motion fields as a feature for face recognition and facial expression recognition systems. In Section 7.2, the process of *common face space* generation is utilised based in the implicit group-wise registration algorithm adapted to the facial expression modelling. Then, Section 7.3 introduces the velocity field based representation of facial expressions (described in Section 7.3.1), and the Point Distribution Model (presented in Section 7.3.2). The robustness of the proposed facial expression representation is demonstrated based on the experimental results of a qualitative and quantitative evaluation (shown in Section 7.4). The obtained results show that the facial expression representation based on stationary velocity fields can be successfully utilised in facial expression recognition, and this parameterisation produces a slightly higher recognition rate than the facial expression representation based on deformation fields. Finally, the concluding remarks are given in Section 7.5.

### 7.1 Introduction

Face is an important medium used not only by humans to communicate, but also reflecting a person's emotional and awareness states, cognitive activity, personality or well-being. Over the last ten years automatic facial expression representation

and recognition have become an area of significant research interest by the computer vision community, with applications in human-computer interaction (HCI) systems, medical/psychological sciences, and visual communications to name a few. Although, significant efforts have been undertaken to improve the facial features extraction process and the recognition performance, automatic facial expression recognition is still a challenging task due to an inherent subjective nature of the facial expressions and their variation over different gender, age, and ethnicity groups. Detailed overviews of existing methodologies, recent advances and challenges can be found in the literature surveys [37, 95] and standard textbooks [86, 139].

The facial expression representation can be seen as a process of extracting features, that can be generic such as local binary patterns [120] or Gabor coefficients [13] or more specific such as landmarks of characteristic points located in areas of major facial changes due to articulation [69], or a topographic context (TC) that treats the intensity levels of an image as a 3-D terrain surface [149]. Recently, in [103, 105] authors postulated that the shape space vectors (SSV) of the statistical shape model (SSM) can constitute a significant feature space for the recognition of facial expressions. The SSM can be constructed in many different ways, and it was developed based on the point distribution model originally proposed by [33]. In [104], the SSM is built based on the control points of the B-Spline surface of the training data set, and in [106] an improved version with multi-resolution correspondence search and multi-level model deformation was proposed. In this chapter, the SSM is generated using the stationary velocity fields obtained from the diffeomorphic face registration.

The idea of using the motion fields as features in computer vision and pattern recognition was used previously for face recognition where the optical flow was computed to robustly recognise face with different expressions based on a single sample per class in the training set [60].

The previous chapters introduced and then utilised the parameterisation of the diffeomorphic transformations via the principal logarithm of non-linear geometrical deformations in medical applications. As the facial shapes (mouth, eyes, eye brows) can be assumed to have constant intra- and inter- subject topology, it is interesting to check the adequacy of the facial expressions represented using stationary velocity fields as a result of performing the diffeomorphic image registration that preserves the spatial topology of objects by maintaining diffeomorphism (detailed description in Section 3.2). Additionally, using this framework (described in details in Chapter 3.2), the log-Euclidean vectorial statistics can be performed on the diffeomorphic vector fields via their logarithm, which always preserve the invertibility constraint contrary to the Euclidean statistics on the deformation fields. In other words, this

provides a mathematically consistent framework to generate the SSM based on the deformation fields parameterised via the stationary velocity fields. Finally, facial expression representation based on the deformation field is compared with facial expression representation based on the stationary velocity field in terms of separability in feature space and recognition performance is evaluated.

## 7.2 Common face space generation

The statistical shape model (SSM) was developed based on the point distribution model and originally proposed by [33]. The model represents the facial expression variations based on the statistics calculated through the corresponding features during the learning process of the training data set. In order to build an SSM using the point landmarks, the correspondence for those facial features between different faces (among the different subjects) in the training data set must be reliably established. This is done here by generating a *mean* face model for the neutral facial expression data set to find first the mappings from any face to the so called *common face space*. Subsequently, by transferring the subject specific facial expressions data set into the common face space, the intra-subject facial expression correspondence is estimated. Finally, the principal component analysis (PCA) is applied to the training data set aligned in the *common face space*, to provide a low-dimensional feature space for facial expression representation.

The overall scheme of system for establishing correspondences between different faces is shown in Figure 7.1.

### 7.2.1 Diffeomorphic implicit group-wise image registration

Generation of the *mean* face model is an essential step during the training process because it allows a subject independent common face space to be established for further analysis.

For a given set of  $n$ -dimensional images representing neutral facial expressions denoted by

$$\mathbf{I}^{\text{ne}} = \{I_k^{\text{ne}} : \Omega \subset \mathbb{R}^n \rightarrow \mathbb{R}, k = 1, \dots, K\} \quad (7.1)$$

where  $K$  is the number of subjects included in training data, the objective is to estimate a set of displacement fields  $\hat{\mathbf{u}}^{\text{ne}}$  to map the images taken from  $\mathbf{I}^{\text{ne}}$  to the *mean* face model  $I^{\text{mean}}$ . In general, this problem can be formulated as a minimisation problem:

$$\hat{\mathbf{u}}^{\text{ne}} = \arg \min_{\mathbf{u}^{\text{ne}}} \epsilon(\mathbf{u}^{\text{ne}}; \mathbf{I}^{\text{ne}}) \quad (7.2)$$

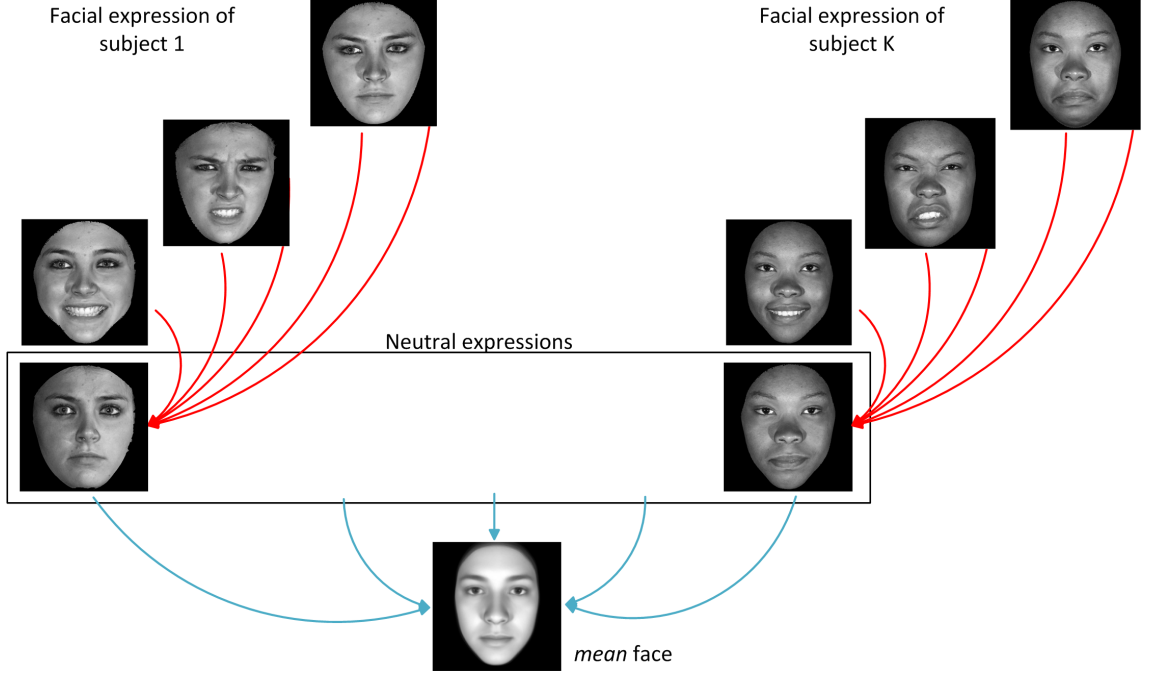


Figure 7.1: Scheme for establishing correspondences between faces using the log-domain implicit group-wise registration.

where  $\epsilon(\mathbf{u}^{ne})$  is defined as

$$\begin{aligned} \epsilon(\mathbf{u}^{ne}) = \sum_k \sum_l \int_{\Omega} Sim(I_k^{ne}(\vec{x} + \vec{u}_k(\vec{x})), I_l^{ne}(\vec{x} + \vec{u}_l)) d\vec{x} \\ + \alpha \sum_k \int_{\Omega} Reg(\vec{u}_k(\vec{x})) d\vec{x} \end{aligned} \quad (7.3)$$

where  $\vec{x} = [x^1, \dots, x^n] \in \Omega$  denotes given voxel positions,  $Sim$  denotes a similarity measure between each pair of the images,  $I_k^{ne}$  and  $I_l^{ne}$  ( $l \neq k$ ) from  $\mathbf{I}^{ne}$ ,  $Reg$  denotes a regularisation term, and  $\alpha$  is a weight of the regularisation term.

The algorithm used for generating the *mean* face model is similar to the work presented in Chapter 5 and [42]. The main difference is in how the deformation fields are parameterised with the stationary velocity field used in the proposed method instead of the Fourier series in [42], and in the method of solving Equation 7.2 with the Demon approach used instead of the linear elastic model. Using the log-domain parameterisation for deformation fields has been reported to produce smoother deformation fields and it allows vectorial statistics to be calculated directly on the velocity fields.

## 7.2. COMMON FACE SPACE GENERATION

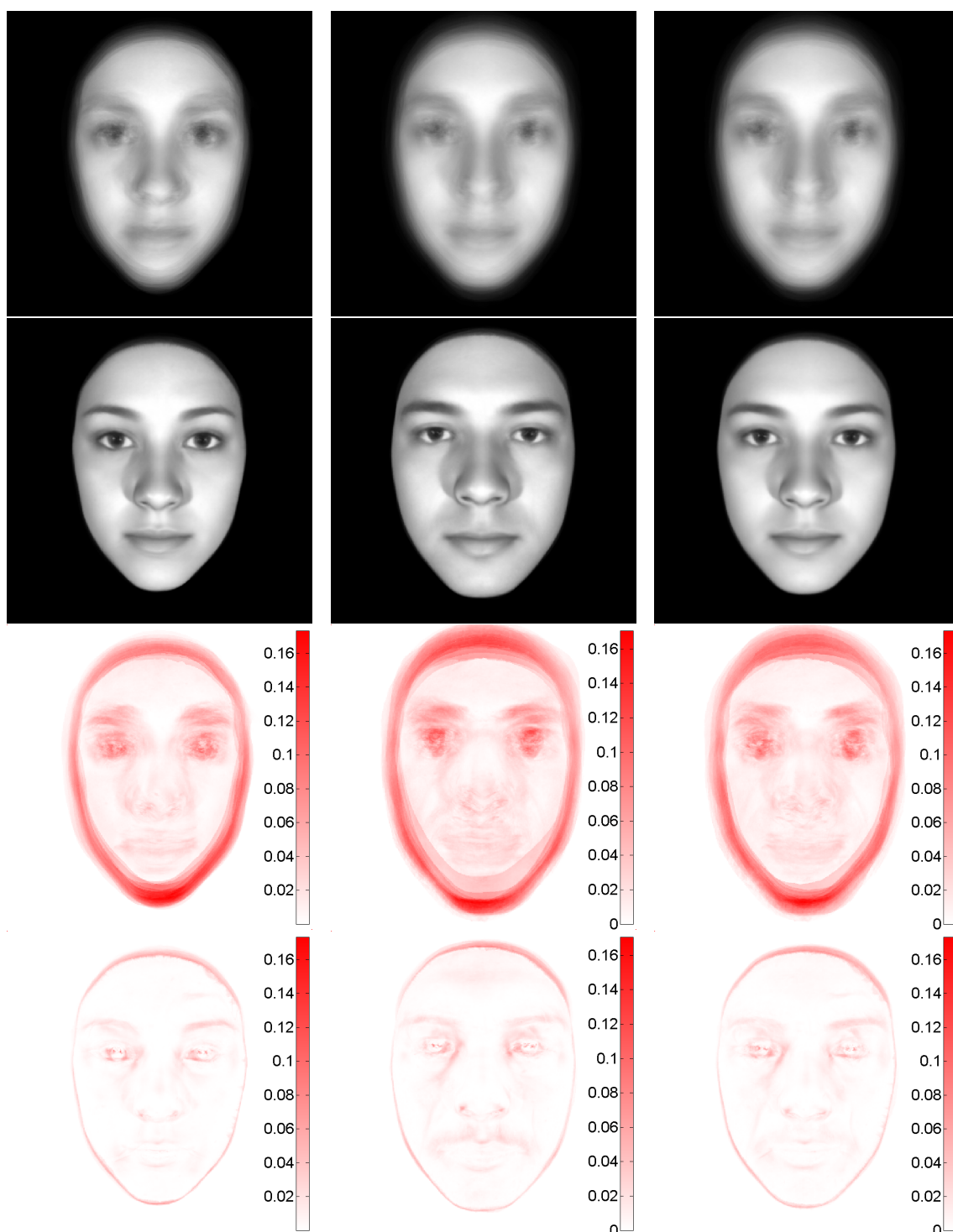


Figure 7.2: Grey-level average of mean face before registration, and after registration, obtained for different sets of images: (from left to right) female data set, male data set, mixed data set. (Top row) shows grey-level average before registration, (upper middle row) shows grey-level average of images after registration, (lower middle row) shows the Intensity Variance ( $IV$ ) (given by Equation 5.19) before registration and (bottom row) shows the  $IV$  after registration.

## 7.3 Facial expression modelling

### 7.3.1 Velocity field based facial expression model

The next step is to warp all other training faces representing different facial expressions to the mean face (the reference face) via transformation  $\varphi_k(\vec{x})$  estimated for neutral expressions. For a given set of facial expression images from subject  $K$ :

$$\mathbf{I}_k^{\text{ex}} = \{I_{km}^{\text{ex}} : \Omega \subset \mathbb{R}^n \rightarrow \mathbb{R}, m = 1, \dots, M\} \quad (7.4)$$

where  $M$  denotes the number of images. The estimated transformation  $\varphi_k(\vec{x})$  is applied to get a set of facial expression images in the common face space (space of the reference image):

$$\mathbf{I}_k^{\text{ceex}} = \{I_{km}^{\text{ex}}(\varphi_k(\vec{x}))\} \quad (7.5)$$

By applying the log-domain image registration approach based on the consistent symmetric Demon algorithm [144], each image in set  $\mathbf{I}_k^{\text{ceex}}$  is registered to the image of neutral expression in common face space  $I_k^{\text{ne}}(\varphi_k(\vec{x}))$ , the set of the velocity fields  $\mathbf{v}_k^{\text{ex}}$  is estimated, and the set of the corresponding deformation fields  $\mathbf{u}_k^{\text{ex}}$  via exponential mapping is calculated as well. Utilising this particular method for image registration has two important advantages. Firstly, the inverse consistency criterion is maintained during the registration process that helps to keep the smooth transformation especially for cases like matching between open-mouth and close-mouth shapes. Secondly, the results of registration are the velocity fields so there is no necessity of calculating the principal logarithm of transformations.

### 7.3.2 Point Distribution Model

The point distribution model originally proposed by [33] is one of the most often used techniques for representing shapes. This model describes a shape as a set of positions (landmarks) in the reference image. The variations between different shapes require establishment of the correspondence between points detected in the reference image and images representing different deformations in the training set. Although this can be relatively reliably achieved during the model training phase by careful time consuming, often manual selection of corresponding points, such task is prone to occurrence of gross errors during the model evaluation where often near real time performance is required. The examples of the manually selected landmarks for neutral, happiness and sadness expression are shown in Figure 7.3. The automatically selected landmarks used later on in the experimental section are obtained with help of the face image registration described in the previous section.

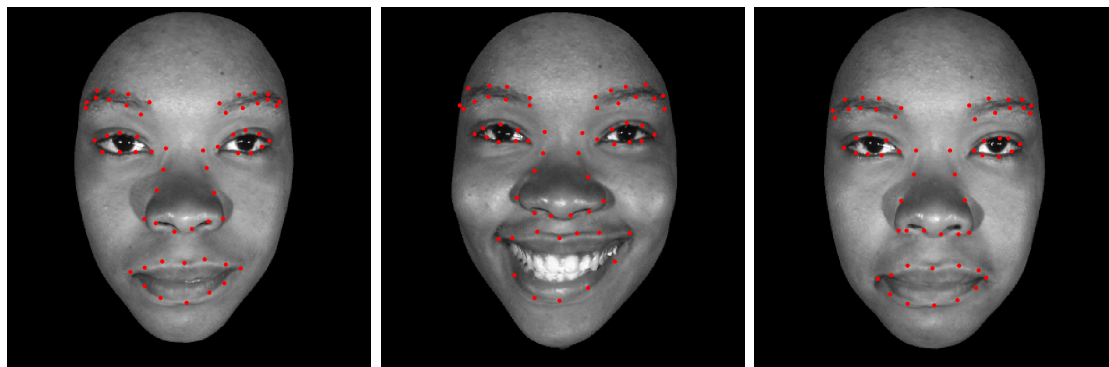


Figure 7.3: Manually selected landmarks for neutral expression (left), happiness expression (middle), and sadness expression (right).

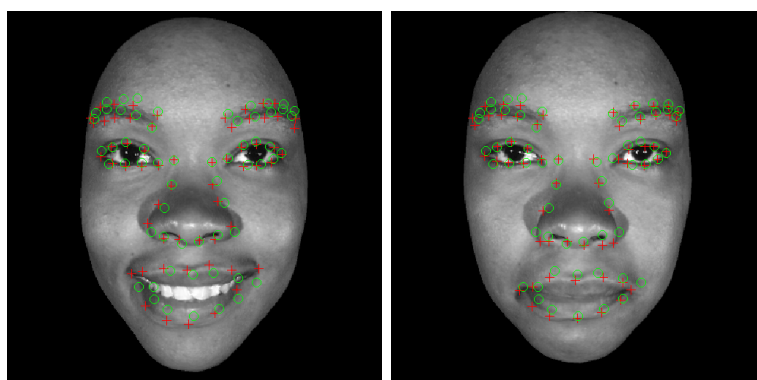


Figure 7.4: Automatically selected (green circles) and manually selected (red crosses) landmarks for happiness expression (left), and sadness expression (right).

The examples of the automatically selected landmarks for happiness and sadness expression are shown in Figure 7.4. In this case, the manually selected landmarks in the model face are automatically mapped onto registered faces.

Using the standard principal component analysis (PCA), each face representation in the training data set can be approximately represented in a low-dimensional shape vector space instead of the original high-dimensional data vector space [16]. Figure 7.5 shows the effect of varying the first three largest principal component of the PDM for automatically selected landmarks, where  $\lambda_r$ , where  $r = 1, 2, 3$  is the eigenvalue of the covariance matrix calculated from the training data set.

Figure 7.6 shows the effect of varying the first three largest principal component of the velocity fields representation, where  $\lambda_r$ , where  $r = 1, 2, 3$  is eigenvalue of the covariance matrix calculated from the training data set. The transformation obtained from the velocity field representation are applied to the *mean* face.

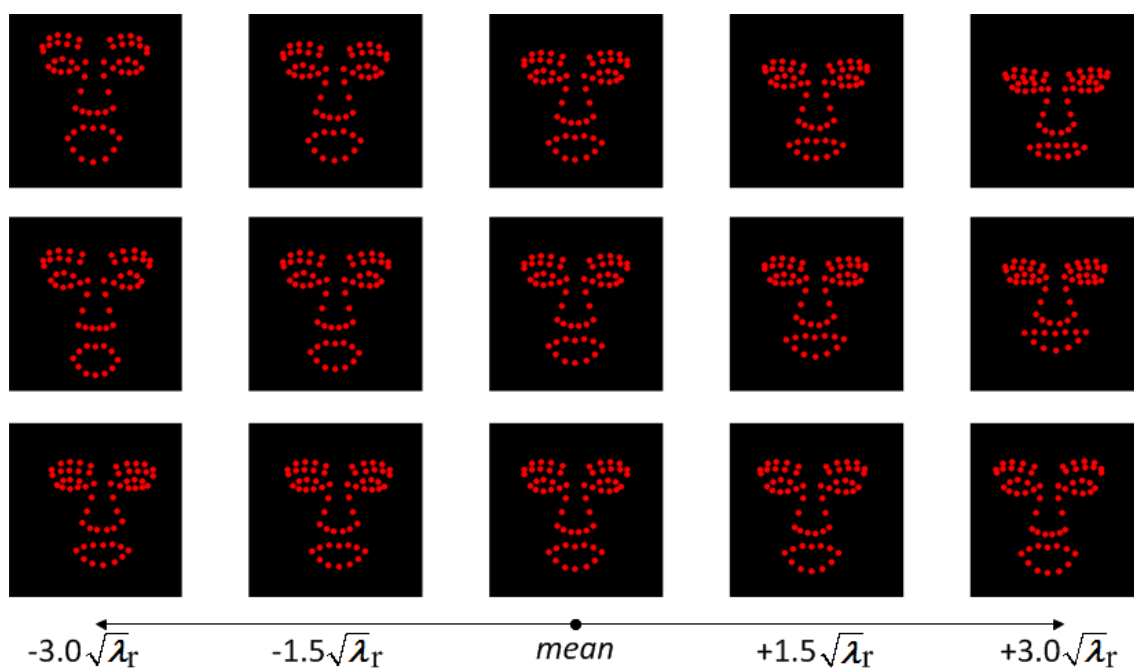


Figure 7.5: Variations of the first (top row), the second (middle row), and the third (bottom row) major mode of the Point Distribution Model for automatically selected landmarks.

## 7.4 Experimental results

The data set used for validation consists of 48 subjects that are selected from the BU-3DFE database [157], with a wide variety of ethnicity, age and gender. Samples of the faces taken from that database are shown in Figure 7.7, and Figure 7.8 shows the various ranges of expression intensity. The data used during the training procedure are excluded from the data used for validation. The implicit log-domain group-wise registration based on the Demon approach minimises the Sum of Squared Difference between images and hence due to different skin patterns an additional image intensity adjustment was performed.

### 7.4.1 Separability analysis

This section studies the properties of the velocity fields based facial expression representation and makes comparison with other representations briefly described in the previous section.

First, to assess whether the Shape Space Vectors based on the velocity fields can be used as a feature space for facial expression analysis and recognition, the separability of the SSV-based features in low-dimensional spaces is examined. Then, the qualitative analysis is conducted using the theoretically derived separability criterion for the different facial expression representations. Finally, the between-

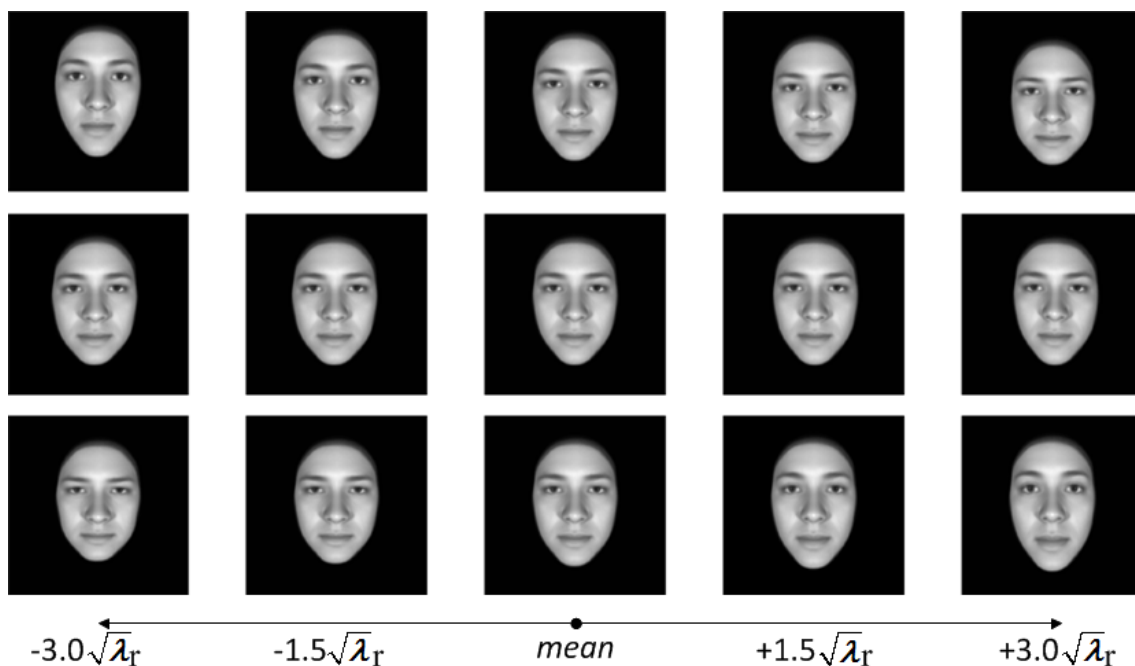


Figure 7.6: Variations of the first (top row), the second (middle row), and the third (bottom row) major mode of the velocity fields representation applied to the unisex *mean* image.

expression separability analysis is evaluated to support further facial expression recognition results.

### Illustrative analysis in low-dimensional spaces

Data set used for classification based validation again consists of 48 subjects, and contains neutral expression, and six basic facial expressions of anger, disgust, fear, happiness, sadness, and surprise with four different expression intensity ranges. These data were divided into two subsets containing 24 subjects with 25 faces per subject representing different expressions. During evaluation, the first subset is chosen to build the SSM of the selected facial expression representation based on the manually selected landmarks (with 60 landmarks per face), the automatically selected landmarks (also with 60 landmarks per face), the deformation fields, and the velocity fields (with 512x512 pixels per image). The second subset is used as testing data (with similar parameters of the facial expression representation). Subjects included in the training data set are not included in the testing data set.

The facial expression representation investigated in this section are the high-dimensional features, and they are hard to be visualised. To obtain the intuitive clustering characteristics of the SSV-based facial expression representation, the first three element of the SSV are used to observe the inter-expression discriminability. For different facial expression representations, the retained energy for the first three

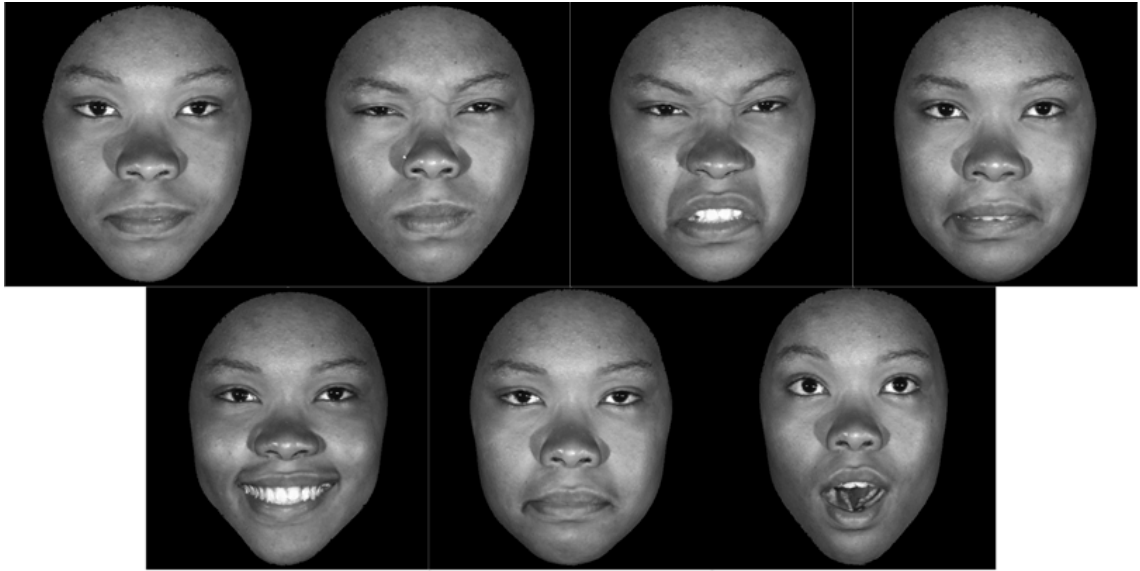


Figure 7.7: Sample subject showing seven basic expressions (from top left to bottom right) neutral, angry, disgust, fear, happiness, sadness, and surprise.



Figure 7.8: Samples of happiness expression for of different expression intensity ranges from low (left), middle, high to highest (right).

principal components has different levels of the variability included in the training data set. For the SSM built from the manually selected landmarks and the automatically selected landmarks, the first three components retain 60.76% and 73.41% of the total data variability, respectively. For the SSM built from the deformation fields, the first three components retain 75.15% data variability, whereas for the model that is built from the velocity fields, the first three components retain 76.08% of the total variability.

Examples of some low-dimensional between-expressions separability visualisations are given in Figures 7.9- 7.12. For the manually selected landmarks (Figure 7.9) and the automatically selected landmarks (Figure 7.10), the pair of expressions such as "happiness vs. surprise" and "sadness vs. surprise" can be very easily separated even in the low-dimensional space, the pair of "happiness vs. sadness" also exhibits good separability but less noticeable than the previous cases. For the deformation field (Figure 7.11) and the velocity field (Figure 7.12) based representations,

the separability for the pairs of expressions such as "happiness vs. surprise" and "sadness vs. surprise" can be also easily identified, but the pair of "happiness vs. sadness" appears to overlap partly together in the low-dimensional space. On the opposite side of the illustrative analysis, the pairs of expressions such as "anger vs. disgust", "anger vs. sadness", or "fear vs. sadness" are completely indistinguishable for each type of the facial expression representations. This suggests that the expression such as anger, fear, and sadness can be easily misclassified.

### Quantitative separability analysis

In order to quantitatively assess the separability of the presented facial expression representations, appropriate criteria are needed. A computable criteria for measurement of within-class and between-class distances for each type of the facial expression representation were applied following the separability investigations of the facial expression features reported by Wang and Yin [149] and Quan et al. [105]. The separability criterion used in this work, is based on the calculation of the average between-class distances. This criterion can be represented by using the so-called the within-class matrix, and the between-class matrix. The within-class scatter matrix  $S_W$  is defined as follows:

$$S_W = \sum_{i=1}^c \frac{1}{n} \sum_{k=1}^{n_i} (\vec{x}_k^i - \vec{m}_i)(\vec{x}_k^i - \vec{m}_i)^T \quad (7.6)$$

and the between-class scatter matrix  $S_B$  is defined as:

$$S_B = \sum_{i=1}^c \frac{n_i}{n} (\vec{m}_i - \vec{m})(\vec{m}_i - \vec{m})^T \quad (7.7)$$

where:  $\vec{x}_k^i$  is a  $d$ -dimensional feature,  $n_i$  is the number of samples in the  $i$ th class,  $n$  is the number of samples in all classes,  $c$  is the number of classes,  $\vec{m}_i$  is the mean of samples in the  $i$ th class defined as:

$$\vec{m}_i = \frac{1}{n_i} \sum_{k=1}^{n_i} \vec{x}_k^i \quad (7.8)$$

$\vec{m}$  is the mean of all the samples:

$$\vec{m} = \sum_{i=1}^c \frac{n_i}{n} \vec{m}_i \quad (7.9)$$

The separability criterion  $J_2(\vec{x})$  is defined as a natural logarithm of the ratio between the within-class scatter matrix's determinant and the between-class scatter matrix's

## 7.4. EXPERIMENTAL RESULTS

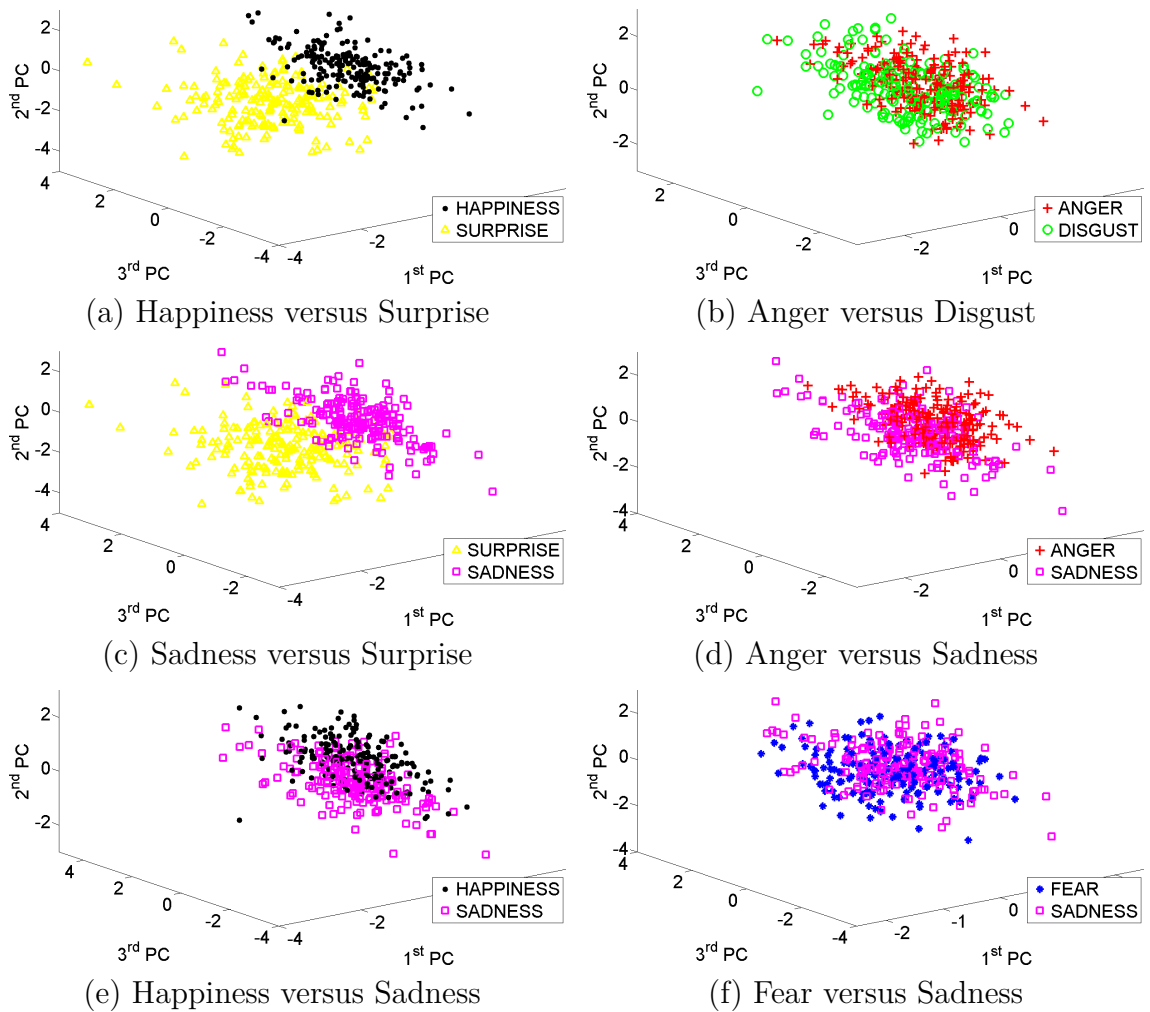


Figure 7.9: Separability Analysis for manually selected landmarks using first three principal components. Figure (a), (c) and (e) shows the pair of expression with the highest value of  $J_2^{ex_i, ex_j}(\vec{x})$  while (b), (d) and (f) shows the pair of expression with the lowest value of  $J_2^{ex_i, ex_j}(\vec{x})$

## 7.4. EXPERIMENTAL RESULTS

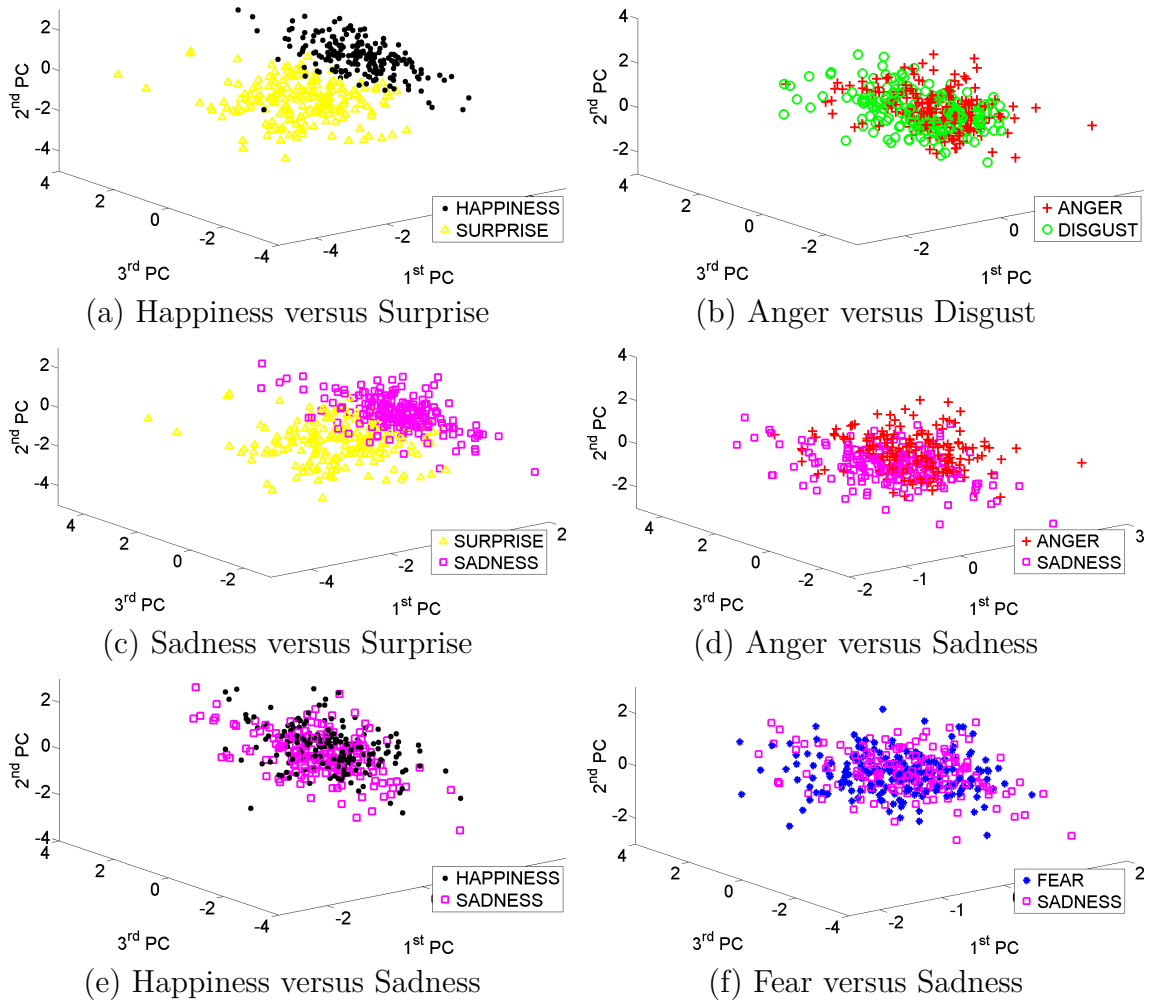


Figure 7.10: Separability analysis for automatically selected landmarks using first three principal components. (a), (c) and (e) show the pairs of expressions with the highest value of  $J_2^{e_{x_i}, e_{x_j}}(\vec{x})$  while (b), (d) and (f) show the pairs of expressions with the lowest value of  $J_2^{e_{x_i}, e_{x_j}}(\vec{x})$

## 7.4. EXPERIMENTAL RESULTS

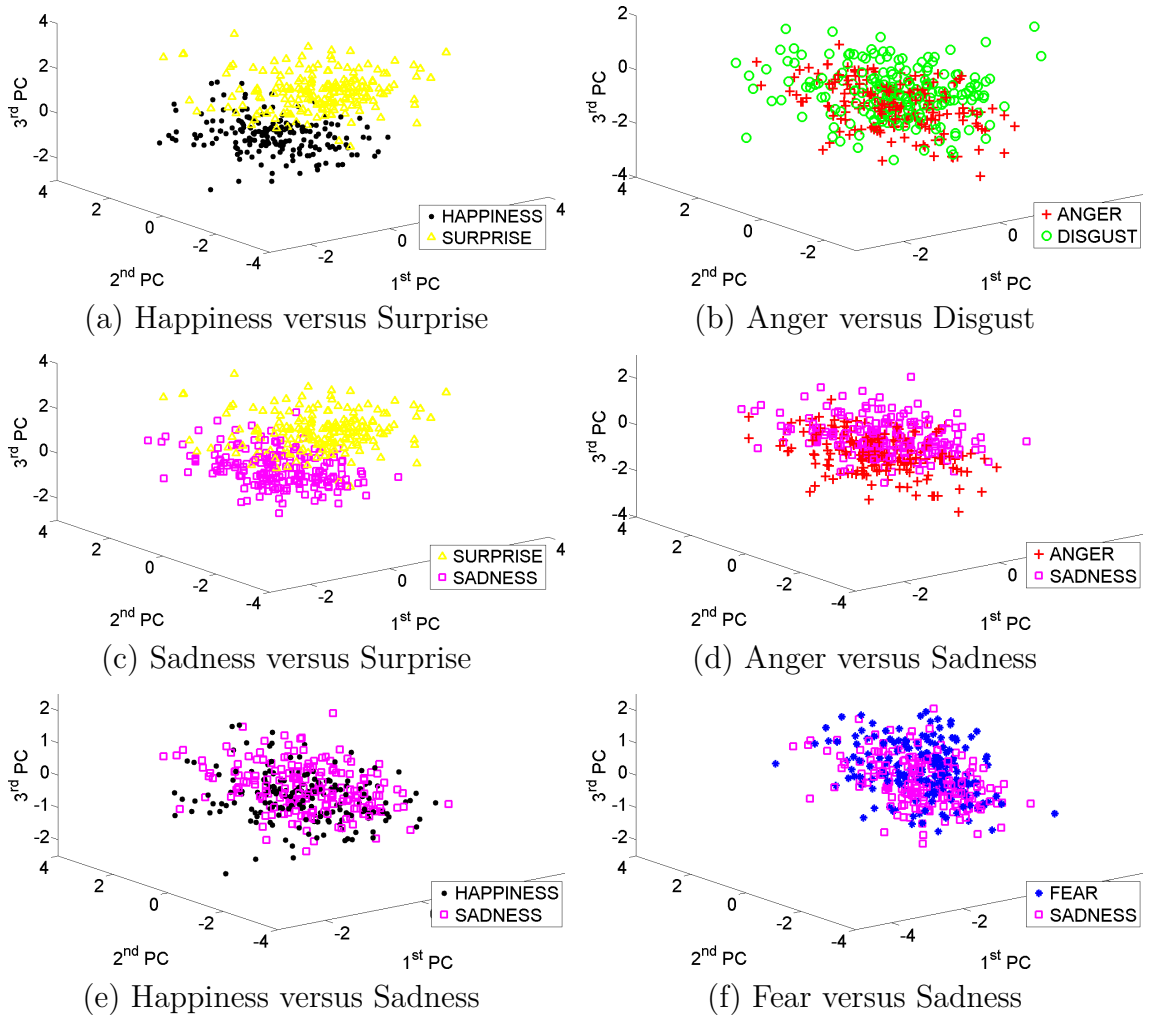


Figure 7.11: Separability analysis for deformation field representation using first three principal components. (a), (c) and (e) show the pairs of expressions with the highest value of  $J_2^{ex_i, ex_j}(\vec{x})$  while (b), (d) and (f) show the pairs of expressions with the lowest value of  $J_2^{ex_i, ex_j}(\vec{x})$

## 7.4. EXPERIMENTAL RESULTS

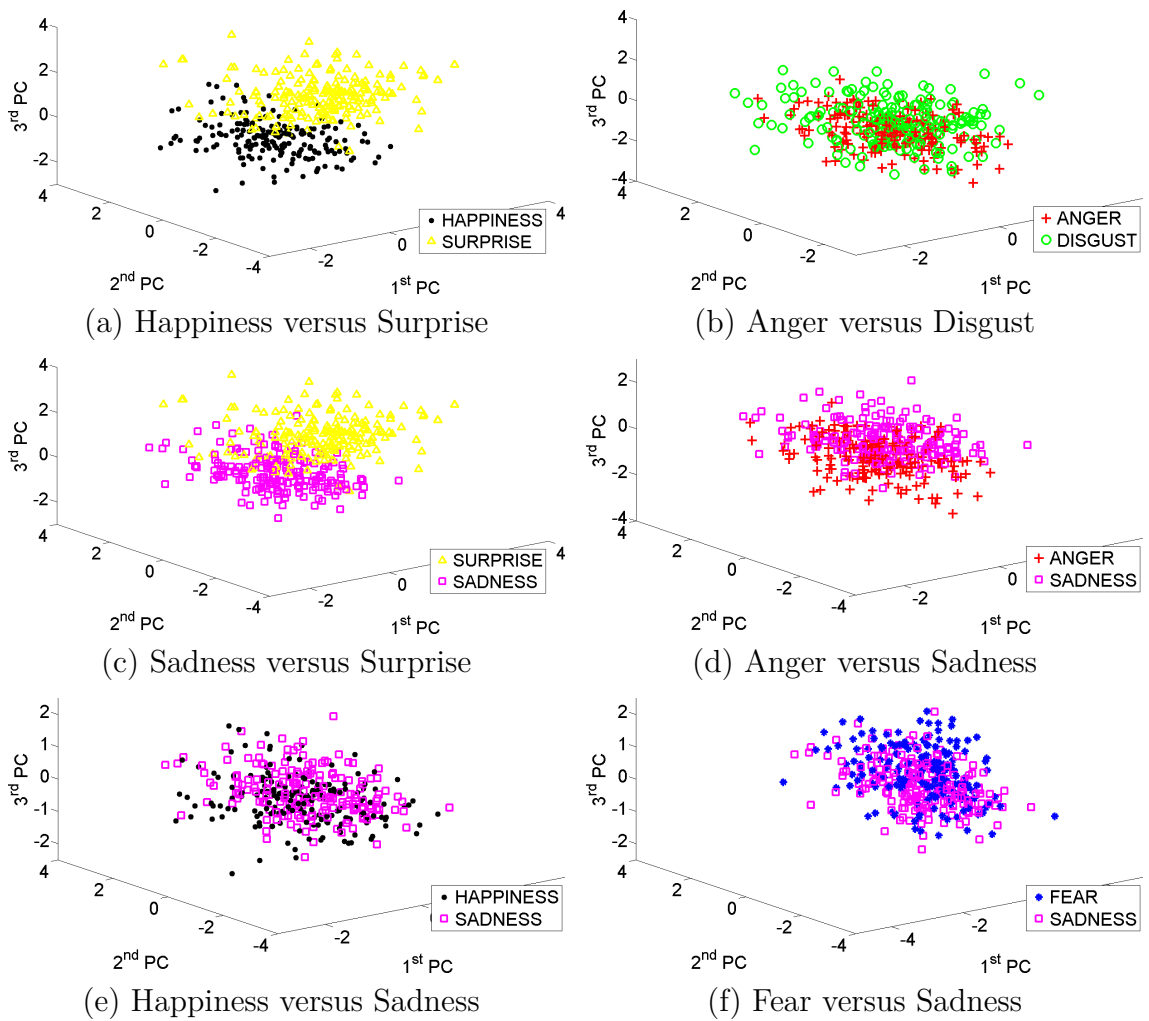


Figure 7.12: Separability analysis for the velocity field representation using first three principal components. (a), (c) and (e) show the pairs of expressions with the highest value of  $J_2^{ex_i, ex_j}(\vec{x})$  while (b), (d) and (f) show the pairs of expressions with the lowest value of  $J_2^{ex_i, ex_j}(\vec{x})$

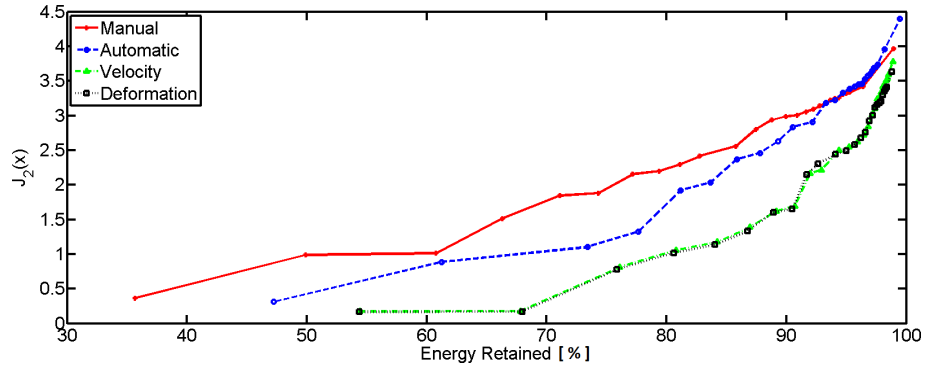


Figure 7.13: Separability of expression for different features in terms of separability criterion  $J_2(\vec{x})$

determinant:

$$J_2(\vec{x}) = \ln \frac{\det(S_B + S_W)}{\det(S_W)} \quad (7.10)$$

This separability criterion is efficient for comparison of different feature selections, lying in the completely different spaces (also with different dimensionalities), and it is intrinsically normalised and reflects the quantity of separability for features between different classes [149, 105]. The larger the value of  $J_2(\vec{x})$  means the better separability.

The separability criterion was evaluated on the different facial expression representations, namely, the manually selected landmarks, the automatically selected landmarks, the full velocity fields, and the full deformation fields and the results of the comparison are shown in Figure 7.13. For the same ratio of retained energy in the training data, the value of  $J_2(\vec{x})$  for the manually selected landmarks is the highest. In the range above 80%, the separability for the automatically selected landmarks is not significantly different from than for the manually selected landmarks. The velocity field and the deformation field based facial expression representation are the worst.

The quantitative analysis in terms of the between-expression separability was also conducted to explain the noticeable difference of the expressions overlapping in the low-dimensional spaces. To quantify the between-expression separability, the two-class case of the separability criterion is evaluated [149]. The within-class scatter matrix  $S_W^{ex_i, ex_j}$  for two-class case ( $c=2$ ) is defined as follows:

$$S_W^{ex_i, ex_j} = \frac{1}{n} \left( \sum_{k=1}^{n_{ex_i}} (\vec{x}_k^{ex_i} - \vec{m}_{ex_i})(\vec{x}_k^{ex_i} - \vec{m}_{ex_i})^T + \sum_{l=1}^{n_{ex_j}} (\vec{x}_l^{ex_j} - \vec{m}_{ex_j})(\vec{x}_l^{ex_j} - \vec{m}_{ex_j})^T \right) \quad (7.11)$$

Table 7.1: Matrix of the expression separability criterion of  $J_2^{ex_i,ex_j}(\vec{x})$  for the manually selected landmarks

	Anger	Disgust	Fear	Happiness	Sadness	Surprise
Anger	-	2.15	2.36	3.71	1.70	4.10
Disgust	-	-	2.43	3.38	2.82	3.27
Fear	-	-	-	2.09	2.05	2.78
Happiness	-	-	-	-	3.95	4.44
Sadness	-	-	-	-	-	3.90
Surprise	-	-	-	-	-	-

Table 7.2: Matrix of the expression separability criterion of  $J_2^{ex_i,ex_j}(\vec{x})$  for the automatically selected landmarks

	Anger	Disgust	Fear	Happiness	Sadness	Surprise
Anger	-	2.11	2.15	3.29	1.57	3.34
Disgust	-	-	2.23	3.31	2.45	3.06
Fear	-	-	-	2.06	1.92	2.51
Happiness	-	-	-	-	3.52	4.02
Sadness	-	-	-	-	-	3.20
Surprise	-	-	-	-	-	-

and the between-class scatter matrix  $S_B^{ex_i,ex_j}$  is defined as:

$$S_B^{ex_i,ex_j} = \frac{n_{ex_i}n_{ex_j}}{n^2}(\vec{m}_{ex_i} - \vec{m}_{ex_j})(\vec{m}_{ex_i} - \vec{m}_{ex_j})^T \quad (7.12)$$

where  $ex_i$  and  $ex_j$  are analysed expressions,  $n_{ex_i}$ ,  $n_{ex_j}$  are the numbers of samples in the  $i$ th and  $j$ th class,  $n = n_{ex_i} + n_{ex_j}$ . For each pair of selected expressions  $J_2^{ex_i,ex_j}(\vec{x})$  of the different facial expression representations was calculated.

Tables 7.1-7.4 show the separability of all pairs of expressions for different facial expression representations. A higher value of  $J_2(\vec{x})$  indicates a better discriminability between two examined expressions. The analysis of all different pairs of the facial expression representation is conducted with the retained energy of the corresponding SSM as close as possible to about 95%. These results support the visual inspection of the qualitative analysis presented in Figures 7.9-7.12. The separability of the pairs of expressions such as "happiness vs. surprise", or "sadness vs. surprise" always reach the high values. The pair of expressions such as "happiness vs. sadness" achieve the highest value for the manually selected landmarks that is consistent with the illustrative analysis done in the previous section, where the SSM based on the manually selected landmarks exhibit much better separability than the other facial expression representations (compare for example Figure 7.9c and Figure 7.10c). On the other side, the most overlapped pairs of expressions presented in the qualitative analysis, achieve very low values of the separability criterion. The lowest value is

Table 7.3: Matrix of the expression separability criterion of  $J_2^{ex_i, ex_j}(\vec{x})$  for the full deformation fields

	Anger	Disgust	Fear	Happiness	Sadness	Surprise
Anger	-	1.81	2.21	2.56	1.51	4.12
Disgust	-	-	2.14	2.19	2.29	3.19
Fear	-	-	-	1.61	1.68	2.69
Happiness	-	-	-	-	2.57	3.40
Sadness	-	-	-	-	-	3.41
Surprise	-	-	-	-	-	-

Table 7.4: Matrix of the expression separability criterion of  $J_2^{ex_i, ex_j}(\vec{x})$  for the full velocity fields

	Anger	Disgust	Fear	Happiness	Sadness	Surprise
Anger	-	1.91	2.21	2.61	1.52	3.94
Disgust	-	-	2.14	2.20	2.32	3.14
Fear	-	-	-	1.62	1.71	2.68
Happiness	-	-	-	-	2.61	3.42
Sadness	-	-	-	-	-	3.46
Surprise	-	-	-	-	-	-

achieved by the pair "anger vs. sadness".

To sum up this section, the computable results from the quantitative analysis are consistent with the illustrative examples presented in the qualitative analysis. The results suggest that the SSV built from the velocity fields can be used as a facial expression representation.

### 7.4.2 Facial expression recognition

The separability analysis conducted in the previous section indicates that the SSV feature space based on the velocity can be used for facial expression modelling and therefore for classification of various facial expressions. Hence, this section presents the extensive experimental validation of the person-independent expression classification. Although, several types of classification methods are evaluated during those experiments, the main emphasis of this research was laid on checking the adequacy of building the SSV based on the velocity fields for facial expression representation.

Data sets used for classification based validation again consists of 48 subjects, and contains neutral expression, and six basic facial expressions of anger, disgust, fear, happiness, sadness, and surprise with four different expression intensity ranges. These data were divided into six subsets containing 8 subjects with 25 faces per subject representing different expressions. During evaluation one subset is selected as the testing set (200 images), and the remaining data are used for the training

(1000 images). None of the subjects included in the training data set is included in the testing data set, because the partitioning is based on the individual subjects, rather than on the individual images. This entire procedure of selecting subsets for testing guarantees that every subject is tested for each classifier method. For each test, all classifiers are reset by default and trained to the initial state using the chosen training data set. The classification experiments were repeated six times, every time with a different selection of the subset used for the testing.

Totally four types of facial expression representations have been used for validation: the manually selected landmarks from the database [157], the automatically detected facial landmarks using the consistent log-domain Demon registration [144], the full deformation fields, and the full velocity fields.

Due to different dimensionality of the feature spaces used for comparison, the size of the SSV for every facial expression representation has been selected to obtain the retained energy of the corresponding SSM as close to each other as possible. For all experiments conducted in this section the SSV for manually selected landmarks has 20 elements corresponding to 95.26%, the SSV for automatically selected landmarks has 16 elements with 95.28% energy retained, whereas the SSVs for both the deformation fields and the velocity field, have 13 elements corresponding to 95.22% and 95.60% respectively.

Four commonly used classification methods were used for evaluation, namely linear discriminant classifier (LDC) related to the linear discriminant analysis (LDA), quadratic discriminant classifier (QDC) linked to the quadratic discriminant analysis (QDA), nearest neighbour classifier (NCC), and naive Bayes classifier (NBC). The detailed description of these methods can be found in most of the textbooks on pattern recognition e.g. [16].

The average recognition rates and standard deviations of all six experiments for different facial expression data are presented in Table 7.10. It can be seen that the LDC classifier reaches the highest recognition rate for every facial expression representation whereas the NCC classifier achieves the lowest recognition rates. As shown in Table 7.10 all facial expression representations achieve a similar recognition rate for the LDC and NBC classifier with the highest rate for the manually selected landmarks whereas the lowest recognition rate for the deformation fields was achieved. For the QDC and NCC classifier the recognition rates are the highest for the manually and automatic selected landmarks, and significantly lower for facial expression representation based on deformation and velocity fields. The manually selected landmarks are included only as a reference for other automatic methods due to the time-consuming process of their selection. The recognition rates obtained using the LDC classifier by the automatic methods are lower (maximum 15.1% less

for the deformation field based representation) than that obtained by using the manual landmark selection process. In the light of the presented results, it can be summarised that the representations of facial expressions that do not require user interaction, reach the recognition rates that are comparable with the recognition rate of the manually selected landmarks. Thus, this suggests that the algorithm used for the image registration process can recover the correct landmark correspondences. Secondly, the information included in the estimated deformation fields or the velocity fields is somehow linked to the information that is given by the selected landmarks. The second observation can lead to a partial explanation of the higher recognition rates achieved for the automatically selected landmark in the cases of the QDC, NCC and NBC methods (results given in Table 7.10). Similar to the manually selected points, automatic landmarks are selected on more representative parts of faces, therefore providing more reliable information about the current *state* of subject. On the other hand, the deformation fields and the velocity fields contain full information that may lead to be more prone to non-valuable information retained in the PCA.

The confusion matrices for LDC for different facial expression representations are given in Tables 7.5 - 7.8. From the view on the classification performance, it can be concluded that the surprise, disgust, happiness and sadness expressions can be classified in most cases with above 75% accuracy, anger with about 70% accuracy, whereas fear is only classified correctly in 61.1%. The best recognition rates (about 90%) are found for surprise, similar to the work reported in [105] for the data sets selected from the same database [157]. Examples of the confusion matrices for other classifier methods included in this comparison, namely QDC, NCC, and NBC are presented in Appendix B.

The results of misclassification support the conclusions of the quantitative separability analysis conducted in the previous section. The pairs of expressions with a low value of separability criterion  $J_2^{ex_i, ex_j}(\vec{x})$  are more prone to be misclassified (e. g. fear and sadness, or anger and sadness). Furthermore, the expression of fear achieves very low values of separability criterion  $J_2^{ex_i, ex_j}(\vec{x})$  for each facial expression representation and consequently as it can be expected, the misclassification error is the highest (often misclassified with happiness or sadness). In the same manner, the expressions with high value of separability criterion  $J_2^{ex_i, ex_j}(\vec{x})$  achieve high recognition rates (e. g. happiness, or surprise). Table 7.9 summarises the success rates of the recognition for the different representations included in Tables 7.5 - 7.8 to emphasise the recognition performance of the six facial expressions using the different facial expression representations. Taking into account the *subjective* nature of the ground truth data and the results achieved by the human observers [105], the

results can be considered as reasonable.

The quantitative comparison of the velocity based facial expression representation with the existing work is a challenging problem. Although the facial expression database [149] evaluated for the experimental section is widely used by the computer vision community, some other work utilised different information (e. g. texture, 3D shapes) and different subset of subjects [105, 86]. Moreover, the comparisons between various facial expression representations are challenging due to different evaluation methodologies.

The qualitative comparison of this approach with the work reported by Quan et al. [105] for the same database shows a similar pattern in characteristics for classified expressions. In spite of evaluating the 3D landmarks in their work, the surprise expression always reaches the highest recognition rate. At the same time, fear is often confused with sadness or with happiness.

The facial expression recognition based on the automatically selected landmarks, the deformation fields, or the velocity fields can be affected by the method used for the generation/detection of those features. In context of the facial expression representation presented in this section, the performance can be considered in terms of the robustness and accuracy of the image registration algorithms used for the automatic landmark localisation, and the deformation fields and the velocity fields estimated. The main drawback of the algorithm used for image registration (described in Section 3.2) is that it relies on the SSD as a similarity measure. Although, the additional pre-processing step was performed to remove the difference between skin patterns for different subjects included in the database, the uncontrolled conditions can still make the image registration process inaccurate and unreliable [149]. Another problem that has to be taken into account is the topology changes between images of the same subject with different facial expressions. For example, the neutral expression image does not contain the texture of open mouth and tooth whereas this pattern is included in images of happiness, disgust, fear and surprise expression. As the matter of fact that these topology changes can also occur for eyes (the squinted eyes for the angry or fear expression), the problem can possibly significantly deteriorate the recognition rates.

In order to check the recognition sensitivity to the quality of the facial expression representation estimation, the recognition rates of the different expression intensity levels were calculated for the different classifier methods. The results obtained from this assessment are shown in Figure 7.14. For the manually selected landmarks, the recognition rates grow when the expression intensity levels increase from low to highest for the LDC and QDC classifier method. For the automatically selected landmarks (Figure 7.14a), the recognition rates grow when the expression intensity

## 7.4. EXPERIMENTAL RESULTS

Table 7.5: Confusion matrix of LDC for manually selected landmarks

Input/ Output	Anger (%)	Disgust (%)	Fear (%)	Happiness (%)	Sadness (%)	Surprise (%)
Anger	<b>74.5</b>	4.7	3.1	3.1	14.6	0.0
Disgust	8.3	<b>81.8</b>	4.7	0.5	3.6	1.0
Fear	7.8	1.6	<b>59.9</b>	11.5	16.1	3.1
Happiness	4.2	2.1	8.3	<b>85.4</b>	0.0	0.0
Sadness	16.7	1.6	4.2	0.0	<b>77.6</b>	0.0
Surprise	1.0	2.1	4.2	0.5	2.6	<b>89.6</b>

Table 7.6: Confusion matrix of LDC for automatic selected landmarks

Input/ Output	Anger (%)	Disgust (%)	Fear (%)	Happiness (%)	Sadness (%)	Surprise (%)
Anger	<b>68.8</b>	5.2	5.2	2.6	18.2	0.0
Disgust	12.5	<b>76.6</b>	5.7	0.5	3.6	1.0
Fear	7.8	2.6	<b>55.2</b>	14.1	19.3	1.0
Happiness	4.1	1.6	11.5	<b>82.3</b>	0.0	0.5
Sadness	19.8	3.1	4.7	0.0	<b>72.4</b>	0.0
Surprise	1.0	3.1	7.8	0.5	2.6	<b>87.0</b>

Table 7.7: Confusion matrix of LDC for full deformation fields

Input/ Output	Anger (%)	Disgust (%)	Fear (%)	Happiness (%)	Sadness (%)	Surprise (%)
Anger	<b>74.5</b>	9.9	1.0	2.6	10.9	1.0
Disgust	9.4	<b>75.5</b>	6.3	5.7	1.6	1.6
Fear	5.7	2.6	<b>56.8</b>	15.6	11.5	7.8
Happiness	2.1	6.3	16.1	<b>74.0</b>	1.0	0.5
Sadness	12.0	0.5	7.3	2.1	<b>78.1</b>	0.0
Surprise	2.6	1.0	2.1	2.1	1.0	<b>91.1</b>

Table 7.8: Confusion matrix of LDC for full velocity fields

Input/ Output	Anger (%)	Disgust (%)	Fear (%)	Happiness (%)	Sadness (%)	Surprise (%)
Anger	<b>77.6</b>	7.8	0.5	2.1	11.5	0.5
Disgust	8.9	<b>77.1</b>	5.2	5.2	2.6	1.0
Fear	4.7	3.6	<b>61.5</b>	9.9	13.0	7.3
Happiness	3.1	6.3	14.1	<b>76.0</b>	0.0	0.5
Sadness	15.1	0.0	6.8	1.6	<b>76.6</b>	0.0
Surprise	1.6	1.6	3.6	1.0	1.6	<b>90.6</b>

Table 7.9: Summary of the recognition rates from Tables 7.5 - 7.8.

Feature/ Expression	Anger (%)	Disgust (%)	Fear (%)	Happiness (%)	Sadness (%)	Surprise (%)
Manual	74.5	81.8	59.9	85.4	77.6	89.6
Automatic	68.8	76.6	55.2	82.3	72.4	87.0
Deformation	74.5	75.5	56.8	74.0	78.1	91.1
Velocity	77.6	77.1	61.5	76.0	76.6	90.6

Table 7.10: Average recognition rates for different classifier methods

Feature/ classifier	LDC (%± SD)	QDC (%± SD)	NNC (%± SD)	NBC (%± SD)
Manually	78.1±4.2	74.0±4.8	61.5±1.1	74.3±2.4
Automatic	73.4±6.0	<b>69.1±6.0</b>	<b>61.9±4.9</b>	<b>70.8±4.0</b>
Deformation	75.0±5.2	58.9±2.9	56.2±5.0	69.1±5.0
Velocity	<b>76.6±4.3</b>	59.3±4.1	57.7±5.1	69.9±5.2

SD: Standard Deviation

levels increase but only from low to high. For the highest expression intensity levels, the recognition rate is similar for the LDC classifier and lower for others. For the deformation field and the velocity field facial expression representations, the recognition rates grow only from low to middle. Then, the recognition rates stay at the similar level or slightly lower for all classifier methods. First of all, these experimental results immediately illustrate that the quality of the automatic landmark selection and the deformation and the velocity fields estimation has a direct impact on the performance of the facial expression recognition systems (especially for the high and highest intensity expression levels); secondly, the facial expression recognition of low-intensity expressions from the single static data can be in some cases an ambiguous task [149].

Comparatively, similar experiments in terms of machine learning methodologies were conducted by Ashburner [5] and the deformation field and velocity field based registration results were utilised to provide the patterns to distinguish the genders and the age of the subjects using the MRI brain images. The assessment was done using both the linear and non-linear support-vector machine classifier (SVM) for 471 subjects' brains where 400 of them were used for learning and the remaining part for testing. In order to get a precise measure of accuracy, the experiments were repeated 50 times. In both cases most of the results, for prediction of the gender and for prediction of the age of the subjects, showed slightly higher accuracy in terms of the predicted sexes (male, female) and distance to real age for the velocity field based descriptors. The improvement was only half percent thereby it was summarised as not significant. Thus, the results given in Table 7.10 where the max-

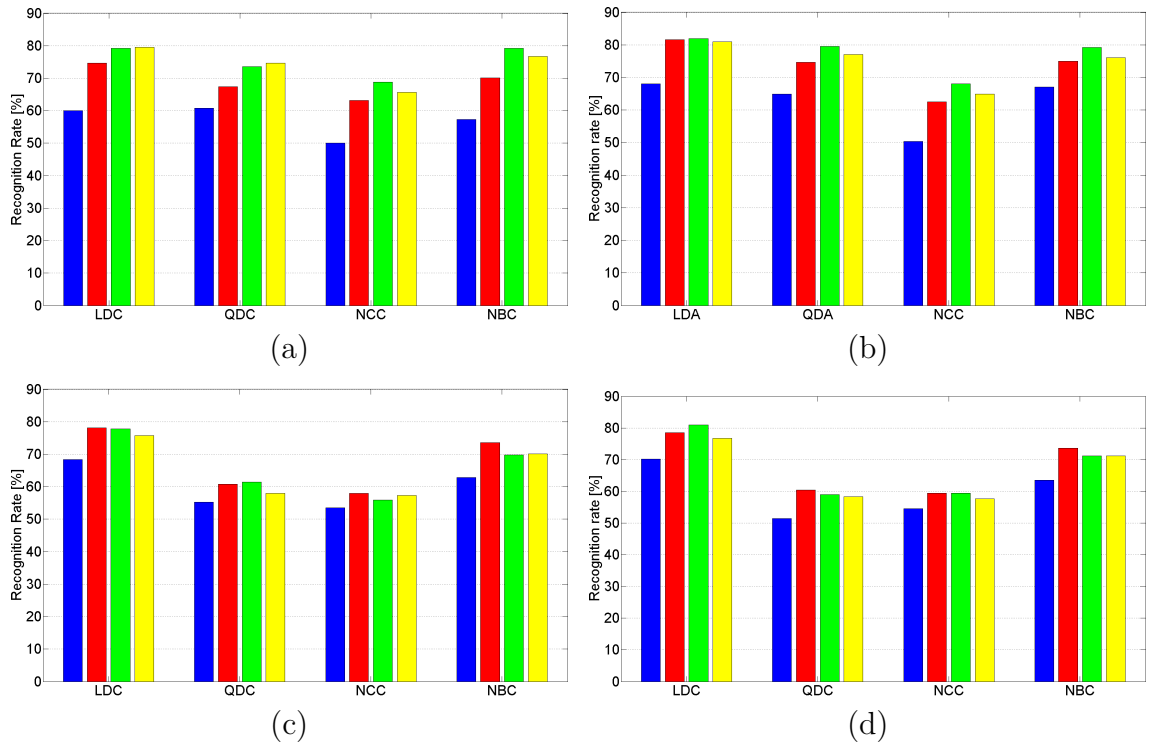


Figure 7.14: Recognition rates of four classification methods for different intensity expression levels: low (blue), middle (red), high (green), and highest (yellow) for the different facial expressions representation: (a) manually selected landmarks, (b) automatically selected landmarks, (c) the deformation fields, and (d) the velocity fields.

imum improvements of the facial expression recognition based on the velocity fields are about 1.6% for the LDC (and minimum 0.4% for the QDC), can be considered as reasonable and somehow comparable to the results of the aforementioned brain data analysis.

## 7.5 Summary

In this chapter, a novel facial expression representation has been introduced for facial expressions modelling and facial expression recognition systems.

The proposed facial expression recognition system generates first the *mean face* by the simultaneous implicit group-wise registration of faces with neutral expression included in the training data set, and this step enables all faces to be mapped to the *common face space* using the estimated transformations and thereby alleviating (at least theoretically) the individual variations such as race, gender, and face shape. Then, the intra- subject face expression registration to the subject-independent *mean face* allows the Statistical Shape Model to be built based on the velocity fields, and trained model of facial expressions is utilised for subject-independent facial

expression recognition.

Prior to the facial expression recognition experiments, the qualitative and the quantitative separability analysis of the different facial expression representations was conducted to assess whether the SSM based on the velocity fields can capture different facial expressions. The visual illustrations of the four different SSVs in the low-dimensional spaces exhibit good clustering properties to distinguish some facial expressions such as surprise, happiness, and sadness. The computable numerical criterion calculated for both the separability analysis and the between-expression separability analysis, confirms the observations from the visual inspections.

The facial expression recognition experiments were conducted using several classification methods such LDC, QDC, NCC, and NBC. The obtained results show that the Shape Space Vectors built based on the velocity fields can be considered as an effective facial expression representation for the Statistical Shape Model. Although, the highest recognition rates for all classification algorithms was reached by the SSV based on the manually selected landmarks, the velocity field based SSV is only 1.5% lower for the LDC classifier. When recognition results achieved using the velocity fields are compared with the other facial expression representations, it can be seen that the SSV built on the velocity fields is able to achieve a comparable recognition rate. Furthermore, referring to the conclusion from the discriminability analysis, the misclassification errors are linked to the pairs of the expressions with lowest values of the separability criterion. This makes all the experimental results from both separability analysis and the recognition experiments consistent with each other.

Future investigations can consider extending the proposed facial expression recognition system to the dynamic sequences. The temporal information estimated by the velocity fields can lead to improvement of the performance of current systems. Although it was not investigated in the work described here, it seems that the velocity field representation can represent other kinds of the expressions such as micro-expressions that are being investigated extensively recently [99, 126] as long as any observable pattern(s) can be captured by the intensity-based image registration. As an illustration, the recent method making an attempt to spot the micro-expressions proposed by Shreve et al. [126] utilised the optical based image registration algorithm, that may suggest the importance of further investigation of the velocity field based approach in this particular area.

# Chapter 8

## Contributions and future works

This chapter summarises the author’s contributions both on the image registration algorithms and their applications presented in this thesis. In addition, the possible extensions and further investigations are proposed and discussed.

### 8.1 Contributions

The first part of the presented work aimed at the investigation on the deformable image registration algorithms, with a particular focus on the methods that produce diffeomorphic transformations. The various diffeomorphic image registration approaches such as the *small step approach* and different formulations of the log-Euclidean framework were validated for medical applications using a wide spectrum of real data sets. The second part of this thesis looked at the possible usage of the aforementioned image registration tools for developing more advanced systems for the motion modelling and the dense deformation field prediction.

The author’s contributions to the methodology of image registration are as follows:

- In contrast to other works, where the Demon approach with the exponential update scheme or the log-domain Demon has been investigated on its own, the presented work considered various novel combinations of the optimisation methods and deformation field parameterisations. Thus, the Newton’s iteration method and the steepest descent-like method and their various versions presented in this thesis can be also considered as new image registration techniques.
- Another contribution described in this thesis, is a robust method for inversion of the deformation field. The presented experimental results showed an

improved performance in terms of the inverse consistency criterion when compared to other methods of inverting deformation fields especially when the large deformation has to be inverted. Additionally, this algorithm can be seen as an extension to the already known procedure, but established via the optimisation framework to make it mathematically consistent. This method can be used in the image registration with the symmetric warping of the input images (also evaluated in this thesis), and other applications are also possible. The method for inversion of the deformation field and the symmetric image registration is published in [96].

- Due to the inherited image registration problems, the quantitative and qualitative examination of commonly known algorithms for the pairwise deformable image registration was conducted in the Chapter 4. The evaluated experiments included not only different approaches, but also different log-domain formulations of those algorithms and took into account various additional constraints such as the inverse consistency criterion or the symmetrisation of the image registration. Moreover, a wide spectrum of medical data was used (MRI of brains, MRI of pelvic-area data, and CT of lungs) thereby the experimental section is more comprehensive than those previously reported. The obtained results leads to the conclusion that the log-Euclidean parameterisation of the deformation fields can be successfully utilised in the biomedical applications. The experimental results suggest also that image registration with symmetrical warping of the input images outperforms the classical approaches. Since, it was shown in this thesis that this symmetrisation can be easily incorporated to the considered algorithms, the advantages of the previously mentioned parameterisation can be simply introduced.
- Chapter 5 presented the log-domain implicit group-wise image registration. Although, in principle it was inspired by the already known group-wise image registration algorithm, the proposed version benefits from the log-domain parameterisation of deformation fields to link the various sets of images related to the different subjects and establishes the *common subject space* and between-subject correspondences therein via the stationary velocity fields. Thus, the proposed method is very efficient because the inverse mappings can be calculated almost without additional cost (by the backward integration of the velocity fields using the fast scaling and squaring algorithm). Secondly, the results of performing the proposed log-domain implicit group-wise registration can be directly used for calculating the vectorial statistics e. g. for analysis of the inter-subject variability. The group-wise registration using stationary

velocity field representation is published in [98].

The second part of this thesis made an attempt to utilise the aforementioned approaches of the diffeomorphic image registration as the principal elements of more sophisticated systems for the movement (position) estimation of the organs in the pelvic-area based on the dense deformation field prediction, or facial expression recognition where the author's contributions can be enumerated as follows:

- Chapter 6 presented a novel technique for estimation of model-based image dense deformation fields with an implicit surface representation used as an effective and robust deformation descriptor. The proposed framework used the *general* (subject independent) motion model estimated from the representative training data set of MRI data and the segmented shapes, and the corresponding displacement fields are parameterised via the stationary velocity fields estimated using a fast and efficient diffeomorphic registration scheme, formulated in the consistent log-Euclidean framework. Opposite to most of the current approaches aiming at prediction of the relevant deformations, the proposed model is subject-independent and furthermore, the log-domain parameterisation ensures the diffeomorphic properties throughout the prediction stage. The presented experimental results on the artificial data demonstrated that with the help of the proposed method, it is possible to predict a dense displacement field solely from the measured deformations of the implicit surface. Additionally, the experiments conducted with the real data showed that it is possible to predict the deformation field and therefore the position of the prostate from shape deformations of the bladder/rectum.
- The second application investigated in Chapter 7 was facial expression recognition using the diffeomorphic image registration framework. The proposed approach generated first the *mean* face by the simultaneous implicit group-wise registration of the faces with neutral expression in the training data set. Therefore, this step enabled all faces to be mapped to the *common face space* using the estimated transformations and thereby alleviating (at least theoretically) the individual variations such as race, gender, and face shape. Then, the intra-subject face expression registration to the subject-independent *mean* face allowed the Statistical Shape Model to be built based on the velocity fields. The trained model of facial expressions can be further utilised for subject-independent facial expression recognition. The results of the facial expression recognition using the velocity field based face representation are published in [98].

Both applications are extensively evaluated based on the real representative data sets of the three-dimensional MRI volumes and the two-dimensional face images, and the obtained results indicate the possibility of the practical usability of the proposed techniques.

## 8.2 Future works

From the methodological perspective of the presented image registration algorithms, the computational burden can be noticeably reduced by the implementing these algorithms based on the graphic processing units (GPU) using the Compute Unified Device Architecture (CUDA) [44]. Most of the operations embedded in the presented registration algorithms are the pixel-wise operations, therefore the parallel implementation should be possible without significant effort. Similarly, the efficient implementation should be introduced to the proposed log-domain implicit group-wise registration where a linear computational requirement with respect to the number of input images has been experimentally found.

The implicit group-wise registration can be conceivably improved by using some pre-processing steps either to select the most representative images to be included in registration or to weight of the impact of the particular images involved in registration on the final *mean*. This pre-processing step can be possibly achieved via some kind of the manifold learning techniques [152].

The quantitative and qualitative analysis of the presented algorithms that was performed in Chapter 4 can be potentially extended by carrying out experiments for functional images such fMRI or PET to check the accuracy of the state-of-the-art algorithms for new types of information fusion. Thus far, only the knowledge about the structures of organs was provided based on the intensity values for the evaluated data sets.

The comparison of the diffeomorphic image registration algorithms can also benefit from including other methodologies, that are only mentioned in this thesis such as the Large Deformation Diffeomorphic Metric Mapping (LDDMM) [15, 14], or geodesic shooting technique [89, 6, 146].

The deformation field prediction system described in Chapter 6 seems to be a valuable contribution to the field of the adaptive radiotherapy of prostate. The limitation of the proposed system in the current implementation such as mono-modality evaluation where the constructed motion model is then evaluated for the measurement coming from the same modality data, can be omitted by finding out the effective measurements that exists in the typical radiotherapy imaging procedures e. g. CBCT. Although it has not been validated experimentally in this thesis, such

surrogates as proposed in this work e. g. the implicit surfaces of bladder or rectum can be perhaps relatively simply extracted (contrary to the direct image registration process) from the low quality CBCT images, small number of ultrasonic scans, or CT projection images.

Another possible application that can utilise the proposed motion model is an image registration framework with statistically derived constraints. The work reported by Albrecht et al. [3], where the Gaussian distribution of the plausible deformation fields is assumed, can be extended to any pre-learned probability e. g. following contributions coming from the work on segmentation from noisy images [161]. Indeed, the similar methodology of driving the updates of the deformation field via specific path but for the discrete case was proposed recently and is known as the GRAM algorithm (GRAM stands for geodesic registration on anatomical manifolds) [52].

The usage of the main eigen modes for the parametric implicit shape representation (introduced in Chapter 6) has a drawback as the sign distance function is not closed under additive operation of the sign distance function. Although it was shown that this theoretical inconsistency does not affect the performance of this shape representation in practice [140], other representations can be used instead. Pohl et al. [101] introduced the concept of the Logarithm of the Odds (LogOdds) for a shape representation. The LogOdds has been shown to demonstrate desirable properties for medical imaging e. g. the representation encodes the shape of an anatomical structure as well as the variations within that structure are embedded in a vector space. Thus, the LogOdds representation that forms a *shape* vector space and together with the stationary velocity log-domain framework, that provides a *displacement* vector space, can establish the dense deformation field prediction system in the mathematical consistent formulation and possibly outperform the current methodology in practical applications.

From the perspective of the facial expressions recognition systems as future investigation, the system utilising the dynamic high-resolution sequences of facial expressions [85] can be potentially considered. The temporal information estimated through the diffeomorphic image registration and parameterised via the velocity fields can lead to performance improvement of the current system. Although it was not investigated in the described work, it seems that the velocity field representation can represent other kinds of the expressions such as micro-expressions that are being investigated recently [99, 126] as long as any observable pattern(s) can be captured by the intensity-based image registration. As an illustration, the recent method making an attempt to spot the micro-expressions proposed by Shreve et al. [126] utilised the optical based image registration algorithm, that may suggest the importance of further investigation of the velocity field based approach in this particular

area.

# References

- [1] <http://www.na-mic.org/Wiki/index.php/Downloads#Data>.
- [2] <http://www.med.harvard.edu/aanlib/home.html>.
- [3] Albrecht Thomas, Lüthi Marcel, and Vetter Thomas. A statistical deformation prior for non-rigid image and shape registration. In *Proc. IEEE Conference on Computer Vision and Pattern Recognition (CVPR)*, pages 1–8, 2008.
- [4] Arsigny Vincent, Commowick Olivier, Pennec Xavier, and Ayache Nicholas. A log-euclidean framework for statistics on diffeomorphisms. In *Proc. 9th International Conference on Medical Image Computing and Computer-Assisted Intervention (MICCAI)*, pages 924–931, 2006.
- [5] Ashburner John. A fast diffeomorphic image registration algorithm. *NeuroImage*, 38(1):95–113, 2007.
- [6] Ashburner John and Friston Karl J. Diffeomorphic registration using geodesic shooting and gauss-newton optimisation. *Neuroimage*, 55(3):954–967, Apr 2011.
- [7] Ashburner John, Andersson J., and Friston K.J. Image registration using a symmetric prior - in three-dimensions. *Human Brain Mapping*, 9(4):212–225, 2000.
- [8] Aubert-Broche Berengere, Griffin M., Pike G. B., Evans A. C., and Collins D. L. Twenty new digital brain phantoms for creation of validation image data bases. *IEEE Transactions on Medical Imaging*, 25(11):1410–1416, 2006.
- [9] Avants Brian B. and Gee James C. Geodesic estimation for large deformation anatomical shape averaging and interpolation. *Neuroimage*, 23 Suppl 1:S139–S150, 2004.
- [10] Avants Brian B., Epstein C. L., Grossman M., and Gee James C. Symmetric diffeomorphic image registration with cross-correlation: evaluating automated

- 
- labeling of elderly and neurodegenerative brain. *Medical Image Analysis*, 12(1): 26–41, Feb 2008.
- [11] Bajcsy Ruzena and Kovačič Stane. Multiresolution elastic matching. *Computer Vision, Graphics, and Image Processing*, 46:1–21, April 1989.
- [12] Baker Simon, Scharstein Daniel, Lewis J. P., Roth Stefan, Black Michael J., and Szeliski Richard. A database and evaluation methodology for optical flow. *International Journal of Computer Vision*, 92:1–31, March 2011.
- [13] Bartlett Marian Stewart, Littlewort Gwen, Fasel Ian, and Movellan Javier R. Real time face detection and facial expression recognition: Development and applications to human computer interaction. In *Proc. Conference on Computer Vision and Pattern Recognition Workshop (CVPRW)*, 2003.
- [14] Beg M. F. and Khan A. Symmetric data attachment terms for large deformation image registration. *IEEE Transactions on Medical Imaging*, 26(9):1179–1189, 2007.
- [15] Beg M. Faisal, Miller Michael I., Trouvé Alain, and Younes Laurent. Computing large deformation metric mappings via geodesic flows of diffeomorphisms. *International Journal of Computer Vision*, 61:139–157, February 2005.
- [16] Bishop Christopher M. *Pattern Recognition and Machine Learning (Information Science and Statistics)*. Springer, 1st ed. 2006. corr. 2nd printing edition, October 2007.
- [17] Bossa Matias, Hernandez Monica, and Olmos Salvador. Contributions to 3d diffeomorphic atlas estimation: application to brain images. In *Proc. 10th International Conference on Medical Image Computing and Computer-Assisted Intervention (MICCAI)*, MICCAI’07, pages 667–674, Berlin, Heidelberg, 2007. Springer-Verlag.
- [18] Bossa Matias, Zacur E., and Olmos Salvador. Algorithms for computing the group exponential of diffeomorphisms: Performance evaluation. In *Proc. IEEE Computer Society Conference Computer Vision and Pattern Recognition Workshops (CVPRW)*, pages 1–8, 2008.
- [19] Bro-Nielsen Morten and Gramkow Claus. Fast fluid registration of medical images. In *Proc. 4th International Conference on Visualization in Biomedical Computing*, pages 267–276, London, UK, 1996. Springer-Verlag.
-

- 
- [20] Bulat Jaroslaw, Duda Krzysztof, Socha Mirosław, Turcza Paweł, Zielinski Tomasz, and Duplaga Mariusz. Computational tasks in bronchoscope navigation during computer-assisted transbronchial biopsy. In *Proc. 8th International Conference on Computational Science, ICCS '08*, pages 178–187, Berlin, Heidelberg, 2008. Springer-Verlag.
- [21] Castadot Pierre, Lee John Aldo, Parraga Adriane, Geets Xavier, Macq Benoît, and Grégoire Vincent. Comparison of 12 deformable registration strategies in adaptive radiation therapy for the treatment of head and neck tumors. *Radiotherapy & Oncology*, 89(1):1–12, Oct 2008.
- [22] Chandrashekara Raghavendra, Rao Anil, Sanchez-Ortiz Gerardo Ivar, Mohiaddin Raad H, and Rueckert Daniel. Construction of a statistical model for cardiac motion analysis using nonrigid image registration. In *Proc. 18th International Conference on Information Processing in Medical Imaging (IPMI)*, volume 18, pages 599–610, Jul 2003.
- [23] Chang Ping-Lin, Chen Dongbin, and Edwards Philip. Registration of a 3d preoperative model with 2d endoscopic images using parallel tracking and mapping (ptam) with colour-consistency. In *Proc. Conference on Medical Image Understanding and Analysis (MIUA)*, pages 179–184, July 2011.
- [24] Chefd’hotel Christophe, Hermosillo Gerardo, and Faugeras Olivier. A variational approach to multi-modal image matching. In *Proc. IEEE Workshop Variational and Level Set Methods in Computer Vision*, pages 21–28, 2001.
- [25] Chefd’hotel Christophe, Hermosillo Gerardo, and Faugeras Olivier. Flows of diffeomorphisms for multimodal image registration. In *Proc. IEEE International Symposium on Biomedical Imaging (ISBI)*, pages 753–756, 2002.
- [26] Christensen G. E., Rabbitt R. D., and Miller M. I. Deformable templates using large deformation kinematics. *IEEE Transactions on Image Processing*, 5(10):1435–1447, 1996.
- [27] Christensen Gary E. and Johnson Hans J. Consistent image registration. *IEEE Transactions on Medical Imaging*, 20(7):568–582, 2001.
- [28] Christensen Gary E, Johnson Hans J, and Vannier Michael W. Synthesizing average 3d anatomical shapes. *Neuroimage*, 32(1):146–158, Aug 2006.
- [29] Cifor Amalia, Risser Laurent, Chung D., Anderson E.M., and Schnabel Julia. Hybrid feature-based log-demons registration for tumour tracking in 2-d liver

- 
- ultrasound images. In *Proc. IEEE International Symposium on Biomedical Imaging (ISBI)*, 2012.
- [30] Clarenz U., Droske M., Henn S., Rumpf M., and Witsch K. Computational methods for nonlinear image registration. In Scherzer O., editor, *Proc. Mathematical Models for Registration and Applications to Medical Imaging, Mathematics in Industry*, volume 10, 2006.
- [31] Collignon A, Maes F, Delaere D, Vandermeulen D, Suetens P, and Marchal G. Automated multi-modality image registration based on information theory. In *Proc. 14th International Conference on Information Processing in Medical Imaging*, pages 263–274, 1995.
- [32] Collins D. Louis and Evans Alan C. Animal: Validation and applications of nonlinear registration-based segmentation. *IJPRAI*, 11(8):1271–1294, 1997.
- [33] Cootes T. F., Taylor C. J., Cooper D. H., and Graham J. Active shape models - their training and application. *Computer Vision and Image Understanding*, 61: 38–59, January 1995.
- [34] Daum Volker, Hahn Dieter, Hornegger Joachim, and Kuwert Torsten. Pca regularized nonrigid registration for pet/mri attenuation correction. In Wells William, Joshi Sarang, and Pohl Kilian, editors, *Proc. MICCAI Workshop on Probabilistic Models For Medical Image Analysis*, pages 127–138, 2009.
- [35] Deriche R. Fast algorithms for low-level vision. *IEEE Transactions on Pattern Analysis and Machine Intelligence*, 12(1):78–87, 1990.
- [36] Ehrhardt Jan, Werner René, Schmidt-Richberg Alexander, and Handels Heinz. Statistical modeling of 4d respiratory lung motion using diffeomorphic image registration. *IEEE Transactions on Medical Imaging*, 30(2):251–265, Feb 2011.
- [37] Fasel Beat and Luetttin Juergen. Automatic facial expression analysis: A survey. *Pattern Recognition*, 36(1):259–275, 2003.
- [38] Fischer Bernd and Modersitzki Jan. Curvature based image registration. *Journal of Mathematical Imaging and Vision*, 18:81–85, January 2003.
- [39] Fischer Bernd and Modersitzki Jan. Ill-posed medicine - an introduction to image registration. *Inverse Problems*, 24(3):034008, 2008.

- 
- [40] Foskey Mark, Davis Brad, Goyal Lav, Chang Sha, Chaney Ed, Strehl Nathalie, Tomei Sandrine, Rosenman Julian, and Joshi Sarang. Large deformation three-dimensional image registration in image-guided radiation therapy. *Physics in Medicine and Biology*, 50(24):5869–5892, Dec 2005.
- [41] Friston K.J., Ashburner J., Kiebel S.J., Nichols T.E., and Penny W.D. *Statistical Parametric Mapping: The Analysis of Functional Brain Images*. Academic Press, 2007.
- [42] Geng Xiujuan, Christensen Gary E, Gu Hong, Ross Thomas J, and Yang Yihong. Implicit reference-based group-wise image registration and its application to structural and functional mri. *Neuroimage*, 47(4):1341–1351, Oct 2009.
- [43] Glocker Ben, Sotiras Aristeidis, Komodakis Nikos, and Paragios Nikos. Deformable medical image registration: setting the state of the art with discrete methods. *Annual Review of Biomedical Engineering*, 13:219–244, Aug 2011.
- [44] Gu Xuejun, Pan Hubert, Liang Yun, Castillo Richard, Yang Deshan, Choi Dongju, Castillo Edward, Majumdar Amitava, Guerrero Thomas, and Jiang Steve B. Implementation and evaluation of various demons deformable image registration algorithms on a gpu. *Physics in Medicine and Biology*, 55(1):207–219, Jan 2010.
- [45] Guimond A., Roche A., Ayache N., and Meunier J. Three-dimensional multimodal brain warping using the demons algorithm and adaptive intensity corrections. *IEEE Transactions on Medical Imaging*, 20(1):58–69, 2001.
- [46] Guimond Alexandre, Meunier Jean, and Thirion Jean-Philippe. Average brain models: A convergence study. *Computer Vision and Image Understanding*, 77(2):192–210, 2000.
- [47] Haber Eldad and Modersitzki Jan. Numerical methods for volume preserving image registration. *Inverse Problems*, Volume 20:1621–1638, 2004.
- [48] Haber Eldad and Modersitzki Jan. Intensity gradient based registration and fusion of multi-modal images. *Methods of Information in Medicine*, 46(3):292–299, 2006.
- [49] Haber Eldad and Modersitzki Jan. Image registration with guaranteed displacement regularity. *International Journal of Computer Vision*, 71(3):361–372, 2007.
-

- 
- [50] Haber Eldad, Horesh R., and Modersitzki Jan. Numerical methods for constrained image registration. *Numerical Linear Algebra with Applications*, 17(2-3): 343–359, 2010.
- [51] Hajnal J. V., Hill L. G. D., and Hawkes J. D. *Medical Image Registration (Biomedical Engineering)*. CRC Press, Cambridge, June 2001.
- [52] Hamm Jihun, Ye Dong Hye, Verma Ragini, and Davatzikos Christos. Gram: A framework for geodesic registration on anatomical manifolds. *Medical Image Analysis*, 14(5):633–642, Oct 2010.
- [53] Han Xiao, Hibbard Lyndon S., and Willcut Virgil. An efficient inverse-consistent diffeomorphic image registration method for prostate adaptive radiotherapy. In *Proc. MICCAI Workshop on Prostate Cancer Imaging. Computer-Aided Diagnosis, Prognosis, and Intervention*, MICCAI’10, pages 34–41, Berlin, Heidelberg, 2010. Springer-Verlag.
- [54] Heinrich Mattias P., Jenkinson M., Brady Mike, and Schnabel Julia. Globally optimal registration on a minimum spanning tree using dense displacement sampling. In *Proc. 15th International Conference on Medical Image Computing and Computer-Assisted Intervention (MICCAI)*, 2012.
- [55] Hermosillo Gerardo and Faugeras Olivier. Dense image matching with global and local statistical criteria: a variational approach. In *Proc. IEEE Computer Society Conference Computer Vision and Pattern Recognition (CVPR)*, volume 1, 2001.
- [56] Hermosillo Gerardo, Chef d’Hotel Christophe, and Faugeras Olivier. A Variational Approach to Multi-Modal Image Matching. Technical Report RR-4117, INRIA, February 2001.
- [57] Hermosillo Gerardo, Chef d’Hotel Christophe, and Faugeras Olivier D. Variational methods for multimodal image matching. *International Journal of Computer Vision*, 50(3):329–343, 2002.
- [58] Hernandez Monica, Olmos Salvador, and Pennec Xavier. Comparing algorithms for diffeomorphic registration: Stationary lddmm and diffeomorphic demons. In Pennec X. and Joshi S., editors, *Proc. International Workshop on the Mathematical Foundations of Computational Anatomy (MFCA)*, September 2008.
- [59] Horn Berthold K. P. and Schunck Brian G. Determining optical flow. *ARTIFICIAL INTELLIGENCE*, 17:185–203, 1981.
-

- 
- [60] Hsieh Chao-Kuei, Lai Shang-Hong, and Chen Yung-Chang. An optical flow-based approach to robust face recognition under expression variations. *IEEE Transactions on Image Processing*, 19(1):233–240, 2010.
- [61] Hu Yipeng, Ahmed Hashim Uddin, Taylor Zeike, Allen Clare, Emberton Mark, Hawkes David, and Barratt Dean. Mr to ultrasound registration for image-guided prostate interventions. *Medical Image Analysis*, 16(3):687–703, Dec 2012.
- [62] Huang Xiaolei, Paragios N., and Metaxas D. N. Shape registration in implicit spaces using information theory and free form deformations. *IEEE Transactions on Pattern Analysis and Machine Intelligence*, 28(8):1303–1318, 2006.
- [63] Johnson Hary J. and Christensen Gary E. Consistent landmark and intensity-based image registration. *IEEE Transactions on Medical Imaging*, 21(5):450–461, 2002.
- [64] Joshi Sarang, Davis Brad, Jomier Matthieu, and Gerig Guido. Unbiased diffeomorphic atlas construction for computational anatomy. *Neuroimage*, 23(1):151–160, 01 2004.
- [65] Keeling Stephen L. and Ring Wolfgang. Medical image registration and interpolation by optical flow with maximal rigidity. *Journal of Mathematical Imaging and Vision*, 23:47–65, July 2005.
- [66] Khan Ali R. and Beg Mirza Faisal. Representation of time-varying shapes in the large deformation diffeomorphic framework. In *Proc. IEEE International Symposium on Biomedical Imaging (ISBI)*, pages 1521–1524, 2008.
- [67] Khan Ali R., Trouve Alain, and Beg Mirza Faisal. Cross-sectional analysis of anatomical shape change over time via statistics on 4d within-subject flows. In *Proc. MICCAI Workshop on Spatio-Temporal Image Analysis for Longitudinal and Time-Series Image Data*, 2010.
- [68] Klein Arno, Andersson Jesper, Ardekani Babak A, Ashburner John, Avants Brian, Chiang Ming-Chang, Christensen Gary E, Collins D. Louis, Gee James, Hellier Pierre, Song Joo Hyun, Jenkinson Mark, Lepage Claude, Rueckert Daniel, Thompson Paul, Vercauteren Tom, Woods Roger P, Mann J. John, and Parsey Ramin V. Evaluation of 14 nonlinear deformation algorithms applied to human brain mri registration. *Neuroimage*, 46(3):786–802, Jul 2009.
- [69] Kobayashi H. and Hara F. Facial interaction between animated 3d face robot and human beings. In *Proc. IEEE Int Conference on Systems, Man, and Cybernetics Computational Cybernetics and Simulation*, volume 4, pages 3732–3737, 1997.
-

- 
- [70] Kuklisova-Murgasova Maria, Cifor Amalia, Napolitano R., Papageorghiou A., Quaghebeur G., Noble Alison, and Schnabel Julia. Registration of 3d fetal brain us and mri. In *Proc. 15th International Conference on Medical Image Computing and Computer-Assisted Intervention (MICCAI)*, 2012.
- [71] Lee Duhgoon, Nam Woo Hyun, Lee Jae Young, and Ra Jong Beom. Non-rigid registration between 3d ultrasound and ct images of the liver based on intensity and gradient information. *Physics in Medicine and Biology*, 56(1):117, 2011.
- [72] Lefébure Martin and Cohen Laurent D. Image registration, optical flow and local rigidity. *Journal of Mathematical Imaging and Vision*, 14:131–147, March 2001.
- [73] Liu Xiaoxiao, Saboo Rohit R, Pizer Stephen M, and Mageras Gig S. A shape-navigated image deformation model for 4d lung respiratory motion estimation. *Proc. IEEE International Symposium on Biomedical Imaging (ISBI)*, 2009:875–878, Jun 2009.
- [74] Liu Xiaoxiao, Davis Bradley, Niethammer Marc, Pizer Stephen, and Mageras. Gig. Prediction-driven respiratory motion atlas formation for 4d image-guided radiation therapy in lung. In *Proc. MICCAI Workshop on Pulmonary Image Analysis*, 09 2010.
- [75] Liu Xiaoxiao, Oguz I., Pizer Stephen. M., and Mageras Gig. S. Shape-correlated deformation statistics for respiratory motion prediction in 4d lung. In *Society of Photo-Optical Instrumentation Engineers (SPIE) Conference Series*, volume 7625 of *Society of Photo-Optical Instrumentation Engineers (SPIE) Conference Series*, March 2010.
- [76] Loeckx Dirk, Maes Frederik, Vandermeulen Dirk, and Suetens Paul. Non-rigid image registration using a statistical spline deformation model. In *Proc. 18th International Conference on Information Processing in Medical Imaging*, pages 463–474, 2003.
- [77] Loeckx Dirk, Maes Frederik, Vandermeulen Dirk, and Suetens Paul. Nonrigid image registration using free-form deformations with a local rigidity constraint. In *Proc. 7th International Conference on Medical Image Computing and Computer-Assisted Intervention (MICCAI)*, pages 639–646, 2004.
- [78] Lu Weiguo, Chen Ming-Li, Olivera Gustavo H, Ruchala Kenneth J, and Mackie Thomas R. Fast free-form deformable registration via calculus of variations. *Physics in Medicine and Biology*, 49(14):3067, 2004.
-

- 
- [79] Lu Xuesong, Zhang Su, Yang Wei, and Chen Yazhu. Sift and shape information incorporated into fluid model for non-rigid registration of ultrasound images. *Computer Methods and Programs in Biomedicine*, 100:123–131, November 2010.
- [80] Maes Frederick, Collignon Andre, Vandermeulen Dirk, Marchal Guy, and Suetens Paul. Multimodality image registration by maximization of mutual information. *IEEE Transactions on Medical Imaging*, 16(2):187–198, 1997.
- [81] Maintz J. B. and Viergever M. A. A survey of medical image registration. *Medical Image Analysis*, 2(1):1–36, Mar 1998.
- [82] Mansi T., Pennec X., Sermesant M., Delingette H., and Ayache N. Logdemons revisited: consistent regularisation and incompressibility constraint for soft tissue tracking in medical images. In *Proc. 13th International Conference on Medical Image Computing and Computer-Assisted Intervention (MICCAI)*, MICCAI’10, pages 652–659, Berlin, Heidelberg, 2010. Springer-Verlag.
- [83] Marchant T. E., Price G. J., Matuszewski B. J., and Moore C. J. Reduction of motion artefacts in on-board cone beam ct by warping of projection images. *British Journal of Radiology*, 84(999):251–264, Mar 2011.
- [84] Matuszewski B. J., Shen J. K., and Shark L.-K. Elastic image matching with embedded rigid structures using spring-mass system. In *Proc. International Conference on Image Processing (ICIP)*, volume 2, 2003.
- [85] Matuszewski B. J., Quan Wei, and Shark L.-K. High-resolution comprehensive 3-d dynamic database for facial articulation analysis. In *Proc. IEEE International Conference on Computer Vision Workshops (ICCVW)*, pages 2128–2135, 2011.
- [86] Matuszewski Bogdan J., Quan Wei, and Shark Lik-Kwan. *Biometrics - Unique and Diverse Applications in Nature, Science, and Technology*, chapter Facial Expression Recognition. InTech, 2011.
- [87] Maurer, C. R. Jr., Qi Rensheng, and Raghavan V. A linear time algorithm for computing exact euclidean distance transforms of binary images in arbitrary dimensions. *IEEE Transactions on Pattern Analysis and Machine Intelligence*, 25(2):265–270, 2003.
- [88] McGlashan Nicholas and King Andrew P. Capturing breathing motion variability using two signal motion models of the heart. In *Proc. Conference on Medical Image Understanding and Analysis (MIUA)*, pages 167–171, July 2011.
-

- 
- [89] Miller Michael I., Trouvé Alain, and Younes Laurent. Geodesic shooting for computational anatomy. *Journal of Mathematical Imaging and Vision*, 24:209–228, March 2006.
- [90] Modersitzki Jan. *Numerical Methods for Image Registration*. Oxford University Press, 2004.
- [91] Modersitzki Jan. Flirt with rigidity–image registration with a local non-rigidity penalty. *International Journal of Computer Vision*, 76:153–163, February 2008.
- [92] Modersitzki Jan. *FAIR: Flexible Algorithms for Image Registration*. SIAM, Philadelphia, 2009.
- [93] Mountney Peter and Yang Guang-Zhong. Motion compensated slam for image guided surgery. In *Proc. 13th International Conference on Medical Image Computing and Computer-Assisted Intervention (MICCAI), MICCAI'10*, pages 496–504, Berlin, Heidelberg, 2010. Springer-Verlag.
- [94] Nithiananthan S., Brock K. K., Daly M. J., Chan H., Irish J. C., and Siewerdsen J. H. Demons deformable registration for cbct-guided procedures in the head and neck: convergence and accuracy. *Medical Physics*, 36(10):4755–4764, Oct 2009.
- [95] Pantic Maja and Rothkrantz Leon J. M. Automatic analysis of facial expressions: The state of the art. *IEEE Transactions on Pattern Analysis and Machine Intelligence*, 22:1424–1445, 2000.
- [96] Papiez Bartłomiej W. and Matuszewski Bogdan J. Direct inverse deformation field approach to pelvic-area symmetric image registration. In *Proc. Conference on Medical Image Understanding and Analysis (MIUA)*, pages 193–197, July 2011.
- [97] Papiez Bartłomiej W., Zielinski Tomasz P., and Matuszewski Bogdan J. Deformable image registration - improved fast free form deformation. In *Proc. 5th International Conference on Computer Vision Theory and Applications (VISAPP)*, volume 1, pages 530–535, May 2010.
- [98] Papiez Bartłomiej W., Matuszewski Bogdan J., Shark Lik-Kwan, and Quan Wei. Facial expression recognition using log-euclidean statistical shape models. In *Proc. 1st International Conference on Pattern Recognition Applications and Methods (ICPRAM)*, 2012.
-

- 
- [99] Pfister T., Li Xiaobai, Zhao Guoying, and Pietikainen M. Recognising spontaneous facial micro-expressions. In *Proc. IEEE International Conference on Computer Vision (ICCV)*, pages 1449–1456, 2011.
- [100] Pluim Josien P. W., Maintz J. B. Antoine, and Viergever Max A. Mutual-information-based registration of medical images: a survey. *IEEE Transactions on Medical Imaging*, 22(8):986–1004, 2003.
- [101] Pohl Kilian M., Fisher John, Shenton Martha, McCarley Robert W., Grimson W Eric L., Kikinis Ron, and Wells William M. Logarithm odds maps for shape representation. In *Proc. 9th International Conference on Medical Image Computing and Computer-Assisted Intervention (MICCAI)*, pages 955–963, 2006.
- [102] Price Gareth and Christopher Moore. Comparative evaluation of a novel 3d segmentation algorithm on in-treatment radiotherapy cone beam ct images. In *Proc. SPIE Conference on Medical Imaging*, volume 6512(3), pages 38.1–38.11, San Diego, USA,, 2007.
- [103] Quan Wei, Matuszewski Bogdan J., Shark Lik-Kwan, and Ait-Boudaoud Djamel. Low dimensional surface parameterisation with applications in biometrics. In *Proc. International Conference on Medical Information Visualisation - BioMedical Visualisation (MediVis)*, pages 15–22, Washington, DC, USA, 2007. IEEE Computer Society.
- [104] Quan Wei, Matuszewski Bogdan J., Shark Lik-Kwan, and Ait-Boudaoud Djamel. 3-d facial expression representation using b-spline statistical shape model. In *Proc. Vision, Video and Graphics Workshop*, 2007.
- [105] Quan Wei, Matuszewski Bogdan J., Shark Lik-Kwan, and Ait-Boudaoud Djamel. Facial expression biometrics using statistical shape models. *EURASIP Journal on Advances in Signal Processing*, 2009:15:4–15:4, January 2009.
- [106] Quan Wei, Matuszewski Bogdan J., and Shark Lik-Kwan. Improved 3-d facial representation through statistical shape model. In *Proc. IEEE International Conference on Image Processing (ICIP)*, pages 2433–2436, 2010.
- [107] Risser Laurent, Heinrich Mattias, and Schnabel Julia. Piecewise-diffeomorphic registration of 3d ct/mr pulmonary images with sliding conditions. In *IEEE International Symposium on Biomedical Imaging (ISBI)*, 2012.
- [108] Roche Alexis, Malandain Grégoire, Pennec Xavier, and Ayache Nicholas. The correlation ratio as a new similarity measure for multimodal image registration. In *Proc. 1st International Conference on Medical Image Computing and*
-

- 
- Computer-Assisted Intervention (MICCAI)*, MICCAI '98, pages 1115–1124, London, UK, 1998. Springer-Verlag.
- [109] Rohr Karl. *Landmark-Based Image Analysis: Using Geometric and Intensity Models*. Kluwer Academic Publishers, Norwell, MA, USA, 2001.
- [110] Ruan Dan, A Jeffrey A. Fessler, Roberson Michael, Balter James, and B Marc Kessler. Nonrigid registration using regularization that accommodates local tissue rigidity. In *Proc. SPIE: Medical Imaging*, 2005.
- [111] Ruan Dan, Esedoglu Selim, and Fessler Jeffrey A. Discriminative sliding preserving regularization in medical image registration. In *Proc. IEEE International Symposium on Biomedical Imaging: From Nano to Macro*, ISBI'09, pages 430–433, Piscataway, NJ, USA, 2009. IEEE Press.
- [112] Rueckert Daniel, Sonoda L. I., Hayes Carmel, Hill Derek L. G., Leach Martin O., and Hawkes David J. Non-rigid registration using free-form deformations: Application to breast mr images. *IEEE Transactions on Medical Imaging*, 18(8):712–721, 1999.
- [113] Rueckert Daniel, Frangi Alejandro F., and Schnabel Julia A. Automatic construction of 3d statistical deformation models using non-rigid registration. In *Proc. 4th International Conference on Medical Image Computing and Computer-Assisted Intervention (MICCAI)*, pages 77–84. Springer-Verlag, 2001.
- [114] Rueckert Daniel, Frangi Alejandro F, and Schnabel Julia A. Automatic construction of 3-d statistical deformation models of the brain using nonrigid registration. *IEEE Transactions on Medical Imaging*, 22(8):1014–1025, Aug 2003.
- [115] Rueckert Daniel, Aljabar Paul, Heckemann Rolf A., Hajnal Joseph V., and Hammers Alexander. Diffeomorphic registration using b-splines. In *Proc. 9th International Conference on Medical Image Computing and Computer-Assisted Intervention (MICCAI)*, pages 702–709, 2006.
- [116] Sarrut David, Boldea Vlad, Miguet Serge, and Ginestet Chantal. Simulation of four-dimensional ct images from deformable registration between inhale and exhale breath-hold ct scans. *Medical Physics*, 33(3):605–617, Mar 2006.
- [117] Schmidt-Richberg Alexander, Ehrhardt Jan, Werner Rene, and Handels Heinz. Slipping objects in image registration: Improved motion field estimation with direction-dependent regularization. In *Proc. 12th International Conference on Medical Image Computing and Computer-Assisted Intervention (MICCAI)*, MICCAI '09, pages 755–762, Berlin, Heidelberg, 2009. Springer-Verlag.
-

- 
- [118] Schnabel Julia A., Rueckert Daniel, Quist Marcel, Blackall Jane M., Castellano-Smith Andy D., Hartkens Thomas, Penney Graeme P., Hall Walter A., Liu Haiying, Truwit Charles L., Gerritsen Frans A., Hill Derek L. G., and Hawkes David J. A generic framework for non-rigid registration based on non-uniform multi-level free-form deformations. In *Proc. 4th International Conference on Medical Image Computing and Computer-Assisted Intervention (MICCAI)*, pages 573–581, 2001.
- [119] Schneider D. C. and Eisert P. Fast nonrigid mesh registration with a data-driven deformation prior. In *Proc. IEEE International Conference on Computer Vision Workshops (ICCVW)*, pages 304–311, 2009.
- [120] Shan Caifeng, Gong Shaogang, and McOwan Peter W. Robust facial expression recognition using local binary patterns. In *Proc. IEEE International Conference on Image Processing (ICIP)*, pages 370–373, 2005.
- [121] Shen Jian-Kun, Matuszewski Bogdan J., Shark Lik-Kwan, and Moore Christopher J. Deformable image registration using spring mass system. In *Proc. the British Machine Vision Conference (BMVC)*, pages 1199–1208, 2006.
- [122] Shen Jian-Kun, Matuszewski Bogdan J., Shark Lik-Kwan, Skalski Andrzej, Zielinski Tomasz, and Moore Christopher J. Deformable image registration - a critical evaluation: Demons, b-spline ffd and spring mass system. In *Proc. 5th International Conference BioMedical Visualization: Information Visualization in Medical and Biomedical Informatics*, pages 77–82, Washington, DC, USA, 2008. IEEE Computer Society.
- [123] Shi Yonghong, Liao Shu, and Shen Dinggang. Learning statistical correlation of prostate deformations for fast registration. In *MICCAI Workshop on Machine Learning in Medical Imaging (MLMI)*, pages 1–9, 2011.
- [124] Shi Yonghong, Liao Shu, and Shen Dinggang. Learning statistical correlation for fast prostate registration in image-guided radiotherapy. *Medical Physics*, 38(11):5980–5991, Nov 2011.
- [125] Söhn M., Birkner M., Yan D., and Alber M. Modelling individual geometric variation based on dominant eigenmodes of organ deformation: implementation and evaluation. *Physics in Medicine and Biology*, 50(24):5893–5908, Dec 2005.
- [126] Shreve M., Godavarthy S., Goldgof D., and Sarkar S. Macro- and micro-expression spotting in long videos using spatio-temporal strain. In *Proc.*
-

- 
- IEEE International Conference Automatic Face & Gesture Recognition and Workshops (FG)*, pages 51–56, 2011.
- [127] Song Joo Hyun, Christensen Gary E., Hawley Jeffrey A., Wei Ying, and Kuhl Jon G. Evaluating image registration using nirep. In *Proc. 4th Workshop on Biomedical Image Registration (WBIR)*, pages 140–150, 2010.
- [128] Staring Marius, Klein Stefan, and Pluim Josien P W. Nonrigid registration with adaptive, content-based filtering of the deformation field. In J.M. Fitzpatrick J.M. Reinhardt, editor, *Proc. of SPIE Medical Imaging: Image Processing*, pages 212–221. SPIE, 2005. Work done at Image Sciences Institute (ISI) (UMC Utrecht, the Netherlands).
- [129] Staring Marius, Klein Stefan, and Pluim Josien P W. Evaluation of a rigidity penalty term for nonrigid registration. In A. Bartoli, N. Navab V. Lepetit, editor, *Proc. Workshop on Image Registration in Deformable Environments*, pages 41–50, 2006. Work done at Image Sciences Institute (ISI) (UMC Utrecht, the Netherlands).
- [130] Staring Marius, Klein Stefan, and Pluim Josien P W. A rigidity penalty term for nonrigid registration. *Medical Physics*, 34(11):4098–4108, Nov 2007.
- [131] Stefanescu Radu, Pennec Xavier, and Ayache Nicholas. Grid powered non-linear image registration with locally adaptive regularization. *Medical Image Analysis*, 8(3):325–342, Sep 2004.
- [132] Studholme Colin and Cardenas Valerie. A template free approach to volumetric spatial normalization of brain anatomy. *Pattern Recognition Letters*, 25: 1191–1202, July 2004.
- [133] Studholme Colin, Hill Derek L. G., and Hawkes David J. An overlap invariant entropy measure of 3d medical image alignment. *Pattern Recognition*, 32(1): 71–86, 1999.
- [134] Suri J. S., Wilson D., and Laxminarayan S. *Handbook of Biomedical Image Analysis: Volume 3: Registration Models (International Topics in Biomedical Engineering)*. Springer-Verlag New York, Inc., 2005.
- [135] Sweet Andrew and Pennec Xavier. A log-euclidean statistical analysis of dti brain deformations. In *Proc. of MICCAI Workshop on Computational Diffusion MRI*, Beijing, China, September 2010.
-

- 
- [136] Tao Guozhi, He Renjie, Datta Sushmita, and Narayana Ponnada A. Symmetric inverse consistent nonlinear registration driven by mutual information. *Computer Methods and Programs in Biomedicine*, 95:105–115, August 2009.
- [137] Thevenaz Philippe, Blu Thierry, and Unser Michael. Interpolation revisited [medical images application]. *IEEE Transactions on Medical Imaging*, 19(7):739–758, 2000.
- [138] Thirion Jean-Philippe. Image matching as a diffusion process: an analogy with maxwell’s demons. *Medical Image Analysis*, 2(3):243–260, Sep 1998.
- [139] Tian Ying-Li, Kanade Takeo, and Cohn Jeffrey F. *Handbook of Face Recognition*, chapter Facial Expression Analysis. Springer, 2011.
- [140] Tsai A., Yezzi, A. Jr., Wells W., Tempany C., Tucker D., Fan A., Grimson W. E., and Willsky A. A shape-based approach to the segmentation of medical imagery using level sets. *IEEE Transactions on Medical Imaging*, 22(2):137–154, 2003.
- [141] Vandemeulebroucke J., Sarrut D., and Clarysse P. Point-validated pixel-based breathing thorax model. In *Proc. International Conference on the Use of Computers in Radiation Therapy (ICCR)*, pages 195–199, Toronto, Canada, jun 2007.
- [142] Vemuri Baba C., Ye J., Chen Y., and Leonard Christiana Morison. Image registration via level-set motion: Applications to atlas-based segmentation. *Medical Image Analysis*, 7(1):1–20, 2003.
- [143] Vercauteren Tom, Pennec Xavier, Malis Ezio, Perchant Aymeric, and Ayache Nicholas. Insight into efficient image registration techniques and the demons algorithm. In *Proc. International Conference on Information Processing in Medical Imaging (IPMI)*, volume 4584 of *Lecture Notes in Computer Science*, pages 495–506, Kerkrade, The Netherlands, July 2007. Springer.
- [144] Vercauteren Tom, Pennec Xavier, Perchant Aymeric, and Ayache Nicholas. Symmetric log-domain diffeomorphic registration: A demons-based approach. In *Proc. 11th International Conference on Medical Image Computing and Computer-Assisted Intervention (MICCAI)*, MICCAI ’08, pages 754–761, Berlin, Heidelberg, 2008. Springer-Verlag.
- [145] Vercauteren Tom, Pennec Xavier, Perchant Aymeric, and Ayache Nicholas. Diffeomorphic demons: Efficient non-parametric image registration. *NeuroImage*, 45(1, Supp.1):S61–S72, March 2009.
-

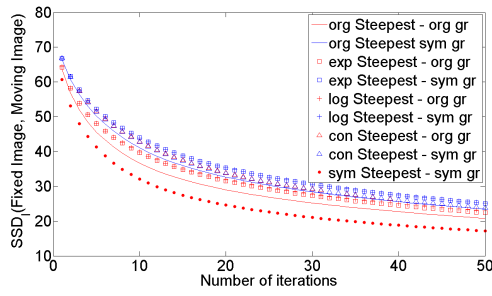
- 
- [146] Vialard Francois-Xavier, Risser Laurent, Holm Darryl, and Rueckert Daniel. Diffeomorphic atlas estimation using karcher mean and geodesic shooting on volumetric images. In *Proc. Conference on Medical Image Understanding and Analysis (MIUA)*, pages 55–59, July 2011.
- [147] Viola Paul and Wells, III William M. Alignment by maximization of mutual information. *International Journal of Computer Vision*, 24:137–154, September 1997.
- [148] Wang He, Dong Lei, O’Daniel Jennifer, Mohan Radhe, Garden Adam S, Ang K. Kian, Kuban Deborah A, Bonnen Mark, Chang Joe Y, and Cheung Rex. Validation of an accelerated ’demons’ algorithm for deformable image registration in radiation therapy. *Physics in Medicine and Biology*, 50(12):2887–2905, Jun 2005.
- [149] Wang Jun and Yin Lijun. Static topographic modeling for facial expression recognition and analysis. *Computer Vision and Image Understanding*, 108(1-2): 19–34, 2007.
- [150] Wang Yongmei Michelle and Staib Lawrence H. Physical model-based non-rigid registration incorporating statistical shape information. *Medical Image Analysis*, 4(1):7–20, 2000.
- [151] Weickert Joachim and Schnörr Christoph. A theoretical framework for convex regularizers in pde-based computation of image motion. *International Journal of Computer Vision*, 45:245–264, December 2001.
- [152] Wolz R., Aljabar P., Hajnal J. V., Lotjonen J., and Rueckert D. Manifold learning combining imaging with non-imaging information. In *Proc. IEEE International Symposium on Biomedical Imaging: From Nano to Macro*, pages 1637–1640, 2011.
- [153] Wu Guorong, Jia Hongjun, Wang Qian, and Shen Dinggang. Sharpmean: groupwise registration guided by sharp mean image and tree-based registration. *Neuroimage*, 56(4):1968–1981, Jun 2011.
- [154] Yacoob Y. and Davis L. S. Recognizing human facial expressions from long image sequences using optical flow. *IEEE Transactions on Pattern Analysis and Machine Intelligence*, 18(6):636–642, 1996.
- [155] Yang Deshan, Li Hua, Low Daniel A, Deasy Joseph O, and Naqa Issam El. A fast inverse consistent deformable image registration method based on sym-

- metric optical flow computation. *Physics in Medicine and Biology*, 53(21):6143–6165, Nov 2008.
- [156] Yi Zhao and Soatto S. Nonrigid registration combining global and local statistics. In *Proc. IEEE Conference on Computer Vision and Pattern Recognition (CVPR)*, pages 2200–2207, 2009.
- [157] Yin Lijun, Wei Xiaozhou, Sun Yi, Wang Jun, and Rosato M. J. A 3d facial expression database for facial behavior research. In *Proc. 7th International Conference on Automatic Face and Gesture Recognition (FGR)*, pages 211–216, 2006.
- [158] Yoo Terry S. *Insight into Images: Principles and Practice for Segmentation, Registration, and Image Analysis*. AK Peters Ltd, 2004.
- [159] Zhang Qinghui, Pevsner Alex, Hertanto Agung, Hu Yu-Chi, Rosenzweig Kenneth E, Ling C. Clifton, and Mageras Gig S. A patient-specific respiratory model of anatomical motion for radiation treatment planning. *Medical Physics*, 34(12):4772–4781, Dec 2007.
- [160] Zhang Yan, Matuszewski Bogdan J., Histace Aymeric, Precioso Frédéric, Kilgallon Judith, and Moore Christopher. Boundary delineation in prostate imaging using active contour segmentation method with interactively defined object regions. In *Proc. MICCAI Workshop on Prostate Cancer Imaging. Computer-Aided Diagnosis, Prognosis, and Intervention, MICCAI’10*, pages 131–142, Berlin, Heidelberg, 2010. Springer-Verlag.
- [161] Zhang Yan, Matuszewski Bogdan J., Histace Aymeric, and Precioso Frédéric. Statistical shape model of legendre moments with active contour evolution for shape detection and segmentation. In *Proc. 14th International Conference on Computer Analysis of Images and Patterns (CAIP)*, CAIP’11, pages 51–58, Berlin, Heidelberg, 2011. Springer-Verlag.
- [162] Zhang Zhijun, Jiang Yifeng, and Tsui Hungtat. Consistent multi-modal non-rigid registration based on a variational approach. *Pattern Recognition Letters*, 27:715–725, May 2006.
- [163] Zikic Darko, Baust Maximilian, Kamen Ali, and Navab Nassir. A general preconditioning scheme for difference measures in deformable registration. In *Proc. IEEE International Conference on Computer Vision (ICCV)*, 2011.
- [164] Zitová Barbara and Flusser Jan. Image registration methods: a survey. *Image and Vision Computing*, 21(11):977–1000, 2003.

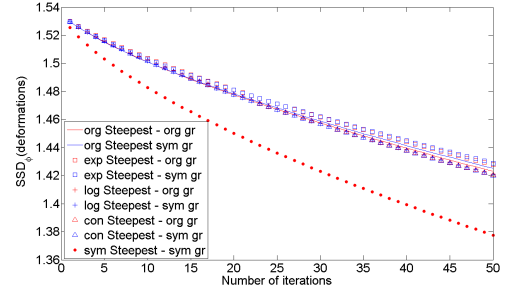
# Appendix A

## Results of registration using partially synthetic data

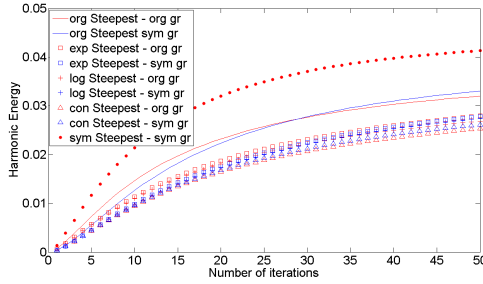
The results for the assessment done for the partially synthetic data are presented in Figure A.3 for the Demon approaches, in Figure A.2 for the Newton's iteration approaches, and in Figure A.1 for the steepest-like approaches. These figures show the evolutions of the several criteria that are chosen to describe the important properties of the deformation fields over the executed iterations. In addition, the evaluated algorithms utilise two types of gradients, gradient calculated using the original version of the algorithm that is denoted in figures as *org gr* and the symmetric gradient that uses the intensity information from the fixed and moving image at the same time is denoted in figures by *sym gr* (Equation 3.22). In the case of image registration with symmetric warping, only symmetric gradient is calculated (Equation 3.56).



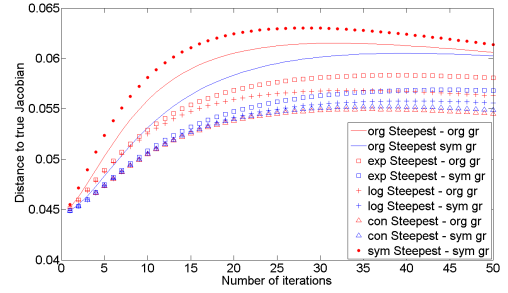
(a)



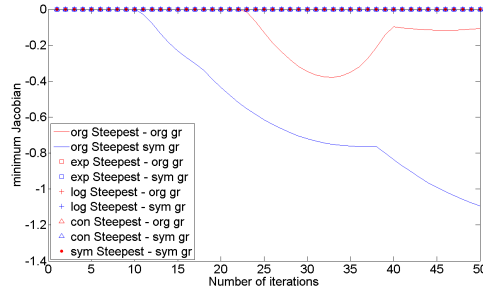
(b)



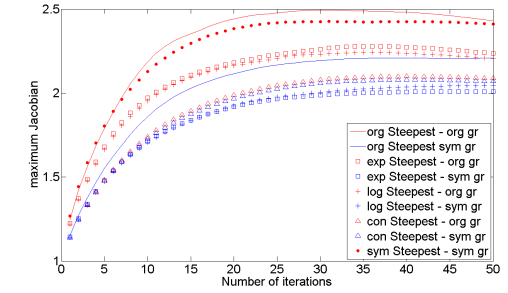
(c)



(d)



(e)



(f)

Figure A.1: Results obtained for the simulated data set using different types of the steepest-like approach (Algorithm 1). The convergence studies are shown for: (a) the average of the  $SSD_I$  between images, (b) the average of the  $SSD_{\vec{\varphi}}$  between estimated deformation field and ground truth deformation field, (c) the average  $HE$ , (d) the average distance to the real Jacobian, (e) the minimum and (f) the maximum determinant of the Jacobian matrix of the estimated transformation.

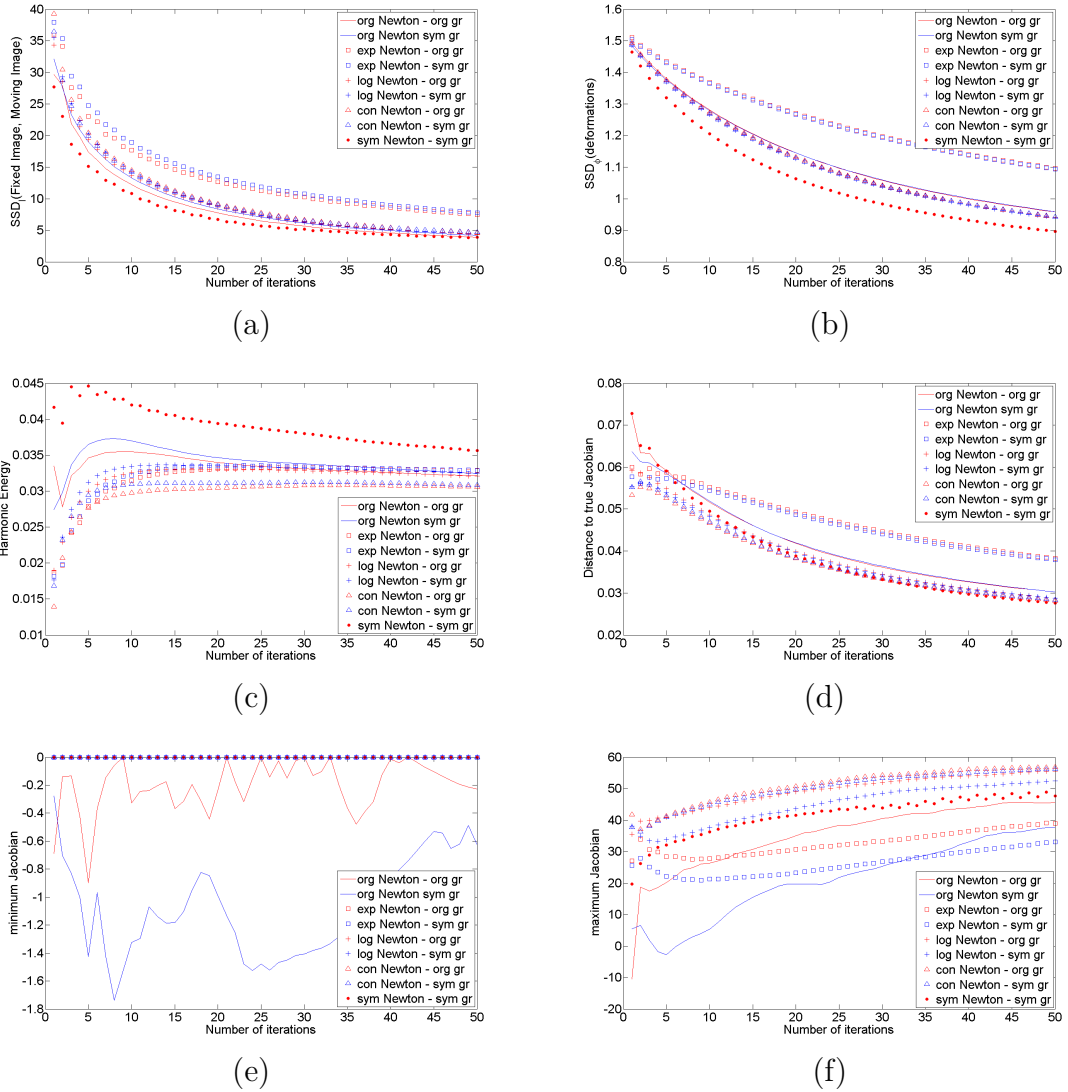
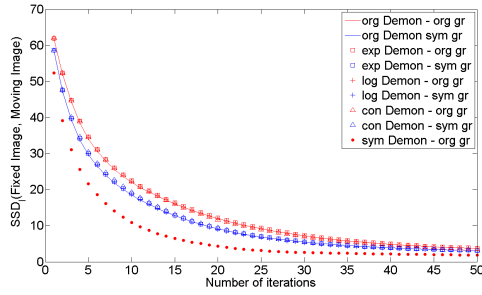
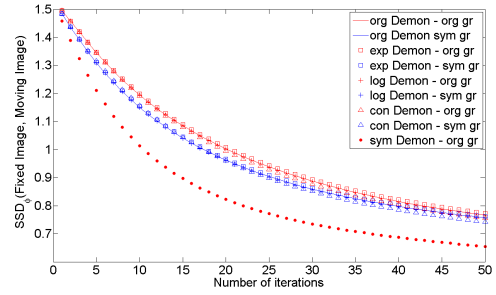


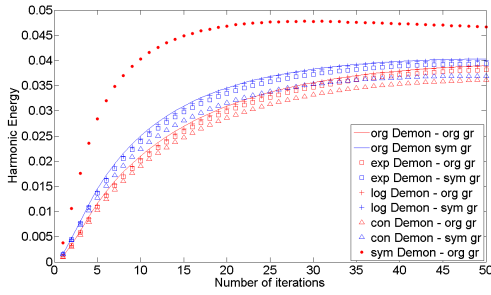
Figure A.2: Results obtained for the simulated data set using different types of the Newton's iteration approach (Algorithm 2). The convergence studies are shown for: (a) the average of the  $SSD_I$  between images, (b) the average of the  $SSD_{\bar{\varphi}}$  between estimated deformation field and ground truth deformation field, (c) the average  $HE$ , (d) the average distance to the real Jacobian, (e) the minimum and (f) the maximum determinant of the Jacobian matrix of the estimated transformation.



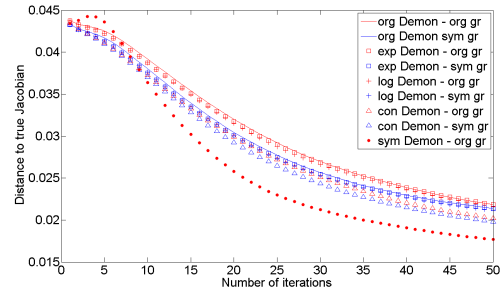
(a)



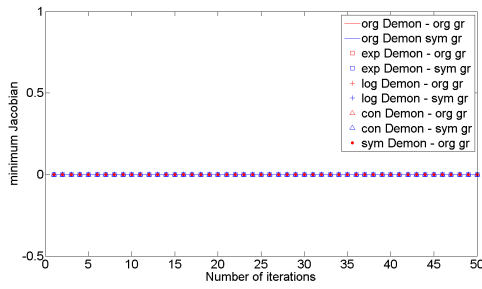
(b)



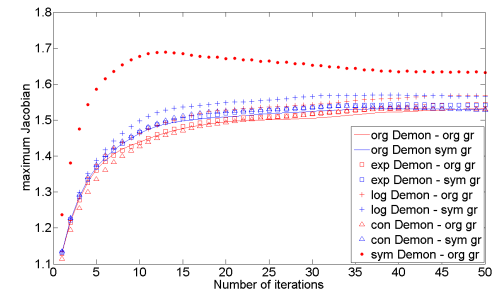
(c)



(d)



(e)



(f)

Figure A.3: Results obtained for the simulated data set using different types of the Demon approach (Algorithm 3). The convergence studies are shown for: (a) the average of the  $SSD_I$  between images, (b) the average of the  $SSD_D$  between estimated deformation field and ground truth deformation field, (c) the average  $HE$ , (d) the average distance to the real Jacobian, (e) the minimum and (f) the maximum determinant of the Jacobian matrix of the estimated transformation.

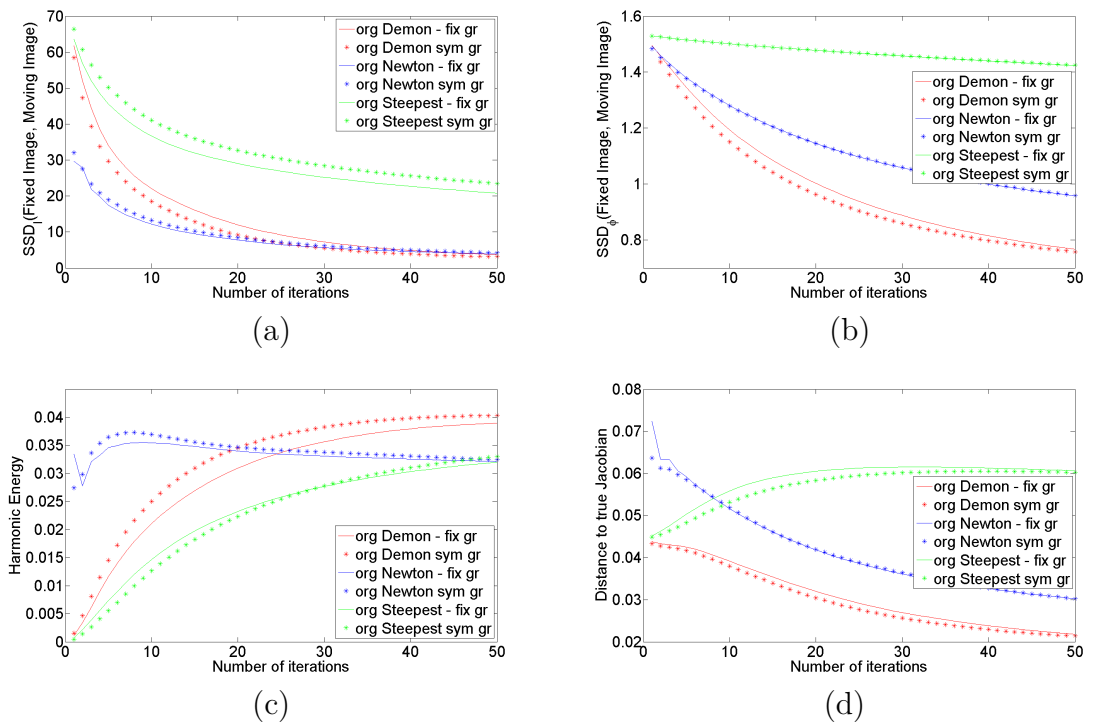


Figure A.4: Results obtained for the synthetic data set using different approaches. The convergence of the average value of: (a) the  $SSD_I$  between images, (b) the  $SSD_{\varphi}$  between the estimated transformation and the ground truth transformation, (c) the  $HE$ , and (d) the distance to the true Jacobian.

# Appendix B

## Results of facial expression recognition experiments

This appendix presents the confusion matrices of the remaining classifier methods for the different features of the Statistical Shape Vectors. The classifiers include the quadratic discriminant classifier (QDC), nearest neighbour classifier (NCC), and naive Bayes classifier (NBC) methods for the manually selected landmarks, the automatically selected landmarks, the deformation fields, and the velocity fields.

Table B.1: Confusion matrix of QDC for the manually selected landmarks

Input/ Output	Anger (%)	Disgust (%)	Fear (%)	Happiness (%)	Sadness (%)	Surprise (%)
Anger	<b>67.2</b>	7.8	4.2	2.1	18.8	0.0
Disgust	10.9	<b>75.5</b>	7.8	1.6	1.0	3.1
Fear	4.7	8.3	<b>63.5</b>	7.8	9.9	5.7
Happiness	1.6	4.7	11.5	<b>80.2</b>	1.0	1.0
Sadness	17.7	1.6	13.0	1.0	<b>64.6</b>	2.1
Surprise	0.5	1.6	4.2	0.5	0.0	<b>93.2</b>

Table B.2: Confusion matrix of QDC for the automatic selected landmarks

Input/ Output	Anger (%)	Disgust (%)	Fear (%)	Happiness (%)	Sadness (%)	Surprise (%)
Anger	<b>63.0</b>	7.3	5.2	2.1	22.4	0.0
Disgust	13.0	<b>67.2</b>	13.0	1.0	1.0	4.7
Fear	7.3	8.9	<b>57.8</b>	9.4	11.5	5.2
Happiness	2.1	3.1	13.0	<b>79.7</b>	0.5	1.6
Sadness	21.9	6.8	12.5	2.1	<b>55.7</b>	1.0
Surprise	0.5	3.1	4.7	0.0	0.5	<b>91.1</b>

Table B.3: Confusion matrix of QDC for the full deformation fields

Input/ Output	Anger (%)	Disgust (%)	Fear (%)	Happiness (%)	Sadness (%)	Surprise (%)
Anger	<b>44.8</b>	24.5	5.2	3.1	21.9	0.5
Disgust	7.8	<b>79.2</b>	7.3	1.6	3.1	1.0
Fear	2.1	15.1	<b>50.5</b>	10.4	14.1	7.8
Happiness	2.6	16.1	27.1	<b>50.0</b>	2.1	2.1
Sadness	17.7	12.0	17.7	3.1	<b>47.4</b>	2.1
Surprise	0.0	6.3	9.9	1.0	1.6	<b>81.3</b>

Table B.4: Confusion matrix of QDC for the full velocity fields

Input/ Output	Anger (%)	Disgust (%)	Fear (%)	Happiness (%)	Sadness (%)	Surprise (%)
Anger	<b>42.2</b>	25.0	5.2	6.3	19.3	2.1
Disgust	9.4	<b>75.0</b>	9.4	2.1	1.0	3.1
Fear	3.6	16.7	<b>46.3</b>	12.0	13.5	7.8
Happiness	2.1	13.0	28.1	<b>50.0</b>	3.1	3.6
Sadness	15.1	10.9	17.7	4.2	<b>49.0</b>	3.1
Surprise	1.0	6.8	7.8	1.0	2.1	<b>81.3</b>

Table B.5: Confusion matrix of NCC for the manually selected landmarks

Input/ Output	Anger (%)	Disgust (%)	Fear (%)	Happiness (%)	Sadness (%)	Surprise (%)
Anger	<b>63.5</b>	6.3	2.6	6.8	19.8	1.0
Disgust	20.3	<b>60.4</b>	5.2	6.3	6.3	1.6
Fear	12.0	3.6	<b>35.9</b>	19.8	17.2	11.5
Happiness	5.7	4.2	8.3	<b>78.1</b>	3.1	0.5
Sadness	27.1	2.6	15.1	6.3	<b>44.8</b>	4.2
Surprise	2.1	2.1	7.8	0.5	1.6	<b>85.9</b>

Table B.6: Confusion matrix of NCC for the automatic selected landmarks

Input/ Output	Anger (%)	Disgust (%)	Fear (%)	Happiness (%)	Sadness (%)	Surprise (%)
Anger	<b>68.2</b>	5.7	5.2	5.7	14.6	0.5
Disgust	18.2	<b>60.4</b>	8.3	4.7	5.7	2.6
Fear	17.2	8.3	<b>36.5</b>	17.2	10.4	10.4
Happiness	6.8	3.6	7.3	<b>79.7</b>	2.1	0.5
Sadness	32.8	1.0	18.8	3.1	<b>41.7</b>	2.6
Surprise	1.6	1.6	8.3	0.5	3.1	<b>84.9</b>

Table B.7: Confusion matrix of NCC for the full deformation fields

Input/ Output	Anger (%)	Disgust (%)	Fear (%)	Happiness (%)	Sadness (%)	Surprise (%)
Anger	<b>61.0</b>	6.3	3.1	7.3	21.9	0.5
Disgust	20.8	<b>48.4</b>	3.6	7.3	16.1	3.6
Fear	12.5	4.2	<b>36.0</b>	22.9	17.7	6.8
Happiness	9.9	8.3	13.0	<b>57.8</b>	8.9	2.1
Sadness	25.5	4.2	6.8	8.3	<b>46.9</b>	8.3
Surprise	2.1	0.5	2.6	1.0	6.8	<b>87.0</b>

Table B.8: Confusion matrix of NCC for the full velocity fields

Input/ Output	Anger (%)	Disgust (%)	Fear (%)	Happiness (%)	Sadness (%)	Surprise (%)
Anger	<b>60.0</b>	7.3	2.6	6.3	22.9	0.0
Disgust	19.8	<b>49.0</b>	8.9	8.9	13.5	3.1
Fear	11.5	5.7	<b>39.1</b>	21.9	16.1	5.7
Happiness	10.4	8.3	10.9	<b>59.9</b>	7.8	2.6
Sadness	25.5	3.1	4.7	8.9	<b>51.6</b>	6.2
Surprise	2.1	1.0	2.6	1.0	7.3	<b>85.9</b>

Table B.9: Confusion matrix of NBC for the manually selected landmarks

Input/ Output	Anger (%)	Disgust (%)	Fear (%)	Happiness (%)	Sadness (%)	Surprise (%)
Anger	<b>75.0</b>	6.3	3.1	2.6	13.0	0.0
Disgust	7.8	<b>79.2</b>	4.7	0.5	5.2	2.6
Fear	6.3	2.6	<b>54.2</b>	12.0	20.3	4.7
Happiness	5.2	0.5	5.2	<b>86.5</b>	1.0	1.6
Sadness	21.3	2.6	9.4	1.0	<b>63.5</b>	2.1
Surprise	3.1	2.1	3.1	1.0	3.1	<b>87.5</b>

Table B.10: Confusion matrix of NBC for the automatic selected landmarks

Input/ Output	Anger (%)	Disgust (%)	Fear (%)	Happiness (%)	Sadness (%)	Surprise (%)
Anger	<b>71.4</b>	4.2	7.3	2.6	14.1	0.5
Disgust	10.4	<b>72.9</b>	6.1	1.0	6.3	3.1
Fear	9.9	4.2	<b>54.7</b>	10.9	17.2	3.1
Happiness	3.6	3.1	10.4	<b>80.7</b>	1.0	1.0
Sadness	24.5	1.6	13.0	0.5	<b>59.4</b>	1.0
Surprise	2.6	2.6	4.7	1.0	3.1	<b>85.9</b>

Table B.11: Confusion matrix of NBC for the full deformation fields

Input/ Output	Anger (%)	Disgust (%)	Fear (%)	Happiness (%)	Sadness (%)	Surprise (%)
Anger	<b>68.2</b>	12.5	5.2	1.6	12.0	0.5
Disgust	8.3	<b>74.0</b>	6.8	6.8	3.6	0.5
Fear	4.2	11.0	<b>52.1</b>	14.6	11.5	6.8
Happiness	3.6	11.0	14.1	<b>69.3</b>	1.6	0.5
Sadness	17.2	4.7	8.9	5.2	<b>63.5</b>	0.5
Surprise	0.0	4.7	5.2	1.0	1.6	<b>87.5</b>

Table B.12: Confusion matrix of NBC for the full velocity fields

Input/ Output	Anger (%)	Disgust (%)	Fear (%)	Happiness (%)	Sadness (%)	Surprise (%)
Anger	<b>71.4</b>	12.0	2.1	1.0	12.5	1.0
Disgust	7.3	<b>75.5</b>	8.3	4.7	4.2	0.0
Fear	5.7	9.4	<b>53.1</b>	10.9	14.6	6.3
Happiness	4.2	9.4	14.6	<b>68.8</b>	2.1	1.0
Sadness	17.2	3.6	12.5	3.1	<b>63.5</b>	0.0
Surprise	1.6	4.2	4.7	1.6	1.0	<b>87.0</b>

# Appendix C

## Publications

- Bartłomiej W. Papież, Tomasz P. Zieliński, Bogdan J. Matuszewski, *Deformable Image Registration - Improved Fast Free Form Deformation*, VISAPP 2010 - Proceedings of the Fifth International Conference on Computer Vision Theory and Applications, Angers, France, May 17-21, 2010 - Volume 1, pp 530-535.
- Bartłomiej W. Papież, Bogdan J. Matuszewski *Direct inverse deformation field approach to pelvic-area symmetric image registration*, MIUA 2011 - Proceedings of the 15th Conference on Medical Image Understanding and Analysis, London, UK, July 14-15, 2011, pp 193-197.
- Bartłomiej W. Papież, Bogdan J. Matuszewski, Lik-Kwan Shark, Wei Quan, *Facial Expression Recognition using Log-Euclidean Statistical Shape Models*, ICPRAM 2012 - Proceedings of the First International Conference on Pattern Recognition Applications and Methods, Vilamoura, Portugal, February 6-8, 2012, pp 351-359.
- Bartłomiej W. Papież, Bogdan J. Matuszewski, *Symmetric image registration with directly calculated inverse deformation field*, The Annals of the British Machine Vision Association, 2012(6), pp 1-14.
- Bartłomiej W. Papież, Bogdan J. Matuszewski, Lik-Kwan Shark, Christopher Moore, *An implicit inter-subject shape driven image deformation model for prostate motion estimation*, 4th MICCAI Workshop on Computational and Clinical Applications in Abdominal Imaging (CCAIAI), Nice, France, October 1st, 2012, pp 218-228.
- Bartłomiej W. Papież, Bogdan J. Matuszewski, Lik-Kwan Shark, Wei Quan, *Facial Expression Recognition using Diffeomorphic Image Registration Framework*, Mathematical Methodologies in Pattern Recognition and Machine Learning - Contributions from the International Conference on Pattern Recognition

---

Applications and Methods, Springer Proceedings in Mathematics & Statistics,  
2012, in press, accepted manuscript